

DEVELOPMENT OF A COMPOSITE MATERIAL SHELL-ELEMENT MODEL  
FOR IMPACT APPLICATIONS

by

Tobias Achstetter  
A Dissertation  
Submitted to the  
Graduate Faculty  
of  
George Mason University  
In Partial Fulfillment of  
The Requirements for the Degree  
of  
Doctor of Philosophy  
Physics

Committee:

\_\_\_\_\_ Dr. Cing-Dao Kan, Committee Chair  
\_\_\_\_\_ Dr. Chi Yang, Committee Member  
\_\_\_\_\_ Dr. Dhafer Marzougui, Committee Member  
\_\_\_\_\_ Dr. Girum Urgessa, Committee Member  
\_\_\_\_\_ Dr. Paul So, Department Chair  
\_\_\_\_\_ Dr. Donna M. Fox, Associate Dean,  
Office of Student Affairs & Special  
Programs, College of Science  
\_\_\_\_\_ Dr. Ali Andalibi, Dean, College of Science

Date: \_\_\_\_\_ Fall Semester 2019  
George Mason University  
Fairfax, VA

Development of a Composite Material Shell-Element Model for Impact Applications

A dissertation submitted in partial fulfillment of the requirements for the degree of  
Doctor of Philosophy at George Mason University

By

Tobias Achstetter  
Master of Science  
George Mason University, 2015  
Bachelor of Science  
University of Stuttgart, 2014

Director: Dr. Cing-Dao Kan, Professor  
Department of Physics and Astronomy

Fall Semester 2019  
George Mason University  
Fairfax, VA

Copyright © 2019 by Tobias Achstetter  
All Rights Reserved

## Dedication

This dissertation is dedicated to my parents, Gabriele and Lothar, and to my fiancée, Emily, for their love and support throughout my research.

## Acknowledgments

I would like to thank my dissertation committee, Dr. Cing-Dao Kan, Dr. Chi Yang, Dr. Dhafer Marzougui and Dr. Girum Urgessa, who provided helpful advice throughout my research.

Thank you to all of the faculty and staff of the Center for Collision Safety and Analysis (CCSA) at George Mason University. I am especially grateful to Professor Cing-Dao Kan for his continued support and advice, both academic and technical, throughout my academic career. I would also like to acknowledge Dr. Chung-Kyu Park and Rudolf Reichert from the CCSA, from whom I have learned a great deal about automotive crash simulations.

I would like to thank Dr. Subramaniam Rajan, Dr. Robert Goldberg, and William Emerling from the Arizona State University (ASU), National Aeronautics and Space Administration (NASA), and the Federal Aviation Administration (FAA) respectively, for their technical and financial support under the project “Development and Implementation of an Orthotropic Plasticity Progressive Damage Model for Transient Dynamic/Impact Finite Element Analysis of Composite Structures”, sponsor award No. 16-847.

Thank you to Allen Sheldon from Honda R&D Americas for the financial support of the project “Development and Validation of Shell-Element Version of Material Model MAT\_213 in LS-DYNA for Simulation of Composite Materials” under award No. 4500302852. My thanks as well to Dr. Sheng Dong from The Ohio State University for the valuable discussions and for providing crush simulation models and results.

Acknowledgments to Gunther Blankenhorn from Livermore Software Technology Corporation (LSTC) for his support while implementing the developed material model and to Dr. John O. Hallquist for providing me with the opportunity to do so.

Deep thanks to Dr. Kelly S. Carney for his guidance and advice on composite materials. The in-depth knowledge he provided during the validation phase of this research was truly appreciated.

I would like to especially thank Paul Du Bois for his invaluable advice and mentorship throughout my PhD research. His expertise was instrumental and I cannot thank him enough for all he has taught me over the years I have been fortunate to work alongside him. Without his support this research would not have been possible.

Finally, I would like to thank my friends and family, especially my parents, Gabriele and Lothar, who have always supported me in all of the decisions I have made. Without them I would not be where I am today. Special thanks to my fiancée, Emily, who always goes above and beyond to support me.

# Table of Contents

	Page
List of Figures . . . . .	vii
List of Tables . . . . .	x
List of Symbols . . . . .	xi
List of Abbreviations . . . . .	xiv
Abstract . . . . .	xv
1 Introduction . . . . .	1
1.1 Background and Motivation . . . . .	1
1.2 Research Objectives . . . . .	2
2 Literature Review . . . . .	5
2.1 Composite Materials . . . . .	5
2.2 Modeling Techniques for Composites . . . . .	7
2.3 Damage and Damage Modeling in Composite Materials . . . . .	11
2.4 Failure and Failure Modeling in Composite Materials . . . . .	13
2.5 Delamination and Delamination Modeling . . . . .	30
2.6 Stochastic Variation of Composite Material Properties . . . . .	35
3 Methodology - Material Model Theory . . . . .	38
3.1 Stress-Strain Relation for an Orthotropic Linear Elastic Composite Material Model for Shell Elements . . . . .	38
3.2 Viscoelasticity . . . . .	44
3.2.1 The Standard Linear Solid Model . . . . .	44
3.2.2 Non-linear Viscoelasticity . . . . .	48
3.2.3 Generalization to 3D . . . . .	49
3.2.4 Strain-Rate Smoothing . . . . .	51
3.3 Viscoplasticity . . . . .	52
3.3.1 Yield Surface . . . . .	55
3.3.2 Non-associated Flow Rule . . . . .	62
3.3.3 Rate Dependency . . . . .	66
3.4 Coupling Viscoelasticity and Viscoplasticity . . . . .	67

3.5	Temperature Dependency . . . . .	69
3.6	Damage . . . . .	72
3.7	Generalized Tabulated Failure Criterion . . . . .	75
4	Implementation . . . . .	78
4.1	Required User Input and Output from History Variables . . . . .	78
4.2	Algorithm . . . . .	84
4.3	Stochastic Options . . . . .	99
4.4	Robustness: Switch to Associated Flow Rule or Radial Return . . . . .	102
5	Single Element Verification . . . . .	109
5.1	Deformation . . . . .	109
5.2	Strain-Rate-Dependency . . . . .	117
5.3	Temperature Dependency . . . . .	124
5.4	Damage . . . . .	128
5.5	Generalized Tabulated Failure Criterion . . . . .	131
5.6	Stochastic Effects . . . . .	138
6	Validation . . . . .	140
6.1	Validation in Ballistic Impact Loadcase . . . . .	140
6.2	Validation in Crush Loadcase . . . . .	155
7	Summary and Conclusion . . . . .	162
A	Appendix A: Matlab/Octave script . . . . .	165
B	Appendix B: Mathematica script . . . . .	166
	Bibliography . . . . .	167

## List of Figures

Figure	Page
1.1 Requirements for a composite material model for crash analysis . . . . .	3
2.1 Constituent materials of composites . . . . .	6
2.2 Architectures of composite materials . . . . .	7
2.3 Micro-mechanics vs macro-mechanics modeling approach . . . . .	8
2.4 Damage mechanisms . . . . .	12
2.5 Failure mechanisms . . . . .	17
2.6 Tsai-Wu failure surface in the x-y-plane . . . . .	20
2.7 Action and failure planes . . . . .	24
2.8 Stresses acting on rotated plane . . . . .	24
2.9 Puck’s master fracture body, representing the inter-fiber fracture surface . .	25
2.10 Puck fracture curve for $\sigma_{11} = 0$ , representing three fracture modes A, B, C	26
2.11 Double Cantilever Beam specimen and test setup . . . . .	31
2.12 End Notched Flexure specimen and test setup . . . . .	32
2.13 Traction separation laws of cohesive material models . . . . .	34
2.14 Cumulative distribution functions . . . . .	37
2.15 Fiber strength distribution of SCS-6 vendor fiber . . . . .	37
3.1 Forms of viscous behavior . . . . .	39
3.2 The plane stress state . . . . .	41
3.3 Standard linear solid model (Maxwell representation) . . . . .	44
3.4 Viscoelastic behavior at different rates . . . . .	46
3.5 Non-linear viscoelastic model . . . . .	48
3.6 Elastic-viscoplastic hardening model . . . . .	53
3.7 Creep and relaxation . . . . .	54
3.8 Example of a yield surface . . . . .	58
3.9 Convexity of surfaces . . . . .	58
3.10 Convexity correction of yield surface . . . . .	60
3.11 Example of a non-convex yield surface in 2D cutting planes . . . . .	61
3.12 Example of a convex yield surface in 2D cutting planes . . . . .	61

3.13	Example flow surfaces . . . . .	66
3.14	Viscoelastic viscoplastic coupling . . . . .	70
3.15	Failure angle . . . . .	76
3.16	Failure surface . . . . .	77
4.1	Required user input for each material direction . . . . .	81
4.2	Material model subroutine flow chart (Part 1) . . . . .	93
4.3	Material model subroutine flow chart (Part 2) . . . . .	94
4.4	Material model subroutine flow chart (Part 3) . . . . .	95
4.5	Material model subroutine flow chart (Part 4) . . . . .	96
4.6	Secant iteration example . . . . .	98
4.7	Possible distribution definitions for stochastic option . . . . .	100
4.8	Yield surface with no solution in non-associated flow . . . . .	103
4.9	Angle between flow and yield surface . . . . .	103
5.1	Boundary conditions of single element verification simulations . . . . .	110
5.2	Single element verification in 1-direction . . . . .	111
5.3	Yield surface evolution tension 1-direction . . . . .	112
5.4	Yield surface evolution compression 1-direction . . . . .	112
5.5	Single element verification in 2-direction . . . . .	113
5.6	Yield surface evolution tension 2-direction . . . . .	114
5.7	Yield surface evolution compression 2-direction . . . . .	114
5.8	Single element verification in 12-shear direction . . . . .	115
5.9	Yield surface evolution shear 12-direction . . . . .	116
5.10	Single element verification in out-of-plane shear directions . . . . .	117
5.11	45° Off-axis single element verification . . . . .	118
5.12	Effect of smoothing on the transverse and longitudinal strain-rates . . . . .	119
5.13	Rate-dependent single element verification . . . . .	121
5.14	Effective plastic strain-rate in compression 2-direction . . . . .	123
5.15	Viscoelasticity verification ( $\beta_{11} = 5000$ ) . . . . .	124
5.16	Viscoelastic stress relaxation and creep . . . . .	125
5.17	Viscoplastic stress relaxation and creep . . . . .	126
5.18	Single element verification of temperature effects . . . . .	128
5.19	Single element verification of damage model . . . . .	130
5.20	Single element verification of stress degradation . . . . .	132
5.21	Failure input . . . . .	134

5.22	Failure surface . . . . .	135
5.23	Verification of Generalized Tabulated Failure Criterion - tension . . . . .	136
5.24	Verification of Generalized Tabulated Failure Criterion - compression and shear	137
5.25	Stochastic single element verification . . . . .	139
6.1	Boundary conditions of the plate in the ballistic impact simulation . . . . .	141
6.2	Isometric view of the ballistic impact simulation setup . . . . .	142
6.3	Composite plate layup and modeling technique with cohesive elements . . .	143
6.4	Ballistic impact simulation material model input . . . . .	146
6.5	Projectile velocities in the LVG impact tests and simulations . . . . .	147
6.6	LVG1075 ballistic impact simulation . . . . .	148
6.7	LVG1074 ballistic impact simulation . . . . .	149
6.8	LVG1076 ballistic impact simulation . . . . .	150
6.9	LVG1076 ballistic impact, failure patterns on impact side, test versus simulation	152
6.10	LVG1076 ballistic impact, failure patterns on back side, test versus simulation	153
6.11	Failure patterns in LVG1075 simulation with rotated mesh . . . . .	154
6.12	LVG1074 ballistic impact, delamination, test versus simulation . . . . .	155
6.13	Crush simulation setup . . . . .	157
6.14	C-Channel modeling techniques, edge view . . . . .	158
6.15	Comparison of C-channel crush simulations using MAT58 and MAT213 . .	160
6.16	Comparison of crush simulations and test results . . . . .	161
B.1	Simplification of Equations 4.26 and 4.27 . . . . .	166

## List of Tables

Table	Page
2.1 LS-DYNA composite material models . . . . .	11
2.2 Required strength and elastic properties for FF . . . . .	23
2.3 Possible 2D stress combinations leading to the different IFF fracture modes	26
2.4 Required strength properties for IFF . . . . .	29
4.1 Required and optional stress vs. strain input . . . . .	79
4.2 MAT213 material cards one through seven . . . . .	80
4.3 Optional damage parameters . . . . .	82
4.4 User history variables (Part 1) . . . . .	85
4.5 User history variables (Part 2) . . . . .	86
4.6 Stochastic definition . . . . .	99
4.7 Stochastic options . . . . .	101
4.8 Occurrences of associated flow and radial return . . . . .	108
6.1 Cohesive material properties . . . . .	142
6.2 LVG ballistic impact tests, impact and rebound/exit velocities (rounded) .	144

## List of Symbols

$\langle \rangle$	Place holder for any variable
$\dot{\langle \rangle}$	Time derivative of $\langle \rangle$
$\Delta \langle \rangle$	Increment of $\langle \rangle$
$\langle \rangle^{fr}$	Fracture $\langle \rangle$ in Puck's failure model
$\langle \rangle^n$	$\langle \rangle$ at time step n
$\langle \rangle^{n+1}$	$\langle \rangle$ at time step n+1
$\langle \rangle_C$	Compressive $\langle \rangle$
$\langle \rangle_e$	Equilibrium $\langle \rangle$
$\langle \rangle_{eff}$	Effective $\langle \rangle$
$\langle \rangle_{el}$	Elastic $\langle \rangle$
$\langle \rangle_{eq}$	Equivalent $\langle \rangle$
$\langle \rangle_f$	Fiber $\langle \rangle$
$\langle \rangle_{fail}$	Failure $\langle \rangle$
$\langle \rangle_{ij}$	Tensor component ij
$\langle \rangle_p$	Plastic $\langle \rangle$
$\langle \rangle_t$	Trial $\langle \rangle$
$\langle \rangle_{tot}$	Total $\langle \rangle$
$\langle \rangle_T$	Tensile $\langle \rangle$
$\langle \rangle_v$	Viscous $\langle \rangle$
$\langle \rangle_y$	Yield $\langle \rangle$
$\mathbf{B}$	Viscoelastic decay matrix
$c_{ij}$	Component of the stiffness matrix
$\mathbf{C}$	Elastic stiffness matrix
$C_p$	Specific heat capacity
$d_{ij}^{kl}$	Damage coefficient in kl-direction due to loading in ij-direction

$e_c$	Compressive fiber mode in the Chang-Chang failure criterion
$e_d$	Compressive matrix mode in the Chang-Chang failure criterion
$e_f$	Tensile fiber mode in the Chang-Chang failure criterion
$e_m$	Tensile matrix mode in the Chang-Chang failure criterion
$E$	Young's modulus
$f$	Yield function
$F_{ij}$	Quadratic coefficient in yield function
$F_k$	Linear coefficient in yield function
$G$	Shear modulus
$G_I$	Strain energy release rate in Mode I
$G_{Ic}$	Mode I interlaminar fracture toughness
$G_{IIc}$	Mode II interlaminar fracture toughness
$h$	Plastic potential function
$H_{ij}$	Coefficient of plastic potential function
$m_{\sigma f}$	Stress magnification factor in Puck's failure criterion
$\mathbf{M}$	Damage tensor
$M_{ii}$	Component of the damage tensor
$p_{\perp\parallel}, p_{\perp\perp}$	Inclination parameter in Puck's failure criterion
$P$	Applied Load
$\mathbf{q}$	Yield stress vector
$R^A$	Fracture resistance of the action plane in Puck's failure criterion
$\mathbf{S}$	Elastic compliance matrix
$S_{ij}$	Failure stress in shear ij-direction
$t$	Time
$T$	Temperature
$U$	Total elastic energy
$U_{45}$	Tensile strength of a 45° off-axis specimen
$W_p$	Plastic work
$X$	Failure stress in the fiber direction
$Y$	Failure stress in matrix direction

$\beta$	Viscoelastic decay constant
$\boldsymbol{\beta}$	Viscoelastic decay vector
$\beta_t$	Taylor-Quinney coefficient
$\varepsilon$	Strain
$\boldsymbol{\varepsilon}$	Strain tensor
$\varepsilon_\eta$	Strain in a damper
$\eta$	Viscosity of a damper
$\theta$	Angle in Generalized Tabulated Failure Model
$\theta_{fr}$	Inclination angle of the fracture plane in Puck's failure criterion
$\lambda$	Plastic multiplier
$\nu$	Poisson's ratio
$\rho$	Density
$\sigma$	Stress
$\boldsymbol{\sigma}$	Stress tensor
$\sigma_{11D}$	Stress value for linear degradation in Puck's failure criterion
$\Phi$	Angle between flow and yield surface

## List of Abbreviations

CFRP	Carbon Fiber Reinforced Plastic
CMC	Ceramic Matrix Composites
CSV	Comma-Separated Value
CT	Computed Tomography
CVI	Chemical Vapor Infiltration
DCB	Double Cantilever Beam
EMA	Exponential Moving Average
ENF	End Notched Flexure
FF	Puck's Fiber Fracture Criterion
IFF	Puck's Inter-Fiber Fracture Criterion
MFB	Puck's Master Fracture Body
MMC	Metal Matrix Composites
NASA	National Aeronautics and Space Administration
NASA-GRC	NASA Glenn Research Center
NCAP	New Car Assessment Program
PMC	Polymer Matrix Composites
SMA	Simple Moving Average
TSSFAC	Timestep Scale Factor
VaRTM	Vacuum assisted Resin Transfer molding

# Abstract

## DEVELOPMENT OF A COMPOSITE MATERIAL SHELL-ELEMENT MODEL FOR IMPACT APPLICATIONS

Tobias Achstetter, PhD

George Mason University, 2019

Dissertation Director: Dr. Cing-Dao Kan

To achieve lower weight of vehicles and higher specific energy absorption in crush load cases, automotive companies are moving towards the utilization of composite materials. While the response to loading of traditional engineering materials, such as plastics and steel, is well understood and can be simulated accurately, designers of composite structures still rely heavily on physical testing of components to ensure the requirements of load bearing capabilities are met. The majority of composite material models that have been developed rely on non-physical material parameters that have to be calibrated in extensive simulations. A predictive model, based on physically meaningful input, is currently not available. The here presented material model is a step towards the goal of a truly predictive material model for composite materials.

The developed orthotropic material model includes the ability to define tabulated hardening curves for different loading directions with strain-rate and temperature dependency. Strain-rate dependency was achieved by coupling the theories of viscoelasticity and viscoplasticity to allow for rate dependency in both the elastic and plastic regions of the material deformation.

In crush and impact load cases the material is loaded beyond its capabilities, and therefore, accurate modeling of damage accumulation and failure is essential. A damage model was implemented, where a reduction of stiffness and stress degradation in the individual material directions can be tracked precisely. Modeling of failure and Finite Element erosion was achieved by implementing a new strain-based generalized tabulated failure criterion, where failure strains can be precisely defined for specific states of stresses.

Most components in the automotive industry are thin in comparison to their dimensions, shell (plane stress) elements are usually the Finite Elements of choice in these applications. Composite materials are generally used in a layup of plies with different fiber directions. These individual plies are very thin which leads to impractically small mesh sizes when modeled with three dimensional solid elements. The developed material model is, therefore, made available for shell elements.

Composite materials show a large variation in their response to loading; the material model incorporates the ability to define a statistical distribution for certain material parameters that were found to be of influence on a component level.

The tabulated nature of the input to the material model allows for the simulation of a large variety of composite materials ranging from fiber reinforced polymers to metal matrix composites.

In extensive verification and validation simulations during and after the development process, accuracy and reliability of the model in numerically challenging situations and realistic loading scenarios was ensured.

The presented material model can be implemented into most available Finite Element software. As part of this research it was implemented into the commercial Finite Element Solver LS-DYNA as \*MAT\_COMPOSITE\_TABULATED\_PLASTICITY\_DAMAGE (\*MAT\_213) for shell elements.

# Chapter 1: Introduction

## 1.1 Background and Motivation

In recent years, the demand for higher fuel efficiency and electric vehicles with a longer range has driven automotive manufacturers to invest in research of advanced composite materials to achieve a weight reduction of their fleets. To meet increasing requirements of passenger safety regulations and consumer tests, such as the US or European New Car Assessment Program (NCAP), automotive companies are moving towards composite materials which can achieve a high specific energy absorption when used efficiently.

As the material of choice in the automotive industry has historically been steel and aluminum, the response to loading of these materials is well understood and can be predicted accurately in simulations. These simulations, to a large extent, support the design process of vehicles. With the introduction of composite materials, the commonly used isotropic material models for metals are no longer able to predict the material response to loading accurately for all automotive materials.

Many anisotropic material models have been developed and implemented into popular finite element codes for composite material applications [1]. However, limitations of the existing material models constrain them for the use in specific load cases. While these models can predict linear loading fairly accurately, most are not well suited for crash analysis. Additionally, input parameters of the existing composite material models are often not physically meaningful and have to be calibrated iteratively in extensive simulations to match test results [2].

Composite materials are more difficult to model due to their non-homogeneous structure and anisotropic, non-linear, strain-rate and temperature dependency in their response to loading. Before failure occurs, composite materials exhibit damage and, therefore, gradually

decrease in the elastic stiffness when un- and reloaded. A numerical material model that has predictive capabilities under these circumstances must incorporate all of these effects. In a recent development, Arizona State University implemented a composite material model to account for most of the stated effects [3]. This model can be used with solid elements to simulate ballistic impacts, as done by the aerospace industry. As most structural parts in the automotive industry are thin in comparison to their dimensions, shell elements are usually the elements of choice in these applications. Therefore, the presented material model was made available for shell elements.

As composite material properties exhibit a strong stochastic variation, the effects of different distributions of material parameters on the macro-scale was evaluated. The user is able to define a stochastic distribution for certain material parameters that were determined to be influential on the component level.

Figure 1.1 summarizes the requirements for the presented material model with regards to the automotive and aerospace industry. In addition, the material model incorporates temperature effects which can be useful in other non-crash related load cases.

## 1.2 Research Objectives

The objective of this research was to develop and implement a composite material model with accurate predictive capabilities for automotive and aerospace crash applications. This orthotropic material model includes the ability to define tabulated hardening curves for different loading directions with strain-rate and temperature dependency. Damage accumulation in cyclic loading and a new generalized tabulated failure criterion were implemented.

As the material model was developed for automotive and aerospace applications, it was implemented for use with shell (plane stress) elements.

The tabulated material model enables simulation engineers to reliably predict the response of composite materials in various loading conditions using physically meaningful material input.

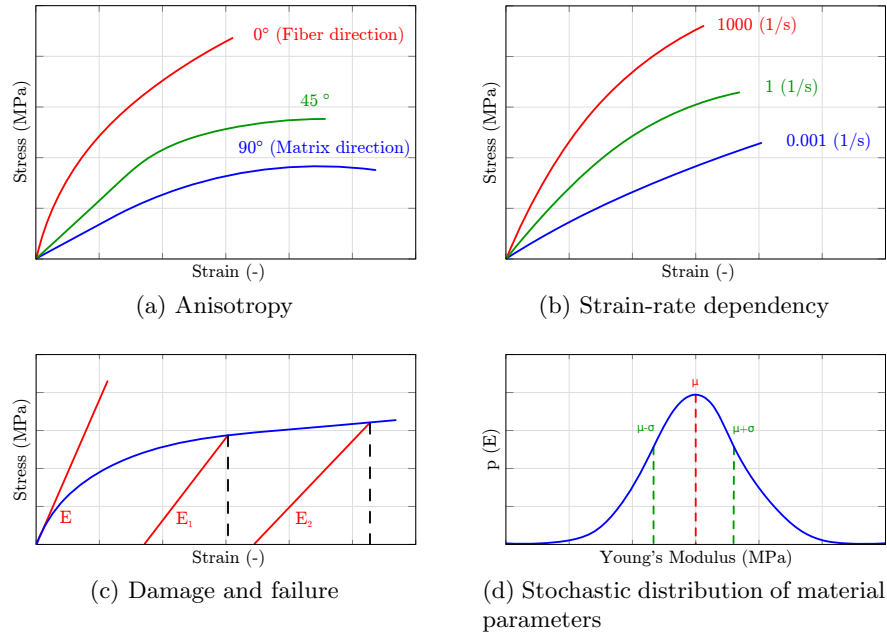


Figure 1.1: Requirements for a composite material model for crash analysis

As composite materials show a large variation in their response to loading, the material model incorporates the ability to define a statistical distribution for certain material parameters that were found to be of influence on a component level. Based on the material property variation of the constitutive materials (fiber and matrix), the variation of the material input for the developed continuum model was studied and its effects quantified.

The new constitutive model for deformation, damage accumulation, and fracture of composite materials was fully verified and its reliability and robustness was examined. During the development process of the material model and after completion of the implementation, the code was tested using single element verification simulations to ensure the basic capabilities were implemented correctly.

The code was then validated in a comparison with a fully validated industry standard material model. These validation simulations were chosen to demonstrate the benefits of the new material model in impact applications. As a baseline comparison, the simulation results were compared to a widely used composite material model that achieves a non-linear

material response using damage mechanics available in the Finite Element solver LS-DYNA [4]. The extensive verification and validation tasks ensure the reliability and robustness of the newly developed material model in large simulation models of more than one million elements.

The following summarizes the objectives of this research:

- Implementation of a fully tabulated material model for deformation with
  - strain-rate dependency
  - temperature dependency
  - damage accumulation
  - fracturefor use with shell elements;
- Physically meaningful material input;
- Implementation of a new tabulated failure criterion;
- Incorporation of capabilities to include statistical variation of material parameters into the material model;
- Verification and validation of the material model based on use cases of the automotive and aerospace industry.

No currently available plane stress material model for composites in commercially used Finite Element software offers all of these capabilities. The presented material model can be implemented into most Finite Element software and as part of this research was implemented into the commercial solver LS-DYNA, which is commonly used in the automotive and aerospace industries.

## Chapter 2: Literature Review

The second chapter describes the theoretical background of composite materials and their damage and failure characteristics. It furthermore outlines current modeling approaches and techniques along with their benefits and limitations.

Real world components made from unidirectional composite materials are generally manufactured with a layup of plies oriented at different angles. As the interlaminar strength holding these plies together can be weaker than the intralaminar strength, composites tend to delaminate under many loading conditions. The material model that was developed and is described in this work is focused on the intralaminar behavior of the composite. To model delamination and the interaction between plies, existing cohesive materials that can be used are described in this chapter.

### 2.1 Composite Materials

A composite is the combination of different materials which results in a new material that better utilizes the beneficial attributes of the constitutive materials while minimizing some of their deficiencies. Composite materials are not a human invention; for example, wood is a natural composite consisting of cellulose fibers and a resinous matrix of another polymer [5]. One of the first human-made composite materials was the combination of mud and straw to build walls of houses. Since then, composite materials have evolved to be one of the most advanced material classes in engineering use, with applications in all kinds of engineering fields ranging from racing bikes to aerospace wings and fuselages.

The sheer number of possible combinations of materials indicates the need for categorization. One way of classifying advanced composite materials is based on the matrix material [1]:

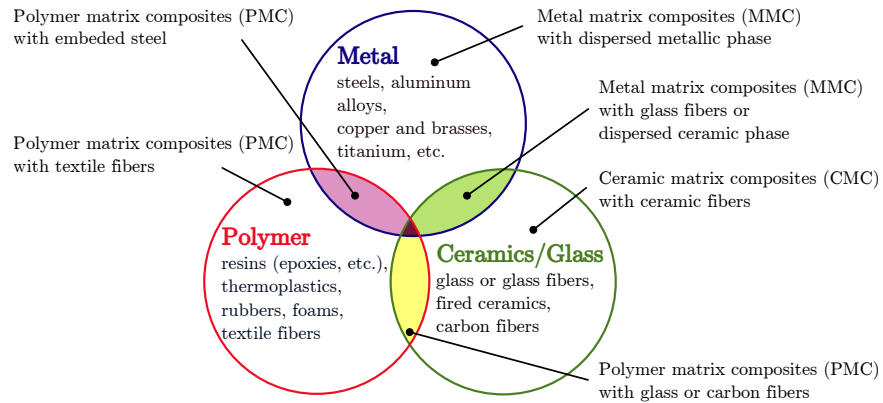


Figure 2.1: Constituent materials of composites (adapted from [5])

- Polymer matrix composites (PMC): Composed of a matrix from either thermosets or thermoplastics and embedded carbon, glass, kevlar or steel fibers.
- Metal matrix composites (MMC): Composed of a metallic matrix (e.g. iron, aluminum, magnesium, copper) and a dispersed ceramic or metallic phase.
- Ceramic matrix composites (CMC): Composed of a ceramic matrix and embedded fibers of other ceramic materials.

Figure 2.1 shows the three different composite material types based on the matrix material.

Another method to classify composite materials is based on the reinforcing material structure [1]:

- Particulate composite materials;
- Fibrous composite materials;
- Laminated composite materials;
- Combination of the first three types.

Figure 2.2 depicts the different reinforcing material structures of composites, with a particulate composite material shown in 2.2a, fibrous composite materials in Figure 2.2b, 2.2c and 2.2d, and a laminate of a continuous fiber reinforced composite shown in Figure 2.2c.

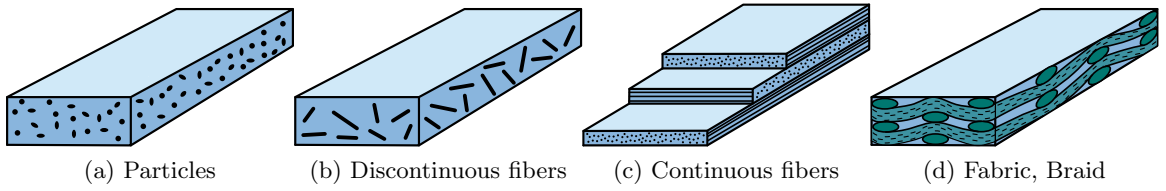


Figure 2.2: Architectures of composite materials

## 2.2 Modeling Techniques for Composites

Composite materials exhibit mechanical properties that are different from many commonly used engineering materials. These conventionally used materials are often homogeneous with the same proportions of their components throughout a given sample. Therefore, they exhibit isotropic mechanical properties, meaning that the material behavior is not dependent on the direction of the applied loading. On the other hand, composites are inhomogeneous and the constitutive materials can generally be distinguished by eyesight. The mechanical properties can depend highly on the orientation of the applied loading. Fiber reinforced composites, for example, are in general much stiffer in the fiber direction than in the transverse direction. Due to their inhomogeneous nature, composites are often studied from a micro-mechanical view, in addition to the macro-mechanical point of view.

In the micro-mechanics-based approach, the interaction of constituent materials is examined on a microscopic scale to determine their effect on the properties of the composite material [1]. The macro-mechanics, or continuum-based approach, presumes the material as homogeneous and the effects of the constituent materials are detected only as averaged (homogenized or “smeared”) apparent macroscopic properties of the composite material [1]. Both approaches have their advantages and disadvantages.

The micro-mechanics approach allows for a relatively easy switch of filler or matrix material and one can model failure mechanisms on the constituent level. It remains challenging, however, to model the bond between the fibers and the matrix material. The macro-mechanics approach, on the other hand, is the preferred method for problems on

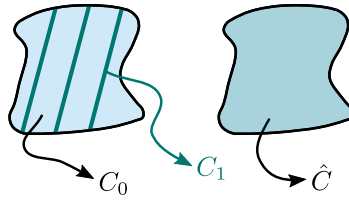


Figure 2.3: Micro-mechanics vs macro-mechanics modeling approach

the component or structural level (e.g., a full vehicle crash simulation) due to its higher computational efficiency. Figure 2.3 shows the difference between the two ways of modeling composites; in the micro-mechanics approach the properties of the fibers ( $\mathbf{C}_1$ ) and the properties of the matrix ( $\mathbf{C}_0$ ) are modeled individually, whereas in the macro-mechanics approach only the resulting properties of the combined material is considered ( $\hat{\mathbf{C}}$ ).

The material model that will be presented in the following chapters follows the macro-mechanics approach. This approach is the more commonly used method in component and full vehicle crash simulations and in structural designs of components due to its higher computational efficiency. Additionally, due to the challenging nature of modeling the fiber-matrix bond, macro-mechanical approaches offer advantages when modeling failure modes of composite materials.

Most commercially used Finite Element software offer options to model composite materials. Table 2.1 summarizes the available composite material models of the general-purpose Finite Element solver LS-DYNA with their capabilities that are important for crash analysis. In crash analysis the material is loaded to the point when breakage of material begins, so damage and failure progression must be considered. Significant strain-rate effects on the response of fiber reinforced composite materials have been studied and were shown in tests with the Split-Hopkinsons bar technique by Gilat et al. [6]. It was concluded that rate sensitive constitutive relations are required for adequate modeling of polymer matrix composites. Shen et al. [7] studied the effects of temperature on composite materials. While temperature did not affect the ultimate tensile strength of the material in the fiber direction, in the transverse (matrix) direction a rise in temperature caused a significant decrease

in the strength of the material. In the following paragraphs the available material models will be discussed, regarding their capabilities of modeling these effects.

Material type 22 is a linear elastic orthotropic material model for use with solid and shell elements. Many available models are at least to some degree based on this most basic model for composites. Brittle failure can be defined following the criteria of Chang and Chang [8]. This material model lacks the capabilities to model material non-linearity, with the exception of shear, due to damage and/or plasticity as well as rate sensitivity.

Material type 54 and 55 are linear elastic composite material models in which non-linearity is assigned entirely to damage accumulation. With MAT54, failure is modeled using the Chang-Chang criterion [8] while MAT55 utilizes the Tsai-Wu criterion [9]. Limited strain-rate sensitivity in both material types can be introduced by defining compressive, tensile, and shear strength values as a function of strain-rates. No rate sensitivity in the elastic region can be defined.

Material type 58 is available for solid and shell elements and models composites as linear elastic. Non-linearity is created entirely due to damage accumulation. MAT58 allows for the definition of rate sensitive moduli in the different material directions and, similarly to MAT54 and MAT55, rate sensitive strength in compression, tension, and shear can be defined [4]. To model damage, the continuum damage model developed by Matzenmiller et al. is utilized [10].

MAT158 is an enhancement of MAT58 and incorporates simple strain-rate effects. A viscous stress tensor is calculated on the basis of a generalized Maxwell model, where up to six terms of the Prony series expansion can be defined through their shear relaxation modulus and shear decay constant. This viscous stress tensor is then superimposed on the rate-independent stress tensor. However, this viscous stress tensor approach only works well for stress increases due to rate effects up to 15% [4].

Material type 59 is an orthotropic linear elastic material model that allows for definition of non-linearity in shear. MAT59 can model limited damage mechanisms as well as brittle failure by defining strength values in the different material directions [4].

Material Type 116, 117 and 118 are available for shell elements only and are used to model the elastic response of composite layups with an arbitrary number of layers through the thickness. They utilize a pre-integration to compute the stiffness for use with the Belytschko-Tsay resultant shell formulation [4]. No damage, failure, rate, or temperature effects can be specified.

MAT161 utilizes continuum damage mechanics to determine the initiation of fiber- or matrix-based failure using a stress to strength ratio in the different coordinate directions. Progressive failure is modeled using the methodology developed by Hashin [11]. MAT162 is a generalization of the failure model in MAT161. Both MAT161 and MAT162 require an additional license from Materials Sciences Corporation, which developed and supports these models.

Shell elements are generally used in automotive crush simulations, therefore, MAT221 and MAT223 cannot be used in these applications and will therefore not be considered.

Material types 261 and 262 are orthotropic continuum damage models for laminated fiber-reinforced composites that are implemented for shells and solid elements [4]. Both consider non-linear behavior in shear loading. Material 261 was developed and implemented by Pinho et al. [12], [13]. In Material 261 the matrix compression failure is based on the Mohr–Coulomb criterion, while for fibre kinking an initial fibre-misalignment angle is considered to trigger failure [12]. Material type 262 was developed and implemented by Maimí et al. [14], [15]. Progressive failure mechanisms in fiber and transverse directions are modeled by a set of scalar damage variables [14].

The goal of this research was to develop a composite material model for automotive and aerospace crash applications. As the material exhibits a wide range of strain-rates in crash analysis and composites show a high sensitivity to strain-rate variations, material models that do not offer these capabilities are not suitable. Four of the presented material models do not offer capabilities to define damage and failure, which renders them unusable for crash applications, and none of the presented composite material models include temperature effects as shown in Table 2.1.

Table 2.1: LS-DYNA composite material models

Material Model	Shells	Damage	Failure	Rate effects	Temperature effects
MAT_22	Yes	No	Yes	No	No
MAT_54	Yes	Yes	Yes	Yes	No
MAT_55	Yes	Yes	Yes	Yes	No
MAT_58	Yes	Yes	Yes	Yes	No
MAT_59	Yes	Yes	Yes	No	No
MAT_116	Yes	No	No	No	No
MAT_117	Yes	No	No	No	No
MAT_118	Yes	No	No	No	No
MAT_158	Yes	Yes	Yes	Yes	No
MAT_161/162	Yes	Yes	Yes	Yes	No
MAT_219	Yes	Yes	Yes	No	No
MAT_221	No	Yes	Yes	No	No
MAT_223	No	Yes	Yes	No	No
MAT_261	Yes	Yes	Yes	No	No
MAT_262	Yes	Yes	Yes	No	No

## 2.3 Damage and Damage Modeling in Composite Materials

Damage in a composite material is the forming of permanent microstructural changes to the material due to irreversible physical (or chemical) processes resulting from thermal or mechanical loading [16]. Different tensile or compression loads and loading directions can lead to micro-mechanical cracks in the matrix, fiber breakage, or to debonding of the fibers.

The response to loading in the fiber direction of composites is primarily characterized by the properties of the fiber due to their high strength and stiffness in comparison to the matrix material. The stiffness of a composite in the fiber direction is generally not impaired by damage of the matrix material. However, loading in the fiber direction may cause damage of said matrix material or the interface between fiber and matrix due to fiber straightening. A composite material damaged in such a way might not show a reduced stiffness in the fiber direction, but its effects will show transverse to the fibers when reloaded. When loaded in compression in the fiber direction, the fibers can kink, and damage to the matrix material can occur that may lead to stiffness reduction in both the initial loading direction and transverse to the fibers.

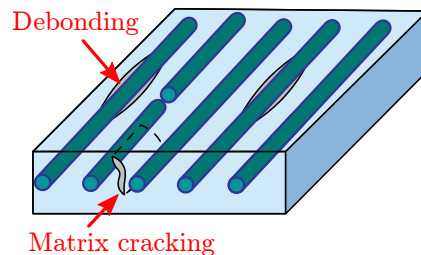


Figure 2.4: Damage mechanisms

Tension transverse to the fibers primarily leads to cracks in the matrix material that tend to propagate to the fiber-matrix bond as it generally offers the lowest strength in comparison to the constitutive materials [10]. Compression in the same direction leads to a crushing of the matrix material that is likely to reduce the stiffness in both the loading direction and in compression in the fiber direction.

Any damage to the matrix material can also have an effect on the material properties in shear loading. When undergoing shear deformations, graphite-epoxy composites form scallops in a saw tooth or wave-like pattern in the damaged resin [10]. This reduces their stiffness in the directions where the matrix properties are of high importance (e.g. compression, shear and tension transverse to the fibers). Figure 2.4 shows typical damage mechanisms of a fiber-reinforced composite.

In continuum damage mechanics, the damage mechanisms are represented by their effect on the macro (or continuum) scale of the composite. The degraded modulus is calculated based on continuum assumptions and either strength or fracture mechanics failure criteria. Strength and fracture mechanics failure criteria can both be utilized to characterize the onset of damage. Other damage models try to model damage mechanisms on the micro-scale such as micro-mechanics of damage, crack opening displacement methods, or computational micro-mechanics. While in continuum damage mechanics the damage is homogenized, micro-mechanic models attempt to simulate the actual geometry of the damage effects [17].

Many available material models for composites include a form of damage modeling to account for material non-linearity (e.g. Matzenmiller's continuum damage approach [10]) and stress degradation, while others use a plasticity approach like Sun et al. [18].

When using the plasticity-based approach, non-linear unloading and strain softening cannot be modeled. However, when using continuum damage mechanics, the shown rate dependency in composite materials is difficult to account for. Additionally, for some epoxy materials the fibers can straighten under tension without the fibers and the fiber-matrix bond breaking. Once the load is released, the stretched geometry is retained. Mathematically, this can be modeled using a plasticity based approach rather than using a damage model.

Damage and failure in composites are due to similar physical changes in the composite material. Unlike failure, damage is limited to the matrix material and fiber-matrix interface. While damage occurs on a micro-scale, failure mechanisms consider macro-mechanical changes in the material.

## **2.4 Failure and Failure Modeling in Composite Materials**

Due to the complexity of failure mechanisms in composites, the mathematical modeling of the relationship between the loading of the material and the initiation and progression of failure is significantly less developed than the analysis of other properties [19].

Traditional failure models for composite materials are able to predict the standard definition of failure in the material. These failure models describe the onset of failure and have therefore limited applicability as erosion criteria in finite element analysis of crush or impact load cases. In these types of loading, element erosion should not occur once a critical load was reached in a particular material direction because other directions might still be able to take significant loads. The traditional failure models are able to predict the onset of breakage well, which is generally the design criterion for composite components. The progressive failure with increasing fiber breakage, fiber-matrix debonding and delamination cannot be modeled with these traditional composite material failure models.

In classical continuum mechanics, the material is regarded, as the name suggests, as a continuum with the same properties throughout the solid. For composites, however, this assumption cannot hold true as the material properties vary significantly between the constituents of fiber and matrix. In many ways a composite could be regarded more as a structure than a material. For these reasons, considering failure mechanisms on the basis of the individual constituents can help to understand the nature of failure mechanisms of a composite. Clearly the strength of a unidirectional fiber reinforced composite depends on the orientation of the applied load with respect to the direction of the fibers. Furthermore, whether the load is applied as tension or as a compressive load is important when considering the different failure modes of a composite.

In the Department of Defense “Composite Materials Handbook”, failure modes in the axial (fiber direction) tension and compression are described and failure modes in the transverse (matrix direction) are reviewed [19].

### **Axial tensile strength**

The distinctions between four different failure modes in the fiber direction and under tensile loading are described in the following section. All of the presented models come with their own limitations in predicting the tensile stress of a composite. The mode in which failure occurs in a composite material is highly dependent upon the type of constituent material and architecture used, as well as manufacturing techniques. All of the models, however, highlight the importance of the variability of fiber strength and the characteristics of the matrix material on the tensile properties of a composite material [19].

- Weakest link failure:

This failure mode assumes that uniform strain exists within the composite and that failure occurs once the failure stress or strain of the fibers is reached. It is not taken into account that the failure strain of the fibers is not uniformly distributed [20]. Once a single fiber ruptures, a catastrophic mode of failure is produced as the fracture propagates freely without resistance [21]. The failure stress (or strain) calculated with

the weakest link approach is very low and, therefore, in practice with realistic layups in structures, failure generally should not be expected in this mode [19].

- Cumulative weakening failure:

If failure does not occur with the weakest link failure mode, the composite can be loaded further. While the stress increases, more fibers will start rupturing randomly throughout the composite with stresses being redistributed equally onto fibers in the vicinity [19]. The material will then fail once a critical load is met, at which point a sufficient number of fibers will have ruptured in the weakest cross section [21]. Fracture of individual fibers can be observed at loads significantly below the failure strength of the composite. The redistribution of load from the broken fiber happens through the matrix and, therefore, the bonding strength between the matrix and fiber is important in this failure mode [20].

- Fiber break propagation failure:

The cumulative weakening failure does not take into account how stress perturbations on fibers in the vicinity of the broken fiber will increase the probability that a second fiber will break; therefore, the likelihood increases that the crack propagates [19]. The failure mode of fiber break propagation failure considers the propagation of fiber breaks as a mechanism of failure [22]. Once the load increases beyond the point of the first initial fiber breakage, fiber ruptures accumulate until the material fails. Some of these fibers fail as a result of the original load, while others rupture because of stress concentrations due to being in the proximity of preceding fiber fractures [23].

- Cumulative group mode failure:

The cumulative group failure mode incorporates three effects that are presumed to be important in axial tensile failure. There exists a variability in fiber strength that leads to distributed fiber fractures at stress below the strength of the composite. Load concentrations form in fibers in the vicinity of a broken fiber that affect the crack propagation to additional fibers. Due to broken fibers and, in turn, stress

concentrations, shear stresses cause matrix failure or fiber-matrix de-bonding which can serve to stop the crack from propagating [22]. This mode of failure can be seen as a generalization of the cumulative weakening model [19].

### **Axial compressive strength**

For compressive loading in the fiber direction, both strength and stability failure has to be considered as microbuckling or kinking can occur to the fibers [19]. Unidirectional carbon fiber reinforced epoxy composites often offer less than 60% of their tensile strength when loaded in compression [24]. As the fibers can buckle, the matrix properties are of great importance in compression and the performance of the composite is limited by the matrix yield strength [19].

### **Matrix mode strength**

Tension and compression orthogonal to the fibers (matrix direction) and shear are the remaining failure modes. The phrasing as “matrix mode strength” is due to the fact that failure in these loading conditions can occur without rupture of fibers. The properties of the matrix material are the dominating factor as the stiff fibers are not aligned in the direction of the loading and therefore cannot carry the majority of the load. In shear, the properties of the composite depend on the plane of loading. In a plane that contains the fibers they are not contributing much to the reinforcement of the material while in a plane normal to the fibers some reinforcement might occur, depending on the volume fraction of filaments [19].

### **Composite strength in structures**

The failure mechanisms that were discussed in the previous paragraphs do not consider the layup of multidirectional laminates. Components made from many different layers of composite plies can sustain higher amounts of intralaminar failure before structural failure occurs. If a laminate from multidirectional plies is considered as a representative volume,

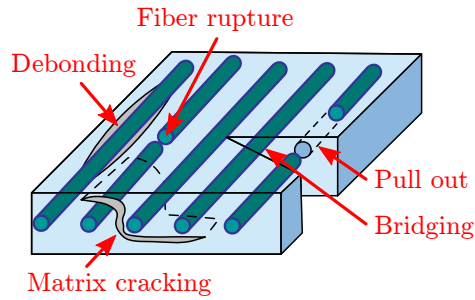


Figure 2.5: Failure mechanisms

the failure in the single ply would have to be viewed as damage mechanisms. The distributed microcracks lead to stiffness reductions of the corresponding ply with other layers picking up the load from the damaged ply. This continues until a macrocrack is formed, stretching over several plies, and the structure fails [14]. Figure 2.5 shows different intralaminar failure modes of a composite materials.

In the following paragraphs, some of the most common existing composite failure criteria will be presented. They have been used with some success to model the failure in fiber reinforced composite materials.

### **Tsai-Wu failure criterion**

The Tsai-Wu failure criterion allows one to model the failure of anisotropic composite materials with different strengths in tension and compression. It is a stress-based failure criterion and describes a surface in the six-dimensional stress space based upon the input of failure stresses in the different material directions.

The basic assumption behind the Tsai-Wu failure criterion is that a failure surface exists in stress space of the following general form [9]:

$$1 = \begin{bmatrix} F_1 & F_2 & F_3 & F_4 & F_5 & F_6 \end{bmatrix} \begin{bmatrix} \sigma_{11} \\ \sigma_{22} \\ \sigma_{33} \\ \sigma_{12} \\ \sigma_{23} \\ \sigma_{13} \end{bmatrix} + \begin{bmatrix} \sigma_{11} \\ \sigma_{22} \\ \sigma_{33} \\ \sigma_{12} \\ \sigma_{23} \\ \sigma_{13} \end{bmatrix}^T \begin{bmatrix} F_{11} & F_{12} & F_{13} & F_{14} & F_{15} & F_{16} \\ F_{21} & F_{22} & F_{23} & F_{24} & F_{25} & F_{26} \\ F_{31} & F_{32} & F_{33} & F_{34} & F_{35} & F_{36} \\ F_{41} & F_{42} & F_{43} & F_{44} & F_{45} & F_{46} \\ F_{51} & F_{52} & F_{53} & F_{54} & F_{55} & F_{56} \\ F_{61} & F_{62} & F_{63} & F_{64} & F_{65} & F_{66} \end{bmatrix} \begin{bmatrix} \sigma_{11} \\ \sigma_{22} \\ \sigma_{33} \\ \sigma_{12} \\ \sigma_{23} \\ \sigma_{13} \end{bmatrix} \quad (2.1)$$

The linear stress terms ( $\sigma_{ij}$ ) take into account differences between positive and negative failure stresses, while the quadratic stress terms ( $\sigma_{ij}\sigma_{ij}$ ) describe an ellipsoid in stress space [9].

For a closed and convex failure surface, the following inequality has to be satisfied:

$$F_{ii}F_{jj} - F_{ij}^2 \geq 0 \quad (2.2)$$

For orthotropic composite materials and assuming symmetry and plane stress, Equation 2.1 can be simplified:

$$1 = \begin{bmatrix} F_1 & F_2 & F_4 \end{bmatrix} \begin{bmatrix} \sigma_{11} \\ \sigma_{22} \\ \sigma_{12} \end{bmatrix} + \begin{bmatrix} \sigma_{11} \\ \sigma_{22} \\ \sigma_{12} \end{bmatrix}^T \begin{bmatrix} F_{11} & F_{12} & 0 \\ F_{12} & F_{22} & 0 \\ 0 & 0 & F_{44} \end{bmatrix} \begin{bmatrix} \sigma_{11} \\ \sigma_{22} \\ \sigma_{12} \end{bmatrix} \quad (2.3)$$

The abstract components of the strength tensor can be expressed in terms of engineering strengths, which can be measured in physical material tests.

Considering uniaxial loading in the fiber, or 1-direction ( $\sigma_{22} = \sigma_{12} = 0$ ), Equation 2.3 simplifies to:

$$1 = F_1\sigma_{11} + F_{11}\sigma_{11}^2 \quad (2.4)$$

And for a positive (tensile) failure stress  $X_T$ , one obtains:

$$1 = F_1 X_T + F_{11} X_T^2 \quad (2.5)$$

While for a negative (compressive) failure stress  $X_C$ , Equation 2.4 simplifies to:

$$1 = -F_1 X_C + F_{11} X_C^2 \quad (2.6)$$

From Equation 2.5 and 2.6 the components of the strength tensor  $F_1$  and  $F_{11}$  can be computed as:

$$F_{11} = \frac{1}{X_T X_C} \quad F_1 = \frac{1}{X_T} - \frac{1}{X_C} \quad (2.7)$$

Similarly, for uniaxial tension and compression in the matrix, or 2-direction, the strength tensor components  $F_2$  and  $F_{22}$  can be obtained:

$$F_{22} = \frac{1}{Y_T Y_C} \quad F_2 = \frac{1}{Y_T} - \frac{1}{Y_C} \quad (2.8)$$

A pure shear test in the 1-2 plane provides the necessary results to obtain the shear components of the strength tensor:

$$F_{44} = \frac{1}{S_{21} S_{12}} \quad F_4 = \frac{1}{S_{21}} - \frac{1}{S_{12}} \quad (2.9)$$

where  $S_{21}$  is the shear stress at failure and  $S_{12}$  is assumed equal to  $S_{21}$ .

Using a combined state of in-plane loading, component  $F_{12}$  can be determined. One option is to use a 45° tension test. For  $\sigma_{11} = \sigma_{22} = \frac{U_{45}}{2}$ , where  $U_{45}$  is the tensile strength of the 45° off-axis specimen, Equation 2.3 simplifies to:

$$\frac{U_{45}^2}{4} (F_{11} + F_{22} + 2F_{12}) + \frac{U_{45}}{2} (F_1 + F_2) = 1 \quad (2.10)$$

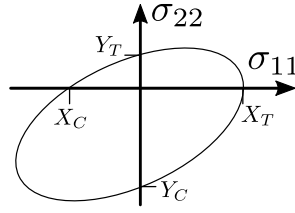


Figure 2.6: Tsai-Wu failure surface in the x-y-plane

From Equation 2.7, 2.8 and 2.10 one obtains:

$$F_{12} = \frac{2}{U_{45}^2} \left[ 1 - \frac{U_{45}}{2} \left( \frac{1}{X_T} - \frac{1}{X_C} + \frac{1}{Y_T} - \frac{1}{Y_C} \right) - \frac{U_{45}^2}{4} \left( \frac{1}{X_T X_C} + \frac{1}{Y_T Y_C} + \frac{1}{S_{21}^2} \right) \right] \quad (2.11)$$

An example of a cutting plane through a Tsai-Wu failure surface is shown in Figure 2.6.

### Chang-Chang failure criterion

The Chang-Chang failure model combines progressive damage and failure and degrades the material properties once failure occurs. The degradation of the material properties is dependent on the failure mechanism that the model predicts [8].

The Chang-Chang failure criterion, in plane-stress for a linear elastic material, is defined as follows in this section [8].

Tensile fiber mode:

$$e_f^2 = \left( \frac{\sigma_{11}}{X_T} \right)^2 + \left( \frac{\sigma_{12}}{S_{21}} \right)^2 \quad (2.12)$$

where failure is reached when  $e_f \geq 1$  and, as a result,  $E_{11}$ ,  $E_{22}$ ,  $G_{12}$ ,  $\nu_{12}$  and  $\nu_{21}$  are set to zero.

Compressive fiber mode:

$$e_c^2 = \left( \frac{\sigma_{11}}{X_C} \right)^2 \quad (2.13)$$

where failure is reached when  $e_c \geq 1$  and, as a result,  $E_{11}$ ,  $\nu_{12}$  and  $\nu_{21}$  are set to zero.

Tensile matrix mode:

$$e_m^2 = \left( \frac{\sigma_{22}}{Y_T} \right)^2 + \left( \frac{\sigma_{12}}{S_{21}} \right)^2 \quad (2.14)$$

Failure due to matrix cracking occurs when  $e_m > 1$  and, therefore, the transverse modulus  $E_{22}$ , shear modulus  $G_{12}$ , and the Poisson's ratio  $\nu_{21}$  are reduced to zero.

Compressive matrix mode:

$$e_d^2 = \left( \frac{\sigma_{22}}{2S_{21}} \right)^2 + \left[ \left( \frac{Y_C}{2S_{21}} \right)^2 - 1 \right] \frac{\sigma_{22}}{Y_C} + \left( \frac{\sigma_{12}}{S_{21}} \right)^2 \quad (2.15)$$

Compressive failure due to crushing of the matrix occurs when  $e_d^2 \geq 1$  and, as a result, the transverse modulus  $E_{22}$ , shear modulus  $G_{12}$ , and the Poisson's ratios  $\nu_{12}$  and  $\nu_{21}$  are reduced to zero.

### **Puck failure criterion**

Puck's failure criterion is stress-based and distinguishes between fiber failure and inter-fiber failure. In contrast to more traditional failure criteria, like the Tsai-Wu failure criterion, Puck's fracture surface consists of two sub-surfaces based on the two considered failure modes: fiber failure and inter-fiber failure. This allows for a better representation of the differences between both fracture types and for a more accurate representation of an ideal failure surface for a unidirectional composite [25].

Fiber Fracture (FF):

The Fiber Fracture part of Puck's model handles the two simple load cases of tension and compression in the fiber direction [26].

The fracture stress in the fiber  $\sigma_{11f}^{fr}$  is computed using Hooke's law while assuming the fracture strain in the fiber is equal to the overall fracture strain in the loading direction. The fracture strain can then be replaced, again using Hooke's law, with the ratio of the strength of the composite in tension ( $X_T$ ) or compression ( $-X_C$ ) respectively, over the homogenized modulus of the composite ( $E_{11}$ ). While the effects of residual stresses and non-linearity are neglected, the stress in the fibers at failure, due to the application of a uniaxial stress,  $\sigma_{11}$  is, therefore, given as follows in Equation 2.16 [25]:

$$\sigma_{11f}^{fr} = E_{11f}\varepsilon_{11}^{fr} = E_{11f}\frac{\pm X_{T/C}}{E_{11}} \quad (2.16)$$

Considering the case of plane stress, the transverse stress ( $\sigma_{22}$ ) does influence the strain in the fiber direction due to the Poisson's effect. This effect is locally magnified as the stress in the matrix is not equally distributed and increases closer to the fiber. Puck takes this into account by the use of a stress magnification factor  $m_{\sigma f}$  [26]. The subscript  $f$  in Equation 2.17 denotes a stress/stiffness/Poisson's ratio in the fiber.

$$\frac{\sigma_{11f}^{fr}}{E_{11f}} - \frac{\nu_{12f}}{E_{22f}}m_{\sigma f}\sigma_{22} = \frac{\sigma_{11}^{fr}}{E_{11}} - \frac{\nu_{12}}{E_{22}}\sigma_{22} \quad (2.17)$$

For the two-dimensional case, it is now assumed that fiber fracture occurs when the stress in the fiber reaches the same stress as given in Equation 2.16 for the one-dimensional case. By using the relations  $\frac{\nu_{12}}{E_{22}} = \frac{\nu_{21}}{E_{11}}$  and  $\frac{\nu_{12f}}{E_{22f}} = \frac{\nu_{21f}}{E_{11f}}$ , from Equations 2.16 and 2.17, then follows [25]:

$$\sigma_{11}^{fr} = \pm X_{T/C} + \left( \nu_{21} - \nu_{21f}\frac{E_{11}}{E_{11f}}m_{\sigma f} \right) \sigma_{22} \quad (2.18)$$

To make use of the failure criterion in Finite Element applications, we can replace the fracture stress  $\sigma_{11}^{fr}$  with an arbitrary stress in the one-direction  $\sigma_{11}$  and define an equivalent

Table 2.2: Required strength and elastic properties for FF

Component	Input parameter
Tensile strength 1-direction	$X_T$
Compressive strength 1-direction	$X_C$
Composite stiffness 1-direction	$E_{11}$
Fiber stiffness 1-direction	$E_{11f}$
Poisson's ratio of the composite	$\nu_{21}$
Poisson's ratio of the fibers	$\nu_{21f}$

stress  $\sigma_{11_{eq}}$  to replace the tensile/compressive strength in Equation 2.18:

$$\sigma_{11_{eq}} = \sigma_{11} - \left( \nu_{21} - \nu_{21f} \frac{E_{11}}{E_{11f}} m_{\sigma f} \right) \sigma_{22} \quad (2.19)$$

where failure is defined to occur once  $\frac{\sigma_{11_{eq}}}{\pm X_{T/C}} \geq 1$ .

For the onset of failure, when the stress in 1-direction  $\sigma_{11}$  reaches the fracture stress  $\sigma_{11}^{fr}$  and, therefore,  $\sigma_{11_{eq}} = \pm X_{T/C}$ , Equation 2.19 then becomes the same as Equation 2.18.

Inter-fiber fracture (IFF):

Puck's inter-fiber fracture criterion is founded on Mohr's hypothesis that the fracture limit of a material is determined by the stresses on the fracture plane [27]. The combination of stresses acting on that plane are related to the strength of the plane to determine whether failure occurs or not [26]. While for a unidirectional loading orthogonal to the fibers, the action plane (Figure 2.7a) on which the stress is applied to is parallel to the fracture plane (Figure 2.7d). Stresses acting on a composite material in a specific plane do not necessarily lead to failure in a plane parallel to that action plane. Due to large variations in stiffness and strength between the material directions owing to the alignment of the fibers, a pure compression loading, shown in Figure 2.7b for example, leads to fracture in a plane at an angle compared to the action plane (see fracture plane in Figure 2.7e). Similarly, for a pure in-plane shear loading, as shown in Figure 2.7c, the failure plane is parallel with the action

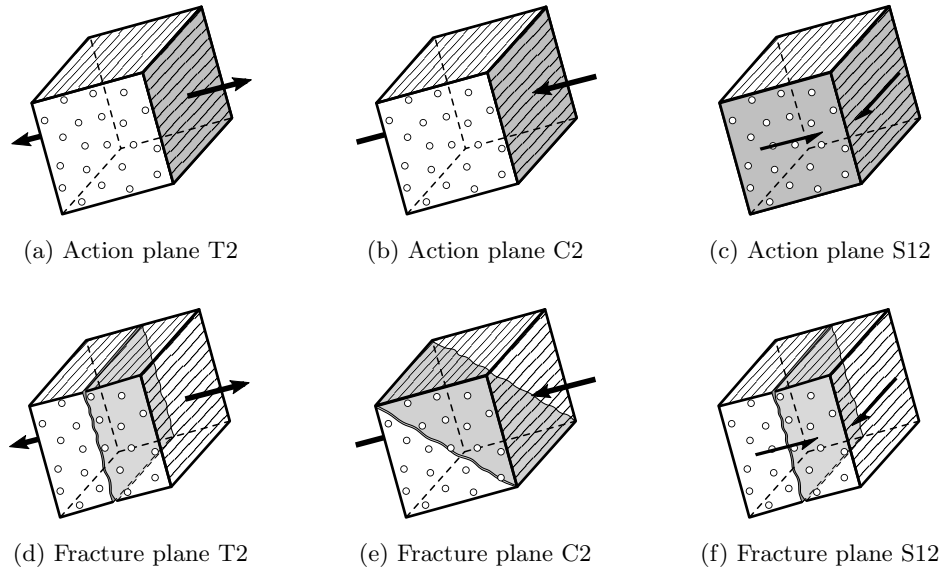


Figure 2.7: Action and failure planes (adapted from [25])

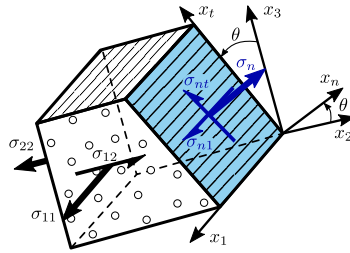


Figure 2.8: Stresses acting on rotated plane

plane that is aligned with the fibers, as depicted in Figure 2.7f.

For a state of plane stress, the stresses acting on an arbitrarily inclined plane that is rotated about the  $x_1$ -axis (parallel to the fibers) are shown in Figure 2.8. The normal and shear stresses acting on this plane at angle  $\theta$  in terms of the applied stresses can be computed following Equations 2.20:

$$\begin{aligned}
 \sigma_{11} &= \sigma_{11} & \sigma_n &= \sigma_{22} \cos^2 \theta \\
 \sigma_{nt} &= -\sigma_{22} \sin \theta \cos \theta & \sigma_{n1} &= \sigma_{21} \cos \theta
 \end{aligned}
 \tag{2.20}$$

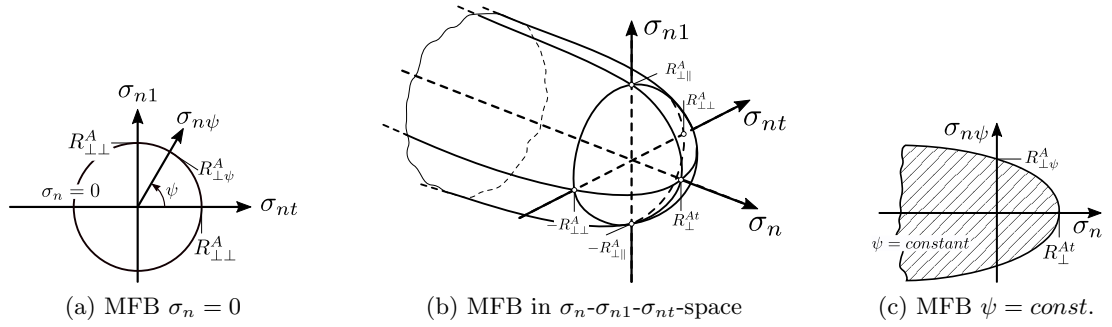


Figure 2.9: Puck’s master fracture body, representing the inter-fiber fracture surface (adapted from [25])

These three stresses act on a common action plane and must, therefore, be compared to the fracture resistance  $R^A$  (superscript A representing the action plane) of this specific action plane and not the strength in the principal material directions [28].

With the assumption that compressive stresses acting on the plane ( $-\sigma_n$ ) impede failure, while tensile stresses ( $+\sigma_n$ ) promote failure, Puck proposes a “Master Fracture Body (MFB)” which is shown in Figure 2.9 [26]. It shows a visual representation of the IFF criterion in the stress space of the action plane ( $\sigma_n, \sigma_{nt}, \sigma_{n1}$ ). As shown in Figure 2.9a for  $\sigma_n = 0$ , failure due to shear acting on the plane is represented by an ellipse which expands for increasing compressive normal stress (impeding failure) and shrinks for increasing tensile normal stresses (promoting failure) as described by the parabola in Figure 2.9c.

For different stresses on this plane, three failure modes are identified and are shown in Table 2.3. For any normal tensile stress, failure occurs in Mode A with a fracture plane angle of zero degrees. If isolated shear stress in the  $n1$ -direction occurs, the material fails at Mode A as well. Mode B and C describe failure due to compressive normal stresses, where Mode B occurs for a combination with  $n1$ -directional stress and leads to a fracture plane at an angle of zero degrees. Mode C describes stress states that lead to an inclined failure plane aligned with the fibers. As the plane is inclined, shear stresses in the  $nt$ -direction develop.

Table 2.3: Possible 2D stress combinations leading to the different IFF fracture modes [26]

Mode A $\theta_{fp} = 0^\circ$	Mode B $\theta_{fp} = 0^\circ$	Mode C $\theta_{fp} \neq 0^\circ$
$\{\sigma_{nT} \ 0 \ 0\}$	$\{\sigma_{nC} \ 0 \ \sigma_{n1}\}$	$\{\sigma_{nC} \ \sigma_{nt} \ \sigma_{n1}\}$
$\{\sigma_{nT} \ 0 \ \sigma_{n1}\}$		$\{\sigma_{nC} \ \sigma_{nt} \ 0\}$
$\{0 \ 0 \ \sigma_{n1}\}$		

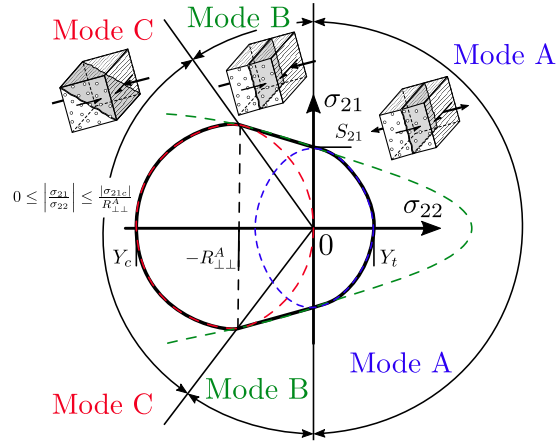


Figure 2.10: Puck fracture curve for  $\sigma_{11} = 0$ , representing three fracture modes A, B, C (adapted from [28])

Three-dimensional stress states could lead to fracture plane stress states of  $\sigma_{nt}$  and  $\sigma_{n1}$  without the occurrence of normal stress  $\sigma_n$ . In this case, the differentiation by Mode A, B and C is no longer adequate [26]. For two-dimensional stress states, the IFF-criterion can be expressed in terms of the principal material directions. The failure envelopes of the three modes are described using three separate equations that describe two ellipses (Mode A and C) and one parabola (Mode B). Figure 2.10 shows an example of the failure envelopes for the different failure modes in the  $\sigma_{22}$ - $\sigma_{21}$ -space.

Mode A ( $\sigma_{22} \geq 0$ ):

For tensile stresses in the 2-direction, failure occurs in a plane normal to the loading direction. The failure envelope in the  $\sigma_{22}$ - $\sigma_{21}$ -space can be described with an ellipse and is defined by Equation 2.21 [28]:

$$\sqrt{\left(\frac{\sigma_{21}}{S_{12}}\right)^2 + \left(1 - \frac{p_{\perp\parallel}^{(+)}}{S_{12}} Y_T\right)^2 \left(\frac{\sigma_{22}}{Y_T}\right)^2} + \frac{p_{\perp\parallel}^{(+)}}{S_{21}} \sigma_{22} = 1 - \left|\frac{\sigma_{11}}{\sigma_{11D}}\right| \quad (2.21)$$

In Figure 2.10, an example of this ellipse is shown as a blue dashed line. The component  $\left|\frac{\sigma_{11}}{\sigma_{11D}}\right|$  in Equation 2.21 describes the degradation effect of stresses occurring in the fiber direction leading to a shrinking of the fracture surface under the condition of geometric similarity [28].

Mode B  $\left(\sigma_{22} < 0 \text{ and } 0 \leq \left|\frac{\sigma_{22}}{\sigma_{21}}\right| \leq \frac{R_{\perp\perp}^A}{|\sigma_{21c}|}\right)$ :

Similar to Mode A, failure in Mode B occurs in a plane with the normal in the 2-direction. The failure curve can be described using a parabola as defined by Equation 2.22 [28]:

$$\frac{1}{S_{21}} \left( \sqrt{\sigma_{21}^2 + \left(p_{\perp\parallel}^{(-)} \sigma_{22}\right)^2} + p_{\perp\parallel}^{(-)} \sigma_{22} \right) = 1 - \left|\frac{\sigma_{11}}{\sigma_{11D}}\right| \quad (2.22)$$

In Figure 2.10, an example of this parabola is shown as a green dashed line.

Mode C  $\left(\sigma_{22} < 0 \text{ and } 0 \leq \left|\frac{\sigma_{21}}{\sigma_{22}}\right| \leq \frac{|\sigma_{21c}|}{R_{\perp\perp}^A}\right)$ :

Mode C describes failure at an inclined fracture plane ( $\theta_{fp} \neq 0$ ) due to a combination of shear and compressive normal stress. Puck showed that the normal stress  $\sigma_n$  in the fracture plane is constant for all possible inclined fracture planes in Mode C failure. Between  $\sigma_{22} = 0$  and,  $\sigma_{22} = -R_{\perp\perp}^A$ , the fracture angle is  $\theta_{fp} = 0$  and the normal stress  $\sigma_n$  is equal to the compressive stress in 2-direction  $\sigma_{22}$ . When the compressive stress exceeds the value of

$-R_{\perp\perp}^A$ , the fracture plane adjusts so that  $\sigma_n = \sigma_{22} \cos^2 \theta_{fp}$  remains constant [28]. For a two-dimensional state of loading stress, failure due to Mode C can therefore be expressed by an ellipse described by Equation 2.23 [28]:

$$\left[ \left( \frac{\sigma_{21}}{2(1 + p_{\perp\perp}^{(-)})S_{21}} \right)^2 + \left( \frac{\sigma_{22}}{Y_C} \right)^2 \right] \frac{Y_C}{-\sigma_{22}} = 1 - \left| \frac{\sigma_{11}}{\sigma_{11D}} \right| \quad (2.23)$$

In Figure 2.10 an example of this ellipse is shown as a red dashed line.

Table 2.4 lists all required parameters for the Puck IFF criterion and recommended values for a Carbon Fiber Reinforced Plastic (CFRP) material. Similar to other failure models, such as Tsai and Wu's, the tensile and compressive strengths in the transverse direction need to be defined as well as the shear strength in-plane. The inclination parameters  $p_{\perp\parallel}^{(+/-)}$  influence the shape of the failure surface and can be determined by fitting Equations 2.21 through 2.23 to experimental observations. Deuschle and Kröplin found values of 0.3 and 0.35 respectively to work well for carbon fiber reinforced plastics [29].  $\sigma_{11D}$  describes the effect of individual fiber fractures due to loading in the fiber direction and leads to a shrinkage of the failure surface while the stress in the fiber direction increases. This continues until failure occurs for a maximum stress as determined by the Fiber Failure criterion. This value can be determined experimentally by combined loading in fiber and transverse direction. Puck recommends a value of approximately 1.1 times the fiber strength in tension or compression respectively [28].

Table 2.4: Required strength properties for IFF

Component	Input parameter	Recommended value for CFRP
Tensile strength 2-direction	$Y_T$	Material-dependent
Compressive strength 2-direction	$Y_C$	Material-dependent
Shear strength in 12-plane	$S_{21}$	Material-dependent
Inclination parameter	$p_{\perp\parallel}^{(-)}$	0.3 [29]
Inclination parameter	$p_{\perp\parallel}^{(+)}$	0.35 [29]
Stress value for linear degradation	$\sigma_{11D}$	$\approx 1.1X_T$ or $\approx -1.1X_C$ [28]

The other parameters that are not given by the user, but are utilized in Equations 2.21 through 2.23, are derived using the following relationships [28]:

$$\begin{aligned}
 R_{\perp\perp}^A &= \frac{S_{21}}{2p_{\perp\parallel}^{(-)}} \left( \sqrt{1 + 2p_{\perp\parallel}^{(-)} \frac{Y_C}{S_{21}}} - 1 \right) \\
 p_{\perp\perp}^{(-)} &= p_{\perp\parallel}^{(-)} \frac{R_{\perp\perp}^A}{S_{21}} \\
 \sigma_{21c} &= S_{21} \sqrt{1 + 2p_{\perp\perp}^{(-)}}
 \end{aligned} \tag{2.24}$$

Unlike in the Tsai-Wu failure model, which is mathematically defined by a single equation, the Puck failure model is defined by essentially five individual surfaces (FF tension, FF compression, Mode A, Mode B, Mode C) and therefore allows for a more accurate modeling of failure in fiber reinforced composites.

Both failure models that were discussed in this chapter allow for modeling of the onset of failure in composite materials. The knowledge of when onset of failure in the component of interest occurs is helpful for designers to dimension layups and thicknesses of a part that is not supposed to fail during its life cycle. In energy absorbing structures, or parts that undergo impact loading, modeling of only the onset of failure is not enough to accurately simulate the material behavior. In these cases, modeling the “post-peak” (maximum stress) behavior of the material is essential.

## 2.5 Delamination and Delamination Modeling

Ply of fiber reinforced composite materials are generally laminated together to create layups that can be individually arranged to fulfill the load bearing capabilities of the composite part. As these plies are combined into a layup, the interface between the two composite laminae is naturally weaker than the fiber reinforced ply itself. Considering delamination as an additional failure mode can, therefore, be critical the capabilities of a part made from composite materials.

Delamination is commonly accounted for by modeling the interface between composite plies using cohesive zone elements. The material input data required for cohesive materials is generally obtained by conducting Double Cantilever Beam (DCB) and end-notched flexure (ENF) tests that will be described in the following two paragraphs. Examples of cohesive zone material models available for the finite element solver LS-DYNA will be discussed later in this section.

### Double Cantilever Beam test

The Mode I composite material delamination that occurs primarily in tension can be characterized using the Double Cantilever Beam specimen. This method is limited to unidirectional carbon and glass fiber laminates. The aim of this test is to determine the Mode I interlaminar fracture toughness  $G_{Ic}$ , which is the critical value of the strain energy release rate  $G_I$  for delamination growth as a result of an opening load or displacement.  $G_I$  is defined as follows [30]:

$$G_I = -\frac{1}{b} \frac{dU}{da} \quad (2.25)$$

where  $U$  is the total elastic energy in the test specimen,  $b$  the specimen width, and  $a$  the delamination length.

Figure 2.11 shows the specimen and test setup. Forces are applied to the end of the Double Cantilever Beam through hinges or loading blocks. The displacement or cross-head movement is controlled while the load and delamination length are measured. With the

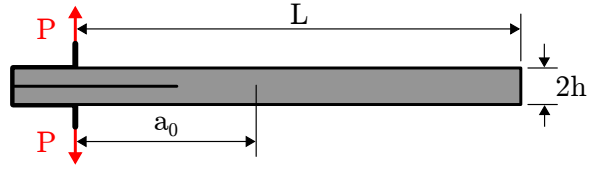


Figure 2.11: Double Cantilever Beam specimen and test setup

information from the load versus opening displacement data, the Mode I interlaminar fracture toughness is calculated using either a modified beam theory or compliance calibration method [30].

The Modified Beam Theory expression for the strain energy release rate of a double cantilever beam, which is clamped at the delamination front, is given as the following equation [30]:

$$G_I = \frac{3P\delta}{2ba} \quad (2.26)$$

where  $P$  is the applied load and  $\delta$  the load point displacement length.

Formula 2.26 will overestimate  $G_I$  due to possible rotation at the delamination front. To correct for this overestimation, a slightly longer delamination length  $a + |\Delta|$  is used, which may be determined in experiments. Therefore, equation 2.26 changes to:

$$G_I = \frac{3P\delta}{2b(a + |\Delta|)} \quad (2.27)$$

### End Notched Flexure test

The Mode II composite material delamination that occurs in shear loading can be characterized using the End-Notched Flexure test. This method is limited to unidirectional carbon and glass fiber laminates. The aim of this test is to determine the Mode II interlaminar fracture toughness  $G_{IIc}$  [31].

Figure 2.12 shows the test setup with the specimen being loaded in the middle between the two supports.

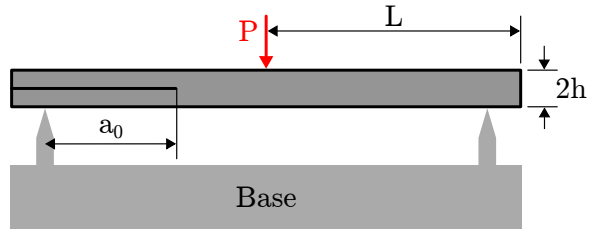


Figure 2.12: End Notched Flexure specimen and test setup

A record of the applied force versus center roller displacement is to be obtained. The Mode II interlaminar fracture toughness,  $G_{IIc}$  is obtained using the Compliance Calibration method. The standard recommends that static Mode II pre-cracking is performed [31]. A procedure is outlined to obtain the non-pre-cracked and pre-cracked toughnesses from the same specimen. In that approach, the advancement of the crack during the non-pre-cracked test creates the pre-crack that is used for the pre-cracked test [31].

Compliance Calibration tests are performed by loading the specimen to the peak Compliance Calibration force (50% of expected value of the critical force at that particular crack length) and then unloading. The force and deflection data are to be recorded continuously, or at frequent and regular intervals, only during the loading portion [31]. Non-pre-cracked and pre-cracked initiation values of  $G_{IIc}$  are to be obtained from the maximum force.

### **Cohesive zone material models to capture delamination**

Cohesive zone material models can capture both Mode I and Mode II fracture behavior as well as combined loading. The different cohesive material models offered in LS-DYNA can be distinguished best by comparing their traction separation laws. Some of the material models offer additional capabilities, such as rate and/or temperature dependency. In the following, five cohesive material models are briefly introduced.

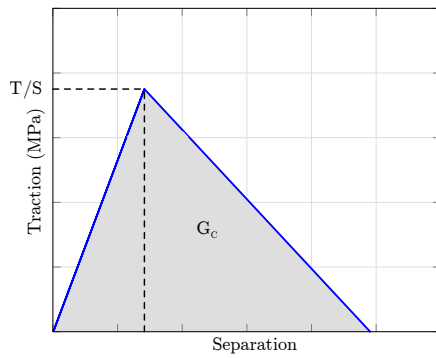
\*MAT\_184 (\*MAT\_COHESIVE\_ELASTIC) is a simple linear elastic model. As input it requires the stiffness in-plane and normal to the plane, as well as the traction at failure for tensile and shear loading [4].

\*MAT\_138 (\*MAT\_COHESIVE\_MIXED\_MODE) is a simplification of \*MAT\_186 and is restricted to linear softening. Traction-separation is modeled as bilinear with a quadratic mixed mode delamination criterion and a damage formulation [4]. Figure 2.13a shows an example of a bilinear traction separation law that can be defined with \*MAT\_138. The area under the curve is the fracture toughness  $G_c$  that is determined by DCB (Mode I) or ENF (Mode II) testing. Parameters  $T$  and  $S$  represent the peak traction in units of stress in normal and tangential direction respectively.

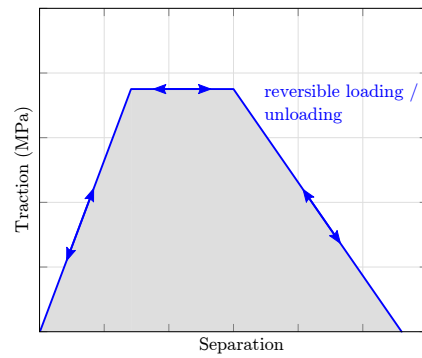
\*MAT\_185 (\*MAT\_COHESIVE\_TH) is a trilinear cohesive material model developed by Tvergaard and Hutchinson [32]. The model is completely reversible with loading and unloading following the same path [4]. Figure 2.13b shows the traction separation law for this material.

\*MAT\_240 (\*MAT\_COHESIVE\_MIXED\_MODE\_ELASTOPLASTIC\_RATE) is similar to \*MAT\_185 in the sense that it is trilinear. Additionally, rate and plasticity effects are considered. Due to the ideal plastic behavior, the loading and unloading paths are different. Using the THERMAL option, some of the material properties can be defined as functions of temperature. As the separation at failure is plastic, no brittle fracture can be modeled with this material type [4]. The material model was developed by Marzi et al. [33] and an example of the traction separation law is shown in Figure 2.13c.

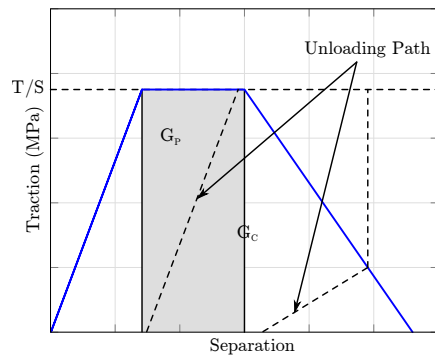
\*MAT\_186 (\*MAT\_COHESIVE\_GENERAL) allows the input of an arbitrarily shaped normalized traction separation law with an example shown in Figure 2.13d. Interaction between Mode I and Mode II is considered by choosing one of three mixed-mode interaction formulations. Damage is modeled irreversible with the unloading and reloading paths pointing to and from the origin respectively [4]. This material model was used by Khaled et al. to simulate the delamination in ballistic impacts of composite plates [34].



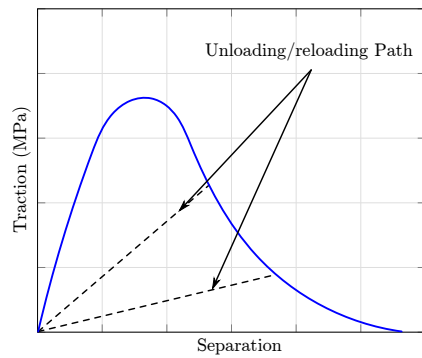
(a) Traction separation law \*MAT\_138



(b) Traction separation law \*MAT\_185



(c) Traction separation law \*MAT\_240



(d) Traction separation law \*MAT\_186

Figure 2.13: Traction separation laws of cohesive material models

## 2.6 Stochastic Variation of Composite Material Properties

Composites exhibit a random variation of their material properties. Even with high standards in quality control, randomness of the material properties can not be fully avoided. Micro-scale variations in material properties are often ignored on structural levels. However, in structures that undergo impact or crash loads, where failure initiation is a highly locally driven event, the variability on the micro-scale in material properties cannot be neglected when accurate results should be obtained. The variability of test and simulation results of composite materials can be attributed to different causes that can be categorized as being of intrinsic or extrinsic nature [35]. Intrinsic properties of the composite can be characterized as the geometric and material properties of the fiber and matrix as well as the geometric features of the architecture. Extrinsic sources are all other factors that are not directly related to the composite material, but influence how results are measured or how the composite material performs. In the following some of the most influential properties are listed.

Intrinsic properties (properties of the material itself)[35]:

- Fiber diameter,
- Fiber arrangement (fiber angles, tow width, tow size),
- Fiber tensile strength,
- Fiber volume fraction,
- Matrix properties,
- Voids in the matrix material [36],
- Fiber matrix bonds,
- Manufacturing (surface treatments, layup process, heat treatments).

Extrinsic properties (external factors that influence the material behavior) [35]:

- Boundary conditions in the material test (e. g. clamping slippage),
- Test temperature,
- Number of experiments,
- Post processing of test results.

This list does not claim comprehensiveness. All of the listed sources of variability are highly coupled. All properties have an influence on the material behavior of the composite and the test or simulation data obtained.

Much research has been conducted to identify which parameters are most important to consider. Goldsmith [36] studied the effect of tow size, tow spacing and voids on the material response and found that voids had the largest influence on transverse stiffness, while tow width, tow spacing and tow volume fraction contributed as well, but did not describe the variability completely. Figure 2.14a shows the cumulative probability plot by Goldsmith [37] for the matrix strength ranging from approximately 100 MPa to 400 MPa. Figure 2.14b shows the transverse tow strength of a woven ceramic matrix composites (5HS CVI (Chemical Vapor Infiltration) SiC/SiC) which ranges from approximately 20 MPa to 90 MPa .

The effect of fiber strength variations have been incorporated using a multi-scale modeling approach to link micro-mechanics and finite element analysis by Ricks et. al [38] and [39]. Figure 2.15 shows an example of a fiber strength distribution that was measured for a SCS-6 fiber, a high-stiffness, high-strength silicon carbide monofilament [38]. The variation of fiber strength of individual fibers is quite large, ranging from about 1500 MPa to around 6000 MPa. While the contribution of fiber strength does generally not influence the deformation and stiffness of a composite component, as soon as fracture occurs local differences in fiber strength lead to variations of fracture patterns and sustainable loads.

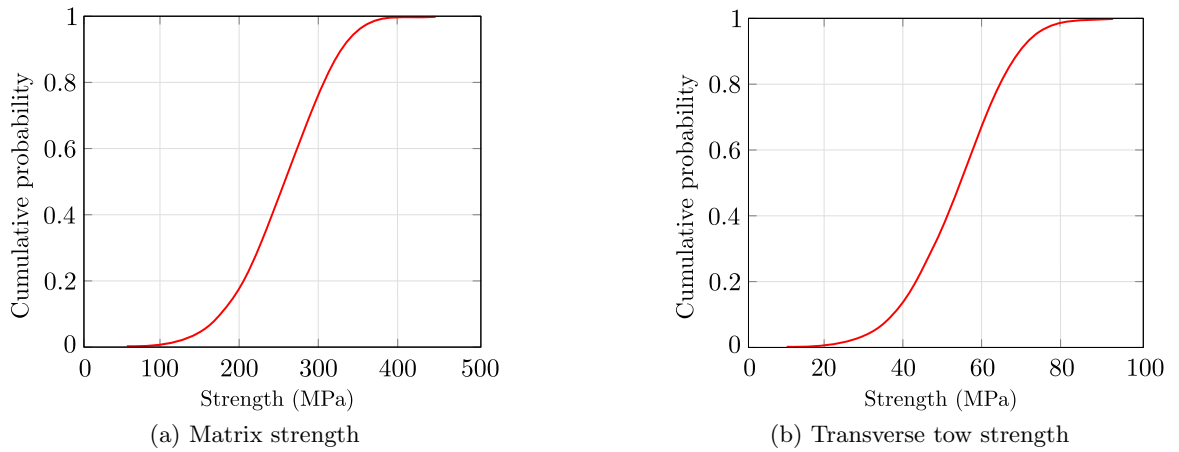


Figure 2.14: Cumulative distribution functions (adapted from [36])

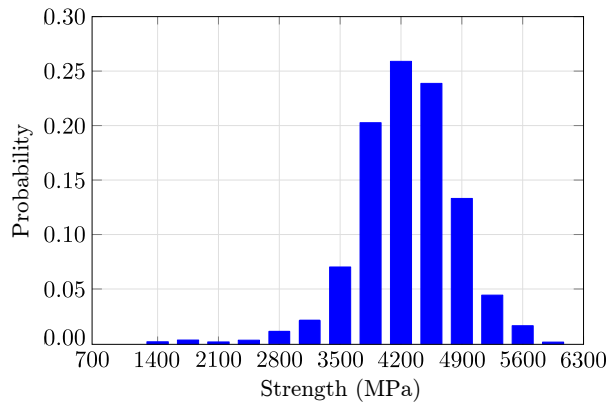


Figure 2.15: Fiber strength distribution of SCS-6 vendor fiber (adapted from [39])

Liu studied the effects of tow volume fraction in textile and braided composites where a multiscale modeling framework was used to analyse the effect on the stress strain response of the material [40]. The stress versus strain curves obtained showed a variation in slope and maximum stresses.

To accurately predict the physical behavior of composites, a material model should incorporate statistical variation of material parameters. Micro-mechanics modeling approaches can be utilized to quantify the effects of variations of material properties of the constituent materials on the continuum behavior of the composite material.

## Chapter 3: Methodology - Material Model Theory

This chapter describes the theory of the newly developed orthotropic viscoelastic viscoplastic material model for composites. Figure 3.1 shows three different types of viscous material behaviors. Viscoelastic behavior, as shown in Figure 3.1a, is typical for polymers and rubbers. This type of material model is used when non-linear behavior without permanent deformation occurs and rate dependency in the elastic region should be modeled. Rate dependency in metals is commonly modeled with a viscoplasticity model, as depicted in Figure 3.1b. Both the yield stress of the material and the hardening can be rate-dependent while the elastic modulus stays constant at different loading rates. Fiber reinforced composites, on the other hand, exhibit characteristics of both viscoelasticity and viscoplasticity with rate dependencies in both the elastic and plastic regions (Figure 3.1c). The presented material model will, therefore, allow for both viscoelastic and viscoplastic behavior in combination. The following sections will describe the theory behind the different parts of the material model and the interaction between them. Section 3.1 presents the linear elastic stress-strain relation for an orthotropic material in plane stress. To allow for rate dependency in the elastic region, classical viscoelasticity is introduced and generalized into three dimensions (Section 3.2). For material directions where plastic deformation occurs, a viscoplastic flow rule models the rate-dependent permanent deformation (Section 3.3). How both viscoelasticity and viscoplasticity are coupled is described in Section 3.4.

### 3.1 Stress-Strain Relation for an Orthotropic Linear Elastic Composite Material Model for Shell Elements

Composites are anisotropic materials, meaning that their physical and mechanical properties are directionally dependent. Typically, the stiffness and strength of a unidirectional

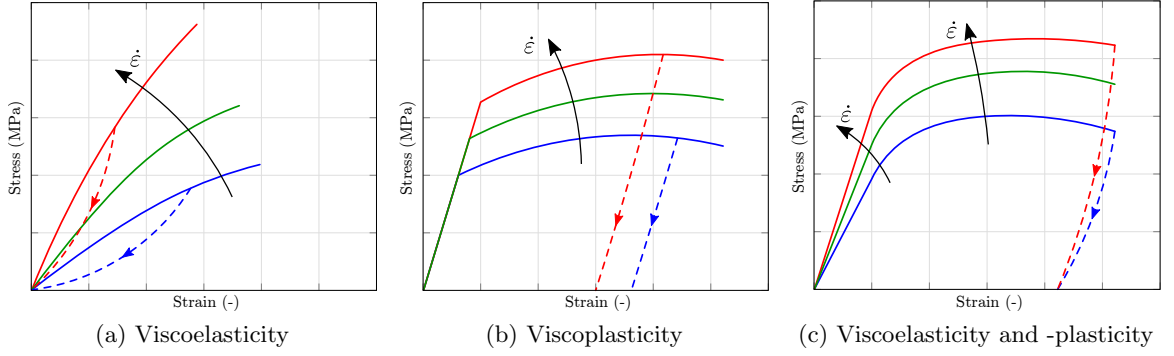


Figure 3.1: Forms of viscous behavior

composite is higher along the fiber orientation, with the properties of the fiber dominating the overall material response in that direction. Orthogonal to the fibers, however, the properties of the matrix material dominate and, therefore, the composite's response to loading is more similar to the response of the matrix material itself. The stress-strain relationship for an anisotropic linear-elastic material is given in Equation 3.1 with  $\mathbf{C}$  being the elastic stiffness matrix:

$$\boldsymbol{\sigma} = \mathbf{C}\boldsymbol{\varepsilon} \quad (3.1)$$

In matrix form and with the assumptions for an orthotropic material, Equation 3.1 can be written as follows:

$$\begin{bmatrix} \sigma_{11} \\ \sigma_{22} \\ \sigma_{33} \\ \sigma_{12} \\ \sigma_{23} \\ \sigma_{31} \end{bmatrix} = \begin{bmatrix} c_{11} & c_{12} & c_{13} & 0 & 0 & 0 \\ c_{12} & c_{22} & c_{23} & 0 & 0 & 0 \\ c_{13} & c_{23} & c_{33} & 0 & 0 & 0 \\ 0 & 0 & 0 & c_{44} & 0 & 0 \\ 0 & 0 & 0 & 0 & c_{55} & 0 \\ 0 & 0 & 0 & 0 & 0 & c_{66} \end{bmatrix} \begin{bmatrix} \varepsilon_{11} \\ \varepsilon_{22} \\ \varepsilon_{33} \\ \varepsilon_{12} \\ \varepsilon_{23} \\ \varepsilon_{31} \end{bmatrix} \quad (3.2)$$

Equation 3.3 shows the orthotropic elastic compliance matrix in terms of the nine independent elastic constants. As the inverse of this matrix, the stiffness matrix is presented in Equation 3.4:

$$\mathbf{S} = \begin{bmatrix} \frac{1}{E_{11}} & -\frac{\nu_{21}}{E_{22}} & -\frac{\nu_{31}}{E_{33}} & 0 & 0 & 0 \\ & \frac{1}{E_{22}} & -\frac{\nu_{32}}{E_{33}} & 0 & 0 & 0 \\ & & \frac{1}{E_{33}} & 0 & 0 & 0 \\ & & & \frac{1}{2G_{12}} & 0 & 0 \\ & \text{Sym} & & & \frac{1}{2G_{23}} & 0 \\ & & & & & \frac{1}{2G_{31}} \end{bmatrix} \quad (3.3)$$

$$\mathbf{C} = \mathbf{S}^{-1} = \begin{bmatrix} \frac{1-\nu_{32}\nu_{23}}{E_{22}E_{33}\Delta} & \frac{\nu_{21}+\nu_{31}\nu_{23}}{E_{22}E_{33}\Delta} & \frac{\nu_{31}+\nu_{21}\nu_{32}}{E_{22}E_{33}\Delta} & 0 & 0 & 0 \\ & \frac{1-\nu_{13}\nu_{31}}{E_{11}E_{33}\Delta} & \frac{\nu_{32}+\nu_{12}\nu_{31}}{E_{11}E_{33}\Delta} & 0 & 0 & 0 \\ & & \frac{1-\nu_{12}\nu_{21}}{E_{11}E_{22}\Delta} & 0 & 0 & 0 \\ & & & 2G_{12} & 0 & 0 \\ & \text{Sym} & & & 2G_{23} & 0 \\ & & & & & 2G_{31} \end{bmatrix} \quad (3.4)$$

$$\text{where : } \Delta = \frac{1 - \nu_{12}\nu_{21} - \nu_{23}\nu_{32} - \nu_{13}\nu_{31} - 2\nu_{12}\nu_{23}\nu_{31}}{E_{11}E_{22}E_{33}}$$

For the compliance and stiffness matrices to be symmetric, the following relations between the Poisson's ratios and Young's moduli have to be satisfied:

$$\frac{\nu_{12}}{E_{11}} = \frac{\nu_{21}}{E_{22}} \quad \frac{\nu_{23}}{E_{22}} = \frac{\nu_{32}}{E_{33}} \quad \frac{\nu_{13}}{E_{11}} = \frac{\nu_{31}}{E_{33}} \quad (3.5)$$

The here described material model should be valid for shell elements and, therefore, we require a plane stress state without a through-thickness stress component, as shown in Figure 3.2. Equation 3.2 is first simplified by only taking into account the normal stresses

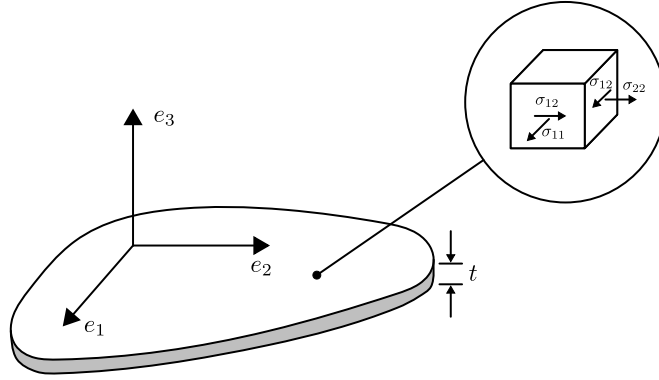


Figure 3.2: The plane stress state, adapted from [41]

$(\sigma_{11}, \sigma_{22}, \sigma_{33})$ . For plane stress we require the through-thickness normal stress to vanish, which then sets this stress ( $\sigma_{33}$ ) to zero:

$$\begin{bmatrix} \sigma_{11} \\ \sigma_{22} \\ 0 \end{bmatrix} = \begin{bmatrix} c_{11} & c_{12} & c_{13} \\ c_{12} & c_{22} & c_{23} \\ c_{13} & c_{23} & c_{33} \end{bmatrix} \begin{bmatrix} \varepsilon_{11} \\ \varepsilon_{22} \\ \varepsilon_{33} \end{bmatrix} \quad (3.6)$$

The third row of Equation 3.6 can now be rearranged to allow for the calculation of the thickness strain ( $\varepsilon_{33}$ ) as a function of the in plane strain ( $\varepsilon_{11}, \varepsilon_{22}$ ) in the absence of through-thickness stress ( $\sigma_{33}$ ):

$$\varepsilon_{33} = -\frac{c_{13}}{c_{33}}\varepsilon_{11} - \frac{c_{23}}{c_{33}}\varepsilon_{22} \quad (3.7)$$

We now replace  $\varepsilon_{33}$  in Equation 3.6 with Equation 3.7, which leaves us with a system of three equations and two unknowns:

$$\begin{bmatrix} \sigma_{11} \\ \sigma_{22} \\ 0 \end{bmatrix} = \begin{bmatrix} c_{11} & c_{12} & c_{13} \\ c_{12} & c_{22} & c_{23} \\ c_{13} & c_{23} & c_{33} \end{bmatrix} \begin{bmatrix} \varepsilon_{11} \\ \varepsilon_{22} \\ -\frac{c_{13}}{c_{33}}\varepsilon_{11} - \frac{c_{23}}{c_{33}}\varepsilon_{22} \end{bmatrix} \quad (3.8)$$

This system of equations can be written in terms of two equations and two unknowns as shown in Equation 3.9 or in a matrix notation as in Equation 3.10:

$$\begin{aligned} \sigma_{11} &= \left(c_{11} - \frac{c_{13}c_{13}}{c_{33}}\right)\varepsilon_{11} + \left(c_{12} - \frac{c_{13}c_{23}}{c_{33}}\right)\varepsilon_{22} \\ \sigma_{22} &= \left(c_{12} - \frac{c_{23}c_{13}}{c_{33}}\right)\varepsilon_{11} + \left(c_{22} - \frac{c_{23}c_{23}}{c_{33}}\right)\varepsilon_{22} \end{aligned} \quad (3.9)$$

$$\begin{bmatrix} \sigma_{11} \\ \sigma_{22} \end{bmatrix} = \begin{bmatrix} c_{11} - \frac{c_{13}c_{13}}{c_{33}} & c_{12} - \frac{c_{13}c_{23}}{c_{33}} \\ c_{12} - \frac{c_{23}c_{13}}{c_{33}} & c_{22} - \frac{c_{23}c_{23}}{c_{33}} \end{bmatrix} \begin{bmatrix} \varepsilon_{11} \\ \varepsilon_{22} \end{bmatrix} \quad (3.10)$$

The calculation of the shear stresses ( $\sigma_{12}, \sigma_{23}, \sigma_{31}$ ) stays unchanged in comparison to the 3D model as follows in Equations 3.11:

$$\sigma_{12} = c_{44}\varepsilon_{12} \quad \sigma_{23} = c_{55}\varepsilon_{23} \quad \sigma_{31} = c_{66}\varepsilon_{31} \quad (3.11)$$

### Constraints on orthotropic elastic constants

Due to the significant variations in stiffness in different directions, Poisson's ratios in composites can often take values higher than unity, which highlights why composites should generally be regarded as structures rather than materials. This is in contrast with the widely known fact that in isotropic materials Poisson's ratios with values larger than one

half are thermodynamically unstable, as this could lead to negative strain energy in specific loading conditions. To avoid numerical “creation of energy”, the sum of the work done by all stress components must be positive. The elastic stiffness matrix must be positive-definite and, therefore, have positive eigenvalues [42]. Assuming only one non-zero stress component, the strain in the direction of the applied stress must be greater than zero to avoid non-physical “creation of energy”. This means that the diagonal elements of the compliance matrix all have to be greater than zero:

$$E_{11}, E_{22}, E_{33}, G_{12}, G_{23}, G_{31} > 0 \quad (3.12)$$

On the other hand, assuming only one non-zero strain component, the stress in the direction of the applied strain must now be greater than zero. This means that the diagonal elements of the stiffness matrix also have to be positive:

$$c_{11}, c_{22}, c_{33}, c_{44}, c_{55}, c_{66} > 0 \quad (3.13)$$

This leads to the following inequalities in terms of Poisson’s ratios:

$$(1 - \nu_{12}\nu_{21}), (1 - \nu_{12}\nu_{12}), (1 - \nu_{12}\nu_{12}) > 0 \quad (3.14)$$

$$\Delta = 1 - \nu_{12}\nu_{21} - \nu_{23}\nu_{32} - \nu_{13}\nu_{31} - 2\nu_{12}\nu_{23}\nu_{31} > 0 \quad (3.15)$$

Using the inequalities from 3.14 and the symmetry conditions from Equations 3.5, the following conditions for the Poisson’s ratios can be formulated:

$$\begin{aligned} |\nu_{21}| &< \sqrt{\frac{E_{22}}{E_{11}}} & |\nu_{12}| &< \sqrt{\frac{E_{11}}{E_{22}}} \\ |\nu_{32}| &< \sqrt{\frac{E_{33}}{E_{22}}} & |\nu_{23}| &< \sqrt{\frac{E_{22}}{E_{33}}} \\ |\nu_{13}| &< \sqrt{\frac{E_{11}}{E_{33}}} & |\nu_{31}| &< \sqrt{\frac{E_{33}}{E_{11}}} \end{aligned} \quad (3.16)$$

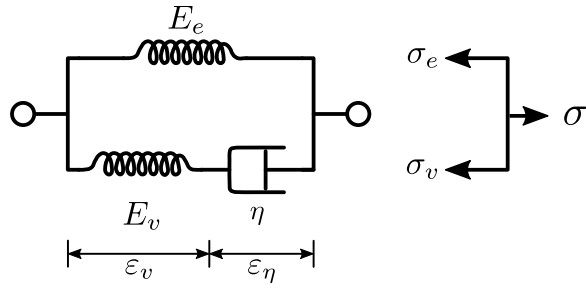


Figure 3.3: Standard linear solid model (Maxwell representation)

While the inequality 3.15 leads to the following conditions using Equations 3.5:

$$\nu_{12}\nu_{23}\nu_{31} < \left[ 1 - \nu_{21}^2 \frac{E_{11}}{E_{22}} - \nu_{32}^2 \frac{E_{22}}{E_{33}} - \nu_{13}^2 \frac{E_{33}}{E_{11}} \right] \frac{1}{2} < \frac{1}{2} \quad (3.17)$$

Measurements on an actual composite structure itself might not necessarily follow these conditions. The presented inequalities are followed to ensure numerical stability.

## 3.2 Viscoelasticity

The theory of viscoelasticity is a well established method to mathematically describe the material behavior of polymers that exhibit both viscous and elastic characteristics when undergoing deformations. Viscous materials resist strain dependent on time, while elastic materials return to their original state once the loading is removed [43]. Figure 3.1a shows the typical response to loading of a viscoelastic polymer. An increase in strain-rate leads to an increase in the Young's modulus, making the material stiffer. When the stress on the material is removed, it returns to its original state with no permanent deformation.

### 3.2.1 The Standard Linear Solid Model

A simple model to describe the behavior of a viscoelastic material is the standard linear solid model (also called 3-parameter model) which includes practically all experimental observations of rate-dependent phenomena [43]. The mechanical behavior of the standard

linear solid model of two springs and one damper, shown in Figure 3.3, can be described using a first order differential equation with constant coefficients. The differential equation can then be solved for both displacement and stress-controlled loading. Using the method of sections, the standard linear solid model can be described by Equation 3.18 [43].

$$\left. \begin{aligned} \sigma &= \sigma_v + \sigma_e \\ \varepsilon &= \varepsilon_v + \varepsilon_\eta \\ \sigma_e &= E_e \varepsilon \\ \sigma_v &= E_v \varepsilon_v \\ \sigma_v &= \eta \dot{\varepsilon}_\eta \end{aligned} \right\} \Rightarrow \dot{\sigma} + \frac{E_v}{\eta} \sigma = (E_e + E_v) \dot{\varepsilon} + \frac{E_e E_v}{\eta} \varepsilon \quad (3.18)$$

For very slow processes ( $\dot{\sigma} \ll \frac{E_v}{\eta} \sigma$  and  $(E_e + E_v) \dot{\varepsilon} \ll \frac{E_e E_v}{\eta} \varepsilon$ ) the final equation shown in 3.18 simplifies to the well-known Hooke's law [43]:

$$\dot{\sigma} + \frac{E_v}{\eta} \sigma = (E_e + E_v) \dot{\varepsilon} + \frac{E_e E_v}{\eta} \varepsilon \Rightarrow \sigma = E_e \varepsilon \quad (3.19)$$

For very fast processes ( $\dot{\sigma} \gg \frac{E_v}{\eta} \sigma$  and  $(E_e + E_v) \dot{\varepsilon} \gg \frac{E_e E_v}{\eta} \varepsilon$ ) the final equation shown in 3.18 simplifies to Equation 3.20 [43]:

$$\dot{\sigma} + \frac{E_v}{\eta} \sigma = (E_e + E_v) \dot{\varepsilon} + \frac{E_e E_v}{\eta} \varepsilon \Rightarrow \sigma = (E_e + E_v) \varepsilon \quad (3.20)$$

Figure 3.4 shows example results of viscoelastic behavior at different constant strain-rates. For a very low strain-rate, the slope of the stress vs. strain response is equal to  $E_e$  and follows the blue curve (see Equation 3.19), while for a high rate the slope approaches  $(E_e + E_v)$  (see Equation 3.20).

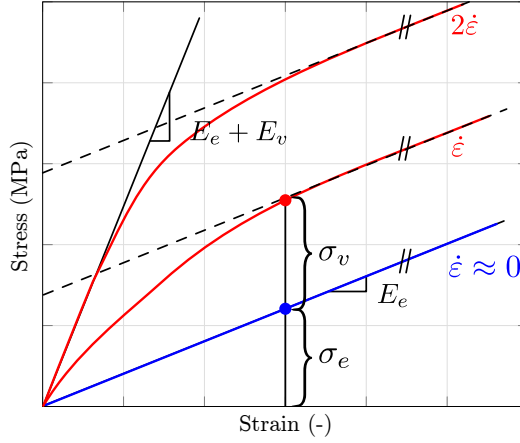


Figure 3.4: Viscoelastic behavior at different rates

One can solve Equation 3.18 to compute the stress at a given time  $\sigma(t)$  for a given strain  $\epsilon(t)$ :

$$\dot{\sigma} + \frac{E_v}{\eta} \sigma = (E_e + E_v) \dot{\epsilon} + \frac{E_e E_v}{\eta} \epsilon$$

$$\left( \dot{\sigma} + \frac{E_v}{\eta} \sigma \right) e^{\frac{E_v}{\eta} t} = \left( (E_e + E_v) \dot{\epsilon} + \frac{E_e E_v}{\eta} \epsilon \right) e^{\frac{E_v}{\eta} t} \quad (3.21)$$

By utilizing the product rule with  $\left( \dot{\sigma} + \frac{E_v}{\eta} \sigma \right) e^{\frac{E_v}{\eta} t} = \left( \sigma e^{\frac{E_v}{\eta} t} \right) \dot{\quad}$ , and  $\left( \epsilon e^{\frac{E_v}{\eta} t} \right) \dot{\quad} = \dot{\epsilon} e^{\frac{E_v}{\eta} t} + \epsilon \frac{E_v}{\eta} e^{\frac{E_v}{\eta} t}$ , Equation 3.21 becomes:

$$\left( \sigma e^{\frac{E_v}{\eta} t} \right) \dot{\quad} = (E_e + E_v) \dot{\epsilon} e^{\frac{E_v}{\eta} t} + E_e \left( \epsilon e^{\frac{E_v}{\eta} t} \right) \dot{\quad} - E_e \dot{\epsilon} e^{\frac{E_v}{\eta} t}$$

$$\left( \sigma e^{\frac{E_v}{\eta} t} \right) \dot{\quad} = E_v \dot{\epsilon} e^{\frac{E_v}{\eta} t} + E_e \left( \epsilon e^{\frac{E_v}{\eta} t} \right) \dot{\quad} \quad (3.22)$$

Integration of Equation 3.22 in the interval from 0 to  $t$  yields:

$$\sigma(t) e^{\frac{E_v}{\eta} t} - \sigma(0) = \int_0^t E_v e^{\frac{E_v}{\eta} t} \dot{\epsilon}(s) ds + E_e \epsilon(t) e^{\frac{E_v}{\eta} t} - E_e \epsilon(0) \quad (3.23)$$

Using the initial conditions of  $\sigma(0) = 0$  and  $\varepsilon(0) = 0$ , one obtains the following results:

$$\sigma(t) = \int_0^t E_v e^{-\frac{E_v}{\eta}(t-s)} \dot{\varepsilon}(s) ds + E_e \varepsilon(t) \quad (3.24)$$

$$\sigma(t) = \sigma_v(t) + \sigma_e(t)$$

$$\sigma_v(t) = \int_0^t E_v e^{-\frac{E_v}{\eta}(t-s)} \dot{\varepsilon}(s) ds \quad (3.25)$$

$$\sigma_e(t) = E_e \varepsilon(t) \quad (3.26)$$

Whereas Equation 3.25 describes the viscous stress over time, Equation 3.26 describes the equilibrium stress.

To compute the viscous stress at time step  $t^{n+1}$ , the viscous stress shown in Equation 3.25 is discretized in time. The integral to calculate the viscous stress is, therefore, split into two integrals from  $t = 0$  to  $t^n$  and from  $t^n$  to  $t^{n+1}$ . It is now assumed that  $\frac{E_v}{\eta} = \text{constant} = \beta$ . After simplifications and numerical integration, assuming a constant strain-rate  $\dot{\varepsilon}$  and stiffness  $E_v$  during one time step, the viscous stress at time step  $t^{n+1}$  can be computed using Equation 3.27.

$$\begin{aligned} \sigma_v(t^{n+1}) &= \int_0^{t^n} E_v e^{-\beta(t^{n+1}-s)} \dot{\varepsilon}(s) ds + \int_{t^n}^{t^{n+1}} E_v e^{-\beta(t^{n+1}-s)} \dot{\varepsilon}(s) ds \\ \sigma_v(t^{n+1}) &= \int_0^{t^n} E_v e^{-\beta(t^{n+1}-t^n+t^n-s)} \dot{\varepsilon}(s) ds + \int_{t^n}^{t^{n+1}} E_v e^{-\beta(t^{n+1}-s)} \dot{\varepsilon}(s) ds \\ \sigma_v(t^{n+1}) &= \int_0^{t^n} E_v e^{-\beta\Delta t} e^{-\beta(t^n-s)} \dot{\varepsilon}(s) ds + \int_{t^n}^{t^{n+1}} E_v e^{-\beta(t^{n+1}-s)} \dot{\varepsilon}(s) ds \\ \sigma_v(t^{n+1}) &= e^{-\beta\Delta t} \int_0^{t^n} E_v e^{-\beta(t^n-s)} \dot{\varepsilon}(s) ds + E_v \dot{\varepsilon}^{n+\frac{1}{2}} \int_{t^n}^{t^{n+1}} e^{-\beta(t^{n+1}-s)} ds \\ \sigma_v(t^{n+1}) &= e^{-\beta\Delta t} \sigma_v(t^n) + E_v \dot{\varepsilon}^{n+\frac{1}{2}} \frac{1 - e^{-\beta\Delta t}}{\beta} \end{aligned} \quad (3.27)$$

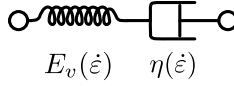


Figure 3.5: Non-linear viscoelastic model

### 3.2.2 Non-linear Viscoelasticity

To allow for an arbitrary tabulated relationship between the Young's modulus and the total strain-rate, the classical linear viscoelasticity described in the previous Section (3.2.1), is replaced by a non-linear viscoelastic model. For this material model, the Young's modulus is derived from the tabulated stress-strain data for every current strain-rate value and, therefore, the stiffness is a function of the strain-rate  $E_v(\dot{\epsilon})$ .

Figure 3.5 shows the modified Maxwell cell to include an arbitrary non-linear spring and damper with the behavior as a function of the strain-rate.

To still allow for the use of the Taylor algorithm from Equation 3.27, the relaxation function in the convolution integral needs to be an exponential with a constant value of the decay constant. Therefore, a constant  $\beta$  is assumed, with a non-linear damper that adjusts to the given non-linear spring in the solid model shown in Figure 3.5.

$$\beta = \frac{E_v(\dot{\epsilon})}{\eta(\dot{\epsilon})} \quad (3.28)$$

By assuming a constant  $\beta$ , Equation 3.27 can be slightly modified to compute the viscous stress and to allow for the non-linear spring  $E_v(\dot{\epsilon})$ :

$$\sigma_v(t^{n+1}) = e^{-\beta\Delta t}\sigma_v(t^n) + E_v(\dot{\epsilon}^{n+\frac{1}{2}})\dot{\epsilon}^{n+\frac{1}{2}}\frac{1 - e^{-\beta\Delta t}}{\beta} \quad (3.29)$$

The choice of a constant decay coefficient allows matching the initial slope of the dynamic stress-strain curves with a single input variable. At large strains this model has limited flexibility to match the measured data, however, at larger strains the viscoplastic fraction of the material law (described in Section 3.3) is expected to dominate the response.

### 3.2.3 Generalization to 3D

For the general 3D case, the equilibrium stiffness matrix with the rate-independent Young's and Shear moduli, derived from the quasistatic input curves, is defined as:

$$\mathbf{C}_e = \mathbf{S}_e^{-1} = \begin{bmatrix} \frac{1}{E_{11e}} & -\frac{\nu_{21}}{E_{22e}} & -\frac{\nu_{31}}{E_{33e}} & 0 & 0 & 0 \\ & \frac{1}{E_{22e}} & -\frac{\nu_{32}}{E_{33e}} & 0 & 0 & 0 \\ & & \frac{1}{E_{33e}} & 0 & 0 & 0 \\ & & & \frac{1}{2G_{12e}} & 0 & 0 \\ & Sym & & & \frac{1}{2G_{23e}} & 0 \\ & & & & & \frac{1}{2G_{31e}} \end{bmatrix}^{-1} \quad (3.30)$$

The total, rate-dependent, stiffness matrix, where the rate-dependent Young's moduli  $E_{ii_{tot}}(\dot{\epsilon})$  correspond to  $E_e + E_v(\dot{\epsilon})$  in the previously discussed one dimensional case, is defined as follows:

$$\mathbf{C}_{tot}(\dot{\epsilon}) = \begin{bmatrix} \frac{1}{E_{11_{tot}}(\dot{\epsilon})} & -\frac{\nu_{21}}{E_{22_{tot}}(\dot{\epsilon})} & -\frac{\nu_{31}}{E_{33_{tot}}(\dot{\epsilon})} & 0 & 0 & 0 \\ & \frac{1}{E_{22_{tot}}(\dot{\epsilon})} & -\frac{\nu_{32}}{E_{33_{tot}}(\dot{\epsilon})} & 0 & 0 & 0 \\ & & \frac{1}{E_{33_{tot}}(\dot{\epsilon})} & 0 & 0 & 0 \\ & & & \frac{1}{2G_{12_{tot}}(\dot{\epsilon})} & 0 & 0 \\ & Sym & & & \frac{1}{2G_{23_{tot}}(\dot{\epsilon})} & 0 \\ & & & & & \frac{1}{2G_{31_{tot}}(\dot{\epsilon})} \end{bmatrix}^{-1} \quad (3.31)$$

The rate-dependent Young's moduli represent the current stiffness at the given time step and are derived from the tabulated stress-strain curves that are user input. While the moduli are rate-dependent, the Poisson's ratios are kept constant throughout the simulation.

Additionally, the viscous stiffness matrix is defined as the difference between the total and the equilibrium stiffness matrix:

$$\mathbf{C}_v(\dot{\epsilon}) = \mathbf{C}_{tot}(\dot{\epsilon}) - \mathbf{C}_e \quad (3.32)$$

The equilibrium trial stress can now be computed using Equation 3.33:

$$\boldsymbol{\sigma}_e^{n+1} = \boldsymbol{\sigma}_e^n + \mathbf{C}_e \dot{\boldsymbol{\epsilon}}^{n+1/2} \Delta t \quad (3.33)$$

To compute the viscous trial stress, the viscoelastic decay vector  $\boldsymbol{\beta}$  and the viscoelastic decay matrix  $\mathbf{B}$  are defined as:

$$\boldsymbol{\beta} = \begin{bmatrix} e^{-\beta_{11}\Delta t} \\ e^{-\beta_{22}\Delta t} \\ e^{-\beta_{33}\Delta t} \\ e^{-\beta_{44}\Delta t} \\ e^{-\beta_{55}\Delta t} \\ e^{-\beta_{66}\Delta t} \end{bmatrix} \quad (3.34)$$

$$\mathbf{B} = \begin{bmatrix} \frac{1-e^{-\beta_{11}\Delta t}}{\beta_{11}\Delta t} & \frac{1-e^{-\beta_{12}\Delta t}}{\beta_{12}\Delta t} & \frac{1-e^{-\beta_{13}\Delta t}}{\beta_{13}\Delta t} & 0 & 0 & 0 \\ \frac{1-e^{-\beta_{12}\Delta t}}{\beta_{12}\Delta t} & \frac{1-e^{-\beta_{22}\Delta t}}{\beta_{22}\Delta t} & \frac{1-e^{-\beta_{23}\Delta t}}{\beta_{23}\Delta t} & 0 & 0 & 0 \\ \frac{1-e^{-\beta_{13}\Delta t}}{\beta_{13}\Delta t} & \frac{1-e^{-\beta_{23}\Delta t}}{\beta_{23}\Delta t} & \frac{1-e^{-\beta_{33}\Delta t}}{\beta_{33}\Delta t} & 0 & 0 & 0 \\ 0 & 0 & 0 & \frac{1-e^{-\beta_{44}\Delta t}}{\beta_{44}\Delta t} & 0 & 0 \\ 0 & 0 & 0 & 0 & \frac{1-e^{-\beta_{55}\Delta t}}{\beta_{55}\Delta t} & 0 \\ 0 & 0 & 0 & 0 & 0 & \frac{1-e^{-\beta_{66}\Delta t}}{\beta_{66}\Delta t} \end{bmatrix} \quad (3.35)$$

The viscous trial stress then follows, as shown in the following equation:

$$\boldsymbol{\sigma}_v^{n+1} = \boldsymbol{\sigma}_v^n \circ \boldsymbol{\beta} + (\mathbf{C}_v(\dot{\boldsymbol{\varepsilon}}) \circ \mathbf{B}) \dot{\boldsymbol{\varepsilon}}^{n+1/2} \Delta t \quad (3.36)$$

where the operator “ $\circ$ ” stands for the Hadamard product (element wise multiplication) between the matrices or vectors.

By summing up both the viscous and the equilibrium stress, the total viscoelastic trial stress is then computed as follows:

$$\boldsymbol{\sigma}_t^{n+1} = \boldsymbol{\sigma}_e^{n+1} + \boldsymbol{\sigma}_v^{n+1} \quad (3.37)$$

### 3.2.4 Strain-Rate Smoothing

As previously described, in the viscoelastic part of the model the Young’s moduli are rate-dependent. To avoid numerical instabilities due to rapidly changing stiffness of the material, smoothing techniques are applied on the total strain-rate.

The simplest way to smooth data is to apply a Simple Moving Average (SMA) which is the unweighted mean of several data points as shown in Equation 3.38:

$$\overline{p}_{SM} = \frac{p_M + p_{M-1} + \dots + p_{M-(n-1)}}{n} = \frac{1}{n} \sum_{i=0}^{n-1} p_{M-i} \quad (3.38)$$

An Exponential Moving Average (EMA) is a first-order response filter which applies weighting factors that decrease exponentially but never reach zero. Equation 3.39 shows the formula for the EMA. At the first time step, no average can be obtained and the  $S_t$  takes the measured value.

$$S_t = \begin{cases} Z_1, & t = 1 \\ (1 - \alpha)Z_t + \alpha S_{t-1}, & t > 1 \end{cases} \quad (3.39)$$

In Equation 3.39 the constant smoothing factor  $\alpha$  represents the degree of weighting increase (with  $0 < \alpha < 1$ ). A higher  $\alpha$  discounts older observations slower.  $Z_t$  is the input value at a time period  $t$  and  $S_t$  is the value of the EMA at any time period  $t$ .

### 3.3 Viscoplasticity

The theory of viscoplasticity is applied to model the irreversible and time-dependent deformation of materials. Figure 3.6 shows an elastic-viscoplastic hardening model. The elastic response of the system is modeled with a one-dimensional linear spring of stiffness  $E$ . When the system is loaded, first only the spring deforms and the system responds linear elastic. Once the yield stress  $\sigma_y$  is reached, which is represented by a sliding frictional element, the system deforms plastically and permanently. This yield stress can be constant or rate-dependent. With plastic deformation occurring, the rate-dependency is modeled using a non-linear damper with viscosity  $\eta$  while the material hardening is represented by another spring of stiffness  $K$ .

In contrast to a rate-independent plastic material, a viscoplastic material can undergo a creep flow as a function of time. Creep describes how a material slowly deforms permanently under a constant stress. Figure 3.7c shows an example of a constant stress load with the corresponding creep in the strain response in Figure 3.7a. Similarly, for a constant strain load (Figure 3.7b) a viscoplastic material will respond with stress relaxation (Figure 3.7d) and, consequently, a continuous decay of the stress over time.

Essential for a viscoplasticity model is the decomposition of the total strain into the sum of a recoverable elastic and a permanent plastic component:

$$\varepsilon = \varepsilon_{el} + \varepsilon_p \tag{3.40}$$

where the elastic strain  $\varepsilon_{el}$  is again related to the elastic stress by means of the standard linear elastic constitutive relation of Equation 3.1.

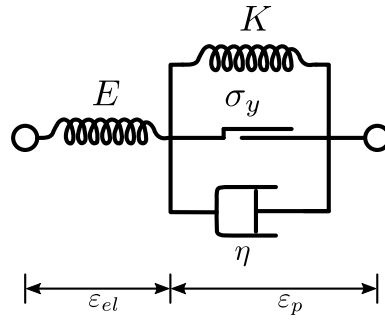


Figure 3.6: Elastic-viscoplastic hardening model

In the example of one-dimensional plasticity theory, the existence of an elastic domain, for which the material behavior is purely elastic, is defined by a yield stress. While the stress is lower than the yield stress  $\sigma_y$ , the material response is linear elastic. This yield stress can be dependent on different variables, such as the plastic strain  $\varepsilon_p$ , the plastic strain-rate  $\dot{\varepsilon}_p$  where rate effects should be captured, and/or the temperature  $T$  in temperature-dependent models:

$$\sigma_y = f(\varepsilon_p, \dot{\varepsilon}_p, T) \quad (3.41)$$

In addition to the elastic constitutive relation, a flow rule is needed to describe the permanent plastic deformation once the yield stress is exceeded. For a loading under tension ( $\sigma > 0$ ) the plastic strain-rate should be positive (stretching) and negative under compression ( $\sigma < 0$ ). The plastic flow rule for a uniaxial model can thus be established as follows [41]:

$$\dot{\varepsilon}_p = \dot{\lambda} \text{sign}(\sigma) \quad (3.42)$$

where the scalar  $\dot{\lambda}$  is the always positive plastic multiplier.

To generalize the described one-dimensional case to three dimensions, a yield function replaces the simple yield stress. This yield function can take many forms and, in this case, will depend on the yield stresses in the different directions and the stress state. The vector  $\mathbf{q}$  represents the yield stresses in different directions that are, in turn, dependent upon the

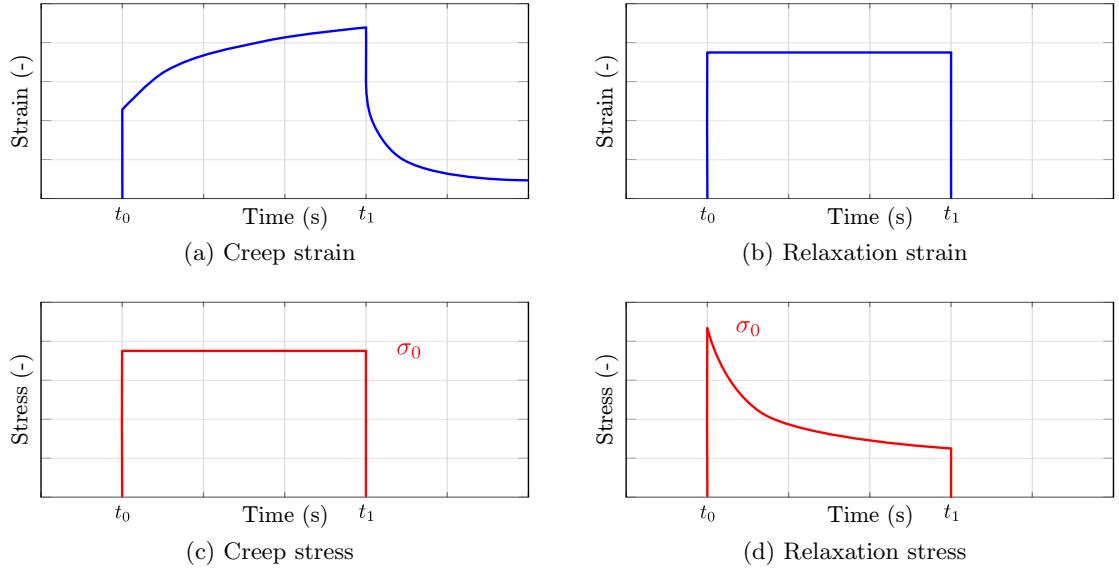


Figure 3.7: Creep and relaxation

plastic strain, temperature, and the plastic strain-rate as previously depicted in Equation 3.41. In the plane stress case, the vector  $\mathbf{q}$  would take the following form:

$$\mathbf{q} = [\sigma_{11yT} \ \sigma_{11yC} \ \sigma_{22yT} \ \sigma_{22yC} \ \sigma_{12y}]^T \quad (3.43)$$

with  $\sigma_{11yT}$  being the yield stress in tension 1-direction and  $\sigma_{11yC}$  the yield stress in compression 1-direction and equivalently for the 2-direction and shear.

The following describes a typical simplified plasticity algorithm in the general case.

1. Assume a purely linear elastic response to obtain the elastic “trial” stress, which is a function of the given total strains.

Compute:  $\boldsymbol{\sigma}_t = \mathbf{C}\boldsymbol{\varepsilon}$

2. Check if the stress is outside, inside, or on the yield surface, which is described by the yield function. Compute the yield function for the given elastic trial stress and yield stresses ( $f(\boldsymbol{\sigma}_t, \mathbf{q})$ ).

- (a)  $0 \geq f(\boldsymbol{\sigma}_t, \mathbf{q})$ : Stress is within or on the yield surface. Material behavior is purely elastic.

Accept “trial” stress as final stress:  $\boldsymbol{\sigma} = \boldsymbol{\sigma}_t$

- (b)  $0 < f(\boldsymbol{\sigma}_t, \mathbf{q})$ : Material behavior is elasto-plastic. Compute  $\dot{\boldsymbol{\varepsilon}}_p(\dot{\lambda})$  that returns the stress state back to the yield surface. Compute final stress as:  $\boldsymbol{\sigma} = \mathbf{C}(\boldsymbol{\varepsilon} - \boldsymbol{\varepsilon}_p)$

In the subsequent sections, the actual chosen yield surface and flow rule will be further explained.

### 3.3.1 Yield Surface

The yield surface for a composite material should allow for directionally different yield stresses and, additionally, should be able to distinguish between tension and compression.

In general, a yield function is mapping from a state of three-dimensional stress (3x3 tensor) to a real value ( $f : \mathbf{R}^{3 \times 3} \rightarrow \mathbf{R}$ ). The most general form of a yield function can be expressed as described by Feng and Yang [44] as:

$$f(\boldsymbol{\sigma}) = a + \mathbf{b}^t \boldsymbol{\sigma} + \boldsymbol{\sigma}^t \mathbf{C} \boldsymbol{\sigma} \quad (3.44)$$

where  $\boldsymbol{\sigma}^t = (\sigma_{11}, \sigma_{22}, \sigma_{33}, \sigma_{12}, \sigma_{13}, \sigma_{23})$ .

Special cases of a yield function of this type include Hill’s anisotropic yield function or the von Mises yield function [44]. In this particular case, a quadratic function based on the generalized Tsai-Wu failure surface [9] is chosen, similar to the yield surface as utilized by Hoffarth [3]. Equation 3.45 shows the quadratic yield function for the plane stress case.

$$f(\boldsymbol{\sigma}) = -1 + \begin{bmatrix} F_1 & F_2 & 0 \end{bmatrix} \begin{bmatrix} \sigma_{11} \\ \sigma_{22} \\ \sigma_{12} \end{bmatrix} + \begin{bmatrix} \sigma_{11} \\ \sigma_{22} \\ \sigma_{12} \end{bmatrix}^T \begin{bmatrix} F_{11} & F_{12} & 0 \\ F_{12} & F_{22} & 0 \\ 0 & 0 & F_{44} \end{bmatrix} \begin{bmatrix} \sigma_{11} \\ \sigma_{22} \\ \sigma_{12} \end{bmatrix} \quad (3.45)$$

Or after multiplication:

$$f(\sigma) = -1 + F_1\sigma_{11} + F_2\sigma_{22} + F_{11}\sigma_{11}^2 + F_{22}\sigma_{22}^2 + 2F_{12}\sigma_{11}\sigma_{22} + F_{44}\sigma_{12}^2 \quad (3.46)$$

where the yield function coefficients  $F_{ii}$  are based on the current yield stresses which are tabulated and defined for different temperatures, plastic strains, and plastic strain-rates.

### Determining the yield function coefficients

The normal and linear yield function coefficients ( $F_1$  and  $F_2$ ), as well as the non-linear coefficients ( $F_{11}$  and  $F_{22}$ ), can be determined by simplifying the yield function (Equation 3.46) for unidirectional loading in tension (subscript T) and compression (subscript C).

$$\begin{aligned} F_1\sigma_{11y_T} + F_{11}(\sigma_{11y_T})^2 = 1 & \quad F_1\sigma_{11y_C} + F_{11}(\sigma_{11y_C})^2 = 1 \\ F_2\sigma_{22y_T} + F_{22}(\sigma_{22y_T})^2 = 1 & \quad F_2\sigma_{22y_C} + F_{22}(\sigma_{22y_C})^2 = 1 \end{aligned} \quad (3.47)$$

Which results in the following equations for the linear and non-linear normal yield function coefficients:

$$\begin{aligned} F_1 &= \frac{1}{\sigma_{11y_T}} - \frac{1}{\sigma_{11y_C}} & F_{11} &= \frac{1}{\sigma_{11y_T}\sigma_{11y_C}} \\ F_2 &= \frac{1}{\sigma_{22y_T}} - \frac{1}{\sigma_{22y_C}} & F_{22} &= \frac{1}{\sigma_{22y_T}\sigma_{22y_C}} \end{aligned} \quad (3.48)$$

Similarly, the yield function coefficient for the shear 12-direction ( $F_{44}$ ) can be determined by solving the yield function for pure 12-shear loading, which results in the following equation:

$$F_{44} = \frac{1}{\sigma_{12y}^2} \quad (3.49)$$

To determine the off-axis coefficient ( $F_{12}$ ), a  $45^\circ$  off-axis test is required, where the off-axis coefficient describes the interactive effects in the yield stresses. A uniaxial test, with loading at a  $45^\circ$  angle from the fiber direction (1-direction) in the 12-plane is conducted. By using the rotation matrix from Equation 3.50, the uniaxial loading at an angle of  $\alpha = 45^\circ$  with respect to the fiber direction, can be transformed into the material coordinate system, as shown in Equation 3.51 [5].

$$\begin{bmatrix} \sigma_{11} \\ \sigma_{22} \\ \sigma_{12} \end{bmatrix} = \begin{bmatrix} \cos^2(\alpha) & \sin^2(\alpha) & 2 \sin(\alpha) \cos(\alpha) \\ \sin^2(\alpha) & \cos^2(\alpha) & -2 \sin(\alpha) \cos(\alpha) \\ -\sin(\alpha) \cos(\alpha) & \sin(\alpha) \cos(\alpha) & \cos^2(\alpha) - \sin^2(\alpha) \end{bmatrix} \begin{bmatrix} \sigma_{xx} \\ \sigma_{yy} \\ \sigma_{xy} \end{bmatrix} \quad (3.50)$$

$$\begin{bmatrix} \sigma_{11} \\ \sigma_{22} \\ \sigma_{12} \end{bmatrix} = \begin{bmatrix} \frac{1}{2} & \frac{1}{2} & 1 \\ \frac{1}{2} & \frac{1}{2} & -1 \\ -\frac{1}{2} & \frac{1}{2} & 0 \end{bmatrix} \begin{bmatrix} \sigma_{45} \\ 0 \\ 0 \end{bmatrix} \quad (3.51)$$

With the system of Equations from 3.51 and the yield function from Equation 3.46, one can compute the off-axis coefficient ( $F_{12}$ ) using the following resulting equation for a given stress in the loading direction:

$$F_{12} = \frac{2}{(\sigma_{45})^2} - \frac{F_1 + F_2}{\sigma_{45}} - \frac{1}{2}(F_{11} + F_{22} + F_{44}) \quad (3.52)$$

Figure 3.8 shows an example of a yield surface that can be described using the chosen yield function.

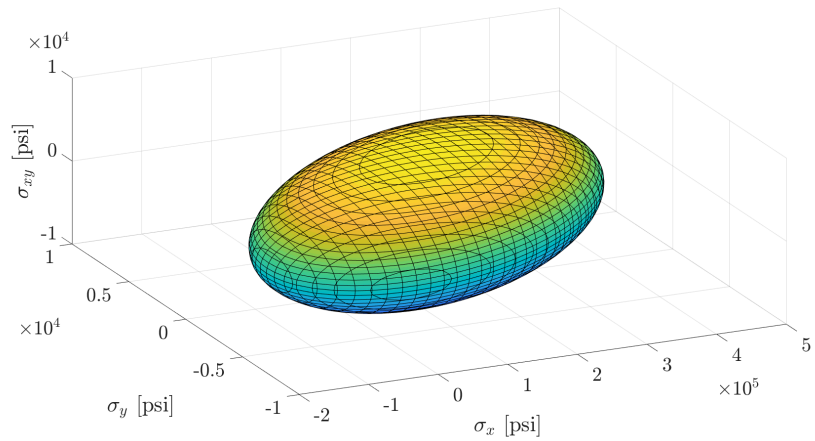


Figure 3.8: Example of a yield surface

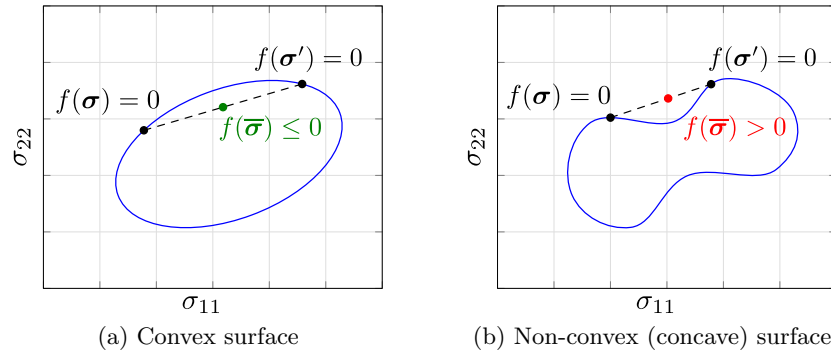


Figure 3.9: Convexity of surfaces

### Convexity of the yield surface

The yield function coefficients are computed based on the yield stresses in the material directions, allowing for different hardening progression in different directions. As the Tsai-Wu based yield surface is very general and dependent upon the yield stresses, it can result in both convex and concave yield surfaces. Figure 3.9a shows an example of a convex surface, while Figure 3.9b shows a concave surface. For numerical stability, in plasticity algorithms in general, the yield surface must be convex at all times [45]. Therefore, if the input parameters do not lead to a convex yield surface, a convex correction must take place.

To verify whether a yield surface is concave or convex, the convex combination of two vectors as described in Equation 3.53 can be used.

$$\bar{\boldsymbol{\sigma}} = \alpha \boldsymbol{\sigma} + (1 - \alpha) \boldsymbol{\sigma}' \quad (3.53)$$

with  $0 \leq \alpha \leq 1$ .

In two dimensions, the combination of two vectors describes a line between the two head points of the vectors as shown in Figure 3.9 as a dashed line.

To ensure convexity, the yield function  $f$  must satisfy the inequality:

$$f(\bar{\boldsymbol{\sigma}}) \leq \alpha f(\boldsymbol{\sigma}) + (1 - \alpha) f(\boldsymbol{\sigma}') \quad (3.54)$$

In two dimensions, this can now be visualized by the green point in Figure 3.9a for a convex surface: where  $f(\bar{\boldsymbol{\sigma}})$  satisfies the convexity condition and by the red point in Figure 3.9b for a non-convex surface; and where  $f(\bar{\boldsymbol{\sigma}})$  does not fulfill the inequality and lies outside of the yield surface. In other words, a surface is convex if any point on a straight line between two points lying on the surface itself falls on the surface or within it.

The yield function  $f$  in Equation 3.54 can be written in terms of the yield function coefficient vector and matrix as:

$$f(\boldsymbol{\sigma}) = a + \mathbf{b}^T \boldsymbol{\sigma} + \boldsymbol{\sigma}^T \mathbf{F} \boldsymbol{\sigma} \quad (3.55)$$

With Equation 3.54 and 3.55 one obtains:

$$a + \mathbf{b}^T \bar{\boldsymbol{\sigma}} + \bar{\boldsymbol{\sigma}}^T \mathbf{F} \bar{\boldsymbol{\sigma}} \leq \alpha \left[ a + \mathbf{b}^T \boldsymbol{\sigma} + \boldsymbol{\sigma}^T \mathbf{F} \boldsymbol{\sigma} \right] + (1 - \alpha) \left[ a + \mathbf{b}^T \boldsymbol{\sigma}' + \boldsymbol{\sigma}'^T \mathbf{F} \boldsymbol{\sigma}' \right] \quad (3.56)$$

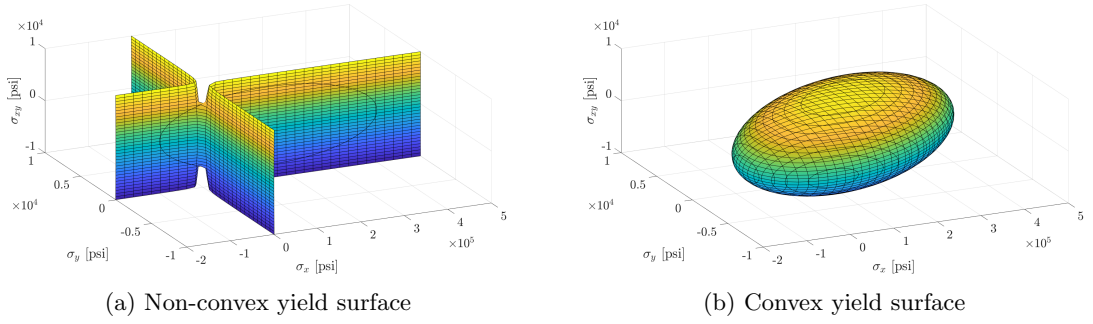


Figure 3.10: Convexity correction of yield surface

The convex combination from 3.53 can now be substituted into Equation 3.56 and, after simplification, this results in the following final equation:

$$(\boldsymbol{\sigma} - \boldsymbol{\sigma}')^T \mathbf{F}(\boldsymbol{\sigma} - \boldsymbol{\sigma}') \geq 0 \quad (3.57)$$

From Equation 3.57 follows the requirement that the matrix  $\mathbf{F}$  has to be positive definite. Therefore, the diagonal components of  $\mathbf{F}$  must be non-negative, whereas the off-diagonal components of  $\mathbf{F}$  must satisfy the following inequalities:

$$\begin{aligned}
 F_{11} \geq 0 \quad F_{22} \geq 0 \quad F_{44} \geq 0 \\
 F_{11}F_{22} - F_{12}^2 \geq 0
 \end{aligned} \quad (3.58)$$

If these inequalities are not satisfied, the yield surface is corrected to be convex. Figure 3.10a shows a non-convex yield surface and Figure 3.10b the convex corrected yield surface where the  $F_{12}$  component of the yield function matrix was changed to produce a convex surface. Two dimensional cutting planes of the same yield surfaces are shown in Figure 3.11 (non-convex) and Figure 3.12 (convex). When viewed in the cutting planes, only the  $\sigma_x - \sigma_y$  plane is effected.

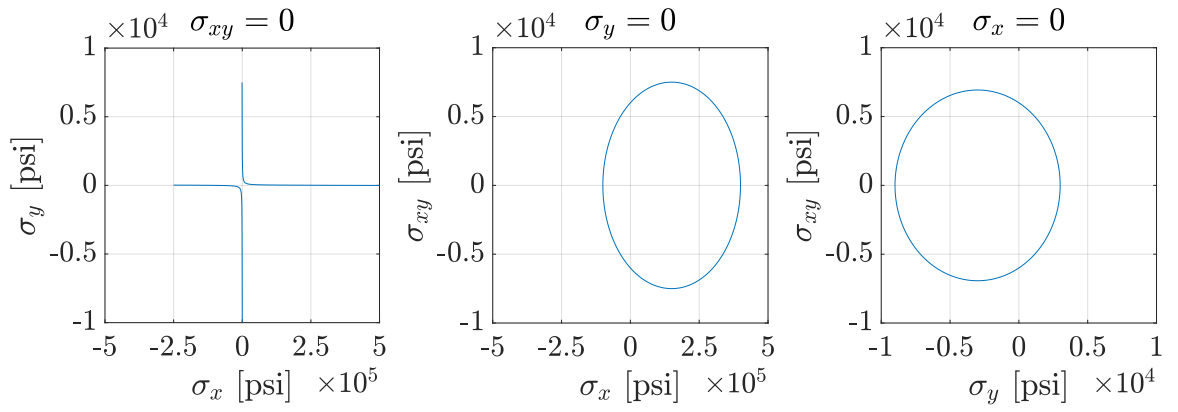


Figure 3.11: Example of a non-convex yield surface in 2D cutting planes

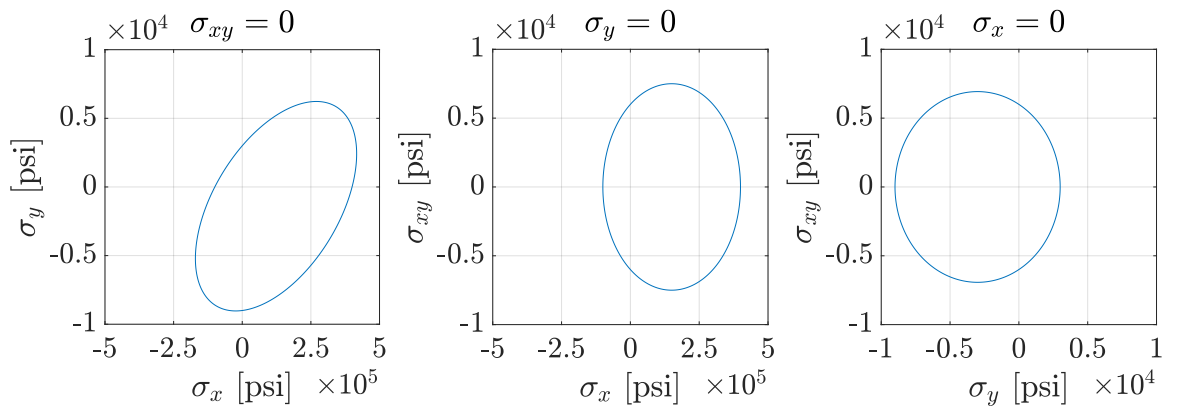


Figure 3.12: Example of a convex yield surface in 2D cutting planes

### 3.3.2 Non-associated Flow Rule

The flow rule in a plasticity model describes the evolution of the plastic flow in the material. Von Mises proposed in 1928 that a plastic potential function  $Q(\boldsymbol{\sigma})$  exists and the plastic strain-rate  $\dot{\boldsymbol{\epsilon}}_p$  could be derived using the following equation [46]:

$$\dot{\boldsymbol{\epsilon}}_p = \dot{\lambda} \frac{\partial Q(\boldsymbol{\sigma})}{\partial \boldsymbol{\sigma}} \quad (3.59)$$

where the plasticity variable,  $\lambda$ , is a proportional positive scalar factor.

In associated flow, the plastic potential function  $Q(\boldsymbol{\sigma})$  is taken to be the same as the yield function ( $f$ ), meaning that the plastic strain-rate is normal to the yield surface. Equation 3.60 shows the associated flow rule [47]:

$$\dot{\boldsymbol{\epsilon}}_p = \dot{\lambda} \frac{\partial f}{\partial \boldsymbol{\sigma}} \quad (3.60)$$

Experiments have shown that this assumption works well to characterize the plastic deformation of metals. For composites, however, a non-associated flow rule has been chosen due to their strong anisotropy. In many unidirectional composites, for example, plastic flow in the fiber direction does not occur at room temperature, and, therefore, a non-associated flow rule was required allowing for non-consistent (non-associated) plastic flow. As a plastic potential for the flow rule, a similar equation as the yield function is used, as shown in Equation 3.61 similar to Hoffarth [3]. However, the equation does not include the linear terms that can differentiate between tension and compression. The plastic potential for the flow rule is now called  $h$ :

$$h^2 = H_{11}\sigma_{11}^2 + H_{22}\sigma_{22}^2 + 2H_{12}\sigma_{11}\sigma_{22} + \frac{1}{2}H_{44}\sigma_{12}^2 + \frac{1}{2}H_{44}\sigma_{21}^2 \quad (3.61)$$

The symmetry of the Cauchy stress is used to combine the two in-plane shear terms  $\sigma_{12}$  and  $\sigma_{21}$ , which yields:

$$h^2 = H_{11}\sigma_{11}^2 + H_{22}\sigma_{22}^2 + 2H_{12}\sigma_{11}\sigma_{22} + H_{44}\sigma_{12}^2 \quad (3.62)$$

Or in matrix notation:

$$h^2 = \begin{bmatrix} \sigma_{11} \\ \sigma_{22} \\ \sigma_{12} \end{bmatrix}^T \begin{bmatrix} H_{11} & H_{12} & 0 \\ H_{12} & H_{22} & 0 \\ 0 & 0 & H_{44} \end{bmatrix} \begin{bmatrix} \sigma_{11} \\ \sigma_{22} \\ \sigma_{12} \end{bmatrix} = \boldsymbol{\sigma}^T \mathbf{H} \boldsymbol{\sigma} \quad (3.63)$$

where  $H_{ij}$  are the independent flow rule coefficients that are assumed to be constant.

Instead of the yield function as in associated flow, the plastic potential function from Equation 3.61 is now used in the flow-law, resulting in non-associated flow:

$$\dot{\boldsymbol{\epsilon}}_p = \dot{\lambda} \frac{\partial h}{\partial \boldsymbol{\sigma}} \quad (3.64)$$

The plastic flow is therefore not necessarily normal to the yield surface. From the flow-law in Equation 3.64 and the plastic potential in Equation 3.61, the plastic strains can be written in terms of the plastic multiplier, plastic potential, and the stresses as follows:

$$\dot{\epsilon}_{11_p} = \frac{\dot{\lambda}}{2h} (2H_{11}\sigma_{11} + 2H_{12}\sigma_{22}) \quad (3.65)$$

$$\dot{\epsilon}_{22_p} = \frac{\dot{\lambda}}{2h} (2H_{12}\sigma_{11} + 2H_{22}\sigma_{22}) \quad (3.66)$$

$$\dot{\epsilon}_{12_p} = \frac{\dot{\lambda}}{2h} (H_{44}\sigma_{12}) \quad (3.67)$$

By defining the “plastic Poisson’s ratios” in terms of these plastic strains from Equations 3.65 and 3.66, for uniaxial loading in the 1-direction, the flow rule coefficients  $H_{ij}$  can be defined as follows [3]:

$$\sigma_{22} = 0 : \quad \nu_{12_p} = -\frac{\dot{\epsilon}_{22_p}}{\dot{\epsilon}_{11_p}} = -\frac{H_{12}}{H_{11}} \quad (3.68)$$

And from uniaxial testing in the 2-direction one obtains:

$$\sigma_{11} = 0 : \quad \nu_{21_p} = -\frac{\dot{\epsilon}_{11_p}}{\dot{\epsilon}_{22_p}} = -\frac{H_{12}}{H_{22}} \quad (3.69)$$

Equations 3.68 and 3.69 will be used to determine the flow rule coefficients in the next subsection.

### Determining the flow-law coefficients

The constant flow-law coefficients have to be determined individually for every composite material and especially for different composite architectures. The procedures to identify the coefficients are first described for a unidirectional composite and later for a braided composite.

Unidirectional composites, in tension at room temperature, behave as linear elastic along the fiber direction (1-direction), meaning the plastic strain in this direction should always be zero. From Equation 3.65 then follows that  $H_{11}$  and  $H_{12}$  must be zero. Orthogonal to the fiber direction (2-direction) for uniaxial loading, Equation 3.61 simplifies to the following:

$$h = \sqrt{H_{22}\sigma_{22}} \quad (3.70)$$

We can assume that the effective stress  $h$  is equal to the stress  $\sigma_{22}$  when uniaxial loading is applied in this direction. It subsequently follows that  $H_{22}$  must be equal to one. Similar to the flow rule coefficient in 2-direction, the in-plane coefficient  $H_{44}$  can be determined.

Using Equation 3.67 with  $h = \sqrt{H_{44}}\sigma_{12}$ , assuming pure in-plane shear loading, yields:

$$\begin{aligned}\dot{\varepsilon}_{12_p} &= \frac{\dot{\lambda}}{2\sqrt{H_{44}}\sigma_{12}} H_{44}\sigma_{12} \\ \dot{\varepsilon}_{12_p} &= \frac{\dot{\lambda}}{2}\sqrt{H_{44}} \\ d\varepsilon_{12_p} &= \frac{d\varepsilon_{eff_p}}{2}\sqrt{H_{44}}\end{aligned}\tag{3.71}$$

where  $d\varepsilon_{eff_p}$  is the effective plastic strain.

Using Equation 3.71, the shear coefficient can be determined by fitting the effective stress versus effective plastic strain curve for the in-plane shear to the effective stress versus effective plastic strain curve based on the transverse tension test [3].

The assumptions for a unidirectional composite do not apply for a braided composite, however, the flow rule coefficients can be determined using similar procedures. In the unidirectional case, no plastic flow was possible in the 1-direction and so  $H_{11} = 0$ . For a braided composite, however, this is not the case and the flow rule can now be simplified for uniaxial loading in the 1-direction as follows:

$$h = \sqrt{H_{11}}\sigma_{11}\tag{3.72}$$

One uses a similar assumption for the 2-direction in the unidirectional case, namely, that the effective stress  $h$  is equal to the stress  $\sigma_{11}$  when loading is applied uniaxial in this direction. It therefore follows, that  $H_{11}$  must now be equal to one. With  $H_{11} = 1$  and Equation 3.68 and 3.69 then follows:

$$\begin{aligned}H_{12} &= -\nu_{12_p} \\ H_{22} &= \frac{\nu_{12_p}}{\nu_{21_p}}\end{aligned}\tag{3.73}$$

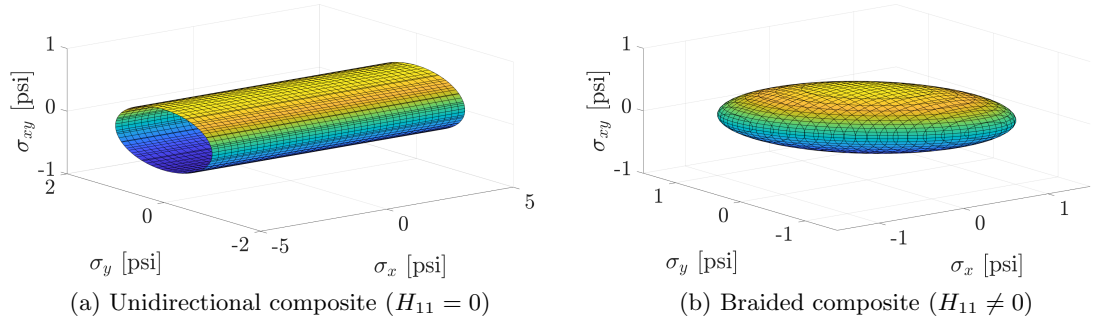


Figure 3.13: Example flow surfaces

The flow-law coefficient for the in-plane shear ( $H_{44}$ ) is determined using the same fitting technique as in the unidirectional case.

Figure 3.13a shows an example of a flow surface for flow rule coefficients of  $H_{11} = 0$ ,  $H_{22} = 1.0$ ,  $H_{12} = 0.0$  and  $H_{44} = 4.2$ , which is typical for a unidirectional composite. The flow surface is open in the fiber direction ( $\sigma_{11}$ ), which means that no plastic flow is possible in that direction.

Figure 3.13b shows an example of a flow surface for flow rule coefficients of  $H_{11} = 1.0$ ,  $H_{22} = 1.0$ ,  $H_{12} = 0.5$  and  $H_{44} = 4.2$ , which could represent a braided composite. Plastic flow is possible in all directions and, therefore, the flow surface is closed.

### 3.3.3 Rate Dependency

To avoid oscillation problems that occur in the total strain-rate due to the elastic components (described in Section 3.2.4), the effective plastic strain-rate is utilized to look up the yield stress for a given loading rate and temperature. This requires the conversion of strain-rate versus stress versus strain tables into effective plastic strain-rate versus stress versus plastic strain tables.

For every increment in the load curve, the equivalent plastic strain-rate can be computed as:

$$\left. \begin{aligned} \Delta\varepsilon &= \varepsilon^{n+1} - \varepsilon^n = \dot{\varepsilon}\Delta t \\ \Delta\lambda &= \lambda^{n+1} - \lambda^n = \dot{\lambda}\Delta t \end{aligned} \right\} \Rightarrow \dot{\lambda} = \frac{\Delta\lambda}{\Delta\varepsilon}\dot{\varepsilon} \quad (3.74)$$

This results in a conversion factor for every increment in the user defined load curve. The average of all factors is used to identify a single conversion factor from total strain-rate to effective plastic strain-rate for every given curve.

The conversion from non-rate-dependent plasticity to viscoplasticity, therefore, only requires changing the strain-rate value in the Table3D, the curve itself need not to be modified further.

This practical approximation works perfectly for bilinear laws and remains acceptable for most yield curves. For a bilinear curve, the equivalent plastic strain-rate will be the same in all points if the curve is defined for a constant total strain-rate.

### 3.4 Coupling Viscoelasticity and Viscoplasticity

Viscoelasticity and viscoplasticity are coupled by replacing the computation of the elastic trial stress for the plasticity algorithm (Section 3.3) by the viscoelastic trial stress as described in Section 3.2.3. The plasticity algorithm stays unchanged, however, the final stress after plasticity is then computed using Equation 3.75:

$$\begin{aligned} \boldsymbol{\sigma}^{n+1} &= \boldsymbol{\sigma}_t^{n+1} - \Delta\boldsymbol{\sigma} \\ \boldsymbol{\sigma}^{n+1} &= \boldsymbol{\sigma}_t^{n+1} - (\mathbf{C}_e + \mathbf{C}_v(\dot{\varepsilon}) \circ \mathbf{B}) : \Delta\lambda \frac{\partial h}{\partial \boldsymbol{\sigma}} \end{aligned} \quad (3.75)$$

The equilibrium and viscous stress have to be updated accordingly to continue to satisfy the requirement that the sum of the viscous and equilibrium stress equal the total stress:  $\boldsymbol{\sigma}^{n+1} = \boldsymbol{\sigma}_e^{n+1} + \boldsymbol{\sigma}_v^{n+1}$ . To avoid relaxation below the quasistatic stress levels, equilibrium

and viscous stress are updated using the following algorithm, where  $f_e$  is the yield function corresponding to the equilibrium stress.

If  $f_e \leq 0$ :

$$\sigma_v^{n+1} = \sigma_v^{n+1} - \Delta\sigma$$

$$\sigma_v^{n+1} = \sigma_v^{n+1} - (\mathbf{C}_e + \mathbf{C}_v(\dot{\varepsilon}) \circ \mathbf{B}) : \Delta\lambda \frac{\partial h}{\partial \sigma} \quad (3.76)$$

$$\sigma_e^{n+1} = \sigma_e^{n+1} \quad (3.77)$$

else:

$$\sigma_v^{n+1} = \sigma_v^{n+1} - \Delta\sigma_v$$

$$\sigma_v^{n+1} = \sigma_v^{n+1} - (\mathbf{C}_v(\dot{\varepsilon}) \circ \mathbf{B}) : \Delta\lambda \frac{\partial h}{\partial \sigma} \quad (3.78)$$

$$\sigma_e^{n+1} = \sigma_e^{n+1} - \Delta\sigma_e$$

$$\sigma_e^{n+1} = \sigma_e^{n+1} - \mathbf{C}_e : \Delta\lambda \frac{\partial h}{\partial \sigma} \quad (3.79)$$

Figure 3.14 visualizes the reasoning behind this process. Consider a bilinear, linear elastic, ideal plastic stress-strain curve for quasistatic loading (green curve) and another bilinear stress-strain curve with the same yield stress but higher Young's modulus for a given higher rate (blue curve).

Figure 3.14a shows the stress state from the previous time step ( $\sigma^n$ ), where the yield stress has just been reached and the viscoelastic trial stress ( $\sigma_t^{n+1}$ ) for a loading at the higher rate is shown in red. The viscoelastic trial stress is the sum of the viscous stress ( $\sigma_v$ ) and the equilibrium stress ( $\sigma_e$ ), where the equilibrium stress has not yet yielded and, therefore, the yield function for the given equilibrium stress is below zero ( $f_e \leq 0$ ). During the plasticity algorithm, the final total stress state ( $\sigma^{n+1} = \sigma_y$ ) and the corresponding plastic strain

increment  $(\Delta\lambda\frac{\partial h}{\partial\sigma})$  are computed. Figure 3.14b shows how the equilibrium and viscous stresses are updated. The total stress is reduced by  $\Delta\sigma$  to return to the yield surface (Equation 3.75). Because the equilibrium stress was within its corresponding yield surface, the equilibrium trial stress is not changed (Equation 3.77). The viscous stress, however, is reduced by  $\Delta\sigma$  following Equation 3.76, fulfilling the requirement of  $\sigma^{n+1} = \sigma_e^{n+1} + \sigma_v^{n+1}$ .

Figure 3.14c again shows the stress state from the previous time step ( $\sigma^n$ ), where the yield stress has been reached for both the total and the equilibrium stress. The viscoelastic trial stress ( $\sigma_t^{n+1}$ ) for a loading at the higher rate is also shown in red. The viscoelastic trial stress is always the sum of the viscous trial stress and the equilibrium trial stress, where the latter is computed using the quasistatic Young's modulus. The equilibrium stress has already yielded and, therefore, the yield function for the given equilibrium stress is above zero ( $f_e > 0$ ). The plasticity algorithm is then entered and the final total stress state ( $\sigma^{n+1} = \sigma_y$ ) and the corresponding plastic strain increment ( $\Delta\lambda\frac{\partial h}{\partial\sigma}$ ) are computed. Figure 3.14d shows how the equilibrium and viscous stresses are updated. The total stress is again reduced by  $\Delta\sigma$  to return to the yield surface (Equation 3.75). Because the equilibrium stress was outside of its corresponding yield surface, the equilibrium trial stress is updated following Equation 3.79. The viscous stress is now reduced by  $\Delta\sigma_v$  following Equation 3.78, again fulfilling the requirement of  $\sigma^{n+1} = \sigma_e^{n+1} + \sigma_v^{n+1}$ .

### 3.5 Temperature Dependency

Mechanical properties of polymeric materials are very temperature sensitive, with the effect increasing as the glass transition temperature is approached. For example, the yield stress of a polymer at the glass transition temperature tends to zero [48]. For many applications it is important to model these effects accurately. In the following text, adiabatic heating effects due to plastic work will be discussed.

When metal deforms plastically, a rise in temperature of the material can be measured. Explanations of this phenomenon discuss the process of hardening due to phase changes of

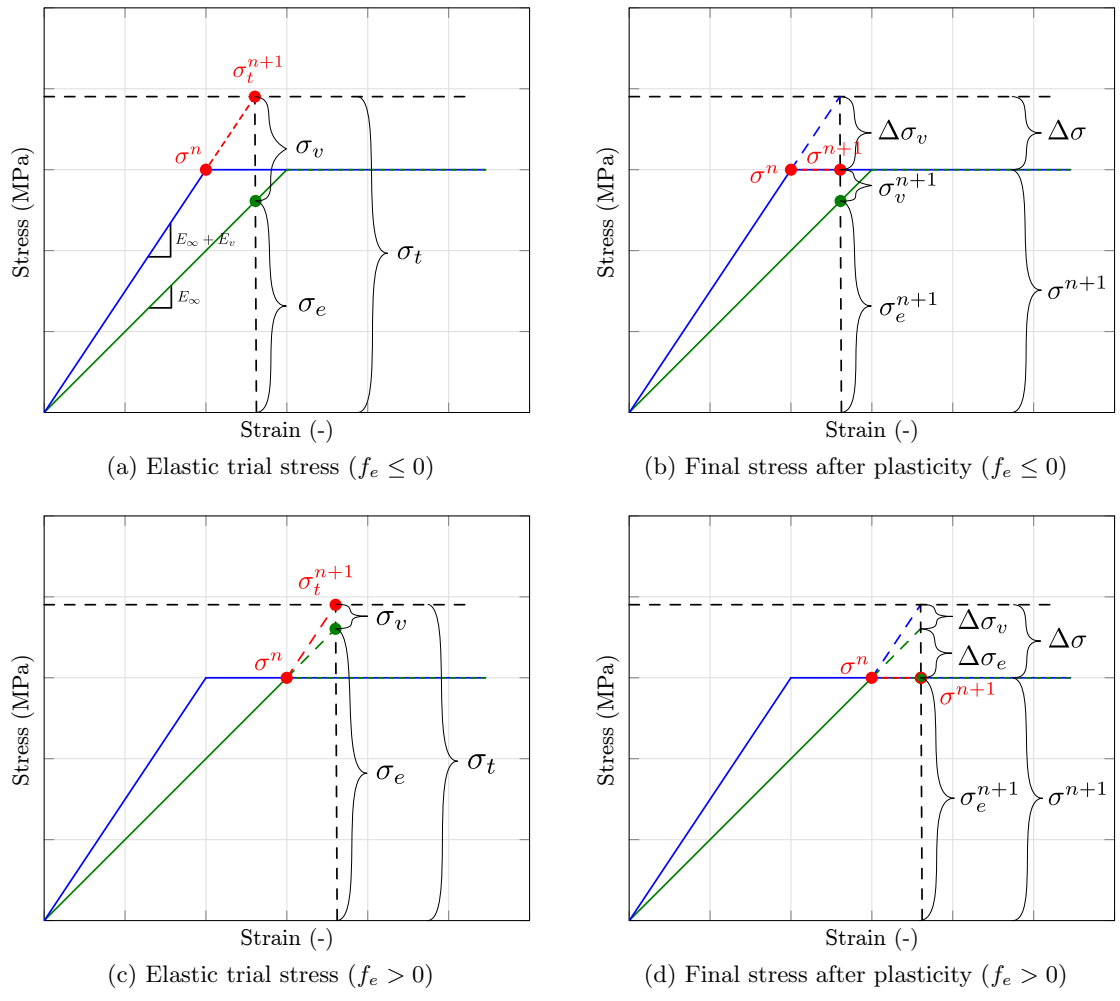


Figure 3.14: Viscoelastic viscoplastic coupling

the material and in turn changes of the internal energy of the material [49]. By comparing the heat equivalent of the work done and the measured heat during the deformation, a change in internal energy of the material can be verified. According to Taylor and Quinney, “When a metal is subjected to plastic distortion most of the work done reappears in the form of heat, but a certain proportion remains latent and is no doubt associated with the changes to which cold working give rise in the physical properties of the metal” [50]. In metals, generally between 5 and 15% of the work done is spent on phase changes of the material, while the majority is converted to heat and leads to a rise in temperature of the specimen. This temperature rise also depends on the rate of loading. If the generated heat has time to conduct away, little temperature rise can be measured (isothermal conditions). When the time scales of the experiment are very short, adiabatic conditions occur and the temperature can rise noticeably [51].

Rittel discussed this phenomenon for polymers [51]. Trojanowski et al. [48] used infrared detectors to monitor temperature rise in epoxy specimens tested in a split Hopkinson pressure bar. The achieved strain-rate was  $2500\frac{1}{s}$  and the measured temperature rise for a specific epoxy reached  $40^{\circ}\text{C}$ .

According to Taylor and Quinney, the adiabatic rise in temperature in a material due to plastic work ( $W_p$ ) can be calculated as follows [50]:

$$d\dot{T} = \frac{\beta_t}{C_p\rho}d\dot{W}_p \quad (3.80)$$

where  $\dot{T}$  is the change in temperature,  $\beta_t$  is the Taylor–Quinney coefficient that represents the proportion of plastic work converted into heat,  $\rho$  is the density, and  $C_p$  is the specific heat at constant pressure.

With the equivalence of plastic work (Equation 3.81), Equation 3.80 can be expressed in terms of the flow rule coefficient and plastic multiplier as follows in Equation 3.82.

$$\dot{W}_p = \boldsymbol{\sigma} : \dot{\boldsymbol{\epsilon}}_p = \boldsymbol{\sigma} : \dot{\lambda} \frac{\partial h}{\partial \boldsymbol{\sigma}} = h \dot{\lambda} \quad (3.81)$$

$$\dot{T} = \frac{\beta_t}{C_p \rho} h \dot{\lambda} \quad (3.82)$$

With the rise in temperature, the polymer matrix material softens, decreasing the yield stress of the material in matrix dominated material directions.

### 3.6 Damage

When a composite material is loaded, irreversible micro-cracks and cavities can form. These defects cause stiffness degradation in the composite [10].

To capture this softening of the stress-strain response, the material model is enhanced by a damage model. Strain equivalence is assumed, meaning that in both the true and effective stress space, elastic and plastic strains are the same [52]. This allows for the damage calculations to be uncoupled and independent of the plasticity algorithm that takes place in the effective stress space.

The effective (undamaged) stresses are related to the true (damaged) stresses by the damage tensor  $\mathbf{M}$ , as shown in Equation 3.83 [53]:

$$\begin{bmatrix} \sigma_{11} \\ \sigma_{22} \\ \sigma_{12} \end{bmatrix} = \begin{bmatrix} M_{11} & 0 & 0 \\ 0 & M_{22} & 0 \\ 0 & 0 & M_{44} \end{bmatrix} \begin{bmatrix} \sigma_{11_{eff}} \\ \sigma_{22_{eff}} \\ \sigma_{12_{eff}} \end{bmatrix} \quad (3.83)$$

The use of a diagonal damage tensor suggests that loading in a specific material direction leads to a reduction in stiffness in this direction only. Experimental research in composites suggests that a load in one material direction can lead to damage in another material direction. The in-plane shear modulus, for example, can decrease with increasing tensile load due to transverse cracking of the matrix [54]. Similarly, the transverse stiffness can be reduced due to damage accumulation in shear loading [55].

These effects are accounted for by including the coupling terms between material directions in the components of the damage tensor. These are computed as follows in Equations 3.84 to 3.88 [56]. The superscripts of the damage coefficients  $d$  denote in which direction the damage is occurring, while the subscripts specify which loading direction caused the damage. For example,  $d_{11C}^{11T}$  would be the coupled damage coefficient for damage in tension 1-direction due to loading in compression 1-direction. Depending on whether the current state of stress is positive or negative, the corresponding component of the damage tensor is computed using the coefficients for tension or compression. This can be viewed for 1-direction tension in Equation 3.84 or 1-direction compression in Equation 3.85.

$$\sigma_{11} > 0 : \quad M_{11} = \left(1 - d_{11T}^{11T}\right) \left(1 - d_{11C}^{11T}\right) \left(1 - d_{22T}^{11T}\right) \left(1 - d_{22C}^{11T}\right) \left(1 - d_{12}^{11T}\right) \quad (3.84)$$

$$\sigma_{11} < 0 : \quad M_{11} = \left(1 - d_{11T}^{11C}\right) \left(1 - d_{11C}^{11C}\right) \left(1 - d_{22T}^{11C}\right) \left(1 - d_{22C}^{11C}\right) \left(1 - d_{12}^{11C}\right) \quad (3.85)$$

$$\sigma_{22} > 0 : \quad M_{22} = \left(1 - d_{11T}^{22T}\right) \left(1 - d_{11C}^{22T}\right) \left(1 - d_{22T}^{22T}\right) \left(1 - d_{22C}^{22T}\right) \left(1 - d_{12}^{22T}\right) \quad (3.86)$$

$$\sigma_{22} < 0 : \quad M_{22} = \left(1 - d_{11T}^{22C}\right) \left(1 - d_{11C}^{22C}\right) \left(1 - d_{22T}^{22C}\right) \left(1 - d_{22C}^{22C}\right) \left(1 - d_{12}^{22C}\right) \quad (3.87)$$

$$M_{44} = \left(1 - d_{11T}^{22C}\right) \left(1 - d_{11C}^{22C}\right) \left(1 - d_{22T}^{22C}\right) \left(1 - d_{22C}^{22C}\right) \left(1 - d_{12}^{22C}\right) \quad (3.88)$$

The damage terms are defined as a function of strain by the user. In the initialization phase, the damage versus strain curves are transformed to damage versus plastic strain curves to track damage accumulation in the different directions independently. The user provided true (damaged) stress versus strain input curves in the individual directions are

converted based on these damage versus strain curves to effective (undamaged) stress versus effective plastic strain curves. This separates damage effects and plasticity in the algorithm. For this conversion, only the plastic strain in the loading direction, for which the stress versus strain curves was defined, is used.

The plastic strains in terms of the plastic multiplier, plastic potential, and the stresses were defined in Equations 3.65 through 3.67. For the normal strains, these equations are again shown in Equation 3.89:

$$\dot{\epsilon}_{11_p} = \frac{\dot{\lambda}}{2h}(2H_{11}\sigma_{11} + 2H_{12}\sigma_{22}) \quad \dot{\epsilon}_{22_p} = \frac{\dot{\lambda}}{2h}(2H_{12}\sigma_{11} + 2H_{22}\sigma_{22}) \quad (3.89)$$

For the two special cases of uniaxial tension or compression in the 1- and 2-direction, this leads to the following plastic strains:

$$\begin{bmatrix} \sigma_{11} & 0 \\ 0 & 0 \end{bmatrix} \Rightarrow \begin{cases} \dot{\epsilon}_{11_p} = \frac{\dot{\lambda}}{2h}(2H_{11}\sigma_{11}) \\ \dot{\epsilon}_{22_p} = \frac{\dot{\lambda}}{2h}(2H_{12}\sigma_{11}) \end{cases} \quad \begin{bmatrix} 0 & 0 \\ 0 & \sigma_{22} \end{bmatrix} \Rightarrow \begin{cases} \dot{\epsilon}_{11_p} = \frac{\dot{\lambda}}{2h}(2H_{12}\sigma_{22}) \\ \dot{\epsilon}_{22_p} = \frac{\dot{\lambda}}{2h}(2H_{22}\sigma_{22}) \end{cases} \quad (3.90)$$

The transversal plastic strains caused by the longitudinal stress components will add to the longitudinal damage if coupled damage terms are defined. This then leads to the output curves not matching the user defined input, as during the curve conversion from true (damaged) stress to effective (undamaged) stress only the longitudinal uncoupled damage in this direction was considered. To counteract this issue, “corrected plastic strains” are defined. Equation 3.91 shows the corrected plastic strains to only consider damage in loading direction:

$$\dot{\epsilon}_{11_{pc}} = \frac{\dot{\lambda}}{2h}(2H_{11}\sigma_{11}) \quad \dot{\epsilon}_{22_{pc}} = \frac{\dot{\lambda}}{2h}(2H_{22}\sigma_{22}) \quad \dot{\epsilon}_{12_{pc}} = \frac{\dot{\lambda}}{2h}(H_{44}\sigma_{12}) \quad (3.91)$$

A formulation based on these corrected plastic strains guarantees that the output curves match the input curves for uniaxial load cases.

### 3.7 Generalized Tabulated Failure Criterion

Failure of material in finite element simulations is generally handled by removing elements from the simulation where stresses or strains are determined to have exceeded a failure criterion. In crash, crush or ballistic impact simulations of composites, however, removing elements from the simulation once a failure criterion is satisfied in only one material direction does lead to non-physical behavior. Consider loading a unidirectional composite in tension 2-direction until matrix cracks or fiber-matrix debonding occurs. In this uniaxial test, the material would now be considered to have “failed”. In reality, however, many if not most fibers might still be intact, and the material can still take load when reloaded in the fiber direction. Following traditional failure models, elements in a finite element simulation would have been eroded and load bearing capabilities in all directions would be lost.

In the following, a flexible erosion criterion for composites is introduced. The erosion criterion can be used both as a traditional composite failure model, or to erode highly deformed elements that have lost most of their load bearing capabilities in the different material directions due to damage. Damage and erosion are therefore handled independent from each other. This allows the use of the damage model to progressively degrade the material in different directions and the Generalized Tabulated Failure Criterion to erode the elements once damage has sufficiently decreased the ability of the material to take any further loads.

To define when erosion should occur, a failure surface is introduced. This surface describes a surface in stress or strain space for which the material fails. If the stress state is within the surface, failure does not occur. Once the stress or strain state lies on or beyond the failure surface, the material fails. In traditional failure models, mathematical functions describe the shape of this surface. This restricts the shape of the surface and failure of a composite may or may not be accurately modeled. To overcome this restriction, a tabulated approach similar to the one described by Goldberg et al. [57] is used.

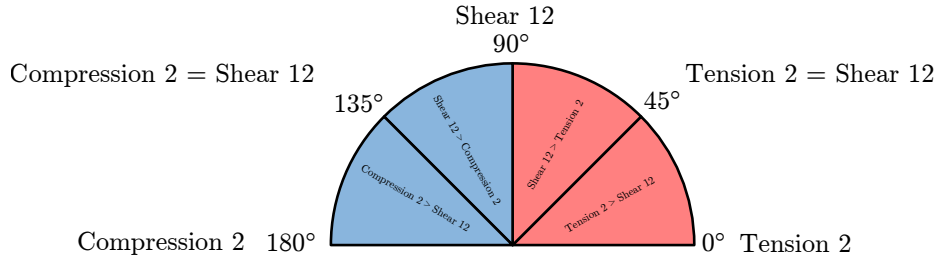


Figure 3.15: Failure angle

To describe a state of plane stress uniquely, two independent variables are necessary. In the following approach, an angle is used as the first independent variable describing the location of a point in the  $\sigma_{22}$ - $\sigma_{12}$  plane:

$$\theta = \cos^{-1} \left( \frac{\sigma_{22}}{\sqrt{\sigma_{22}^2 + \sigma_{12}^2}} \right) \quad (3.92)$$

The meaning of this angle in bi-axial loading is visualized in Figure 3.15. In the case of pure Tension 2-direction loading ( $\sigma_{12} = 0$  and  $\sigma_{22} > 0$ ) the computed angle  $\theta$  is zero, whereas in the case of pure Shear 12-direction loading ( $\sigma_{22} = 0$ ) the computed angle is  $90^\circ$ .

As the second independent variable, the value of the stress in 1-direction  $\sigma_{11}$  is used. These two independent variables describe the location of a point on the failure surface, while a dependent variable defines the magnitude of said failure surface. In contrast to Goldberg et al. [57], the dependent variable of choice is an equivalent strain, as defined in Equation 3.93:

$$\varepsilon_{eq} = \sqrt{\varepsilon_{11}^2 + \varepsilon_{22}^2 + 2\varepsilon_{12}^2} \quad (3.93)$$

This equivalent strain is then compared with the user-defined value of an equivalent failure strain  $\varepsilon_{fail}$  for the given angle and shear stress.

$$d = \frac{\varepsilon_{eq}}{\varepsilon_{fail}} \quad (3.94)$$

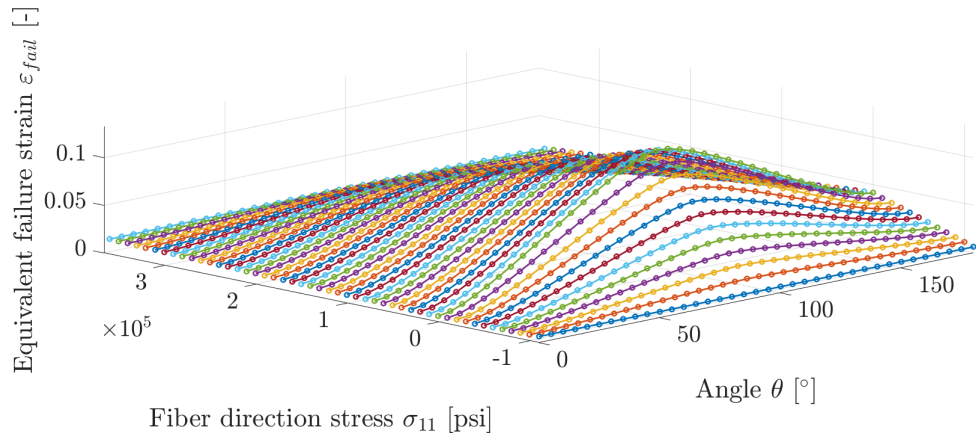


Figure 3.16: Failure surface

For  $d \geq 1$  the element fails and is eroded. The possibility to define a discrete value for any state of plane stress allows one to include actual experimental data to construct the failure surface. Failure variables for states of stress where the user cannot obtain experimental values can be calculated using traditional analytical failure models or numerical experiments.

Figure 3.16 shows an example of such a failure surface. The in-plane axis “Fiber direction stress” and “Angle” describe the state of stress the element undergoes, while the out-of-plane axis “Equivalent failure strain” describes the magnitude of strains at which the element is eroded.

## Chapter 4: Implementation

This chapter focuses on the implementation of the material model that is described in Chapter 3. The described methodology can be implemented into most of the currently available Finite Element codes. The implementation into the commercial Finite Element solver LS-DYNA is described in the following text. LS-DYNA is written in the FORTRAN programming language; as such, FORTRAN was chosen for the developed material subroutine.

First, the required user input is discussed and then the algorithm is explained on the basis of a high-level flowchart. The plasticity algorithm was based on the works by Hofarth [58], although additional capabilities and improvements have been added including visoelastic-viscoplastic rate effects, improvements to the damage model, and a Generalized Tabulated Failure model. Furthermore, capabilities of defining stochastic variation for a selection of material parameters have been implemented.

### 4.1 Required User Input and Output from History Variables

A minimum of five stress versus strain input curves are required to utilize the material model. Table 4.1 lists the results from uniaxial tension and compression tests, as well as in-plane shear, that serve as input to the material model. Optionally, the stress versus strain results from a 45° off-axis in-plane test can be defined. Leaving the off-axis input empty modifies the yield function by setting  $F_{12}$  to zero (see Equation 3.55).

In Figure 4.1 the structure of the required input for one material direction is shown. For the material direction (e.g. Tension 1-direction) a Table 3D ID is defined. This Table 3D holds a minimum of one Table 2D ID for a given temperature value. In the Table 2D a minimum of two strain-rate values and corresponding stress versus strain input curves have

Table 4.1: Required and optional stress vs. strain input

Material direction	Input variable (Table 3D ID)
Tension 1-direction	LT1
Tension 2-direction	LT2
Compression 1-direction	LT4
Compression 2-direction	LT5
Shear 12-plane	LT7
45° Off-axis 12-plane (optional)	LT10

to be defined. If no rate effects are to be included, both curves can be given the same stress versus strain data.

In addition to the tabulated stress versus strain curves for the different material directions, several scalar values have to be defined in the actual material card. Table 4.2 shows the input to the material card excluding the options for failure modeling. Some of the common options that are shared with many other composite materials, like the material direction definition using *AOPT*, are not discussed. The user is here referred to the LS-DYNA materials user manual [4].

As with any other LS-DYNA material, a material identification number (*MID*) has to be defined as well as the density ( $\rho$ ).

The moduli in the different material directions are needed for the initial time step calculation, but will not influence the material response as the moduli are obtained from the stress versus strain input in each of the material directions.

The elastic Poisson's ratios have to be defined as well as the shear moduli in the different material planes, similar to many other LS-DYNA composite materials.

The parameter *PTOL* sets the yield function tolerance that is used during the plasticity algorithm during the secant iteration. When leaving this value blank, a default value of  $1.0e^{-6}$  is used.

Changing the *TCSYM* parameter allows for the specification of tension-compression symmetry in all material directions. In certain load cases, like minimally constrained single

Table 4.2: MAT213 material cards one through seven

Variable	Symbol	Description
MID	–	Material identification.
RO	$\rho$	Mass density
EA	$E_a$	Young's modulus in a-direction.
EB	$E_b$	Young's modulus in b-direction.
EC	$E_c$	Young's modulus in c-direction.
PRBA	$\nu_{ba}$	(elastic) Poisson's ratio ba.
PRCA	$\nu_{ca}$	(elastic) Poisson's ratio ca.
PRCB	$\nu_{cb}$	(elastic) Poisson's ratio cb.
GAB	$G_{ab}$	Shear modulus a-b plane.
GBC	$G_{bc}$	Shear modulus b-c plane.
GCA	$G_{ca}$	Shear modulus c-a plane.
PTOL	–	Yield function tolerance.
FILT	–	Factor for strain rate filtering (optional)
VEVP	–	Flag to control viscoelastic viscoplastic behavior.
TCSYM	–	Flag for handling tension-compression asymmetry.
H11 - H44	$H_{ii}$	Plastic flow rule coefficients.
LTi	–	Table 3D ID's
YSC	–	Curve ID containing stress vs. strain curve ID's vs. yield strain
TEMP	$T$	Temperature to be used in the simulation.
DC	–	Damage Curve ID.
FTYPE	–	Faiure criterion type.
FV2	–	Table ID for the table containing the stresses vs. curve ID pairs for the failure model
CP	$C_p$	Specific heat capacity
BETAT	$\beta_t$	Taylor-Quinney coefficient
BETA11 – BETA66	$\beta$	Decay constants for the relaxation matrix of the viscoelastic law

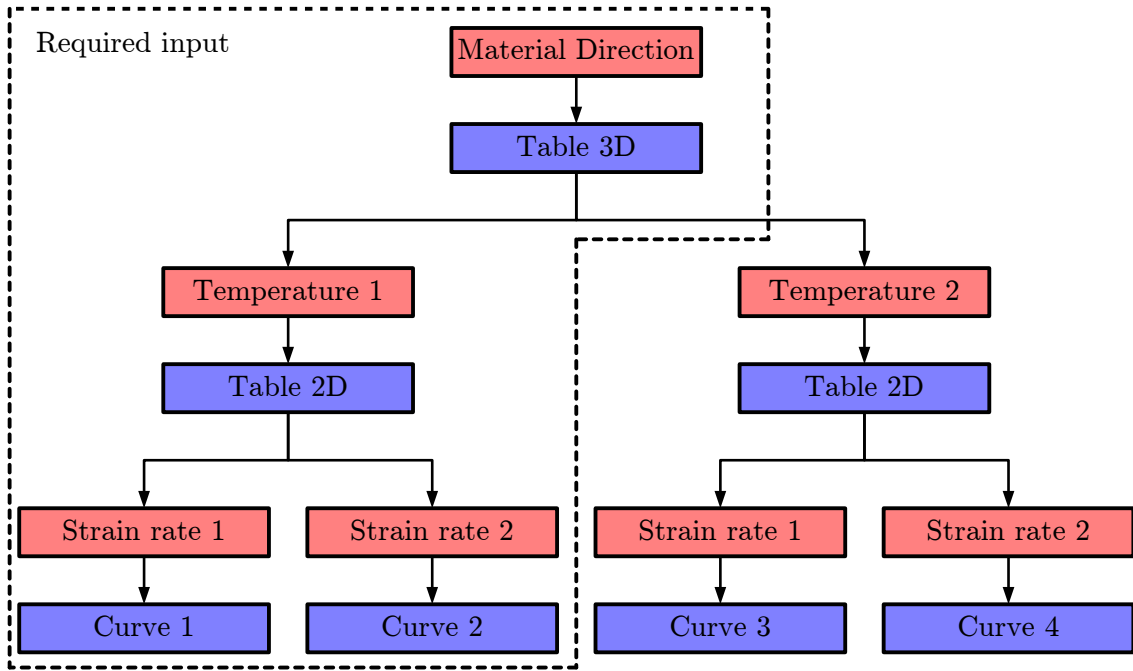


Figure 4.1: Required user input for each material direction

element simulations, tension-compression asymmetry might cause oscillations in the off-axis direction as the modulus can switch between the tensile and compressive modulus for stresses alternating between positive and negative values. The LS-DYNA material keyword manual [4] describes the different options in detail.

Next in the input are the plastic flow rule coefficients that are determined using the plastic Poisson's ratios, as described in Section 3.3.2. For the shell element model, the flow rule coefficients  $H_{11}$ ,  $H_{22}$ ,  $H_{12}$  and  $H_{44}$  are required while  $H_{23}$  and  $H_{13}$  can be used to adjust the plastic flow in the thickness direction. For purely elastic directions (e.g. the fiber direction in unidirectional composites), the corresponding flow rule coefficient  $H$  should be zero. Additionally, the defined stress versus strain input curve for this direction should be linear, with a yield strain value (defined in the YSC curve) that is larger than the maximum strain that is defined in the stress versus strain input curve. The Table 3D ID's are defined as LT1 through LT10, as shown in Table 4.1.

Table 4.3: Optional damage parameters

ID	Parameter	Description	ID	Parameter	Description
1	$d_{11T}^{11T}(\varepsilon_{11T})$	D. in T1; due to T1	37	$d_{11C}^{11C}(\varepsilon_{11C})$	D. in T1; due to C1
2	$d_{22T}^{22T}(\varepsilon_{22T})$	D. in T2; due to T2	38	$d_{22C}^{11C}(\varepsilon_{11C})$	D. in T2; due to C1
4	$d_{11C}^{11C}(\varepsilon_{11C})$	D. in C1; due to C1	40	$d_{22C}^{11C}(\varepsilon_{11C})$	D. in C2; due to C1
5	$d_{22C}^{22C}(\varepsilon_{22C})$	D. in C2; due to C2	42	$d_{12}^{11C}(\varepsilon_{11C})$	D. in S12; due to C1
7	$d_{12}^{12}(\varepsilon_{12})$	D. in S12; due to S12	45	$d_{11T}^{22C}(\varepsilon_{22C})$	D. in T1; due to C2
13	$d_{22T}^{11T}(\varepsilon_{11T})$	D. in T2; due to T1	46	$d_{22T}^{22C}(\varepsilon_{22C})$	D. in T2; due to C2
15	$d_{11C}^{11T}(\varepsilon_{11T})$	D. in C1; due to T1	48	$d_{11C}^{22C}(\varepsilon_{22C})$	D. in C1; due to C2
16	$d_{22C}^{11T}(\varepsilon_{11T})$	D. in C2; due to T1	50	$d_{12}^{22C}(\varepsilon_{22C})$	D. in S12; due to C2
18	$d_{12}^{11T}(\varepsilon_{11T})$	D. in S12; due to T1	61	$d_{11T}^{12}(\varepsilon_{12})$	D. in T1; due to S12
21	$d_{11T}^{22T}(\varepsilon_{22T})$	D. in T1; due to T2	62	$d_{22T}^{12}(\varepsilon_{12})$	D. in T2; due to S12
23	$d_{11C}^{22T}(\varepsilon_{22T})$	D. in C1; due to T2	64	$d_{11C}^{12}(\varepsilon_{12})$	D. in C1; due to S12
24	$d_{22C}^{22T}(\varepsilon_{22T})$	D. in C2; due to T2	65	$d_{22C}^{12}(\varepsilon_{12})$	D. in C2; due to S12
26	$d_{12}^{22T}(\varepsilon_{22T})$	D. in S12; due to T2			

The curve ID defined as variable  $YSC$  contains all stress versus strain curve ID's with the corresponding yield strain. This yield strain is needed to compute the modulus in the given direction and loading condition (tension/compression, temperature, and rate) and the initial yield stress for these conditions. The initial temperature to be used in the simulation is defined as parameter  $TEMP$ . A set of corresponding stress versus strain curves for this temperature should be provided.

Optionally, parameter  $DC$  holds the damage curve ID of a curve of the different coupled and uncoupled damage terms with corresponding curve IDs, which specify the damage with respect to the strain. Table 4.3 shows all possible damage terms with ID one through seven corresponding to the uncoupled terms and all other damage parameters to the coupling terms. As an example, the damage parameter  $d_{11C}^{11T}$  with ID 15 holds the damage values versus the tensile strain in 1-direction due to loading in tension 1-direction that effects the material response when reloaded in compression 1-direction. In other words, damage parameter 15 describes the damage in compression 1-direction due to loading in tension 1-direction.

The Generalized Tabulated Failure Model described in Section 3.7 can be utilized by using cards eight and nine of the MAT213 material card. Setting *FTYPE* to three and specifying a Table ID for variable *FV2* that defines the shear stress versus curve ID's invokes the tabulated failure model. For every given shear stress, an angle versus equivalent failure strain curve has to be defined, creating a failure surface in the shear stress and angle space as described in Section 3.7.

For a detailed interpretation of simulation results obtained with this new material model, many history variables can be output. History variables in LS-DYNA provide additional output on material model specific variables that might be of interest to the user. Tables 4.4 and 4.5 list all history variables the material model provides as user output and the corresponding history variable number to access them in LS-PrePost, the free of charge pre- and post-processing utility by Livermore Software Technology Corp. The numbering of these history variables is likely to change in the future and the user of the material model is encouraged to obtain the most up to date list from the LS-DYNA materials manual [4].

The yield stresses in the different material directions and the effective plastic strain and strain-rate is stored in history variables and can be accessed.

LS-DYNA, by default, outputs stresses and strains in the d3plot files in the global coordinate system. The user can change this behavior by setting *CMPFLG* in the keyword *\*DATABASE\_EXTEND\_BINARY* (see [59]) to print out all stresses and strains in the local material coordinate system. However, if both the global and local stresses and strains are of interest, the user history variables of the material model allow access to the local material stresses and strains without changing this option. All variables that can be accessed as user history variables are always in the local material coordinate system.

Typical material model output like the strains, plastic strains and stresses are made available to the user as history variables. Strain-rate dependent input can be defined with the material model and, therefore, the total strain-rates in the different material directions are accessible as history variables. The maximum damage parameter of all coupled and uncoupled terms and the damage accumulation in any particular material direction is stored,

as well as some important failure parameters, like whether the integration point has failed, the equivalent erosion strain and the erosion angle. The temperature throughout the simulation can be tracked using a history variable if temperature effects are considered. Whether associated flow or radial return had to be used to compute a valid stress state on the yield surface is tracked cumulatively in history variables to allow for a tracking of deviations from the main material law. The user is urged to verify that radial return occurrences are kept to a minimum. If the user defines stochastic variations of material parameters, the scale factors for the different variables are stored in additional history variables. These scale factors are constant over time and therefore do not have to be tracked. The user can output this variables for visualization purpose after the initialization of the simulation and then later remove these variables from the output to reduce the size of the output files. Section 4.3 describes in detail how stochastic variations can be defined.

The specific numbering of the history variables is available in the LS-DYNA material manual [4].

## **4.2 Algorithm**

This section describes the algorithm used in the implementation of the material model. During the initialization phase, several pre-processing steps are performed to check and prepare the user data to the correct format used by the stress update routine. The following paragraphs explain the necessary pre-processing operations, the main stress update routine, and finally the Generalized Tabulated Failure Criterion subroutine.

### **Pre-processing**

During the initialization phase of a simulation, the user-defined input curves are read in and converted from stress versus total strain to effective stress versus effective plastic strain.

Table 4.4: User history variables (Part 1)

LS-PrePost	Symbol	Description
13	$\sigma_{11yT}$	Yield stress in tension a-direction
14	$\sigma_{22yT}$	Yield stress in tension b-direction
15	$\sigma_{11yC}$	Yield stress in compression a-direction
16	$\sigma_{22yC}$	Yield stress in compression b-direction
17	$\sigma_{12y}$	Yield stress in shear a-b plane
18	$\sigma_{45y}$	Yield stress in 45° off-axis a-b plane
19	$\varepsilon_{effp}$	Effective plastic strain
20	$\dot{\varepsilon}_{effp}$	Effective plastic strain rate
21	$\varepsilon_{11}$	Strain in a-direction
22	$\varepsilon_{22}$	Strain in b-direction
23	$\varepsilon_{33}$	Strain in c-direction
24	$\varepsilon_{12}$	Tensorial shear strain in a-b plane
25	$\varepsilon_{23}$	Tensorial shear strain in b-c plane
26	$\varepsilon_{13}$	Tensorial shear strain in a-c plane
27	$\varepsilon_{11pT}$	Tensile plastic strain in a-direction
28	$\varepsilon_{22pT}$	Tensile plastic strain in b-direction
29	$\varepsilon_{33pT}$	Tensile plastic strain in c-direction
30	$\varepsilon_{11pC}$	Compressive plastic strain in a-direction
31	$\varepsilon_{22pC}$	Compressive plastic strain in b-direction
32	$\varepsilon_{33pC}$	Compressive plastic strain in c-direction
33	$\varepsilon_{12p}$	Tensorial plastic shear strain in a-b plane
34	$\sigma_{11}$	Stress in a-direction
35	$\sigma_{22}$	Stress in b-direction
36	$\sigma_{12}$	Stress in shear a-b plane
37	$\sigma_{23}$	Stress in shear b-c plane
38	$\sigma_{13}$	Stress in shear a-c plane
39	$\dot{\varepsilon}_{11T}$	Strain rate in a-direction tension
40	$\dot{\varepsilon}_{22T}$	Strain rate in b-direction tension
41	$\dot{\varepsilon}_{11C}$	Strain rate in a-direction compression
42	$\dot{\varepsilon}_{22C}$	Strain rate in b-direction compression
43	$\dot{\varepsilon}_{12}$	Tensorial strain rate in ab-direction
44	$max(d)$	Maximum damage
45	-	Dissipated plastic energy
46	-	Integration point failed if 0
47	$\varepsilon_{fail}$	Equivalent erosion strain
48	$\theta$	Erosion angle
49	-	Percent erosion strain reached

Table 4.5: User history variables (Part 2)

LS-PrePost	Symbol	Description
69	-	Uncoupled and coupled damage in T1
70	-	Uncoupled and coupled damage in T2
71	-	Uncoupled and coupled damage in C1
72	-	Uncoupled and coupled damage in C2
73	-	Uncoupled and coupled damage in S12
79	$T$	Temperature
81	-	Occurrences of associated flow
82	-	Occurrences of radial return
83	$E_{11T}; \sigma_{11yT}$	Stochastic scale factor for tension 1
84	$E_{22T}; \sigma_{22yT}$	Stochastic scale factor for tension 2
85	$E_{11C}; \sigma_{11yC}$	Stochastic scale factor for compression 1
86	$E_{22C}; \sigma_{22yC}$	Stochastic scale factor for compression 2
87	$G_{12}; \sigma_{12y}$	Stochastic scale factor for shear 12
88	$\varepsilon_{fail}$	Stochastic variation of equivalent failure strain

First, the conversion from stress versus total strain to effective stress versus total strain takes place, as shown in Equation 4.1 for the example of tension 1-direction:

$$\sigma_{11T}, \varepsilon_{11T} \Rightarrow \tilde{\sigma}_{11T} = \frac{\sigma_{11T}}{1 - d_{11T}^{11T}}, \varepsilon_{11T} \quad (4.1)$$

where  $d_{11T}^{11T}$  is the uncoupled damage parameter for damage in tension 1-direction due to loading in the same direction. For cases without damage defined in the corresponding direction, the effective stress will equal the true stress; therefore, no conversion will take place.

In a second step, the effective stress versus total strain data is converted to effective stress versus plastic strain, as shown in the following equation:

$$\tilde{\sigma}_{11T}, \varepsilon_{11T} \Rightarrow \tilde{\sigma}_{11T}, \varepsilon_{11pT} = \varepsilon_{11T} - \frac{\tilde{\sigma}_{11T}}{E_{11T}} \quad (4.2)$$

As described by Goldberg et al. [45], the effective stress versus plastic strain is then converted to effective stress versus effective plastic strain using Equation 4.3 for the example in the 1-direction.

$$\begin{aligned}
 \sigma_{11}d\varepsilon_{11_p} &= hd\varepsilon_{eff_p} \\
 \sigma_{11}d\varepsilon_{11_p} &= \sqrt{H_{11}}\sigma_{11}d\varepsilon_{eff_p} \\
 d\varepsilon_{eff_p} &= \frac{\sigma_{11}d\varepsilon_{11_p}}{\sqrt{H_{11}}\sigma_{11}} \\
 \varepsilon_{eff_p} &= \int \frac{\sigma_{11}d\varepsilon_{11_p}}{\sqrt{H_{11}}\sigma_{11}} \tag{4.3}
 \end{aligned}$$

The curves modified in this way are output to the user who is urged to verify that the effective stress versus effective plastic strain curves at different rates and temperatures for the individual directions do not intersect. Intersections of these curves can cause numerical issues and would lead to unsatisfactory simulations results or even error terminations.

In addition to the stress versus strain input curves, the damage versus strain input is modified to be stored in terms of plastic strains.

### Stress update

The following operations are executed when the material model subroutine is called to perform the stress update. The steps are executed for each integration point of all elements at every time step.

1. Start: input to the stress updated routine are the strain increments  $\Delta\varepsilon$ , the stresses from the previous timestep  $\sigma^n$ , and the time step  $\Delta t$ .
2. Transformation of stresses and strain increments from the global coordinate system to the material coordinate system. The angles between the element local system and

the material system remain constant during the simulation, therefore, the formulation is corotational.

3. Read scalar user material input from keyword cards:  $H_{11}$ ,  $H_{22}$ ,  $H_{12}$ ,  $H_{23}$ ,  $H_{13}$ ,  $H_{44}$ ,  $FILT$ ,  $VEVP$ ,  $\beta_{11}$ ,  $\beta_{22}$ ,  $\beta_{12}$ ,  $\beta_{44}$ ,  $C_p$ ,  $\beta_t$  and  $YIELDTOL$ . Apply default values for undefined parameters. Read Table 3D ID's for stress versus strain tables from the material card  $LT_i$ .
4. Compute total strain from strain increments:  $\varepsilon^{n+1} = \varepsilon^n + \Delta\varepsilon$ .
5. Read required user history variables (plastic strain, corrected plastic strain) from previous time step.
6. Compute strain-rate from strain increments and apply smoothing if  $FILT$  is defined.
 
$$\dot{\varepsilon}_{cur}^{n+1} = \frac{\Delta\varepsilon}{\Delta t}, \quad \dot{\varepsilon}_{avg} = \frac{\dot{\varepsilon}_{cur}^{n+1} + \dot{\varepsilon}_{cur}^n + \dot{\varepsilon}_{cur}^{n-1} + \dot{\varepsilon}_{cur}^{n-2}}{4}, \quad \dot{\varepsilon}^{n+1} = (1 - FILT)\dot{\varepsilon}_{avg} + FILT\dot{\varepsilon}^n.$$
 Save strain-rates to history variables.
7. Look up rate-independent and rate-dependent Young's and shear moduli in different material directions from input stress versus strain curves for given strain-rates and temperature  $E(\dot{\varepsilon}, T)$ ,  $G(\dot{\varepsilon}, T)$ . If defined, apply stochastic variation scale factors to Young's and Shear moduli.
8. Compute rate-independent stiffness matrix based on rate-independent moduli:  $\mathbf{C}_e$ . The rate-independent moduli are derived from the user-defined stress versus strain curves for the lowest defined strain-rate, based on the user-defined yield strain (from curve YSC).
9. Compute rate-dependent stiffness matrix based on rate-dependent moduli:  $\mathbf{C}_{tot}$ . The rate-dependent moduli are derived from the user-defined stress versus strain curves for the given strain-rate, based on the user-defined yield strain (from curve YSC). For stiffness matrix construction, read Poisson's ratios from material card and recompute if constraints are not satisfied (see Section 3.1).

10. Read previous equilibrium and viscous stress from history  $\boldsymbol{\sigma}_e^n, \boldsymbol{\sigma}_v^n$ .
11. If damage is defined: look up damage coefficients for corrected plastic strains from last time step in different directions; convert true stresses, equilibrium stresses, and viscous stresses to effective stresses.
12. Compute equilibrium stresses:  $\boldsymbol{\sigma}_e^{n+1} = \boldsymbol{\sigma}_e^n + \mathbf{C}_e : \Delta \boldsymbol{\varepsilon}$ .
13. If VEVP = 0: set viscous stress to zero  $\boldsymbol{\sigma}_v^{n+1} = 0$ , stiffness matrix is rate-independent:  $\mathbf{C} = \mathbf{C}_e$ . Where VEVP is the flag that determines which viscoelastic-viscoplastic option to use.
14. If VEVP = 1 or 2: compute viscoelastic decay vector and matrix  $\boldsymbol{\beta}(\beta, \Delta t), \mathbf{B}(\beta, \Delta t)$ ; compute viscous stiffness matrix  $\mathbf{C}_v = \mathbf{C}_{tot} - \mathbf{C}_e$  and viscous stress  $\boldsymbol{\sigma}_v^{n+1} = \boldsymbol{\sigma}_v^n \circ \boldsymbol{\beta} + (\mathbf{C}_v(\dot{\boldsymbol{\varepsilon}}) \circ \mathbf{B}) \Delta \boldsymbol{\varepsilon}^{n+1}$ .
15. Compute (visco)elastic trial stress  $\boldsymbol{\sigma}_t^{n+1} = \boldsymbol{\sigma}_e^{n+1} + \boldsymbol{\sigma}_v^{n+1}$ .
16. If VEVP = 2: viscoelastic trial stress is accepted as final stress  $\boldsymbol{\sigma}^{n+1} = \boldsymbol{\sigma}_t^{n+1}$ ; jump to step 31.
17. Check if Flow surface is convex, if not: error termination.
18. Look up quasistatic yield stresses for given temperature and effective plastic strain from previous time step  $\mathbf{q}(T, \varepsilon_{eff_p}^n)$  from the user-defined input stress versus strain curves. If stochastic variation is defined: apply corresponding scale factors to yield stresses.
19. Check if (visco)elastic trial stresses are below yield stresses for linear elastic directions (directions with  $H = 0.0$ ). If not, set yield stress in this direction equal to corresponding trial stress  $q = \sigma_t^{n+1}$  to prevent an error termination as no plastic flow is possible in linear elastic directions and stress state would not be possible to “return” to yield surface.

20. Compute yield function coefficients  $F_i$  and  $F_{ij}$  as functions of the yield stresses.
21. If yield surface is non-convex: convex correction of yield surface  $F_{12} = -\frac{1}{2}\sqrt{F_{11}F_{22}}$ .
22. Compute yield function for (visco)elastic trial stress  $f(\boldsymbol{\sigma}_t^{n+1}, \mathbf{F})$ .
23. Compute derivatives with respect to trial stresses of yield function and flow potential  $\frac{\partial f}{\partial \boldsymbol{\sigma}_t}$  and  $\frac{\partial h}{\partial \boldsymbol{\sigma}_t}$ .
24. Decide whether or not time step at integration point is elastic ( $f \leq 0$ ) or plastic ( $f > 0$ ). If elastic: set  $\Delta\lambda = 0$  and jump to step 31.
25. Compute angle between flow and yield surface (see Section 4.4). If angle  $\Phi > 90^\circ$ , change direction of flow  $\frac{\partial h}{\partial \boldsymbol{\sigma}} \Rightarrow \frac{\partial f}{\partial \boldsymbol{\sigma}} \frac{\boldsymbol{\sigma} \cdot \frac{\partial h}{\partial \boldsymbol{\sigma}}}{\boldsymbol{\sigma} \cdot \frac{\partial f}{\partial \boldsymbol{\sigma}}}$  to prevent error termination.
26. Plasticity algorithm: compute effective plastic strain increment  $\Delta\lambda$  using secant iteration. This process is described in detail in the following paragraph.
27. Compute elasto-plastic final stress:

$$\boldsymbol{\sigma}^{n+1} = \boldsymbol{\sigma}_t^{n+1} - \mathbf{C} : \Delta\lambda \frac{\partial h}{\partial \boldsymbol{\sigma}} \quad (4.4)$$

and plastic strain increments:

$$\Delta\varepsilon_{11_p} = \frac{\Delta\lambda}{2h} (2H_{11}\sigma_{11} + 2H_{12}\sigma_{22}) \quad (4.5)$$

$$\Delta\varepsilon_{22_p} = \frac{\Delta\lambda}{2h} (2H_{12}\sigma_{11} + 2H_{22}\sigma_{22}) \quad (4.6)$$

$$\Delta\varepsilon_{12_p} = \frac{\Delta\lambda}{2h} (H_{44}\sigma_{12}) \quad (4.7)$$

By summing the plastic strain from the previous time step and the computed increments, the new plastic strain can be computed.

28. If VEVP=1: compute yield function for equilibrium stress and compute elasto-plastic equilibrium and viscous stress.

If  $f^e < 0$ :

$$\boldsymbol{\sigma}_v^{n+1} = \boldsymbol{\sigma}_v^{n+1} - (\mathbf{C}_e + \mathbf{C}_v(\dot{\boldsymbol{\varepsilon}}) \circ \mathbf{B}) : \Delta\lambda \frac{\partial h}{\partial \boldsymbol{\sigma}} \quad (4.8)$$

Else:

$$\boldsymbol{\sigma}_v^{n+1} = \boldsymbol{\sigma}_v^{n+1} - (\mathbf{C}_v(\dot{\boldsymbol{\varepsilon}}) \circ \mathbf{B}) : \Delta\lambda \frac{\partial h}{\partial \boldsymbol{\sigma}} \quad (4.9)$$

$$\boldsymbol{\sigma}_e^{n+1} = \boldsymbol{\sigma}_e^{n+1} - \mathbf{C}_e : \Delta\lambda \frac{\partial h}{\partial \boldsymbol{\sigma}} \quad (4.10)$$

29. If damage is defined: look up damage coefficients for current corrected plastic strains in different directions; convert effective stresses, equilibrium stresses, and viscous stresses to true stresses.

30. If heat capacity defined: compute temperature increase due to adiabatic heating as a result of plastic work.

31. End of plasticity algorithm.

32. Compute elastic (VEVP=2) or elasto-plastic (VEVP=1/2) thru thickness strain.

33. If heat capacity defined: compute temperature raise due to viscoelastic energy dissipation.

34. Update history variables for temperature, stresses and strains.

35. If failure defined: call failure subroutine.

36. Material system to global system transformation of stresses.

37. End of stress update routine.

Figures 4.2 through 4.5 show a high level flowchart of the stress update routine for better visualization. The numbering is the same as of the algorithm description above.

### Plasticity algorithm

The implemented plasticity algorithm in the material model is similar to plasticity in other material models and further information on computational plasticity can be found in literature, e.g. by Neto et al. [41].

After the (visco-)elastic trial stress is computed, if the yield function for the given stress is positive, the time step is elasto-plastic. This means that the computed trial stress lies outside of the yield surface and has to be returned to it following the relation  $\boldsymbol{\sigma}^{n+1} = \boldsymbol{\sigma}_t^{n+1} - \mathbf{C} : \Delta\lambda \frac{\partial h}{\partial \boldsymbol{\sigma}}$ . The objective of the plasticity algorithm is to compute the plastic multiplier increment  $\Delta\lambda$ , that returns the stress state to the yield surface. In the following paragraph, the general plasticity algorithm is described:

1. Set the lower bound for the plastic multiplier increment:  $\Delta\lambda^1 = 0$ .
2. Calculate the upper bound for the plastic multiplier increment:  $\Delta\lambda^2 = \frac{\frac{\partial f}{\partial \boldsymbol{\sigma}} : (\boldsymbol{\sigma}_t^{n+1} - \boldsymbol{\sigma}^n)}{\frac{\partial f}{\partial \boldsymbol{\sigma}} \mathbf{C} : \frac{\partial h}{\partial \boldsymbol{\sigma}}}$ .

Note that the superscript here does not mean to the power of two.

3. Compute the new stress state for  $\Delta\lambda^2$  and the corresponding yield function value.
4. If  $f(\Delta\lambda^2) < 0$ , go to step 6.
5. Else: increase  $\Delta\lambda^2$  by a factor of 1.1 to compute a new estimate. Compute the new stress state for the new estimate of  $\Delta\lambda^2$  and the corresponding yield function. Repeat the process until a new estimate of  $\Delta\lambda^2$  produces a yield function value below zero. If no solution can be found within 1000 iterations: adjust the flow rule to change direction towards the yield surface:  $\frac{\partial h}{\partial \boldsymbol{\sigma}} \Rightarrow \frac{\partial f}{\partial \boldsymbol{\sigma}} \frac{\boldsymbol{\sigma} : \frac{\partial h}{\partial \boldsymbol{\sigma}}}{\boldsymbol{\sigma} : \frac{\partial f}{\partial \boldsymbol{\sigma}}}$  to prevent error termination. If that was tried before, but did not lead to a valid stress state within the yield surface, project radially towards the origin of the stress space. Go back to step 1.

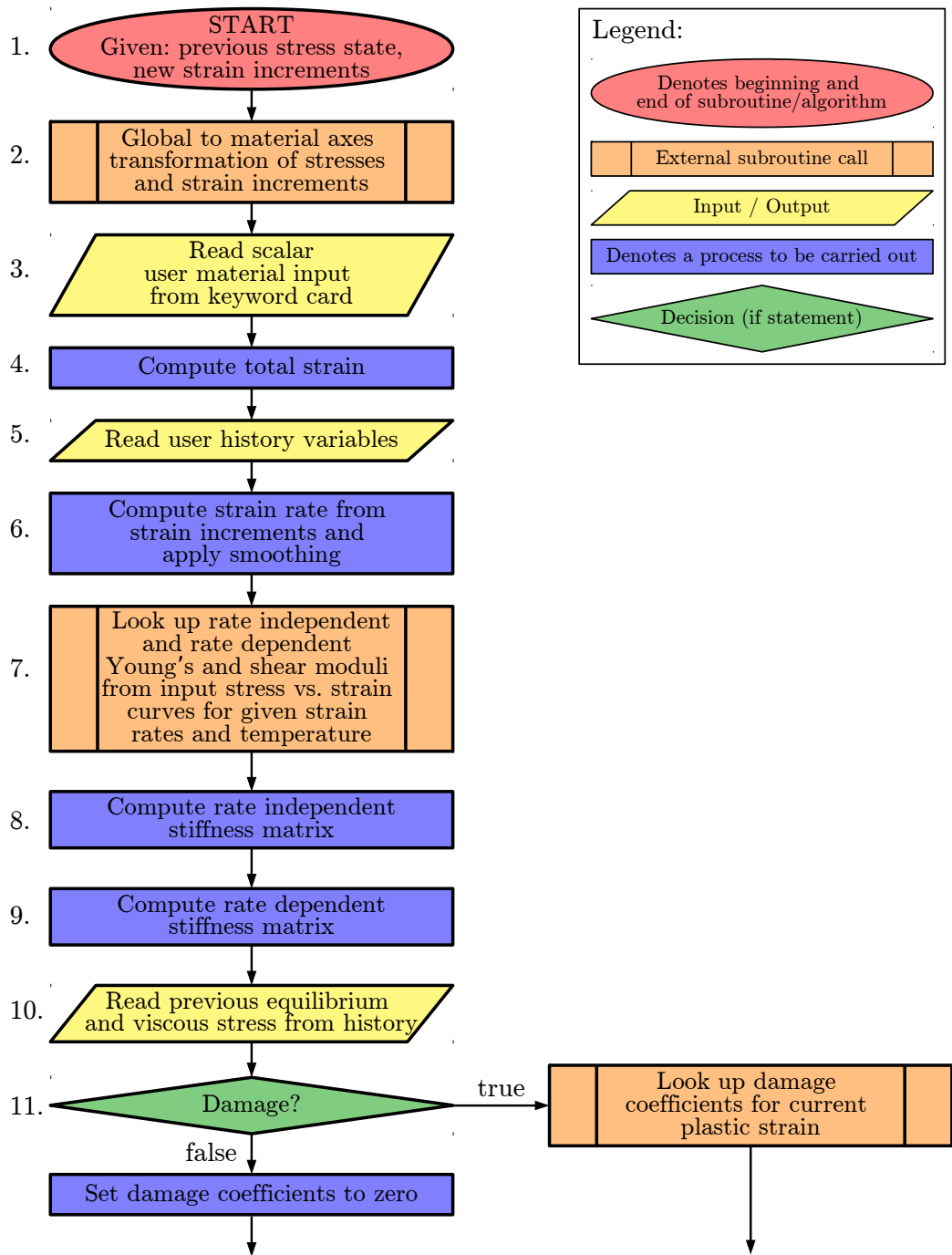


Figure 4.2: Material model subroutine flow chart (Part 1)

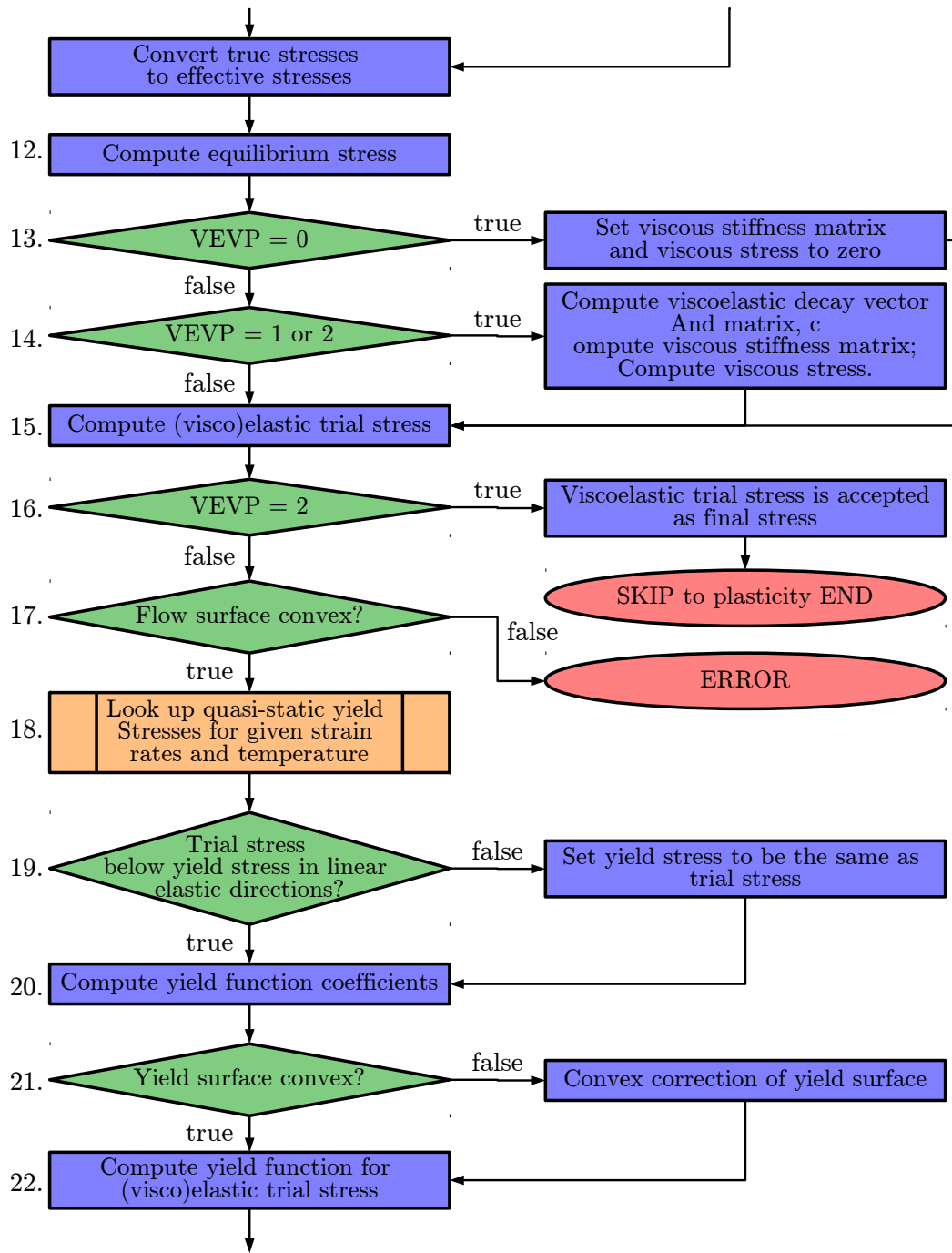


Figure 4.3: Material model subroutine flow chart (Part 2)

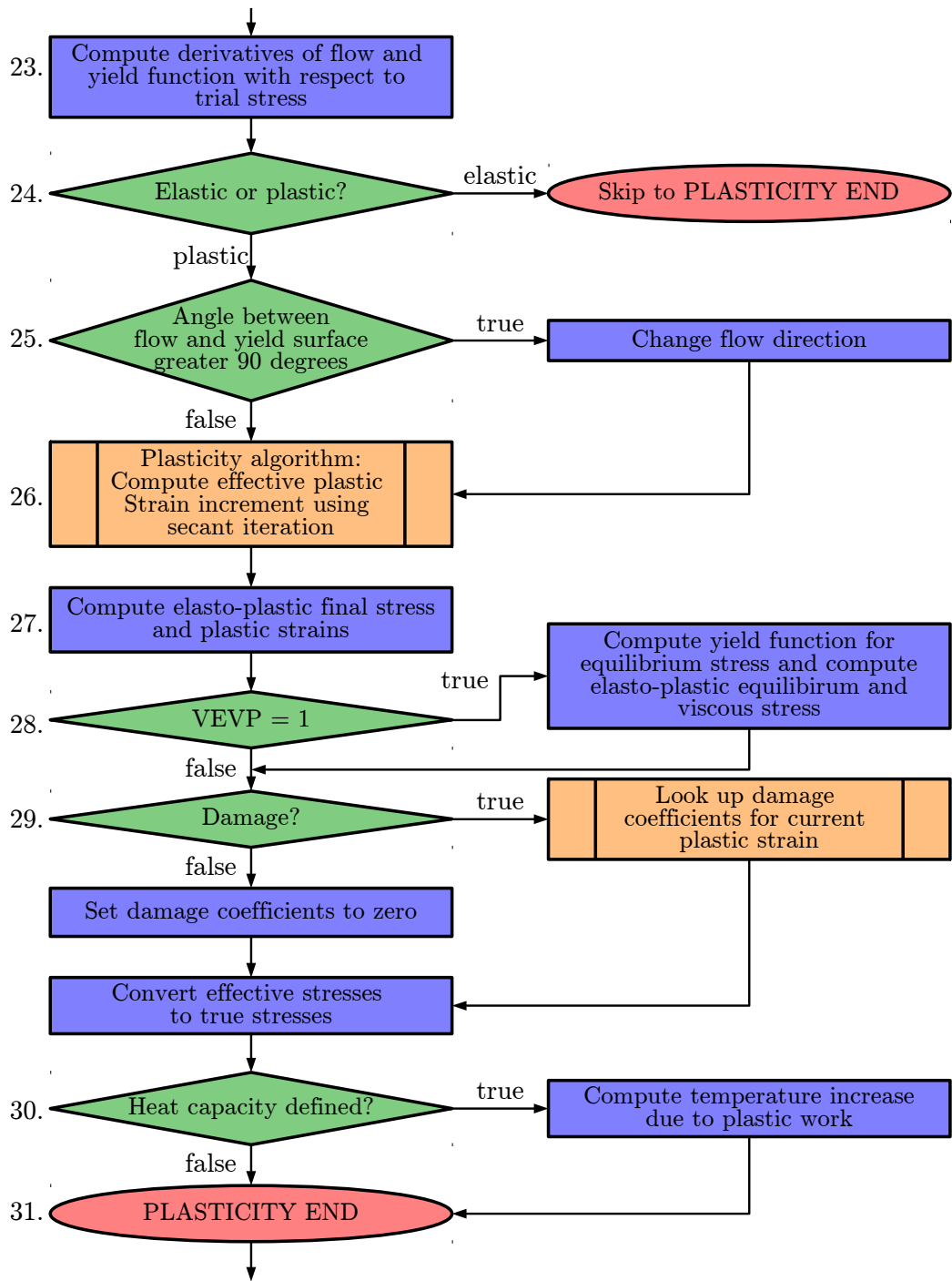


Figure 4.4: Material model subroutine flow chart (Part 3)

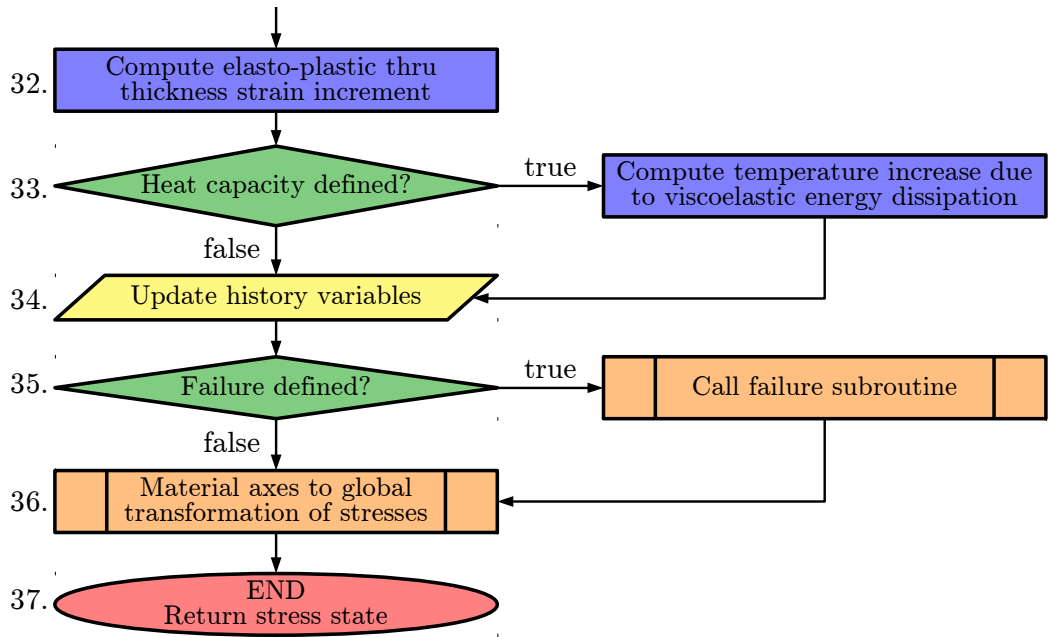


Figure 4.5: Material model subroutine flow chart (Part 4)

6. A value of  $\Delta\lambda^1$  with a corresponding yield function value above zero and a value of  $\Delta\lambda^2$  with a corresponding yield function value below zero have been found in the previous step. For a convex yield surface, this means a value of the plastic multiplier increment can be found between the two values for which the yield function takes a value of zero, indicating a stress state on the yield surface. The secant iteration algorithm is used to find the plastic multiplier increment for which:  $f(\Delta\lambda) \approx 0$ .

Secant iteration:

- (a) Compute new estimate for plastic multiplier increment:  $\Delta\lambda^3 = \Delta\lambda^1 - f^1 \frac{\Delta\lambda^2 - \Delta\lambda^1}{f^2 - f^1}$  and the corresponding yield function  $f^3$ . See Figure 4.6a for an example of the first iteration of the secant algorithm, where from the first two estimates of  $\Delta\lambda^1$  and  $\Delta\lambda^2$  the new estimate  $\Delta\lambda^3$  is computed.
- (b) After the first iteration of the secant algorithm, the decision on the two new starting values of  $\Delta\lambda$  is made based on the computed yield function value  $f^3$ , as

shown in Equations 4.11 to 4.13. If the yield function value is within the range of the user-defined value for the yield function tolerance, and therefore close to zero, the value of the new estimate  $\Delta\lambda^3$  is accepted as the plastic multiplier increment (Equation 4.11). If the yield function value is greater than zero (see Equation 4.12), the starting value of  $\Delta\lambda^1$ , which corresponded to a positive yield function value as well, is replaced with the new estimate  $\Delta\lambda^3$ . The second estimate  $\Delta\lambda^2$ , corresponding to a negative yield function value, is kept the same as in the previous iteration. If the yield function value is lower than zero (see Equation 4.13 and the example in Figure 4.6a), the starting value of  $\Delta\lambda^2$  is replaced with the new estimate  $\Delta\lambda^3$  as both values correspond to negative yield functions. The starting value  $\Delta\lambda^1$  is now kept constant between the first and second iteration. In the cases shown in Equations 4.12 and 4.13, the yield function has not converged to zero and the secant iteration has to be repeated with the new values of  $\Delta\lambda^1$  and  $\Delta\lambda^2$ . The algorithm proceeds as previously described in step (a) and as an example in Figure 4.6b.

$$f^3 \approx 0 \Rightarrow \Delta\lambda = \Delta\lambda^3 \quad (4.11)$$

$$f^3 > 0 \Rightarrow \begin{cases} \Delta\lambda^1 = \Delta\lambda^3, & f^1 = f^3 \\ \Delta\lambda^2 = \Delta\lambda^2, & f^2 = f^2 \end{cases} \quad (4.12)$$

$$f^3 < 0 \Rightarrow \begin{cases} \Delta\lambda^1 = \Delta\lambda^1, & f^1 = f^1 \\ \Delta\lambda^2 = \Delta\lambda^3, & f^2 = f^3 \end{cases} \quad (4.13)$$

7. Once the secant iteration finds a solution for which the yield function corresponding to  $\Delta\lambda$  is equal to zero, the goal of the plasticity algorithm has been achieved and the new elasto-plastic stress can be computed as:  $\boldsymbol{\sigma}^{n+1} = \boldsymbol{\sigma}_t^{n+1} - \mathbf{C} : \Delta\lambda \frac{\partial h}{\partial \boldsymbol{\sigma}}$ .

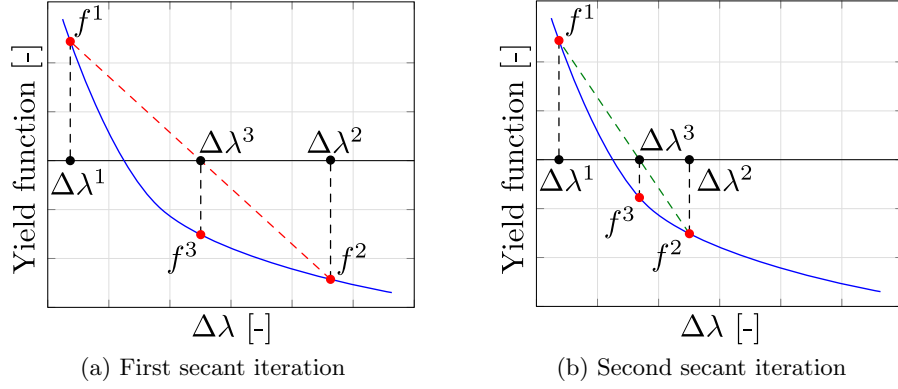


Figure 4.6: Secant iteration example

### Generalized Tabulated Failure Criterion subroutine

In the following, the algorithm of the Generalized Tabulated Failure Criterion is shown.

1. Compute the equivalent strain:  $\varepsilon_{eq} = \sqrt{\varepsilon_{11}^2 + \varepsilon_{22}^2 + 2\varepsilon_{12}^2}$ .
2. Compute the angle representing the in-plane stress state:  $\theta = \cos^{-1} \left( \frac{\sigma_{22}}{\sqrt{\sigma_{22}^2 + \sigma_{12}^2}} \right)$ .
3. Look up the equivalent failure strain  $\varepsilon_{fail}$  for the given angle  $\theta$  and fiber direction stress  $\sigma_{11}$  from the user-defined angle versus equivalent failure strain input curves.
4. If a stochastic variation is defined: apply the stochastic scale factor to the equivalent failure strain value.
5. Compute  $d = \frac{\varepsilon_{eq}}{\varepsilon_{fail}}$ .
6. Save the equivalent strain, angle and  $d$  value to the history variables.
7. If  $d \geq 1$ : set failure tracking variables to mark the integration point as failed.

Table 4.6: Stochastic definition

*MAT_213 tabulated input	Order in stochastic definition
Tension 1-direction	1
Tension 2-direction	2
Compression 1-direction	3
Compression 2-direction	4
Shear 12-plane	5
Equivalent failure strain	6

### 4.3 Stochastic Options

Stochastic variations of material parameters can be defined for the new material model. The user can input stochastic distributions of scale factors for each of the material directions and the equivalent failure strain shown in Table 4.6. The stochastic option for this material was implemented into LS-DYNA as `*DEFINE_STOCHASTIC_VARIATION_MAT213` [59].

An example for this new LS-DYNA keyword card is shown in LS-DYNA Keyword 4.1. In this example, the stochastic definition is given the ID (`id_sv`) 1 which is valid for part ID (`pid`) 2. The variable `IRNG` defines whether a pseudo or a true random number generator should be used. This way a user can obtain the same results when running the same input several times (pseudo-random) or possibly achieve variation in the results (true-random). For `IRNG=0`, as in the shown example, a pseudo-random number generator creates the random scale factors. The `VARTYP` variable defines what type of stochastic variation should be used. Setting `VARTYP` to one allows for the definition of a uniform random distribution in the interval `R1` to `R2` (see Figure 4.7a). If the variable should not follow a distribution, the user can set `VARTYP` to zero and therefore set all scale factors to one, which leaves the material parameters unchanged. With `VARTYP` equal to zero, the result of the material model will be the same as not including the stochastic option at all. Other options allow for the definition of a Gaussian distribution (Figure 4.7b) or a distribution following an input curve of a probability distribution function or a cumulative distribution function (Figure 4.7c). The use of the `CORLGRP` variable allows to specify which of the

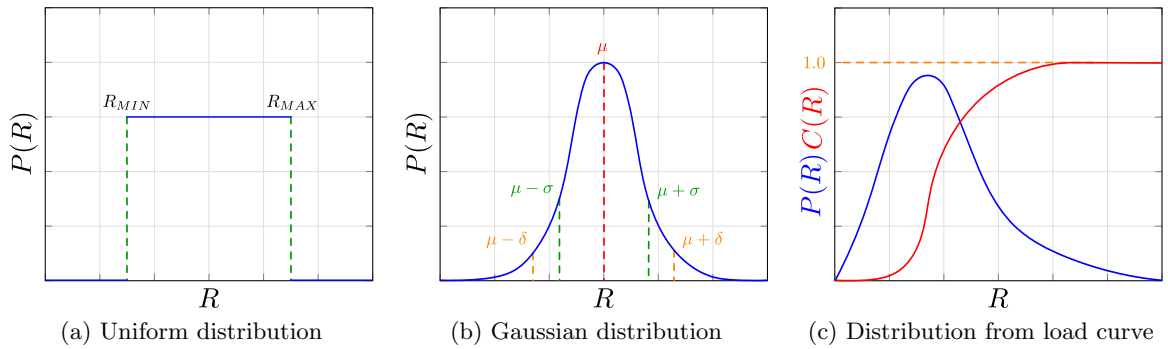


Figure 4.7: Possible distribution definitions for stochastic option

parameters should be correlated or not. An example input could correlate the deformation related variables (Tension and Compression in 1 and 2-direction, Shear 12) by specifying the same integer value for their CORLGRP parameter and leaving the failure parameter independent by assigning a different value to CORLGRP. Table 4.7 shows an overview of all available options and explanations for the new keyword [59].

LS-DYNA Keyword 4.1: \*DEFINE\_STOCHASTIC\_VARIATION\_MAT213 input

```

*DEFINE_STOCHASTIC_VARIATION_MAT213
$#   id_sv      pid      pid_typ      irng
      1          2          0          0
$#   vartyp     corlgrp      r1          r2          r3
      1          0          0.75        1.25
      1          0          0.75        1.25
      1          0          0.75        1.25
      1          0          0.75        1.25
      1          0          0.75        1.25
      1          0          0.75        1.25

```

Table 4.7: Stochastic options (adapted from [59])

Variable	Description
ID_SV	Stochastic variation ID. A unique ID number must be used.
PID	*PART ID or *SET_PART ID.
PID_TYP	Flag for PID type. If PID and PID_TYP are both 0 then the properties defined here apply to all shell and solid parts using materials with the STOCHASTIC option. EQ.0: PID is a *PART ID. EQ.1: PID is a *SET_PART ID
IRNG	Flag for random number generation. EQ.0: Use deterministic (pseudo-) random number generator. The same input always leads to the same distribution. EQ.1: Use non-deterministic (true) random number generator. With the same input a different distribution is achieved in each run.
VARTYP	Variation type for scaling the yield stress. EQ.0: The scale factor is 1.0 everywhere. EQ.1: The scale factor is a random number in the uniform random distribution in the interval defined by R1 and R2. EQ.2: The scale factor is a random number obeying the Gaussian distribution defined by R1, R2 and R3. EQ.3: The scale factor is defined by the probability distribution function defined by curve LCID. EQ.4: The scale factor is defined by the cumulative distribution function defined by curve LCID.
CORLGRP	Correlation group number. If CORLGRP is 0, then the random number for the distribution is uncorrelated with all the other distributions. The same random number is used for evaluating all the distributions having the same positive integer value for CORLGRP.
R1, R2, R3	Real values to define the stochastic distribution.
LCID	Curve ID defining the stochastic distribution.

## 4.4 Robustness: Switch to Associated Flow Rule or Radial Return

In certain loading conditions and for specific user input, the non-associated flow rule might not be able to find a solution that returns the trial stress to the yield surface. To visualize this issue, the following input is used:

- Flow rule coefficients:  $H_{11} = 0.01$ ,  $H_{22} = 1.0$ .
- Yield stresses:  $\sigma_{11y_T} = 1430$ ,  $\sigma_{22y_T} = 42$ ,  $\sigma_{11y_C} = 510$ ,  $\sigma_{22y_C} = 145$ ,  $\sigma_{12y} = 63$ ,  $\sigma_{45y} = 68$ .

The yield stresses result in a yield surface, as shown in Figure 4.8a, where a projected view on the x-y-plane is shown. Figure 4.8b shows the same yield surface zoomed in on the initial stress state (blue circle) and the elastic trial stress (red circle). Due to the chosen flow rule coefficients, the plasticity algorithm is searching for possible stress states that should lie within the yield surface along the green line, with the estimates computed by the plasticity algorithm shown as green circles. None of the computed stress estimates lie within the yield surface and, therefore, no solution in the non-associated case with the chosen flow rule coefficients can be found. The problem lies in the angle between the yield surface and the flow direction being greater than  $90^\circ$ . Figure 4.9 visualizes a case where this angle  $\Phi$  is greater than  $90^\circ$  and so the flow direction points away from the yield surface.

When the non-associated flow rule is not able to find a solution on the yield surface, the flow rule is first modified to be associated. The plastic work equation is changed to use the yield function instead of the plastic potential, where the variable  $k$  is introduced to keep the equation at consistent dimensions:

$$\dot{W}_p = \boldsymbol{\sigma}_t : \dot{\boldsymbol{\epsilon}}_p = \boldsymbol{\sigma}_t : \dot{\lambda} \frac{\partial h}{\partial \boldsymbol{\sigma}_t} = \boldsymbol{\sigma}_t : \dot{\lambda}^{mod} \frac{\partial f}{\partial \boldsymbol{\sigma}_t} k \quad (4.14)$$

where variables  $h$ , and  $k$  are in units of stress while the yield function  $f$  is dimensionless.

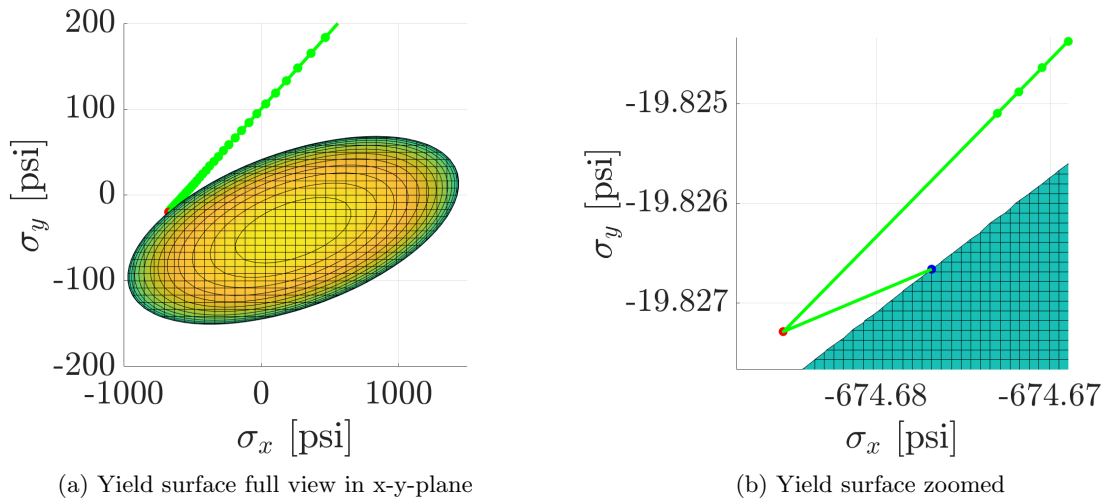


Figure 4.8: Yield surface with no solution in non-associated flow

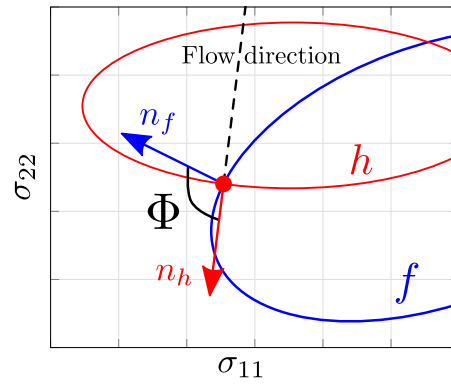


Figure 4.9: Angle between flow and yield surface

It is now ensured, that the scalar plastic multiplier increment  $\dot{\lambda}$  stays unchanged in Equation 4.14 and, therefore, the following should be true:

$$\dot{\lambda}^{mod} = \dot{\lambda} \quad (4.15)$$

Scale factor  $k$  can then be computed to ensure Equation 4.15 holds true.

$$\boldsymbol{\sigma}_t : \frac{\partial h}{\partial \boldsymbol{\sigma}_t} = \boldsymbol{\sigma}_t : \frac{\partial f}{\partial \boldsymbol{\sigma}_t} k \quad \Rightarrow \quad k = \frac{\boldsymbol{\sigma}_t : \frac{\partial h}{\partial \boldsymbol{\sigma}_t}}{\boldsymbol{\sigma}_t : \frac{\partial f}{\partial \boldsymbol{\sigma}_t}} \quad (4.16)$$

Consequently, Equation 4.14 simplifies to:

$$\dot{W}_p = \boldsymbol{\sigma}_t : \dot{\lambda} \frac{\partial f}{\partial \boldsymbol{\sigma}_t} \frac{\boldsymbol{\sigma}_t : \frac{\partial h}{\partial \boldsymbol{\sigma}_t}}{\boldsymbol{\sigma}_t : \frac{\partial f}{\partial \boldsymbol{\sigma}_t}} \quad (4.17)$$

This effectively modifies the direction of the plastic strain increment without changing the magnitude of the plastic strain increment. In many situations where the angle between the flow direction and yield surface could lead to the plasticity algorithm not finding a solution, modification of the flow rule to be associated can prevent this issue.

In some rare cases in complex loading conditions, even associated flow in anisotropic materials might not allow for the plasticity algorithm to find a valid stress state on the yield surface in the direction of plastic flow. To increase the robustness of the material model, error terminations due to this problem have to be prevented.

For the very rare instances where both the non-associated flow rule and associated flow rule fail to find a solution, the flow direction is changed to project radially towards the origin of the stress space to ensure a solution within the yield surface is found. Instead of projecting non-associated towards  $-\mathbf{C} \frac{\partial h}{\partial \boldsymbol{\sigma}_t}$ , the projection from the trial stress towards the origin is in the direction of  $-\boldsymbol{\sigma}_t$ , as shown in Equation 4.18:

$$\boldsymbol{\sigma}^{n+1} = \boldsymbol{\sigma}_t^{n+1} - \mathbf{C} \Delta \lambda \frac{\partial h}{\partial \boldsymbol{\sigma}_t} \quad \Rightarrow \quad \boldsymbol{\sigma}^{n+1} = \boldsymbol{\sigma}_t^{n+1} - \Delta \lambda \boldsymbol{\sigma}_t n = \boldsymbol{\sigma}_t^{n+1} - \mathbf{C} \mathbf{C}^{-1} \Delta \lambda \boldsymbol{\sigma}_t n \quad (4.18)$$

where  $n$  ensures that the plastic multiplier keeps the same length as in the non-associated case.

Similar to Equation 4.14, the scale factor  $n$  can then be computed from the plastic work equation:

$$\dot{W}_p = \boldsymbol{\sigma}_t : \dot{\boldsymbol{\epsilon}}_p = \boldsymbol{\sigma}_t : \dot{\lambda} \frac{\partial h}{\partial \boldsymbol{\sigma}_t} = \boldsymbol{\sigma}_t : \dot{\lambda} \mathbf{C}^{-1} \boldsymbol{\sigma}_t n \quad (4.19)$$

$$n = \frac{\boldsymbol{\sigma}_t : \frac{\partial h}{\partial \boldsymbol{\sigma}_t}}{\boldsymbol{\sigma}_t : \mathbf{C}^{-1} \boldsymbol{\sigma}_t} \quad (4.20)$$

And therefore Equation 4.19 simplifies to:

$$\dot{W}_p = \boldsymbol{\sigma}_t : \dot{\lambda} \mathbf{C}^{-1} \boldsymbol{\sigma}_t \frac{\boldsymbol{\sigma}_t : \frac{\partial h}{\partial \boldsymbol{\sigma}_t}}{\boldsymbol{\sigma}_t : \mathbf{C}^{-1} \boldsymbol{\sigma}_t} \quad (4.21)$$

This change of the plastic flow direction can be physically expressed by deriving the flow rule coefficients and therefore plastic Poisson's ratios that this modification produces. For the case of radial return, from Equation 4.19 follows that:

$$\frac{\partial h}{\partial \boldsymbol{\sigma}_t} = \mathbf{C}^{-1} \boldsymbol{\sigma}_t n \quad \Rightarrow \quad \mathbf{C} \frac{\partial h}{\partial \boldsymbol{\sigma}_t} = \mathbf{I} \boldsymbol{\sigma}_t n \quad \Rightarrow \quad \mathbf{C} \mathbf{H} \frac{1}{h_t} \boldsymbol{\sigma}_t = \mathbf{I} \boldsymbol{\sigma}_t n \quad \Rightarrow \quad \mathbf{C} \mathbf{H} = \mathbf{I} n h_t \quad (4.22)$$

where  $\mathbf{I}$  is a 3x3 identity matrix.

Equation 4.22 can now be expressed in tensor notation:

$$\begin{bmatrix} c_{11} & c_{12} & 0 \\ c_{12} & c_{22} & 0 \\ 0 & 0 & c_{44} \end{bmatrix} \begin{bmatrix} H_{11} & H_{12} & 0 \\ H_{12} & H_{22} & 0 \\ 0 & 0 & H_{44} \end{bmatrix} = nh_t \begin{bmatrix} 1 & 0 & 0 \\ 0 & 1 & 0 \\ 0 & 0 & 1 \end{bmatrix} \quad (4.23)$$

Two equations of this system can be written as:

$$c_{12}H_{11} + c_{22}H_{12} = 0 \quad \Rightarrow \quad \frac{c_{12}}{c_{22}} = -\frac{H_{12}}{H_{11}} = \nu_{12}^p \quad (4.24)$$

$$c_{12}H_{22} + c_{11}H_{12} = 0 \quad \Rightarrow \quad \frac{c_{12}}{c_{11}} = -\frac{H_{12}}{H_{22}} = \nu_{21}^p \quad (4.25)$$

With the projection operator from Equation 3.10, the ratios of the two dimensional stiffness matrix coefficients are calculated as follows:

$$\frac{c_{12}}{c_{22}} = \frac{q_{12} - \frac{q_{13}q_{23}}{q_{33}}}{q_{22} - \frac{q_{23}q_{23}}{q_{33}}} \quad (4.26)$$

$$\frac{c_{12}}{c_{11}} = \frac{q_{12} - \frac{q_{13}q_{23}}{q_{33}}}{q_{22} - \frac{q_{23}q_{23}}{q_{33}}} \quad (4.27)$$

where the factors  $q_{ij}$  are the components of the three dimensional stiffness matrix from Equation 3.4.

From Equations 4.26 and 4.27 then follows through simplifications (see Appendix B) that:

$$\frac{c_{12}}{c_{22}} = \nu_{12} \quad (4.28)$$

$$\frac{c_{12}}{c_{11}} = \nu_{21} \quad (4.29)$$

Using Equations 4.24, 4.25 and 4.28, 4.29, in the case of radial return the plastic Poisson's ratios, that can be derived from the modified radial flow surface, are equal to the elastic Poisson's ratios:  $\nu_{12} = \nu_{12}^p$  and  $\nu_{21} = \nu_{21}^p$ . The imposed plastic Poisson's ratios, that are assumed during the radial return, do therefore not lead to unreasonable values.

Both the solution obtained using associated flow and the radial return are a deviation from the non-associated theory described in Chapter 3. However, an error termination of the simulation in the rare cases where the non-associated flow is not able to produce a valid solution is both not acceptable and not practical in industry scale simulations.

During a simulation, the material subroutine is entered for every integration point at every timestep. For example, in a ballistic impact simulation conducted using the new material model, a composite plate was modeled with 396,508 fully integrated elements with four integration points in-plane and two integration points through the thickness. The total number of integration points in the example simulation was, therefore, 3.172 million. The same ballistic impact simulation was then conducted using four different timestep scale factors (TSSFAC) ranging from 0.6 to 0.9. The timestep scale factor provides an option to scale the calculated timestep that is computed based on material parameters and element size to insure stability in the explicit integration solution.

Table 4.8 lists the statistics of the four simulations regarding occurrences of associated flow and radial return. Accumulated, approximately between 116 and 173 billion times a stress state was computed by the material model, depending on the timestep scale factor. With increasing scale factors from 0.7 to 0.9, the occurrences of both associated flow and radial return increased as well. In this particular case, the ideal TSSFAC of the four cases was 0.7 with the lowest occurrences of both associated flow and radial return. For a scale factor of 0.7, associated flow was used in 1.86 million cases (1 in  $\approx 80,000$ ).

Changing from non-associated flow to associated flow does change the behavior of the model in these rare instances; however, associated plasticity is very commonly used to model plastic behavior in materials and, therefore, can be regarded as an acceptable solution. The associated flow rule still did not prevent the error in just 14 cases out of 149 billion (1 in 10.6

Table 4.8: Occurrences of associated flow and radial return

TSSFAC	Stress Computations	Associated Flow	Radial Return
0.6	$1.73547e^{11}$	2,409,659 (0.00139%)	35 ( $2.01675e^{-8}\%$ )
0.7	$1.48783e^{11}$	1,862,589 (0.00125%)	14 ( $9.40971e^{-9}\%$ )
0.8	$1.30695e^{11}$	3,981,398 (0.00305%)	49,801 ( $3.81046e^{-5}\%$ )
0.9	$1.15669e^{11}$	9,149,765 (0.00791%)	421,582 ( $3.64471e^{-4}\%$ )

billion), where radial return was used to find a valid stress state within the yield surface.

Due to the extremely rare occurrence of the radial return, its effect on the overall results of the simulation were negligible for timestep scale factors of 0.6 and 0.7. In industrial use of finite element software it is quite common to increase the timestep of the simulation, for example by introducing mass scaling or by increasing the timestep scale factor, for faster turn-around times to get results. When increasing the timestep, the probability of not finding a valid solution using non-associated flow increases. In a future version of the material model, a warning flag should be implemented that outputs the percentages of how often the radial return method had to be applied, so the user can make adjustments to the used timestep to find the right balance of accuracy and efficiency.

## Chapter 5: Single Element Verification

The single element verification simulations in this chapter were conducted using material test data obtained by Arizona State University and The Ohio State University of a unidirectional T800/F3900 composite [60]. The graphite fiber T800 from Toray has a high failure strain and the F3900 resin is a toughened epoxy with small elastomeric particles which form an interface between fiber plies to resist impact damage and delamination [61].

### 5.1 Deformation

Load controlled single element verification simulations were conducted to demonstrate the orthotropic elasto-plastic behavior in the different material directions. The required tabulated user input (see Table 4.1) was populated with the corresponding stress versus strain curves from quasistatic, room temperature, uniaxial tension and compression tests in fiber and transverse direction, as well as results from a shear test in the 1-2 plane [60]. Optionally, 45°-off axis tension results can be input. To verify the elasto-plastic part of the model, no rate dependency was defined and therefore the VEMP variable was left at the default value (zero). As boundary conditions, only necessary nodal constraints were applied. Figure 5.1 shows the boundary conditions for all single element cases. For example, for loading in tension 1-direction only the loading direction (x-axis) was constrained in the two nodes on the opposite sides of the loaded nodes. These minimal boundary conditions help to identify potential numerical instabilities as the elements are free to move out-of-plane or in-plane orthogonal to the loading direction. LS-DYNA Keyword card 5.1 shows the complete input card used for the load controlled single element simulations. The flow rule coefficients  $H_{11}, H_{22}, H_{12}, H_{23}, H_{13}, H_{44}$  were obtained using the procedures described in Section 3.3.

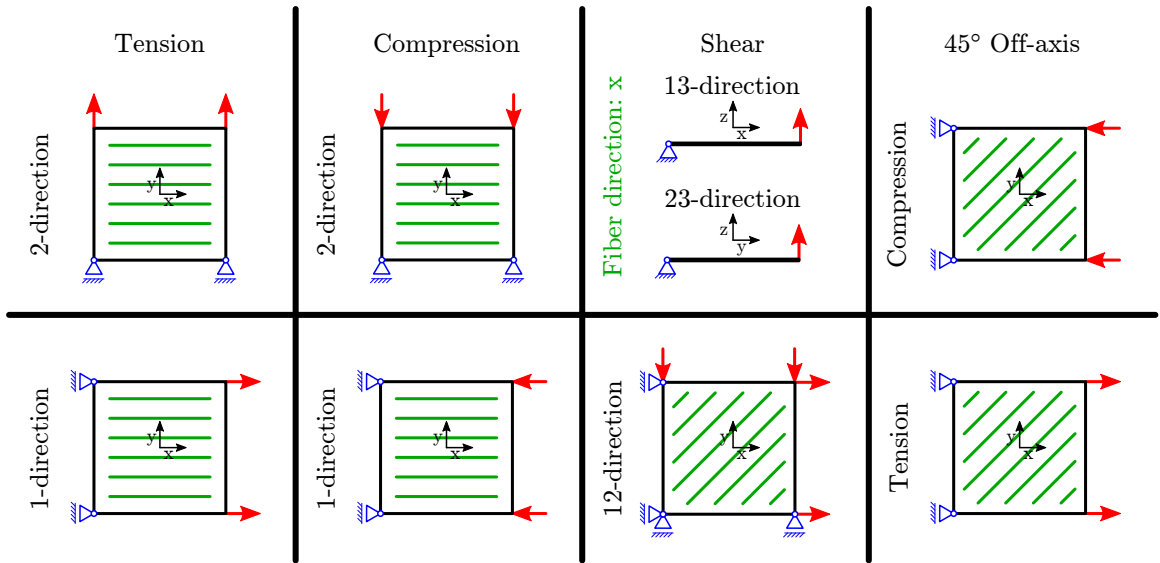


Figure 5.1: Boundary conditions of single element verification simulations

#### LS-DYNA Keyword 5.1: \*MAT\_213 input

```

*MAT_213
$# mid ro ea eb ec prba prca prcb
$# 1 1.4521E-4 23.46E6 1.066E6 0.966E6 0.016800 0.027000 0.4390
$# gab gbc gca ptol aopt macf FILT VEVP
$# 0.5795E6 0.37615E6 0.32635E6 2.0
$# xp yp zp a1 a2 a3
$# v1 v2 v3 d1 d2 d3 beta tcsym
$# H11 H22 H33 H12 H23 H13 H44 H55
$# 0.00000 1.00000 0.000000 -0.77600 0.000000 4.23900
$# H66 LT1 LT2 LT3 LT4 LT5 LT6 LT7
$# 1001 1002 1004 1005 1007
$# LT8 LT9 LT10 LT11 LT12 YSC TEMP DC
$# 1010 100
$# FTYPE PFAIL FV1 FV2 FV3 FV4 FV5 FV6
$# FV7 FV8 FV9 FV10 FV11 FV12 CP BETAT
$# beta11 beta22 beta33 beta12 beta31 beta32 beta44 beta55
$# beta66

```

#### Tension and compression in 1-direction

Load driven tension and compression simulations were conducted in the fiber direction. Figure 5.2 shows the stress versus strain input curves (blue) and the simulation output (red).

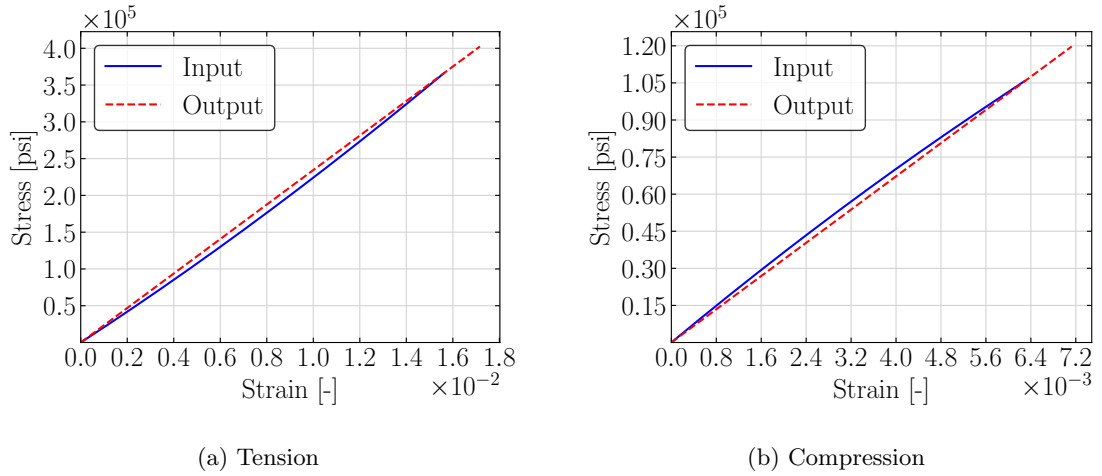


Figure 5.2: Single element verification in 1-direction

The unidirectional T800/F3900 behaves linear elastic in the 1-direction and therefore, the flow rule coefficient in this direction ( $H_{11}$ ) was set to zero. The modulus in this direction ( $E_{11}$ ) is then determined by the slope of the line between the origin of the given stress strain curve and the defined “yield strain / yield stress” value from the data provided in the YSC field of the material models keyword card. Figures 5.3 and 5.4 show the evolution of the yield surface in cutting planes along the stress axis in tension and compression respectively. In Figure 5.3 on the left the cutting plane for  $\sigma_{12} = 0$  is shown with the 2D elliptic yield surface. The stress states throughout the simulation are marked by the small colored crosses with the first one at a state of zero stress in the origin. As the element is loaded, the state of stress moves along the x-axis with only  $\sigma_{11}$  increasing. The “yield stress” was chosen to lie beyond the curve as no yielding can occur in the linear elastic fiber direction and therefore, the yield surface is not reached in tension and compression in 1-direction. In Figure 5.4 on the left, the same yield surface can be seen in the  $\sigma_{11}$ - $\sigma_{22}$ -plane with the states of stress decreasing along the  $\sigma_x$ -axis.

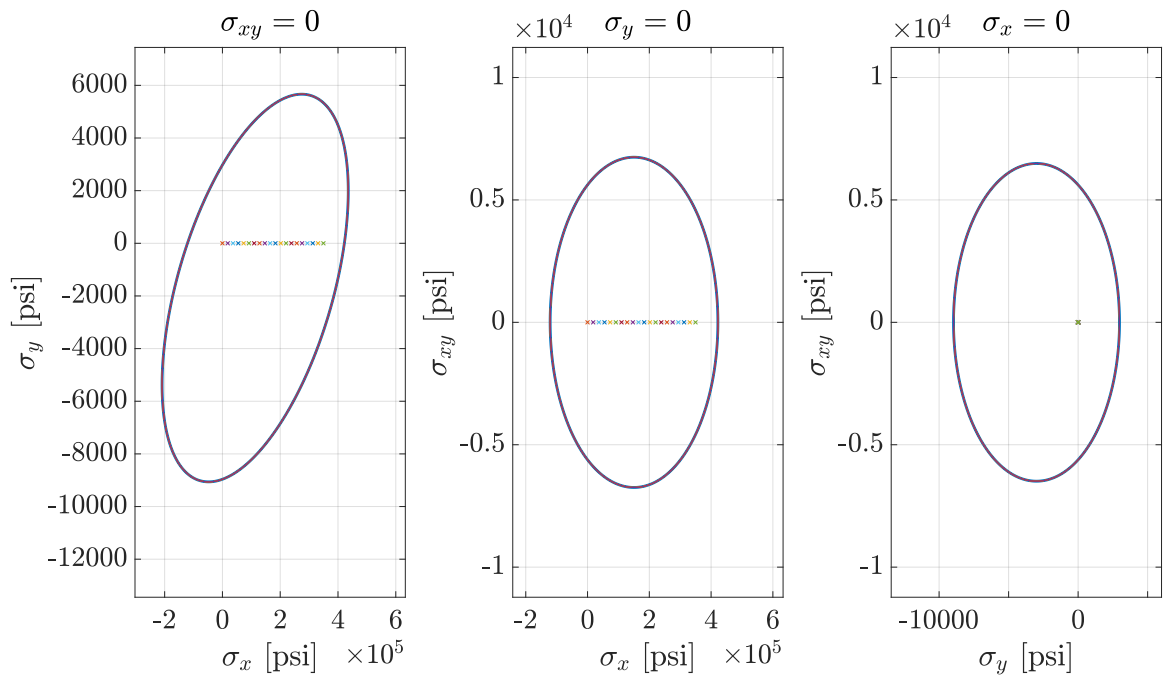


Figure 5.3: Yield surface evolution tension 1-direction

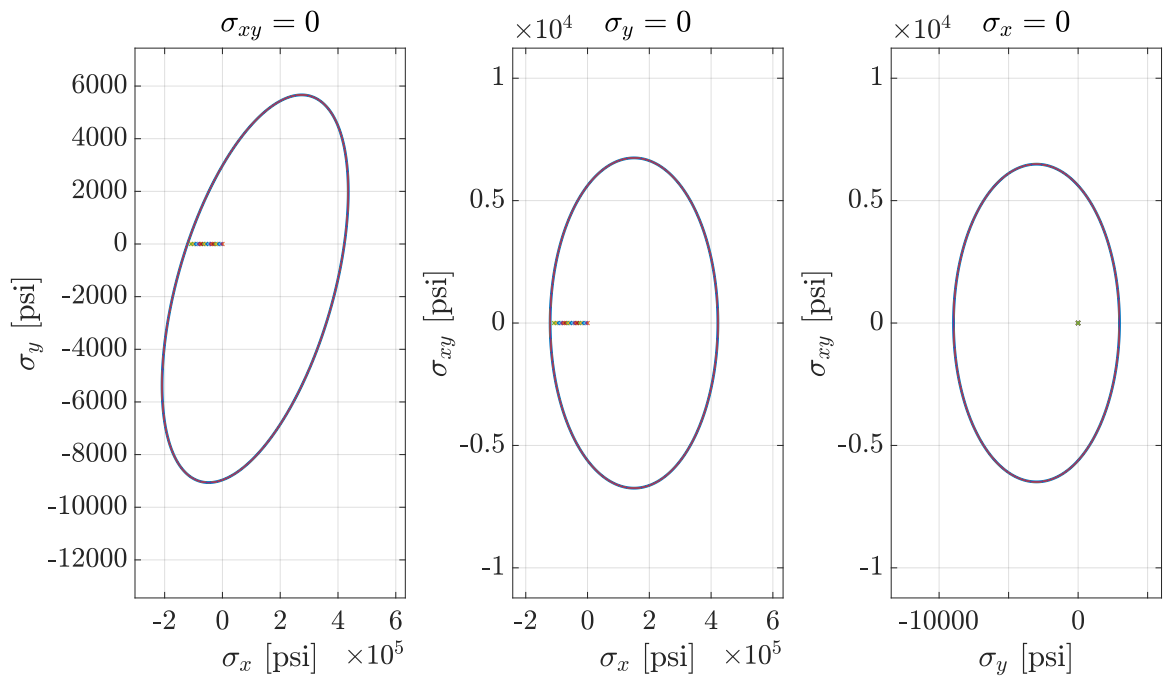


Figure 5.4: Yield surface evolution compression 1-direction

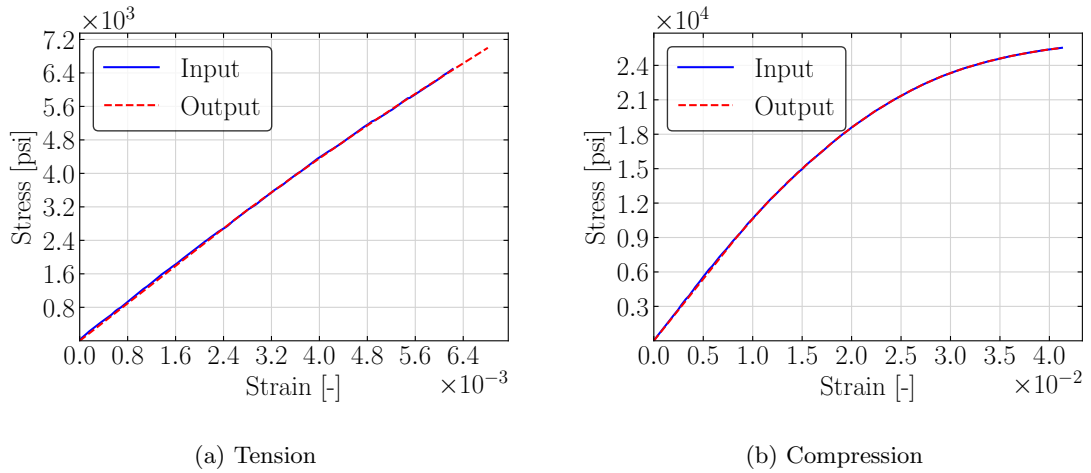


Figure 5.5: Single element verification in 2-direction

### Tension and compression in 2-direction

In the 2-direction, the matrix material properties are dominating the composite response and plastic deformation of the polymer can occur. The results of load controlled single element simulations in tension and compression in 2-direction are shown in Figure 5.5. In tension 2-direction, the composite behaves almost linear elastic with very little plasticity in the response. In compression, however, the material yields once the yield surface is reached and permanent deformation occurs. The yield surface for tension 2-direction is shown in Figure 5.6, where the elliptic yield surface expands with increasing  $\sigma_{22}$ . Figure 5.7 shows the yield surface evolution in compression 2-directional loading. As the stress decreases in 2-direction, the yield surface expands and the corresponding state of stress lies on the yield surface.

### In-plane shear

A single shell element with an edge length of one is loaded in pure in-plane shear (12-shear) by applying equal forces in tension on two nodes on the side at  $x = 1$  and in compression on two nodes on the edge at  $y = 1$  (see Figure 5.1). Figure 5.8 shows the stress versus

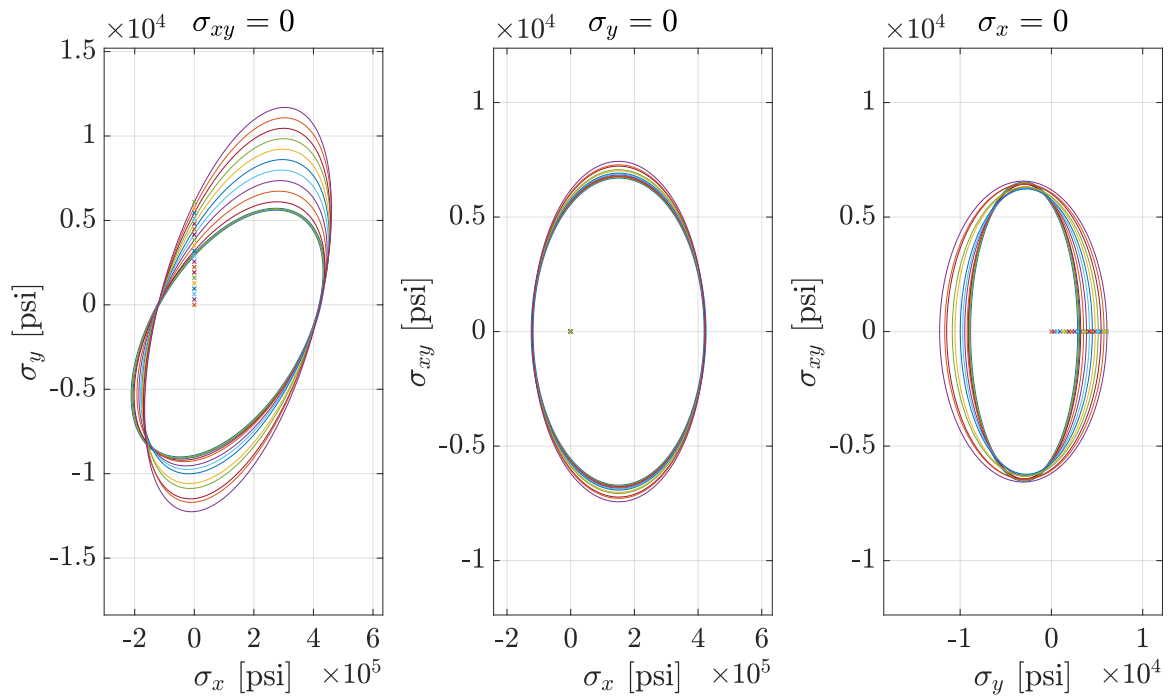


Figure 5.6: Yield surface evolution tension 2-direction

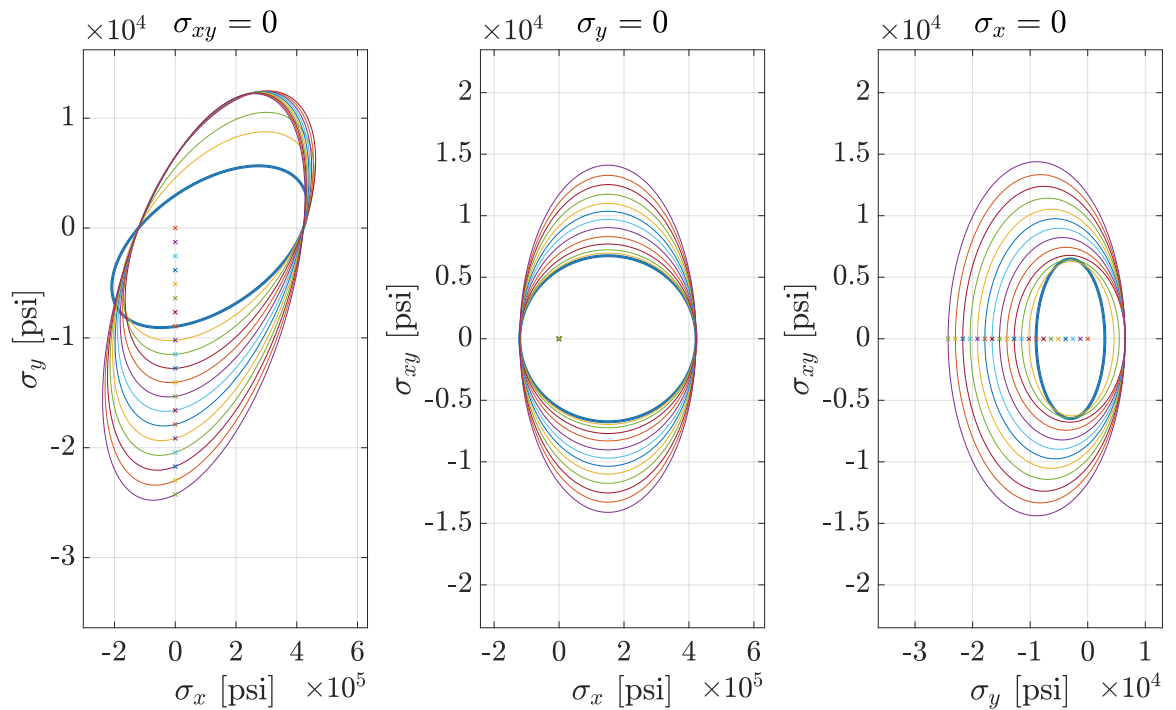


Figure 5.7: Yield surface evolution compression 2-direction

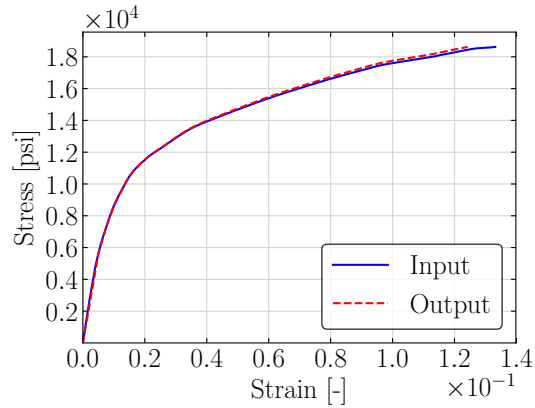


Figure 5.8: Single element verification in 12-shear direction

strain results. In shear loading, the fibers are not able to carry the majority of the load and therefore, the matrix material properties are of great importance in shear loading. As the matrix material is a polymer, the shear response shows a very non-linear elasto-plastic response. In Figure 5.9 the yield surface evolution in the in-plane shear case is shown. The yield surface expands along with increasing  $\sigma_{12}$  stress while the yield stress in the linear elastic direction (1-direction) stays unchanged.

### Out-of-plane shear

Pure out-of-plane shear loading is difficult to achieve in shell elements. To obtain the highest proximity to pure shear loading for 13-directional shear the two nodes at  $x = 1$  were constrained in y-translation while the nodes at  $x = 0$  were fixed in all translational degrees of freedom. Additionally, rotation around the y-axis was constrained. Loading was applied in z-direction at the nodes at  $x = 0$ . Similarly, the boundary conditions were set up for 23-directional shear loading with the element rotated around the z-axis for  $90^\circ$ . As described in Section 3.3.1, the out-of-plane shear stresses are not considered in the yield criterion. The out-of-plane stresses are updated linear elastically according to Equation

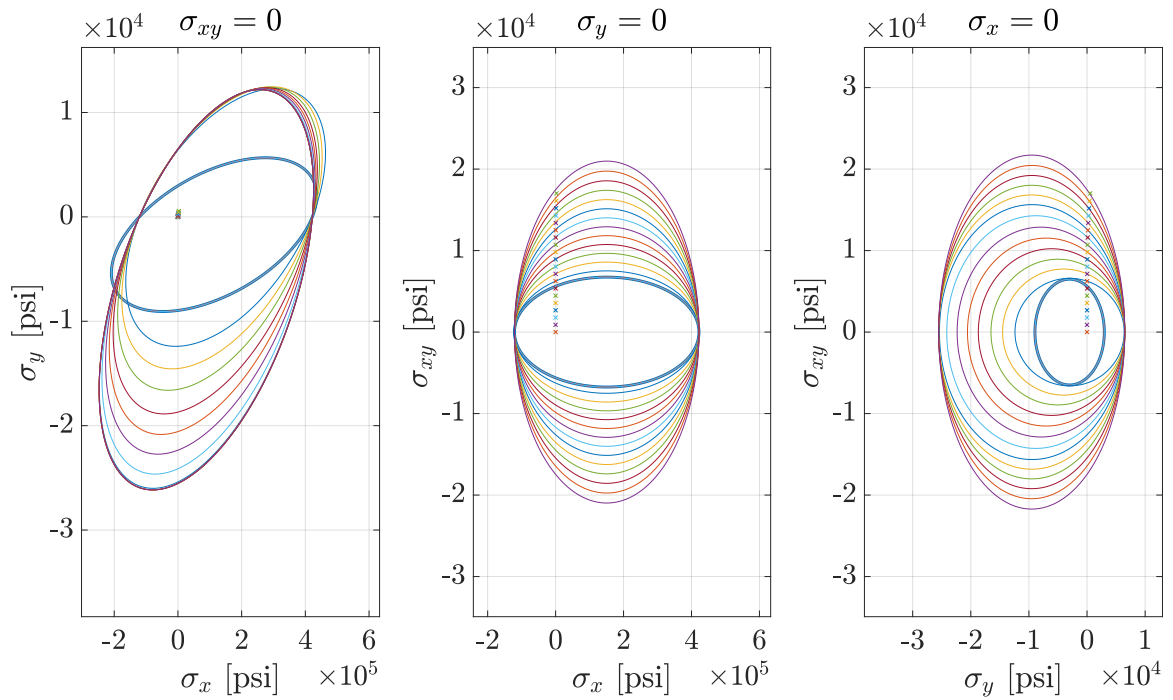


Figure 5.9: Yield surface evolution shear 12-direction

3.11. Figure 5.10 shows the stress versus strain results for out-of-plane shear in the 23-directional plane and the 13-directional plane.

#### 45° off-axis

In addition to the normal and shear cases, elements with fiber angles of 45° with respect to the loading direction, were analyzed. The yield stresses from the user defined 45°-off-axis stress versus strain input curves are used when the yield surface is constructed. However, due to the numerical necessity of convexity of the yield surface, this off-axis yield stress might be adjusted automatically throughout the simulation to ensure a convex yield surface. This convex correction leads to the possibility that the 45°-off-axis input curves cannot be matched in the simulation. Figure 5.11 shows the results of 45° single element simulations in tension and compression. The stress output in both tension and compression does not match the input exactly once plasticity should have occurred. This mismatch can be explained with the convex correction of the yield surface. The yield surface in Figure

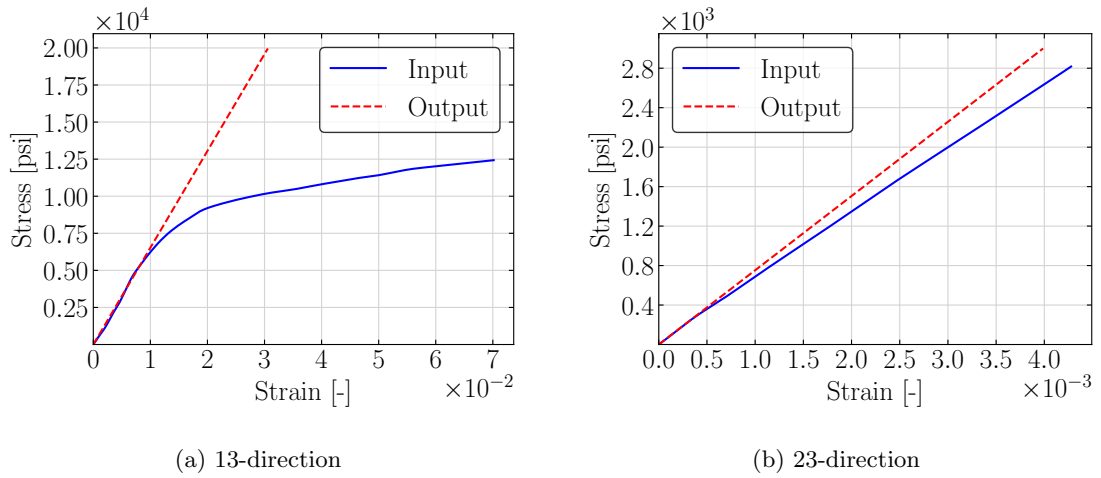


Figure 5.10: Single element verification in out-of-plane shear directions

5.9 on the left shows how for tensile and compressive stresses as well as biaxial loading with the same sign (i.e. stress state in the upper right or lower left quadrants) the yield stress increases in comparison to uniaxial loading. Therefore, yielding in 45°-off-axis loading might occur at a greater magnitude of strain than the input.

## 5.2 Strain-Rate-Dependency

A major capability that has been implemented is the option to define strain-rate-dependent stress versus strain input curves. To verify that the material model can match the user input, the previously used quasistatic T800/F3900 stress versus strain input was scaled up in all directions to create input curves for higher rates. The used scale factor for the input at a rate of  $10\frac{1}{s}$  was 1.2, while the input at a rate of  $100\frac{1}{s}$  was scaled up by 1.4. These scaling values were chosen arbitrarily, but are not physically unrealistic.

### Rate smoothing

In Section 3.3.3 the implementation of the smoothing of the total strain-rates was described. As the stiffness of a composite can vary with the loading rate, oscillations in the

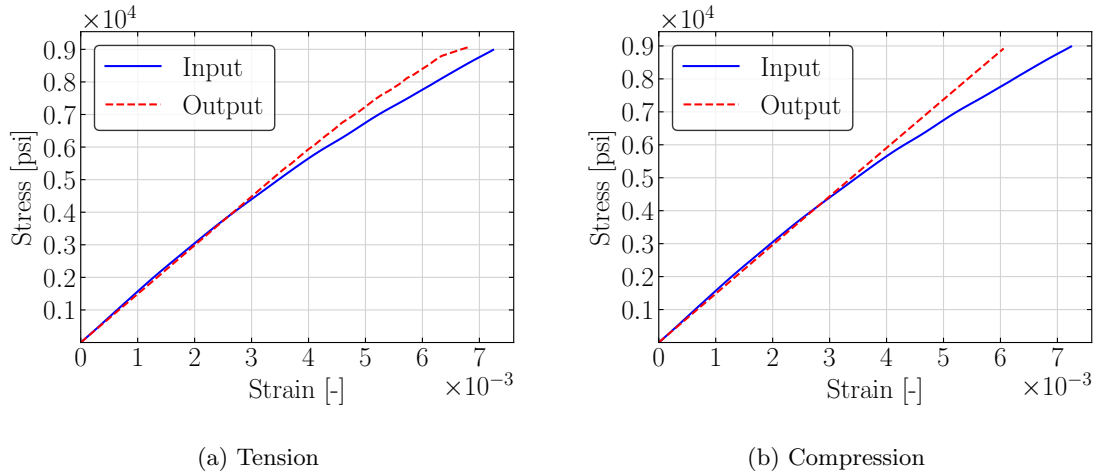


Figure 5.11: 45° Off-axis single element verification

total strain-rate lead to sudden stiffness changes in the material model. This can lead to numerical instabilities and therefore, the need for smoothing of said strain-rates. The correct implementation of this option is verified by looking at the off-axis strain-rate in a single element simulation. Figure 5.12 shows the total strain-rates in the loading direction (compression 2-direction) in blue and the off-axis strain-rate (tension 1-direction) in red. For a *FILT* value of zero (Figure 5.12a) the off-axis strain-rate oscillates between values of 30% of the loading rate and zero. When setting *FILT* to a very low value (here 0.01 in Figure 5.12b) the smoothing effect is almost entirely due to the moving average filter. By increasing *FILT* to higher values (e.g. 0.9 in Figure 5.12c), the exponential moving average filter is utilized to a higher degree and increases the effect of smoothing.

### Tension 1

To verify the rate dependency of the model, single element simulations in the different material directions are conducted at seven different loading rates. The material input was defined for rates of  $1.0\frac{1}{s}$ ,  $10\frac{1}{s}$  and  $100\frac{1}{s}$ . The seven different loading rates were chosen to test the interpolation between the rate-dependent input curves and the correct handling of

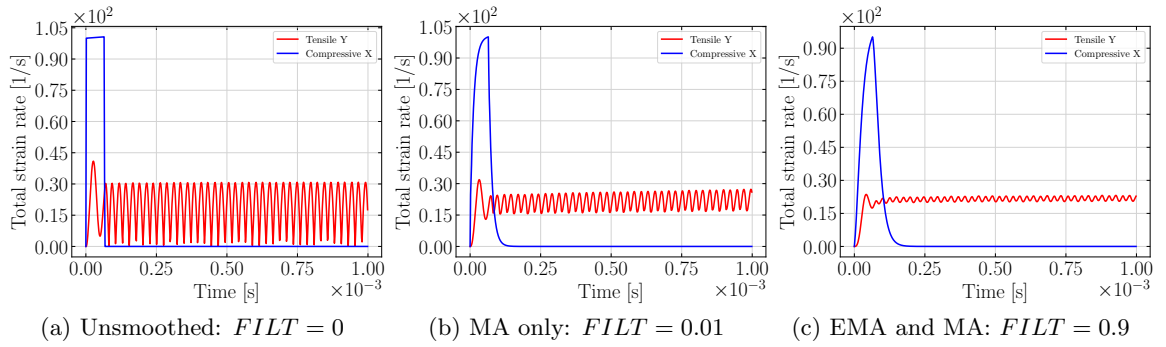


Figure 5.12: Effect of smoothing on the transverse and longitudinal strain-rates

rates below the lowest defined curve as well as rates beyond the highest defined rate. In cases that exceed the user-defined input strain-rates, the curve defined for the highest rate should be chosen and no extrapolation of the data should occur. The elements are loaded displacement controlled at rates of  $0.5 \frac{1}{s}$ ,  $1.0 \frac{1}{s}$ ,  $5.0 \frac{1}{s}$ ,  $10.0 \frac{1}{s}$ ,  $55.0 \frac{1}{s}$ ,  $100.0 \frac{1}{s}$  and  $150.0 \frac{1}{s}$ . After the maximum deformation is reached, the nodal displacement is stopped, and the nodes are kept in place.

Stress versus strain results for the seven loading rates in tension 1-direction are shown in Figure 5.13a. As the flow rule coefficient in the 1-direction was defined as zero (no plastic flow in this direction), the material behaves linear elastic in the fiber direction. The rate-dependent simulations in this direction are consequently a good verification test of the rate dependency of the computed modulus from the stress versus strain input curves.

For a loading rate of  $0.5 \frac{1}{s}$  (green curve in Figure 5.13a), which is a strain-rate below the first user-defined stress versus strain input curve of  $1.0 \frac{1}{s}$ , the output lies on top of this lowest given input curve. When the loading rate is increased to  $5.0 \frac{1}{s}$  (blue curve in Figure 5.13a), roughly half-way between the first input curve and the second input curve, the modulus is interpolated between the two given curves and the stress versus strain output lies between the two input curves for  $1.0 \frac{1}{s}$  and  $10.0 \frac{1}{s}$ . When the loading rate matches the highest user-defined input rate (here  $100.0 \frac{1}{s}$ ), or exceeds it ( $150.0 \frac{1}{s}$ ), the output matches the highest input curve.

All simulations were conducted with the viscoelastic-viscoplastic option (VEVP=1), while keeping the viscoelastic  $\beta$  values at the default value of 0.001. This allowed for rate dependency in the elastic region while not allowing for noticeable viscoelastic decay in the stress response. As the total loading rate drops to zero when the deformation of the elements is stopped, higher viscoelastic  $\beta$  values would lead to a decay of the stress over time. The verification of this capability is explained in more detail in the text below (see “Viscoelasticity only, VEVP = 2”).

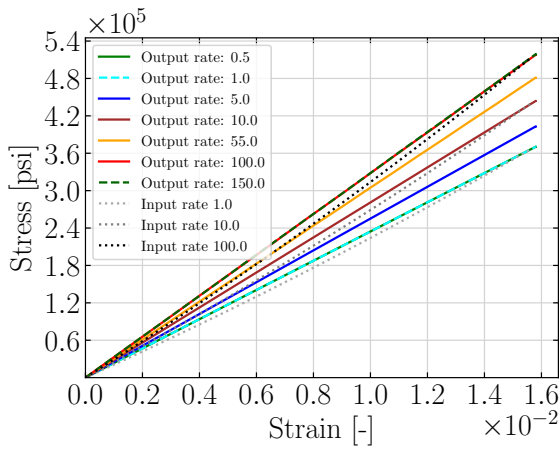
## **Tension 2**

Similar single element verification simulations as for tension 1-direction were conducted in the 2-direction. Due to the non-zero flow rule coefficient in the 2-direction, plastic deformation can occur. Again, seven loading rates were chosen to cover the spectrum of the user-defined input rates. The results of the seven simulations are shown in Figure 5.13b. The stress versus strain output matches the corresponding input curve at the given loading rate with interpolation between the user input being handled correctly.

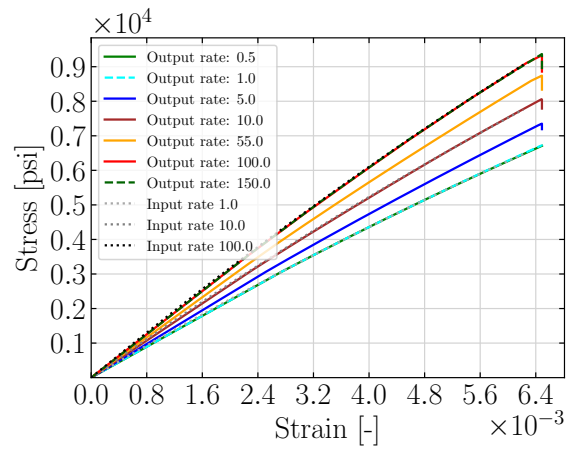
Some stress decay can be seen at the end of the output curves at the higher loading rates. This stress decay only represents the viscoplastic relaxation due to the decay of the effective plastic strain-rate when the loading is suddenly stopped and the nodes are held in place. The viscoplastic “overstress” due to the rate effects is therefore slowly reduced to zero. As previously explained, the viscoelastic  $\beta$  values were set to very low values and therefore, no viscoelastic decay can occur and the stress does not decay all the way to the quasistatic value.

## **Compression 1**

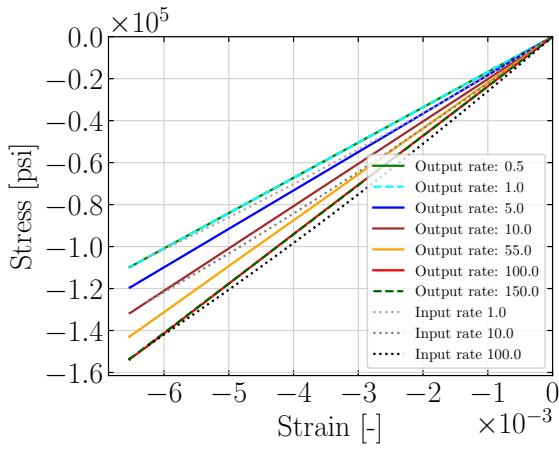
The results of the compression 1-direction simulations show similar behavior as the 1-direction and are shown in Figure 5.13c. Again, no viscoelastic stress decay can be seen and, as the 1-direction is linear elastic, no viscoplastic decay occurs. The results match the user-defined stress versus strain input at the corresponding loading rates.



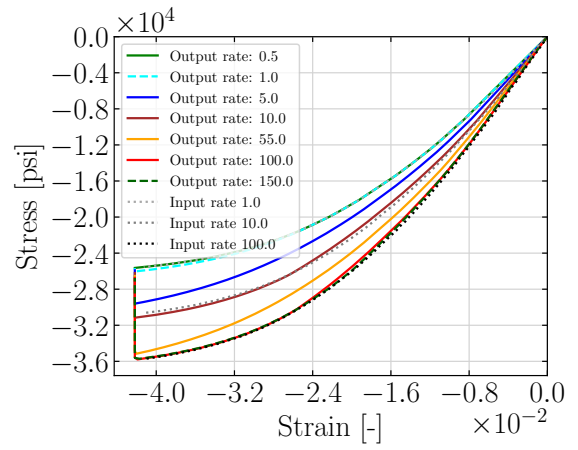
(a) Tension 1



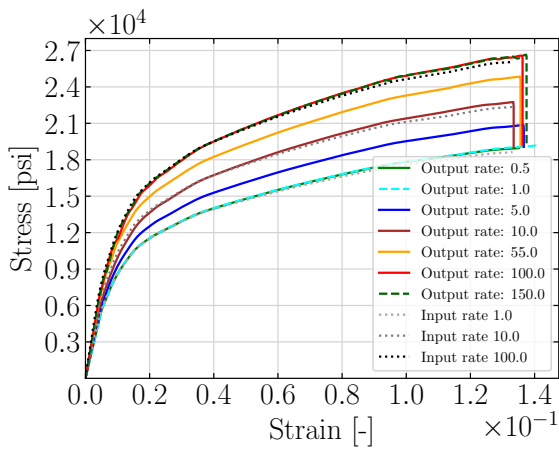
(b) Tension 2



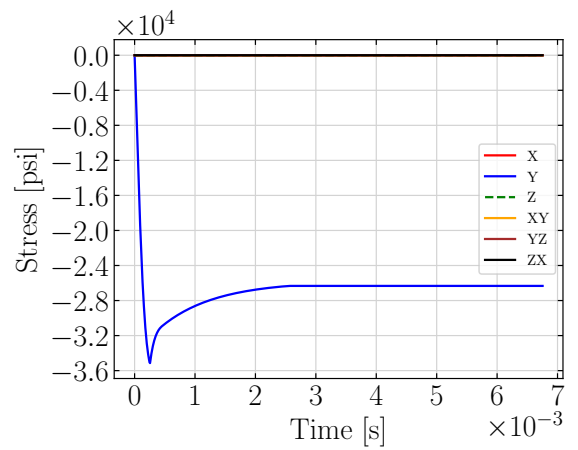
(c) Compression 1



(d) Compression 2



(e) Shear 12



(f) Compression 2 - stress versus time (150 1/s)

Figure 5.13: Rate-dependent single element verification

## Compression 2

The most non-linear behavior in the T800/F3900 composite occurs in the 2-direction compression and in-plane shear. It is, therefore, a good test case for the viscoplastic stress decay. Figure 5.13d shows the results for the seven different loading rates. The stress versus strain results in the y-direction match the input at the corresponding rate.

Figure 5.14 shows the effective plastic strain-rate versus time for a loading rate of  $5.0\frac{1}{s}$  and  $10.0\frac{1}{s}$ . The effective plastic strain-rate increases from the onset of plastic deformation with decreasing slope of the stress versus strain input curve as a lower slope indicates faster plastic deformation with respect to the constant total strain-rate. As the nodes are held in place at the maximum displacement, the effective plastic strain-rate then slowly decreases from its maximum value towards zero. The decreasing effective plastic strain-rate then leads to yield stress interpolations for the lower effective plastic strain-rate values and the stress decays over time. In the stress versus strain plots in Figure 5.13, this effect is not very visible, as the strain does not increase further, leading to a vertical drop in the stress versus strain response. To visualize the decay over time, an additional plot of the stress over time is shown in Figure 5.13f. This stress relaxation effect is explained in more detail in the paragraph “Viscoplasticity only (VEVP=0)” below.

## Shear 12

The results of pure in-plane shear single element simulations at seven different loading rates are shown in Figure 5.13e. With increasing loading rates, the stress versus strain response of the material model matches the corresponding input curve. Viscoplastic stress relaxation occurs when the maximum deformation is reached and the nodes are held in place.

## Viscoelasticity only (VEVP = 2)

The implemented material model can be used as a purely viscoelastic material by setting VEVP to two. This also allows verification of the viscoelastic effects, independent of the plasticity algorithm. Figure 5.15 shows the results of single element simulations at four

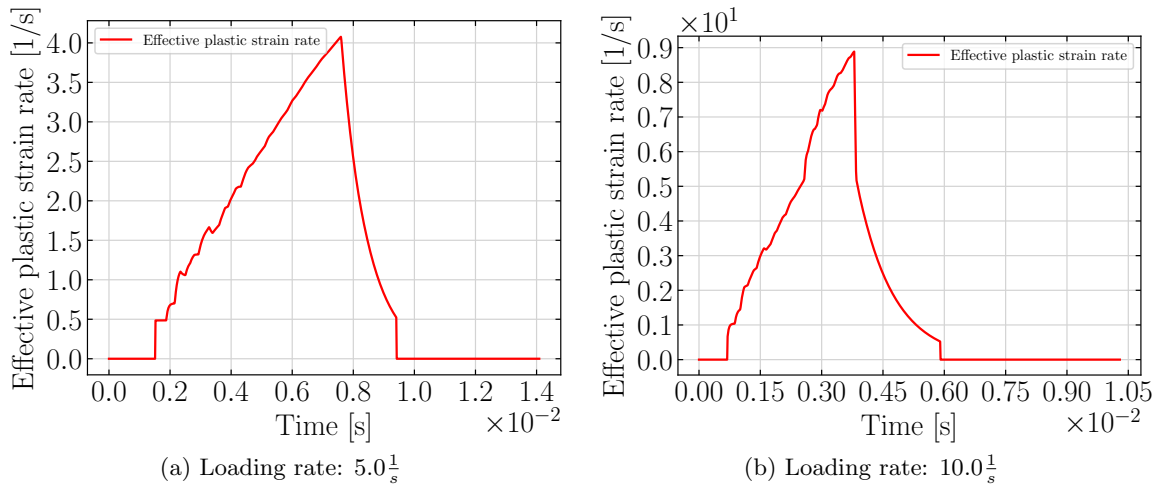


Figure 5.14: Effective plastic strain-rate in compression 2-direction

different loading rates and a high viscoelastic decay constant  $\beta_{11}$  of 5000. With increasing loading rates the modulus increases while at higher strains the slope of the stress versus strain response tends towards being equal to the quasistatic modulus, as is typical for viscoelastic behavior.

Using the same input, except with a lower decay constant, the effect of viscoelastic stress relaxation and creep is shown in Figure 5.16. The top left picture (Figure 5.16a) shows a constant strain load and the corresponding stress response of the material model for a decay constant of zero. As the decay value is chosen as zero, no viscoelastic stress relaxation can occur, and the stress stays constant for a given strain. When  $\beta_{11}$  is set to a non-zero value (here  $\beta_{11} = 50$ ) the same constant strain load (Figure 5.16c), as previously shown, now leads to stress relaxation (Figure 5.16d). For a constant stress load on the single element (Figure 5.16f), the strain in the element increases slowly (Figure 5.16e). This phenomenon is called “creep”. When the stress is removed, the strain does not drop to zero but also decays. This damping effect of creep and relaxation helps to ensure numerical stability when rate-dependent moduli are defined.

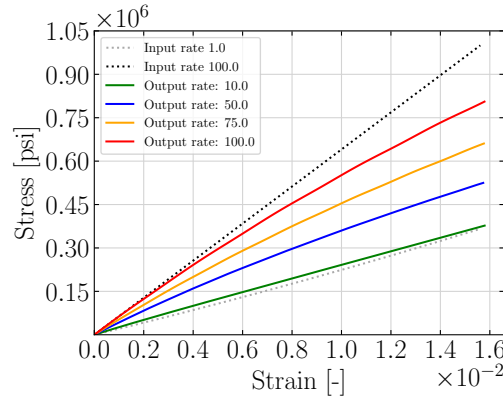


Figure 5.15: Viscoelasticity verification ( $\beta_{11} = 5000$ )

### Viscoplasticity only (VEVP = 0)

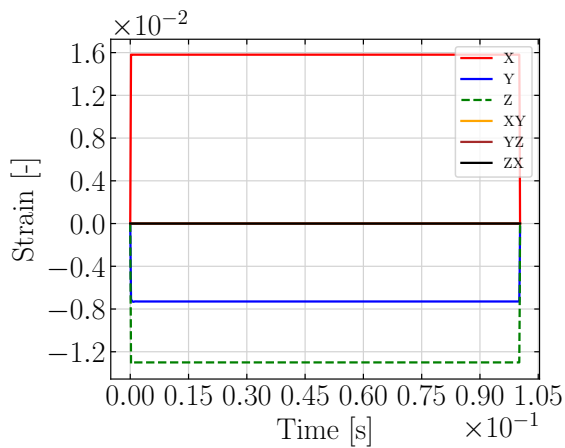
To verify the viscoplastic implementation, input was defined that does not include rate effects in the elastic region. Figure 5.17a shows the stress versus strain input with two curves defined for strain-rates of  $1.0 \frac{1}{s}$  and  $100.0 \frac{1}{s}$  with different yield stresses.

When the element is loaded at a constant rate (constant slope of strain versus time), as shown in Figure 5.17b, the stress increases following the corresponding input curve at that rate. As maximum displacement is reached, the nodes to which the displacement was applied were then held in place. This leads to stress relaxation as the stress versus time plot in Figure 5.17c shows.

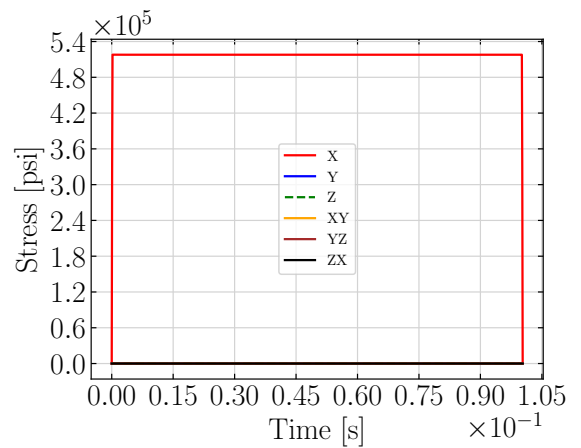
In Figure 5.17d the strain response to a constant stress load (Figure 5.17e) is shown. The strain increases slowly until the yield strain for the applied stress is reached.

## 5.3 Temperature Dependency

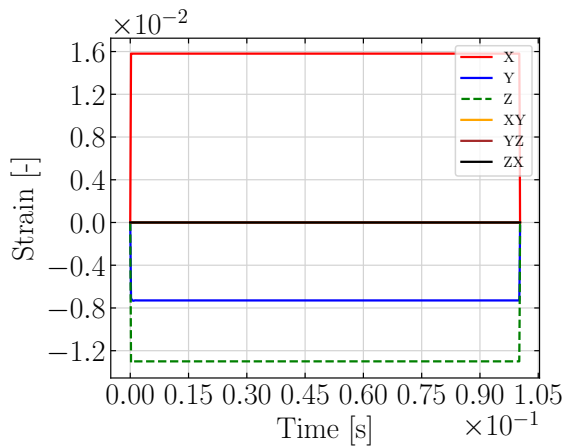
Temperature dependency of the material model was verified in a single element simulation in compression 2-direction. In this test, the effect of temperature on the yield stress and the effect of the Taylor-Quinney coefficient (beta), describing the ratio of plastic work that is converted to heat, is verified. The higher the Taylor-Quinney coefficient (beta) value,



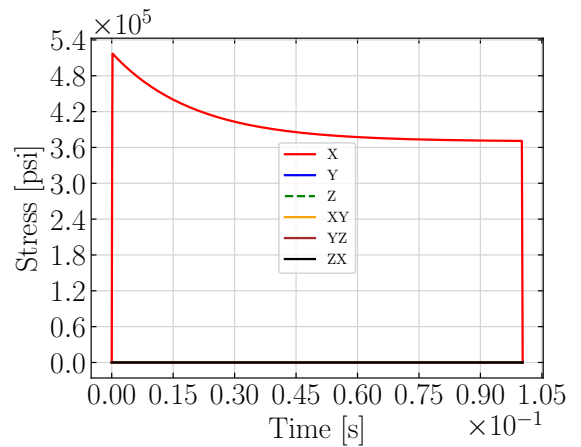
(a) Constant strain load ( $\beta_{11} = 0$ )



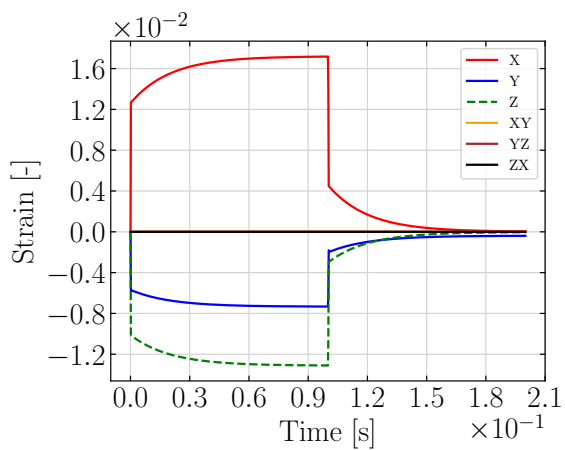
(b) Stress output ( $\beta_{11} = 0$ )



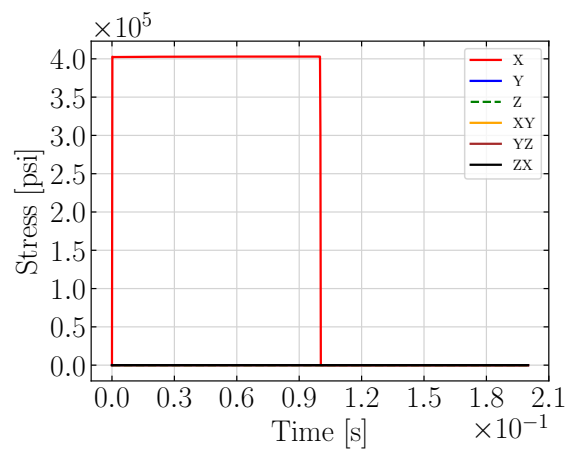
(c) Constant strain load ( $\beta_{11} = 50$ )



(d) Stress relaxation ( $\beta_{11} = 50$ )

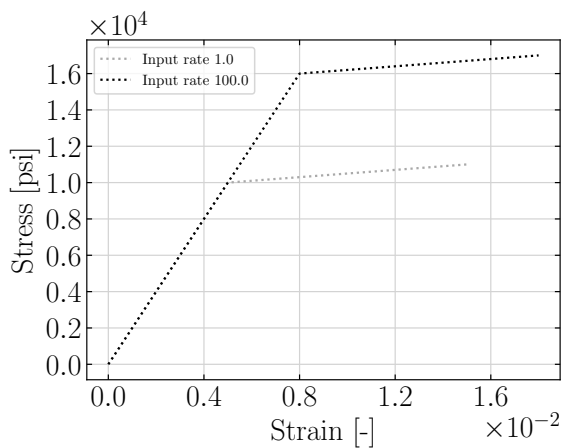


(e) Creep strain ( $\beta_{11} = 50$ )

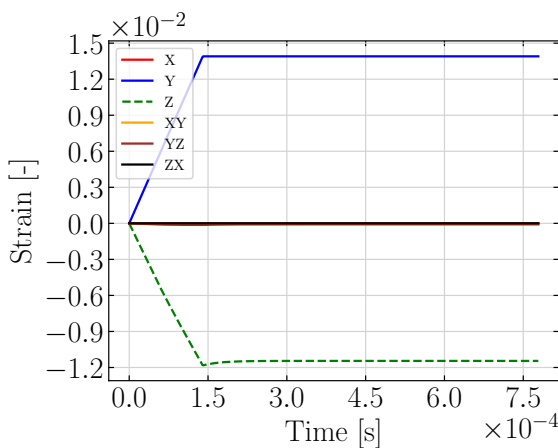


(f) Constant stress load ( $\beta_{11} = 50$ )

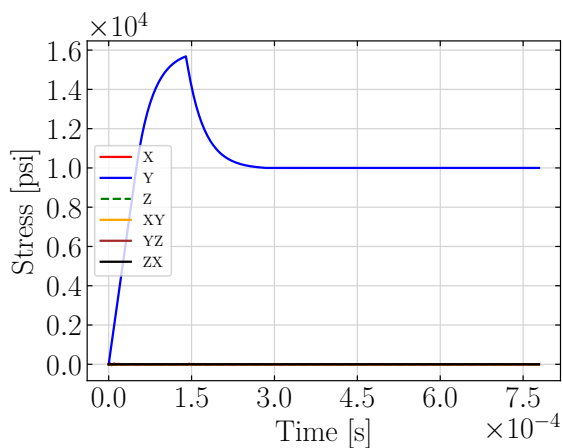
Figure 5.16: Viscoelastic stress relaxation and creep



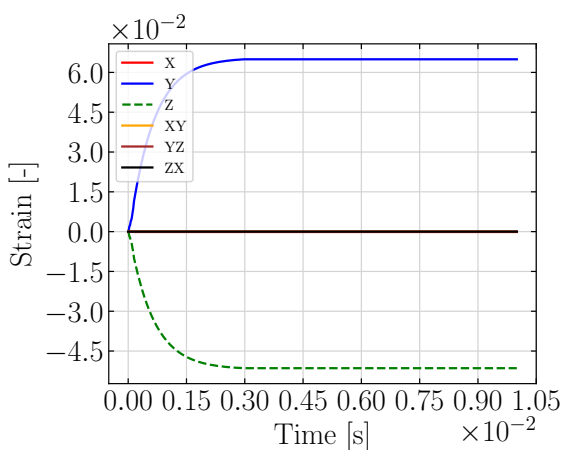
(a) Input curves



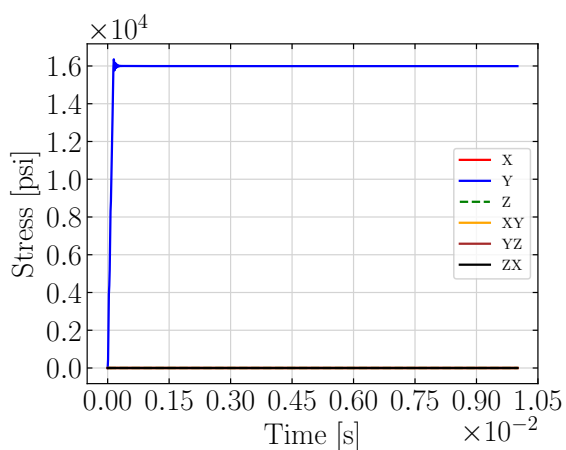
(b) Constant strain load



(c) Stress relaxation



(d) Creep strain



(e) Constant stress load

Figure 5.17: Viscoplastic stress relaxation and creep

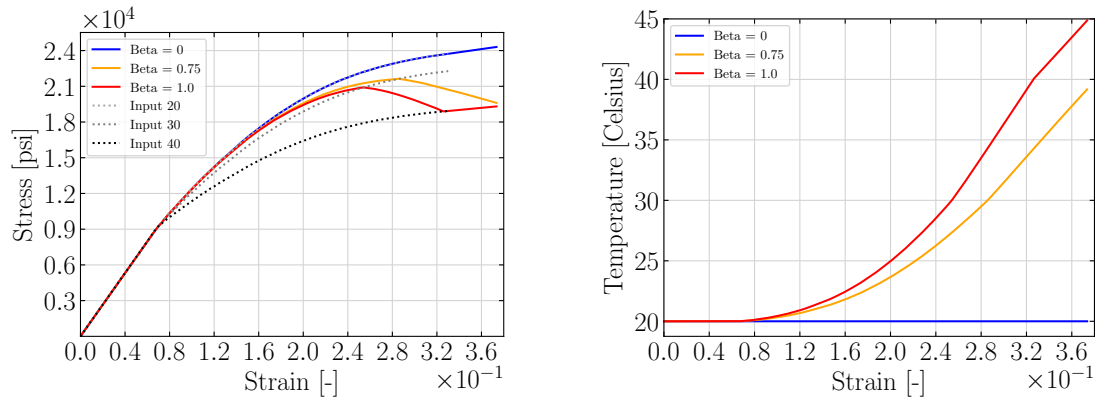
the more the loaded element should heat up throughout the simulation. If temperature-dependent stress versus strain curves are defined by the user, this rise in temperature leads to a change in the yield stress of the material.

In this particular test, three temperature-dependent curves are defined in the loading direction: a room temperature curve at 20°C; a scaled-down curve for 30°C; and as input for a temperature of 40°C another curve that was created by scaling down the room temperature input. Figure 5.18a shows the input curves for the different temperatures as gray and black dotted lines. As the specific heat capacity of the material, a value from literature for an epoxy material was obtained. Battaglia et al. measured a specific heat capacity of  $817 \frac{J}{kgK}$  for a CN 90 epoxy at 300° Kelvin [62]. Converted to imperial units, an input of the specific heat capacity to the material model was used:  $c_p = 817 \frac{J}{kgK} = 817 \frac{m^2}{s^2K} \approx 1,200,000 \frac{in^2}{s^2K}$ .

In Figure 5.18a, the stress versus strain results for three different values of beta are shown. Corresponding in Figure 5.18b, the temperature versus strain is plotted. For an input of beta=0, no plastic work is converted to heat and the temperature does not increase from the initial room temperature of 20°C (blue curve in Figure 5.18b). Therefore, the yield stress does not decrease and the output stress versus strain curve matches the input for 20°C throughout the simulation (blue curve in Figure 5.18a).

For a higher value of beta of 0.75, 75% of plastic work is converted to heat and the temperature rises with increasing plastic strain to around 40°C (orange curve in Figure 5.18b). While the temperature rises from 20°C to 30°C, the yield stress is interpolated between the corresponding input curves (orange curve in Figure 5.18a). For temperatures between 30°C to 40°C, the yield stress decreases faster as the distance between the input curves corresponding to these temperatures is greater.

For a maximum beta of one, the temperature rise with increasing strain is shown in Figure 5.18b. The temperature increases to around 45°C for a strain of approximately 37%. In the corresponding stress versus strain plot, the yield stress decreases according to the temperature in the material until the input curve for the highest temperature of 40°C



(a) Temperature effects on stress versus strain results in compression 2-direction (b) Temperature versus strain in compression 2-direction

Figure 5.18: Single element verification of temperature effects

is reached (red curve in Figure 5.18a). No extrapolation of the yield stress is done with further increasing temperatures and therefore, the stress versus strain output matches the input curve defined for the highest temperature even if the temperature in the material goes beyond this value.

## 5.4 Damage

Stiffness degradation of the material is modeled using the capabilities to define damage. By defining a curve listing the chosen damage parameter versus its corresponding curve ID, the user can define in which material directions damage should be accounted for and which uncoupled and/or coupled damage terms should be active. Table 4.3 in the implementation chapter lists all available damage parameters.

Uncoupled damage was verified by loading and unloading a single element force controlled in compression 2-direction. Damage parameter five, describing damage in compression 2-direction due to loading in the same direction, was defined with a corresponding strain versus damage curve. LS-DYNA Keyword 5.2 shows the damage definition for this

verification test case. No damage accumulates in the elastic region up to a strain of 0.0083 while it increases linearly up to a value of 0.1 at a total strain of 4% as defined in the curve with ID 10005 in LS-DYNA Keyword 5.2.

#### LS-DYNA Keyword 5.2: \*MAT\_213 input

```

*DEFINE_CURVE_TITLE
  Damage parameter vs. Curve ID
$#   lcid   sidr   sfa   sfo   offa   offo   dattyp
      50
$# Damage in C2, due to loading in C2
$# damage_parameter   curve_id
      5               10005
$
*DEFINE_CURVE_TITLE
  Damage in C2, due to loading in C2
$#   lcid   sidr   sfa   sfo   offa   offo   dattyp
      10005
$#   strain   damage
           0       0
           0.0083  0
           0.04   0.1

```

Figure 5.19a shows the stress versus strain output for the single element that was loaded force-driven in compression 2-direction to a stress of -20,000 psi, -23,000 psi, and finally -25,000 psi with unloading to states of zero stress in between. The blue curve in Figure 5.19a shows the results for a simulation with the damage model inactive, while the red curve shows the results for the damaged material. The slopes of the unloading and reloading paths are reduced due to the accumulation of damage and the reduction of stiffness of the material.

In another simulation, coupled damage was verified by loading a single element in compression 2-direction, unloading to a state of zero stress, and then reloading in tension 2-direction. LS-DYNA Keyword 5.3 shows the input to the damage model with damage parameter 46 active, describing damage in tension 2-direction due to loading in compression 2-direction. For a compressive loading up to a strain of 0.04, the stiffness when reloaded in tension 2-direction should be reduced by a factor of 0.5, as defined in curve 10046 and as shown in LS-DYNA Keyword 5.3.

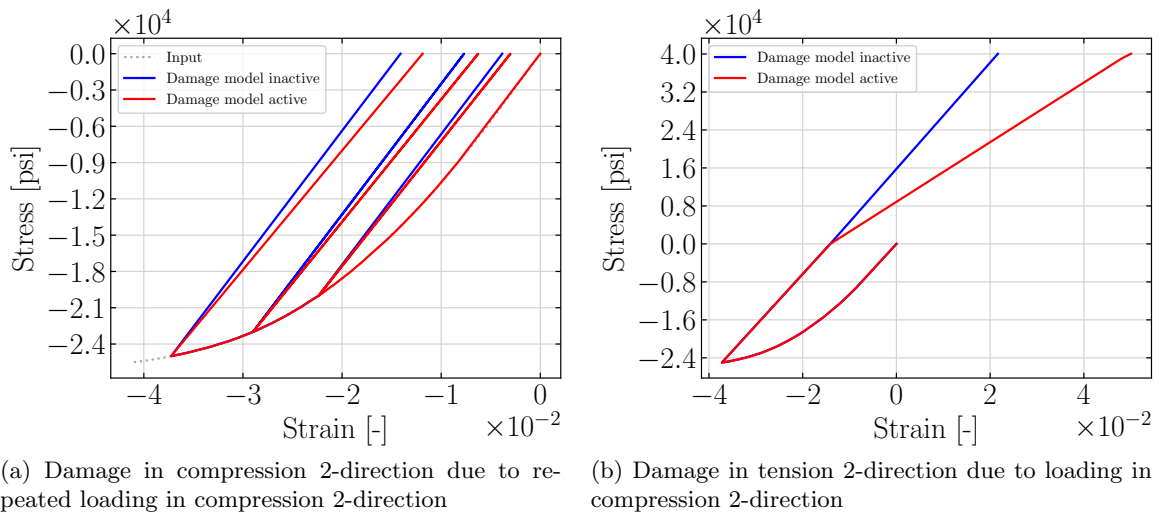


Figure 5.19: Single element verification of damage model

Figure 5.19b shows the stress versus strain results with the damage model inactive (blue curve) and active (red curve). While the unloading from compression followed the same path in both simulations, the modulus in tension 2-direction was reduced by a factor of close to 0.5 when the damage model was active.

This verifies that both uncoupled and coupled damage were giving results as intended.

#### LS-DYNA Keyword 5.3: \*MAT\_213 input

```

*DEFINE_CURVE_TITLE
Damage parameter vs. Curve ID
$#      lcid      sidr      sfa      sfo      offa      offo      dattyp
          50
$# Damage in T2, due to loading in C2
$#      damage_parameter      curve_id
          46                  10046
$
*DEFINE_CURVE_TITLE
Damage in T2, due to loading in C2
$#      lcid      sidr      sfa      sfo      offa      offo      dattyp
10046
$#      strain      damage
          0          0
          0.0083    0
          0.04      0.5

```

The damage model can be used to model stress degradation in the material. This was verified by defining a true stress versus strain curve as shown as a blue curve in Figure 5.20b with the stress level dropping with increasing strain. For the plasticity algorithm, a monotonically increasing effective stress versus strain curve is needed and the material model will not accept the input if this is not the case. In the pre-processing stage, the user-defined true stress versus strain input is converted using the damage parameter input to compute the effective stress versus strain curve as described in Equation 4.1. Therefore, the user can define the intended true stress versus strain input curve and corresponding effective stress versus strain curve that should be monotonically increasing. In Figure 5.20b, for example, the effective stress versus strain curve flattens out and behaves ideal plastically. With a given effective stress and true stress versus strain curve, the corresponding damage input can be computed that converts the true stress input into the desired effective stress curve. Figure 5.20a shows the matching damage versus strain curve that converts the blue true stress versus strain input curve from Figure 5.20b to the dashed black effective stress curve.

A simple script that computes the damage versus strain input for a given true stress input curve and desired effective stress curve is shown in Appendix A. The script was tested with Octave [63] and Matlab [64] and a description on how to use it is shown in Appendix A.

The simulation results with the described input are shown as a red dashed curve in Figure 5.20b. The output matches the blue input curve. With the approach discussed in this section, stiffness and stress degradation in individual material directions can be accurately defined.

## 5.5 Generalized Tabulated Failure Criterion

The Generalized Tabulated Failure Criterion is verified in single element simulations using the T800/F3900 data. A tabulated failure surface was constructed using the experimentally obtained failure strains from the uniaxial tension, compression and in-plane shear tests. To verify the newly developed failure model works as intended, the traditional definition of

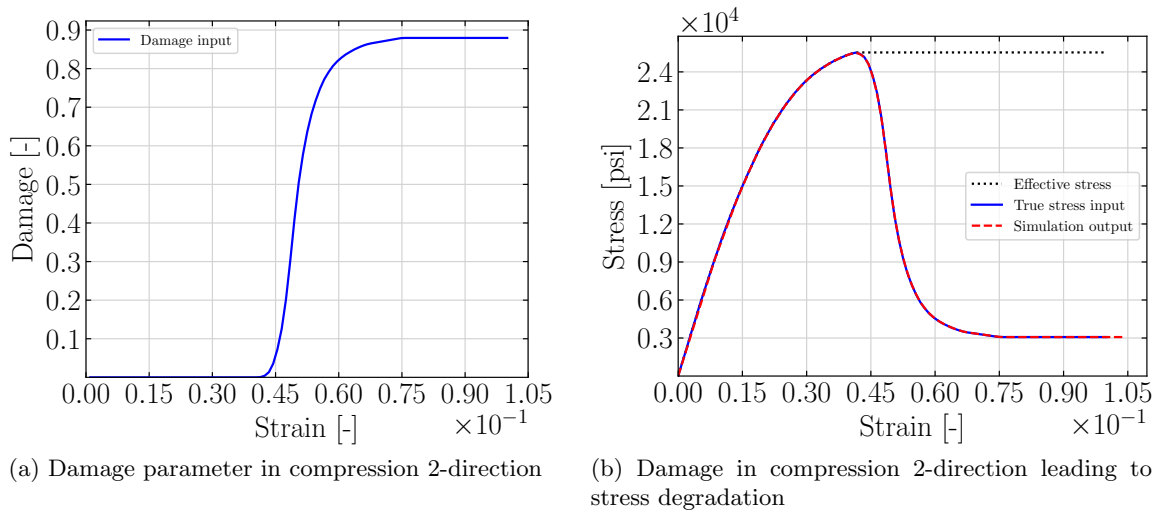


Figure 5.20: Single element verification of stress degradation

“failure” is used, i.e. erosion occurs once the load bearing capabilities have been exceeded in any single material direction. As previously described in Section 3.7, using the failure model in such a way does not provide physical results in a crash, crush or ballistic impact load case, where material behavior after reaching the maximum stress is of importance.

The user has to define a table of fiber direction stresses with corresponding angle versus equivalent failure strain curves. It is very important to highlight that the equivalent failure strain is not equal to the failure strain in loading direction obtained in a uniaxial material test. Due to Poisson’s effects, straining in the transverse direction will occur and the equivalent failure strain will be higher than the strain in loading direction. The Generalized Tabulated Failure Criterion should only be used in conjunction with the LS-DYNA keyword card `*DEFINE_ELEMENT_EROSION_SHELL`. With this card, the number of integration points per layer that fails a layer, and the number of failed layers that triggers element erosion have to be defined [59].

To analyze whether the element erosion criterion works as intended, consider for example loading in tension 2-direction ( $\sigma_{12} = 0$  and  $\sigma_{22} \geq 0$ ). Equation 3.92 can then be solved for an expected angle of zero degrees that represents this state of stress, as shown in Equation

5.1. For this angle, the equivalent failure strain from a uniaxial tension test in the matrix direction is given by Equation 3.93, where  $\varepsilon_{22}$  is the tensile strain in 2-direction at failure,  $\varepsilon_{11}$  is the compressive 1-direction strain at failure in the 2-direction test, and  $\varepsilon_{12}$  is the in-plane shear strain at failure in the 2-direction test.

For shear in 12-direction, Equation 5.2 yields an angle of  $90^\circ$ , while in compression 2-direction the computed angle is  $180^\circ$  (Equation 5.3).

$$\begin{array}{l} \sigma_{12} = 0 \\ \sigma_{22} \geq 0 \end{array} \quad \theta = \cos^{-1} \left( \frac{\sigma_{22}}{\sqrt{\sigma_{22}^2 + \sigma_{12}^2}} \right) = \cos^{-1} \left( \frac{\sigma_{22}}{\sqrt{\sigma_{22}^2}} \right) = \cos^{-1}(1) = 0^\circ \quad (5.1)$$

$$\begin{array}{l} \sigma_{22} = 0 \\ \sigma_{12} \neq 0 \end{array} \quad \theta = \cos^{-1} \left( \frac{\sigma_{22}}{\sqrt{\sigma_{22}^2 + \sigma_{12}^2}} \right) = \cos^{-1}(0) = 90^\circ \quad (5.2)$$

$$\begin{array}{l} \sigma_{12} = 0 \\ \sigma_{22} \leq 0 \end{array} \quad \theta = \cos^{-1} \left( \frac{\sigma_{22}}{\sqrt{\sigma_{22}^2 + \sigma_{12}^2}} \right) = \cos^{-1} \left( \frac{\sigma_{22}}{\sqrt{\sigma_{22}^2}} \right) = \cos^{-1}(-1) = 180^\circ \quad (5.3)$$

The graph in Figure 5.21 shows the equivalent failure strain input to the single element verification simulations. The equivalent failure strain values are defined by the user as a function of the angle are shown. Only three discrete points on the failure curve at zero fiber direction stress are known and values of stress states in between were interpolated using splines. The curve from Figure 5.21 was used as the input for zero fiber direction stress.

In addition to the three equivalent failure strains for the tensile and compressive matrix direction and in-plane shear, the failure strain for pure tension and compression 1-direction loading were the final two points used to construct the example failure surface. The defined fiber direction stresses should cover the expected range up to the failure stress in a pure tension or compression 1-direction material test. Therefore, for the highest expected tensile stress in the fiber direction, the equivalent failure strain for this stress state was input to the failure model. For all angles from  $0^\circ$  to  $180^\circ$  the tensile 1-direction failure strain was

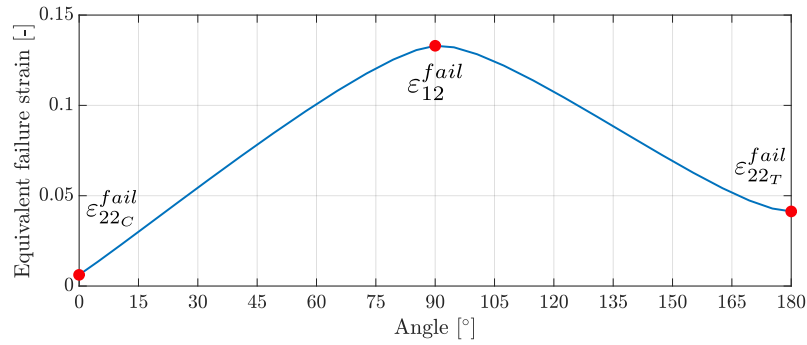


Figure 5.21: Failure input

used as the equivalent failure strain. Equivalently, for compression in 1-direction, failure strain for uniaxial compressive loading was input to the failure model.

The resulting failure surface is shown in Figure 5.22. The curve at zero fiber direction stress (green) represents the equivalent failure strains for tension and compression 2-direction tests and shear in the absence of fiber direction stresses. To the left, for a failure stress of  $\sim 366,000$  psi, the equivalent failure strain determined in a pure tension 1-direction test is the input for all angles as represented by the light blue line. Similarly, for a pure compression 1-direction loading, at the compressive failure stress of  $\sim -110,000$  psi, the failure strain in this loading condition is defined for all angles (blue curve). All other shown lines for fiber direction stresses between zero and the failure stresses were linearly interpolated. This effectively leads to element erosion becoming more likely with increasing fiber direction stress in combined loading conditions.

Single element verification simulations were conducted to test the failure model. The results for both tension 1- and 2-direction are shown in Figure 5.23. Figure 5.23a shows the strain versus time for tension 1-direction. The element is failing right when the user-defined failure strain in this direction, represented by the dotted grey line, is reached by the strain in loading direction (X). According to Equation 3.92, the fiber direction stress  $\sigma_{11}$  is not influencing the angle and is, therefore, of no importance for failure in pure fiber direction loading. In tension 1-direction, the angle oscillates between  $0^\circ$  and  $180^\circ$ . As the

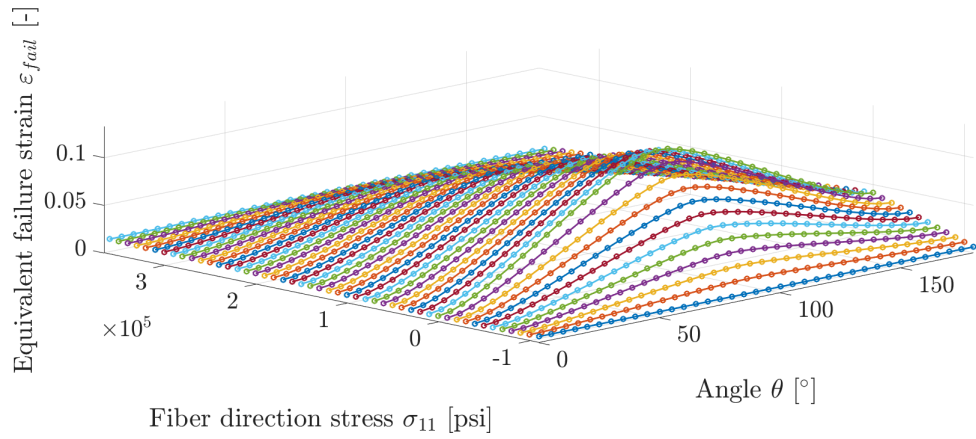
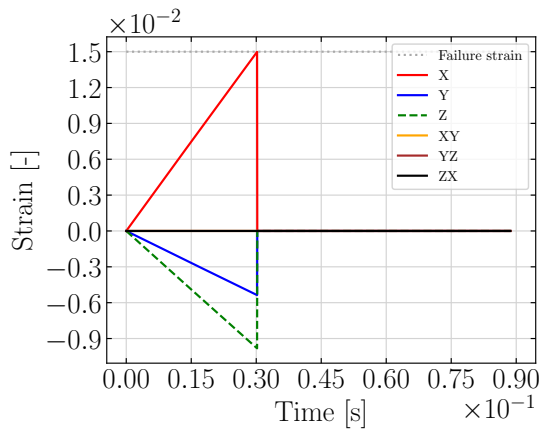


Figure 5.22: Failure surface

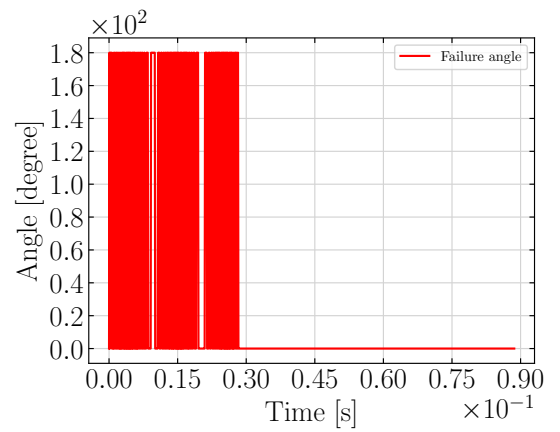
element is loaded uniaxial, in theory a matrix direction stress of zero would occur, leading to an analytical angle of  $90^\circ$  as shown in Equation 5.2. In numerical simulations, however, a value of zero rarely occurs. Due to numerical noise, the value of the off-axis (tension and compression 2-direction), stress oscillates between low values of positive and negative stress and therefore between  $0^\circ$  and  $180^\circ$ . The oscillation of the angle does not cause the equivalent failure strain to oscillate as the values for both zero and  $180^\circ$  are (and should be) defined as the same in pure 1-directional loading (see Figure 5.22).

Figures 5.23c and 5.23d show the strain versus time and angle versus time for tension 2-direction respectively. The element again fails as the user-defined failure strain in the loading direction is reached. In the angle vs. time plot of Figure 5.23d, the angle stays at the previously computed analytical result (Equation 5.1) of zero.

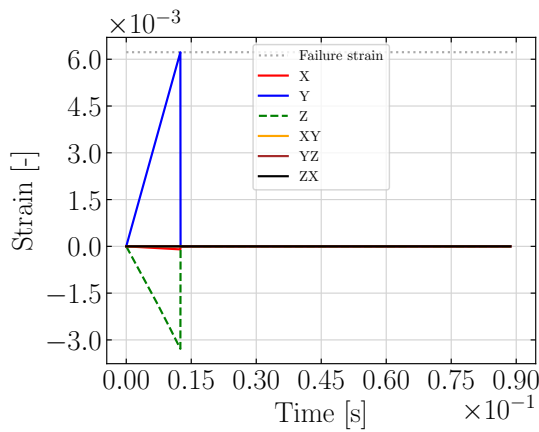
The results of single elements loaded in compression are shown in Figure 5.24. In both compression 1 and 2-direction, the element fails once the failure strain in the respective direction is reached. In compression 1-direction, the angle again oscillates between  $0^\circ$  and  $180^\circ$ , for the same reason as described for the tensile load case. The angle in the 2-direction stays at the analytically computed value of  $180^\circ$  until failure occurs, as was shown in Equation 5.3.



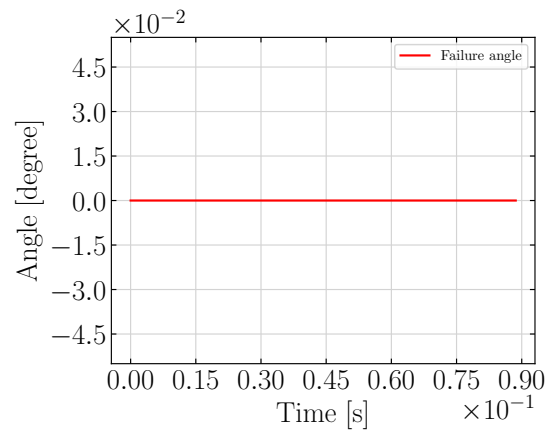
(a) Strain vs. time tension 1



(b) Angle vs. time tension 1

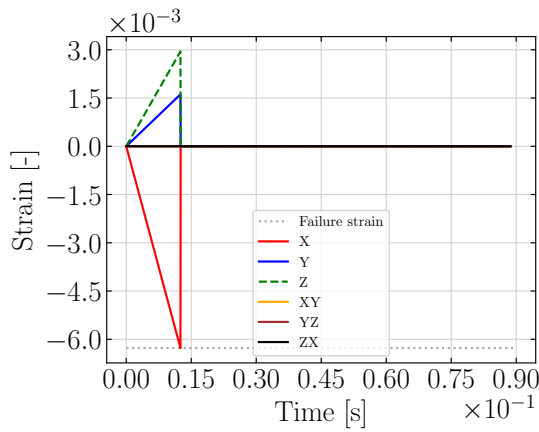


(c) Strain vs. time tension 2

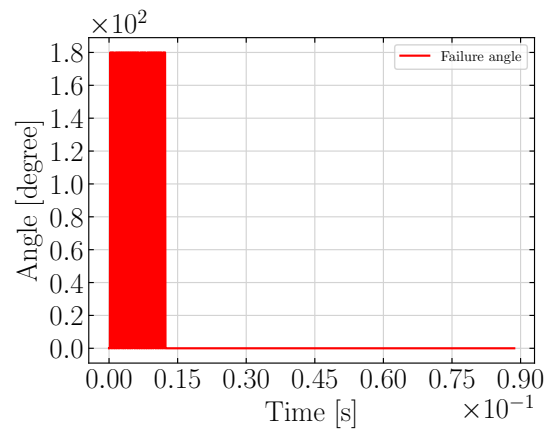


(d) Angle vs. time tension 2

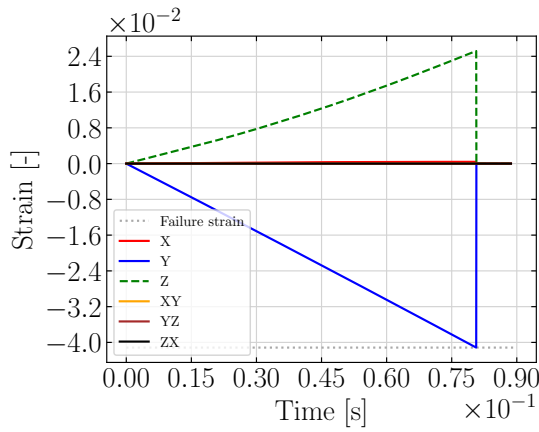
Figure 5.23: Verification of Generalized Tabulated Failure Criterion - tension



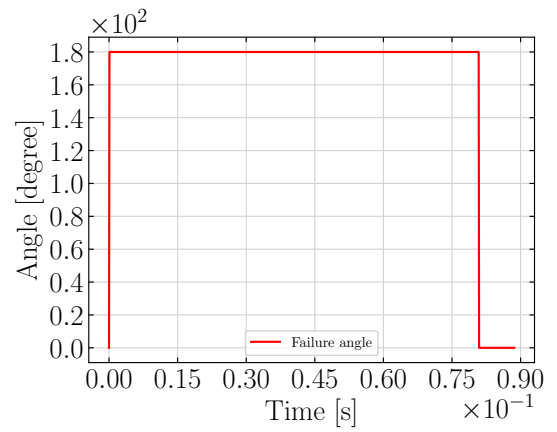
(a) Strain vs. time compression 1



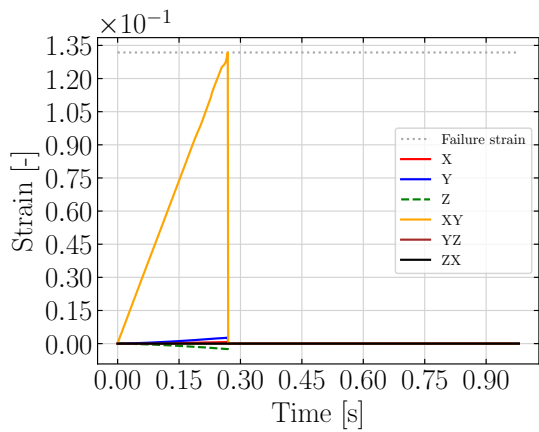
(b) Angle vs. time compression 1



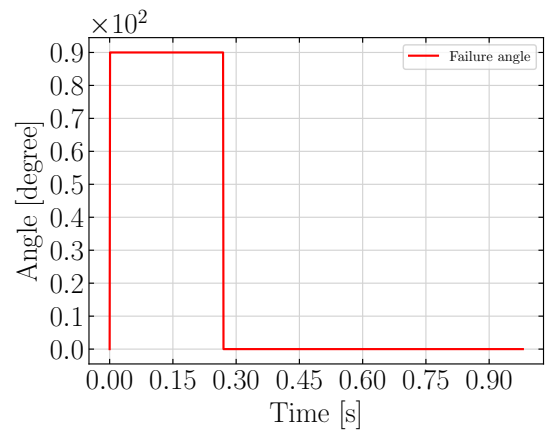
(c) Strain vs. time compression 2



(d) Angle vs. time compression 2



(e) Strain vs. time shear 12



(f) Angle vs. time shear 12

Figure 5.24: Verification of Generalized Tabulated Failure Criterion - compression and shear

Figures 5.24f and 5.24e show the computed angle and strain versus time for an in-plane shear verification simulation with the failure model active. The element fails once the user-defined shear failure strain is reached. The angle in the pure in-plane shear loading simulation matches the analytically computed value of 90° from Equation 5.2.

Overall, the Generalized Tabulated Failure Criterion is able to accurately represent the user-defined input of different failure strains in the material directions, and will cause element erosion at the correct strain.

## 5.6 Stochastic Effects

The correct implementation of the stochastic variation of material parameters was evaluated in single element simulations. The elements were loaded displacement-controlled in tension and compression, 1- and 2-direction. LS-DYNA Keyword card 5.4 shows the definition of the stochastic variations for the different material directions.

LS-DYNA Keyword 5.4: Stochastic verification input

```

*DEFINE_STOCHASTIC_VARIATION_MAT213
$#   id_sv      pid   pid_typ   irng      numv   num_beg
    1          2     0         1         1
$#   vartyp   corlgrp   r1      r2      r3
    1          0     0.9     1.1
    1          0     0.9     1.1
    1          0     0.9     1.1
    1          0     0.9     1.1
    1          0     0.9     1.1

```

In the first line of the keyword card the definition is given the ID one and is defined for the part with ID 2. PID\_TYP is set to zero, which indicates that PID is referencing an individual part and not a part set. By setting IRNG to one, a non-deterministic (true) random number generator is used to achieve a difference in results between simulation runs. Lines two through six follow the actual definitions of variations of the material parameters. VARTYP = 1 defines a uniform distribution between the lower and upper bounds R1 and R2 that are defined as 0.9 and 1.1 respectively for all material parameters. The definition as shown in LS-DYNA Keyword card 5.4 should lead to scaling of the input curves in all material directions by factors varying with a uniform random distribution between 0.9 and

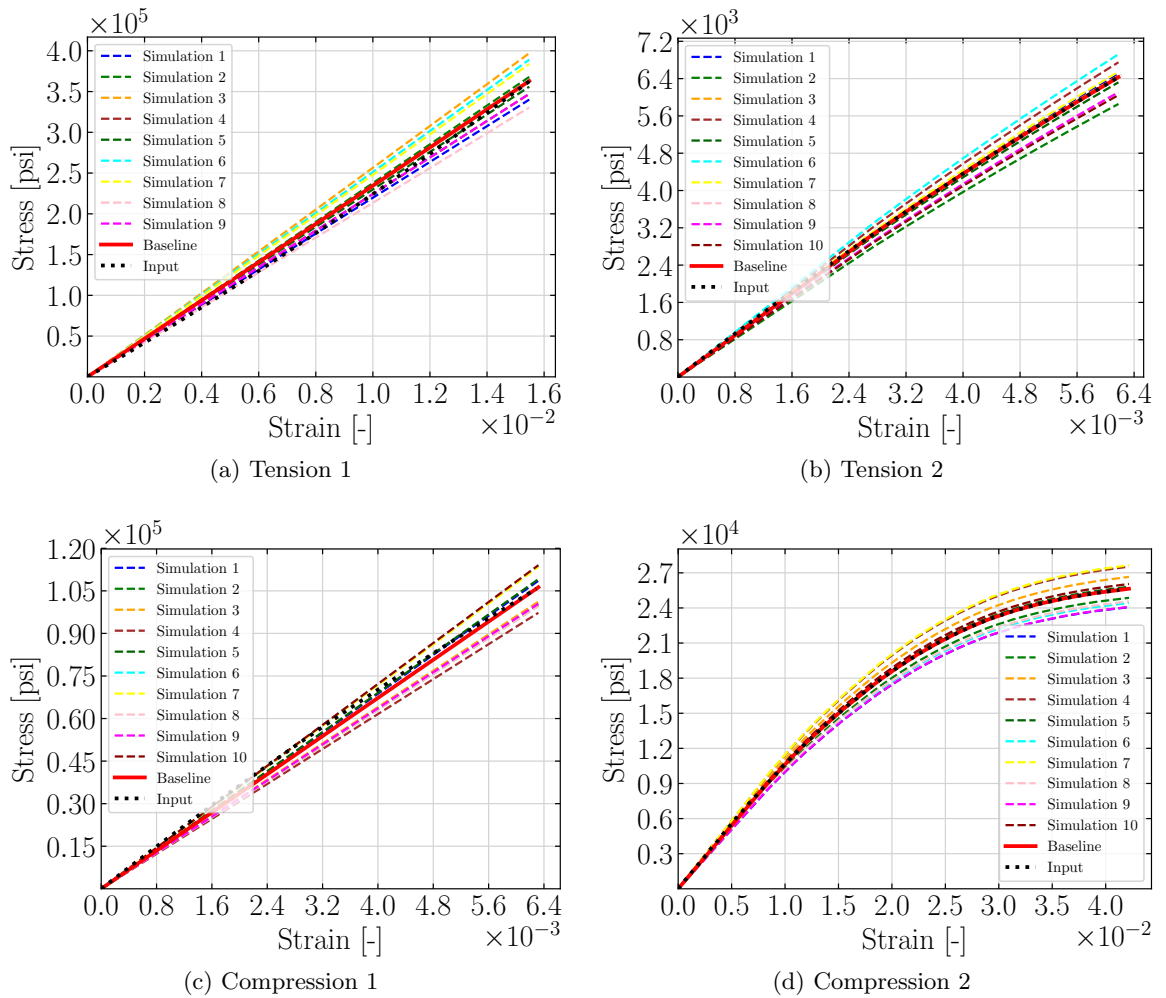


Figure 5.25: Stochastic single element verification

1.1. For a more detailed description of how stochastic variations are defined for the material model see Section 4.3. Figure 5.25 shows the results of ten single element simulations in the five material directions. The solid red line represents the deterministic results without a stochastic variation defined, while the dotted black line shows the input stress versus strain curve provided by the user. The results from the simulations with stochastic variation defined are shown as dashed lines. In all directions, a scaling of the output curve by a factor in the range of 0.9 and 1.1 is achieved in both the elastic and plastic region. This confirms that the defined variations are accurately represented.

## Chapter 6: Validation

In Chapter 5 the material model was verified using single element simulations. The verification ensures that the code produces the expected results in a stable manner. However in verification simulations, it is only ensured that the model works as intended. Additional validation simulations were performed to test the physical usefulness of the developed model. Due to the lack of required mechanical property test data of crush tests, ballistic impact tests were chosen to highlight the capabilities of the material model. For the tested composite material in the ballistic impact, extensive material data was available. The ballistic impact simulations additionally highlight the versatility of the model as they were simulated using the same approach as the crush simulation shown in Section 6.2.

### 6.1 Validation in Ballistic Impact Loadcase

Several high velocity ballistic impact tests were conducted at NASA Glenn Research Center (NASA-GRC) to validate the developed material model. Square 16 ply unidirectional T800/F3900 composite panels with the dimensions of 12" x 12" x 0.122" were impacted by projectiles with the weight of approximately 50 grams. The composite panels were manufactured with a layup of  $[0, 90, +45, -45]_{2S}$ . The cylindrical clamping of the panel had an inner radius of 5" and an outer radius of 6".

In the simulation model, the square plate was modeled as a round plate that covered the region of the clamping. The overhanging parts of the plate were not modeled, as they were not considered to be important to the overall behavior of the plate. The panel was meshed relatively coarsely in the clamping region while using a finer mesh in the impact region. Based on the physical tests, the simulations were set up with single point constraints in the region of the clamping. Figure 6.1 shows the simulation setup to replicate the real life

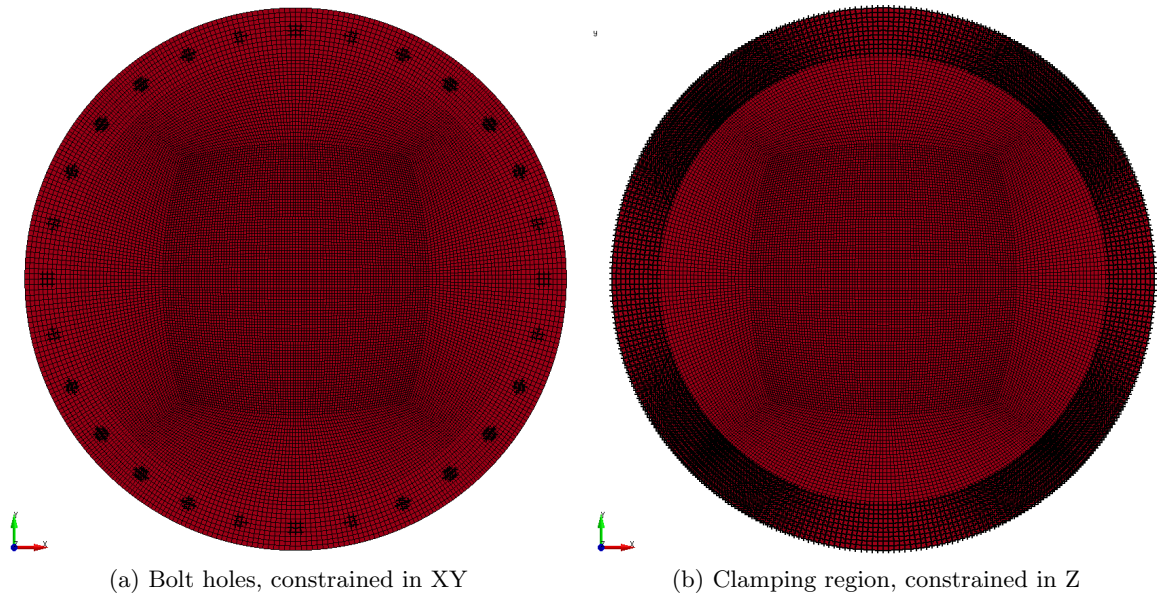


Figure 6.1: Boundary conditions of the plate in the ballistic impact simulation

boundary conditions without having to rely on modeling of the clamping plates to reduce the CPU time of the simulations. The bolts in the test were simulated by constraining the nodes in the bolt holes in-plane (Figure 6.1a), while the nodes on top and on the bottom of the plate in the clamping region were constrained out-of-plane (in impact direction, see Figure 6.1b).

The projectile then impacts the plate in the center of the panel, as shown in an isometric view of the simulation setup in Figure 6.2.

Every ply of the composite layup was modeled with an individual shell element while also accounting for delamination by modeling the interface between the plies using cohesive elements. Figure 6.3 on the left shows the layup of the shell elements with their thickness shown and on the right with only the mid-plane of the shell elements. The solid cohesive elements share the nodes with the shell elements and the cohesive material model chosen was `*MAT_COHESIVE_MIXED_MODE` (MAT138). Table 6.1 lists the material property values after they were adjusted to match DCB and ENF tests (see Section 2.5).

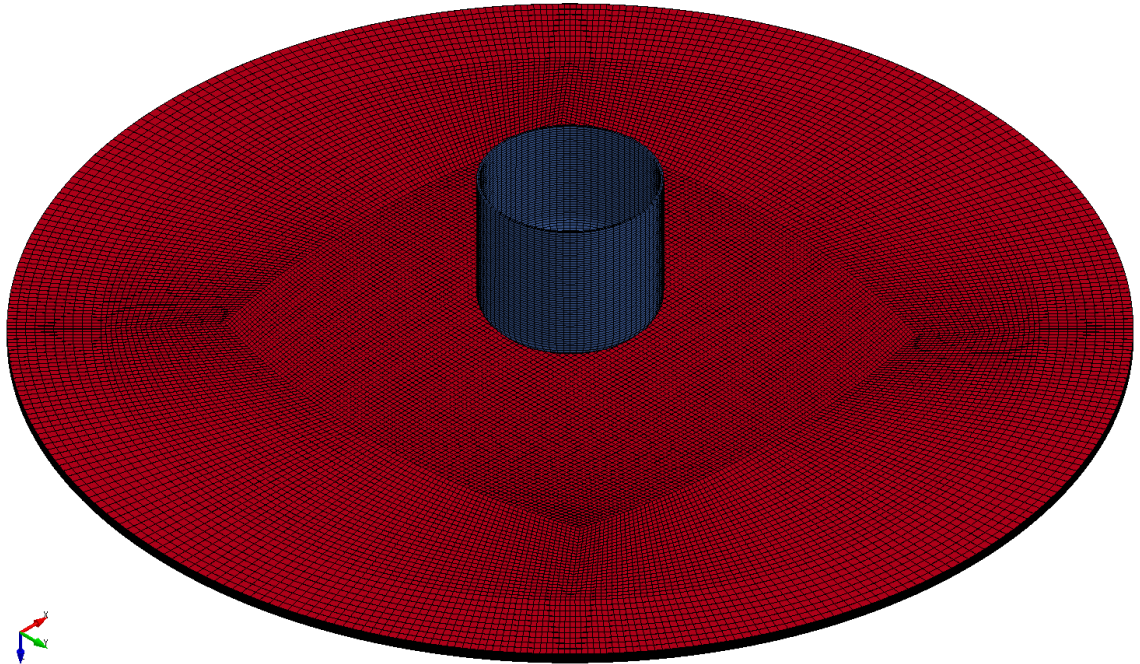


Figure 6.2: Isometric view of the ballistic impact simulation setup

Table 6.1: Cohesive material properties

LS-DYNA variable	Description	Value
EN	Normal stiffness	$6.16e^8$ [ <i>psi / in</i> ]
ET	In-plane stiffness	$6.16e^8$ [ <i>psi / in</i> ]
GIC	Energy release rate for mode I	4.28 [ <i>psi · in</i> ]
GIIC	Energy release rate for mode II	14.5 [ <i>psi · in</i> ]
XMU	Exponent of the mixed mode criteria	1.0 [–]
T	Peak traction in normal direction	4000 [ <i>psi</i> ]
S	Peak traction in tangential direction	8000 [ <i>psi</i> ]

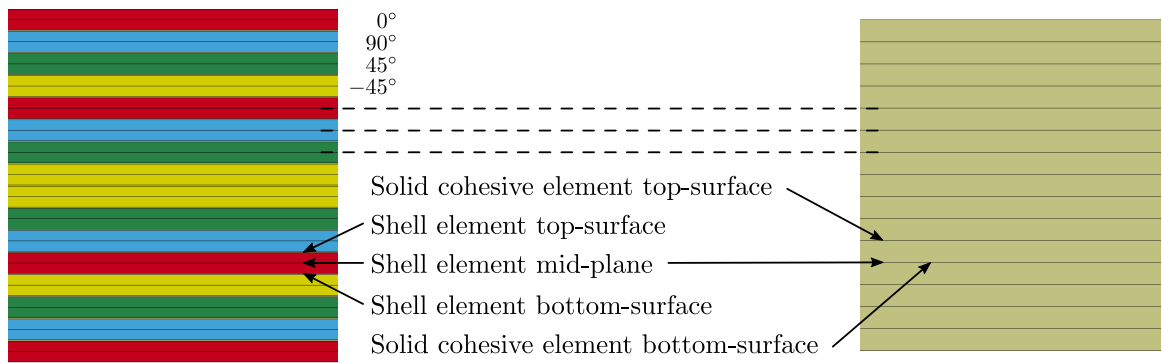


Figure 6.3: Composite plate layup and modeling technique with cohesive elements

In Table 6.2 all ballistic impact tests conducted by NASA-GRC are listed, sorted by impact velocities. For the lower velocities of 116 ft/s up to 384 ft/s, the projectile rebounded off the plate with the velocity shown in the “Rebound Velocity” column. The higher velocities from 417 ft/s to 535 ft/s penetrated the plate and exited with a velocity as shown in the column “Exit velocity”.

The impact velocities of the tests LVG1075, LVG1074 and LVG1076 (highlighted in bold font) were chosen to be simulated as they were in the region of the ballistic limit velocity, the highest impact velocity at which the plate is able to contain the projectile. Additionally, an impact velocity between LVG1075 and LVG1075, 406 ft/s, was simulated to verify that consistent results in the region of the ballistic limit velocity are obtained.

In finite element simulations, failure of materials is generally modeled by eroding elements when stresses or strains reach a critical level. In engineering materials, when physical material tests are conducted, the test is usually stopped once the force drops, which is considered as “failure” for the material. Composite materials, however, might still be able to take load in the other material directions. Consider, for example, a tensile load transverse to the fibers that leads to damage by debonding between fibers and the matrix material. The material is now considered to have “failed”, however, most fibers will still be intact and the material could very well still take tensile loads in the fiber direction. If in a finite element simulation the element that reached that critical stress or strain in tension 2-direction is

Table 6.2: LVG ballistic impact tests, impact and rebound/exit velocities (rounded)

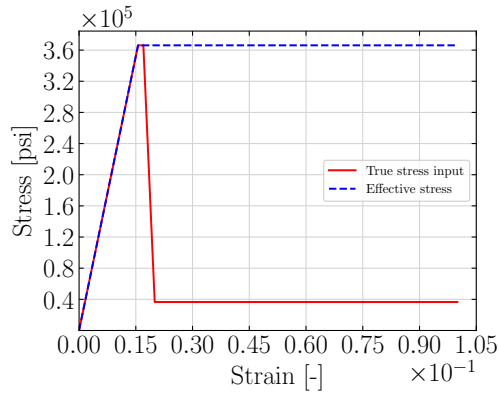
Test ID	Impact Velocity [ft/s]	Rebound velocity [ft/s]	Exit velocity [ft/s]
LVG1065	116	69	-
LVG1067	155	84	-
LVG1073	172	89	-
LVG1069	178	79	-
LVG1070	181	94	-
LVG1068	182	97	-
LVG1066	185	104	-
LVG1064	237	116	-
<b>LVG1075</b>	<b>385</b>	<b>46</b>	-
<b>LVG1074</b>	<b>417</b>	-	<b>25</b>
<b>LVG1076</b>	<b>453</b>	-	<b>114</b>
LVG1063	535	-	263

now eroded, the load bearing capabilities in other directions would be lost as well. The finite element should therefore not be eroded once the “failure” strain measured in uniaxial tension and compression tests is reached. Instead, in this validation study, the implemented damage model was used to degrade the stress in the direction where the “failure” strain from the uniaxial test occurred. The stiffness and stress were degraded to a level of 10% of the maximum stress and stiffness and the element therefore lost most of its load bearing capabilities in this direction while maintaining it in others. Figure 6.4 shows the stress versus strain and damage input to the material model that achieved this behavior. Similar to the methodology described in Section 5.4, a true stress versus strain (red) and an effective stress versus strain curve (dashed blue) were defined as shown in Figure 6.4a. From these curves, the damage versus strain curve was computed (Figure 6.4b), which converted the true stress curve into the monotonically increasing effective stress curve (see Appendix A for a damage curve calculation script). Input to the material model were then the true stress versus strain curve and the damage curve for the uncoupled damage term. Similarly, the input for tension 2-direction and 12-shear is prepared as shown in Figure 6.4c through 6.4f. The stress versus strain input for compression in 1 and 2-direction was left unchanged from the material test data (see Figures 5.2b and 5.5b).

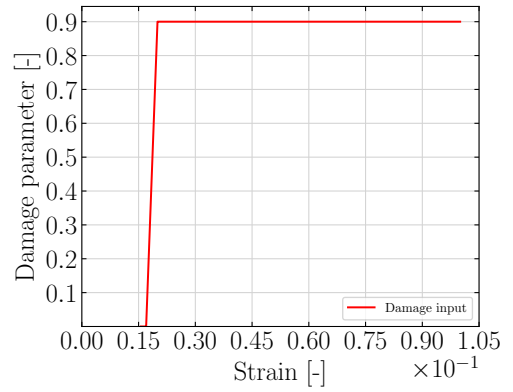
As previously described, elements should not be eroded once the critical stress or strain is reached in a single loading direction. However, as in ballistic impacts where the projectile might fully penetrate the plate, some erosion of elements inevitably needs to take place to create the opening for the projectile. The Generalized Tabulated Failure Criterion was used to define a high equivalent erosion strain of 80% in all loading conditions by defining two curves with two angles each ( $-180^\circ$  and  $180^\circ$ ) with a corresponding equivalent erosion strain of 0.8 for both angles. Only when the element deforms very drastically will it erode to avoid numerical instabilities and to allow for the projectile to penetrate the plate. The material input was the same in the three ballistic impact simulations.

Figure 6.5 shows the projectile velocities over time for the simulations. A positive velocity indicates the projectile was traveling forward, while a negative velocity can be observed for a rebounding projectile. The solid red line represents the velocity in the LVG1076 simulation over time, while the horizontal dashed red line marks the exit velocity of 114 ft/s (1368 in/s) that was measured in the physical impact test. The projectile initially had the impact velocity of 453 ft/s (5436 in/s) and was then slowed down while penetrating the composite plate. It exited the plate with a velocity 6.2% of the delta v higher than the measured velocity. However, if the physical test was repeated several times at the exact same velocity, the variation in the results would likely be higher than the difference between the test and simulation. In both the LVG1074 and LVG1075 simulations, the projectile velocity at the end of the simulation was 3.1% of the delta v below the measured exit velocity (LVG1074) and rebound velocity (LVG1075). The difference between test and simulation was again relatively small, and the measured variations in tests would likely be higher. The additional simulated impact velocity between LVG1075 and LVG1074 of 406 ft/s (4872 in/s) shows a resultant rebound velocity that falls between the rebound and exit velocities of LVG1075 and LVG1074 (orange curve in Figure 6.5).

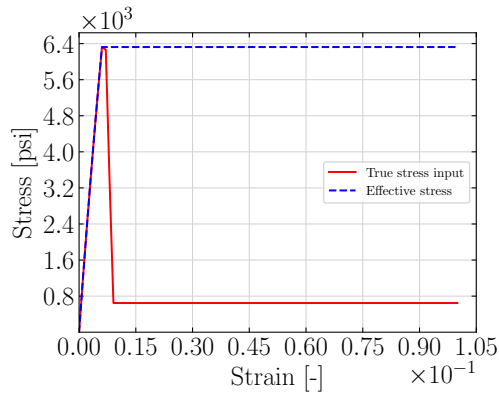
Figure 6.6 shows isometric views of the impacted region on the back side of the plate in the LVG1075 simulation, where, in the physical test, the projectile rebounded the plate with a relatively low velocity of 46 ft/s. In the simulation, the projectile caused significant



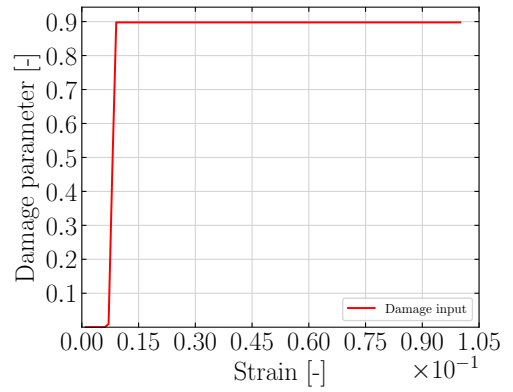
(a) Tension 1-direction stress vs. strain input



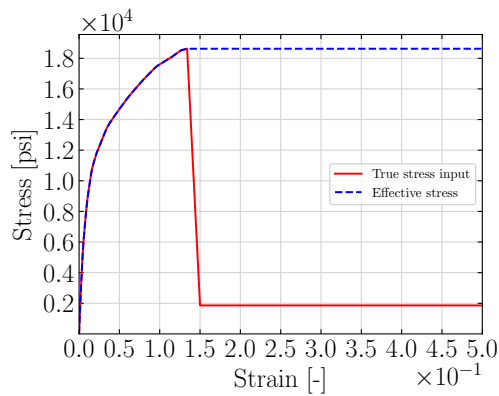
(b) Tension 1-direction damage vs. strain input



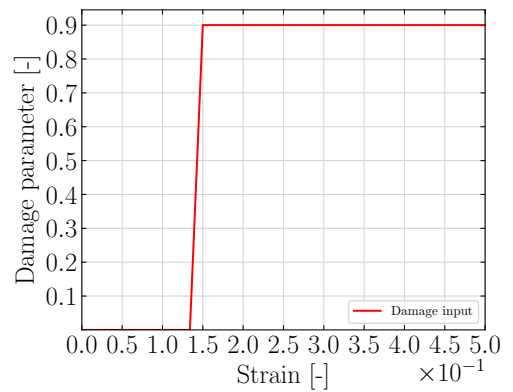
(c) Tension 2-direction stress vs. strain input



(d) Tension 2-direction damage vs. strain input



(e) Shear 12-direction stress vs. strain input



(f) Shear 12-direction damage vs. strain input

Figure 6.4: Ballistic impact simulation material model input

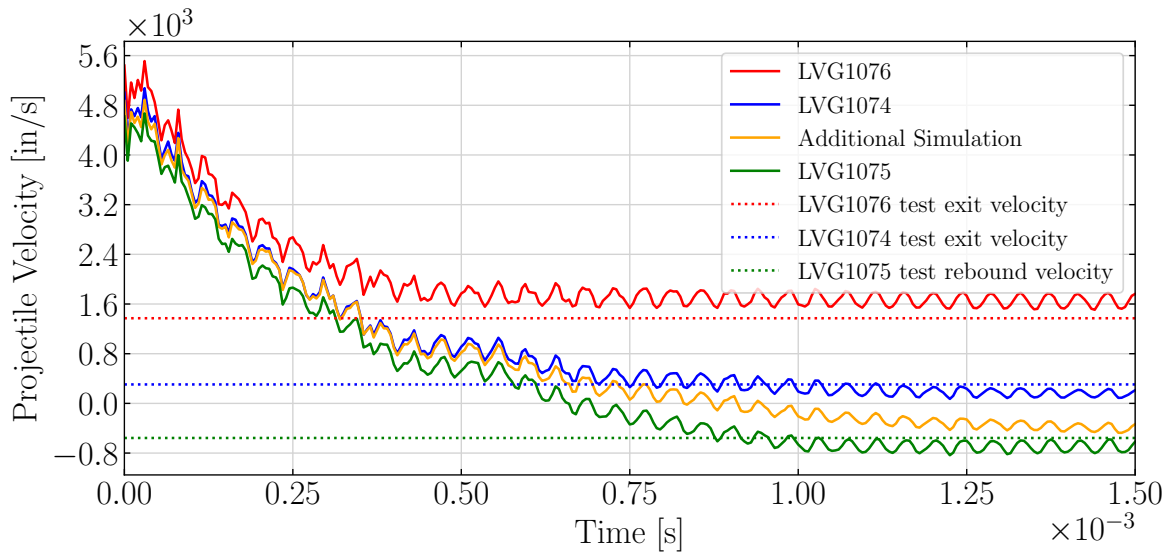


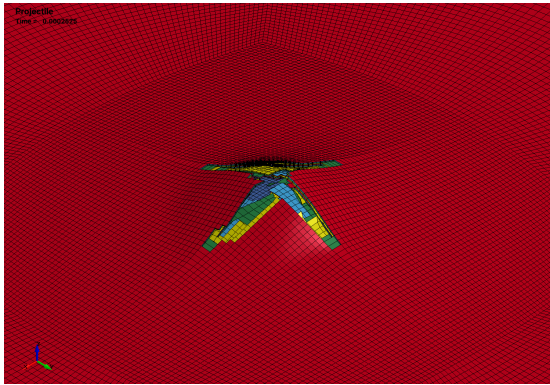
Figure 6.5: Projectile velocities in the LVG impact tests and simulations

damage to the plate leading to rupture in a “cross-like” pattern. However, the projectile did rebound the plate in the simulation, similarly to the test.

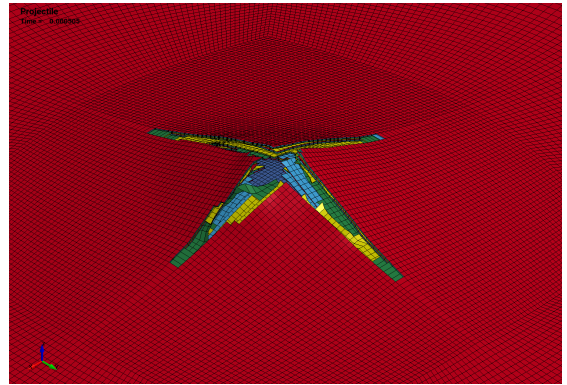
Figure 6.7 shows isometric views of the impacted region on the back side of the plate in the LVG1074 simulation, where, in the physical test, the projectile penetrated the plate and exited with a relatively low velocity of 25 ft/s. In the simulation, similar to the lower velocity (LVG1075) analysis, the plate again ruptured in a similar pattern. However, as the velocity plot in Figure 6.5 showed, the projectile then continued to travel forward with a positive velocity, similar to that of the test.

Figure 6.8 shows isometric views of the impacted region on the back side of the plate in the LVG1076 simulation, where, in the physical test, the projectile penetrated the plate and exited with a velocity of 114 ft/s. As in the test, the projectile ruptured the plate and exited through the back side. The initial velocity was significantly reduced and the exit velocity matched the measured test velocity fairly well.

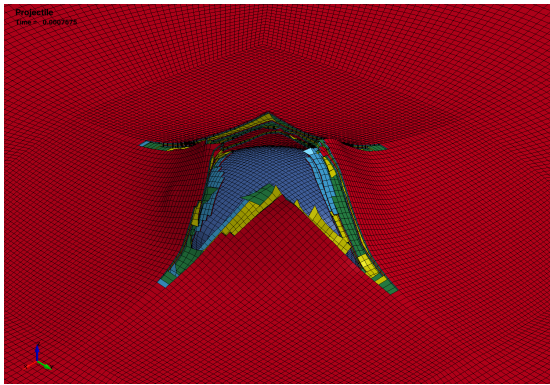
The failure patterns in the three different tests were relatively similar, as such, only one exemplary test result is compared to the patterns obtained in the corresponding simulation. Figure 6.9a shows the impacted side of the composite plate post-test at the LVG1076 impact



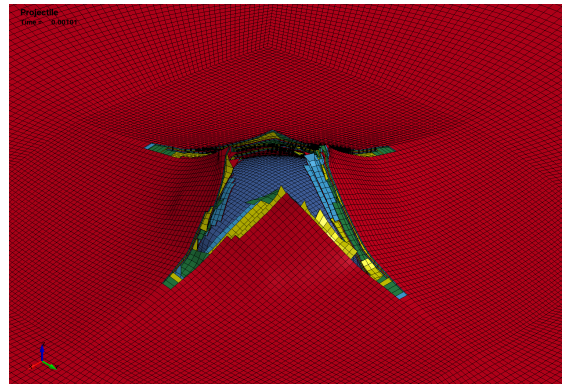
(a)  $t = 0.00025s$



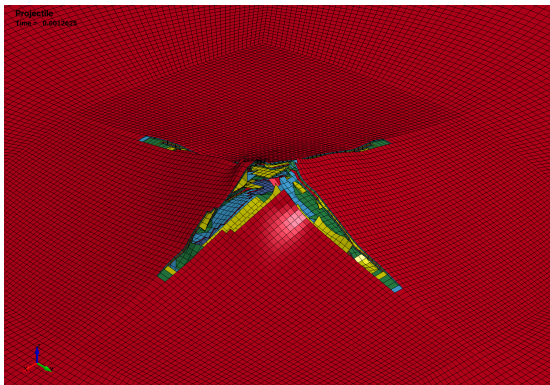
(b)  $t = 0.00050s$



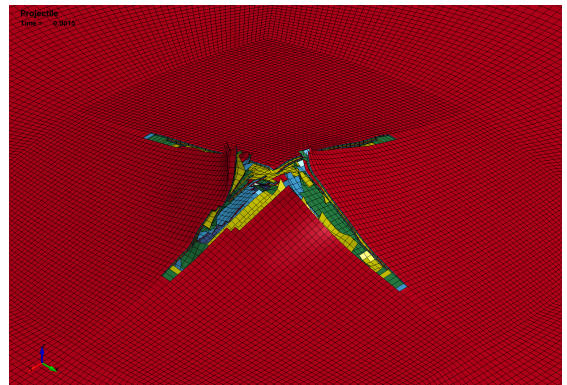
(c)  $t = 0.00075s$



(d)  $t = 0.00100s$

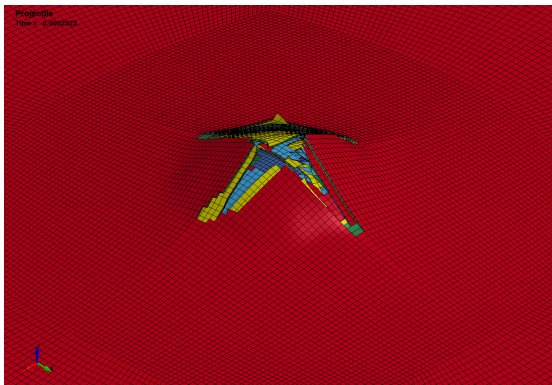


(e)  $t = 0.00125s$

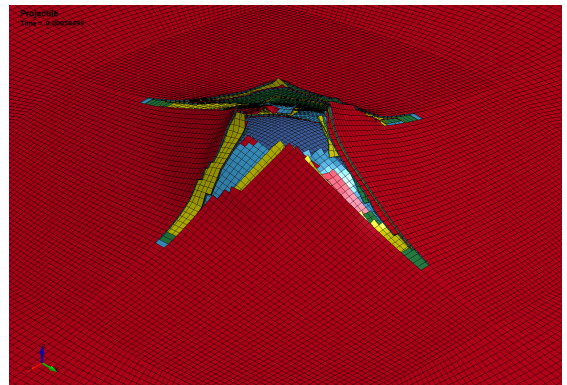


(f)  $t = 0.00150s$

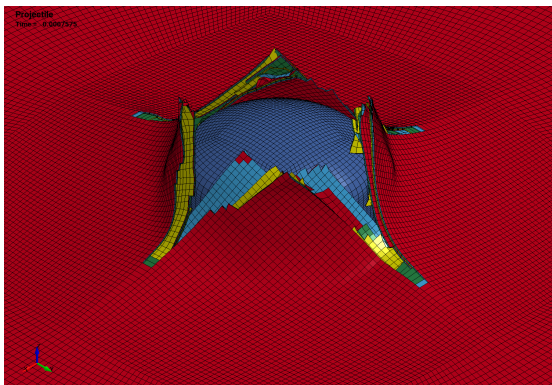
Figure 6.6: LVG1075 ballistic impact simulation



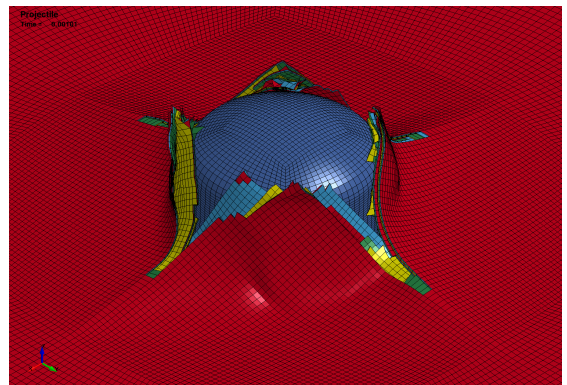
(a)  $t = 0.00025\text{s}$



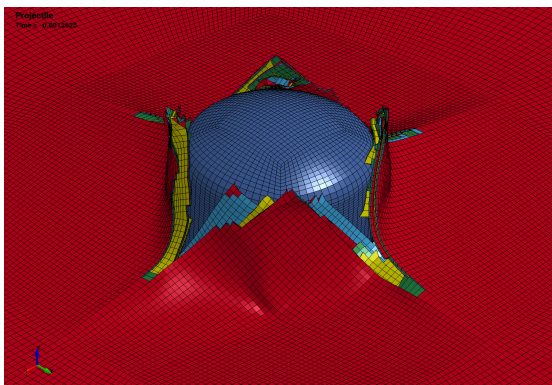
(b)  $t = 0.00050\text{s}$



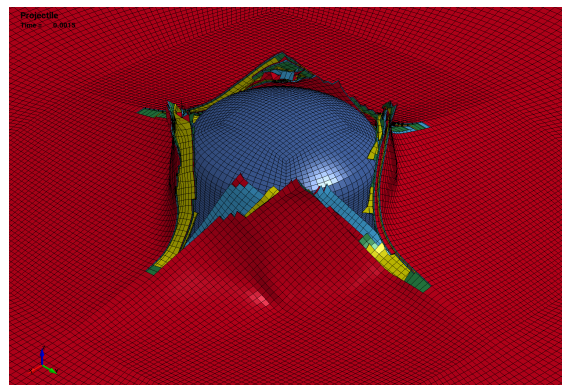
(c)  $t = 0.00075\text{s}$



(d)  $t = 0.00100\text{s}$

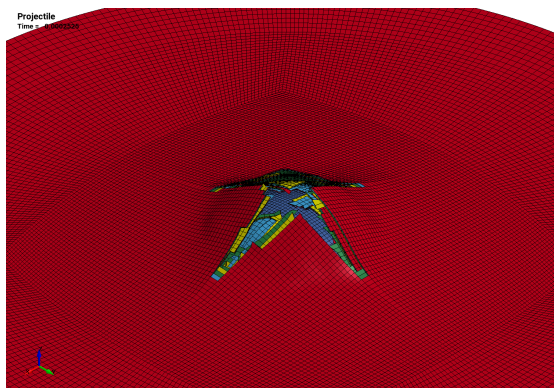


(e)  $t = 0.00125\text{s}$

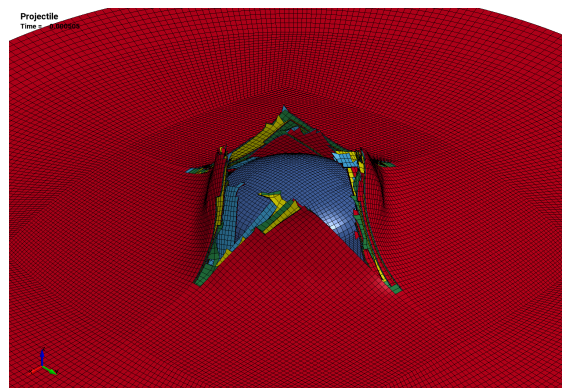


(f)  $t = 0.00150\text{s}$

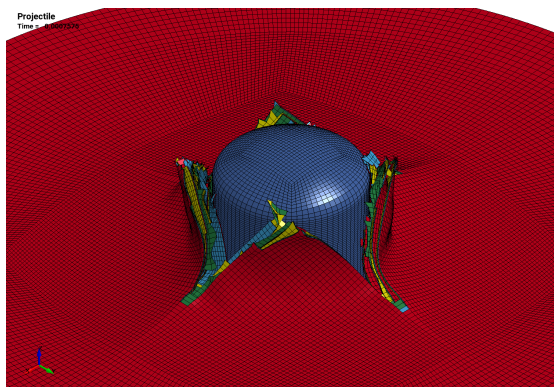
Figure 6.7: LVG1074 ballistic impact simulation



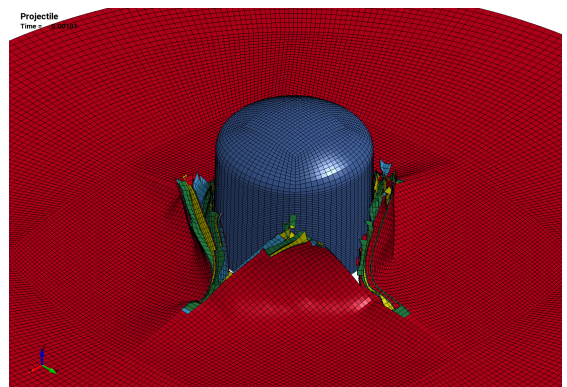
(a)  $t = 0.00025s$



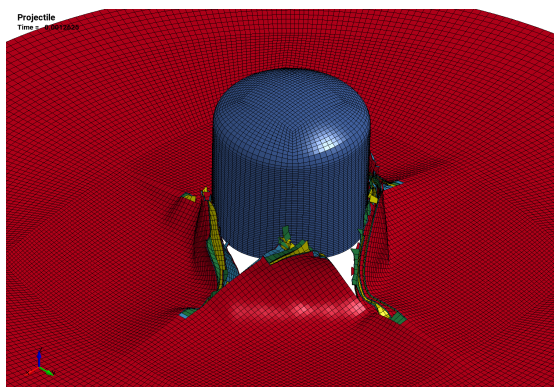
(b)  $t = 0.00050s$



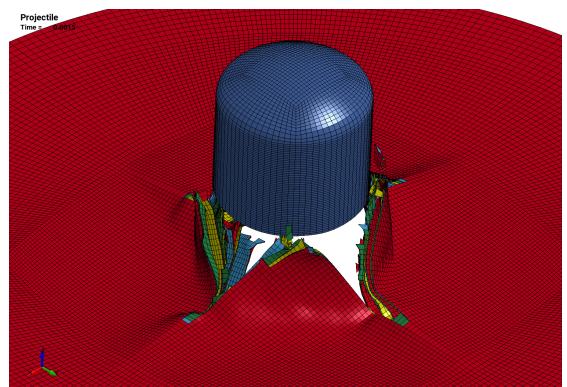
(c)  $t = 0.00075s$



(d)  $t = 0.00100s$



(e)  $t = 0.00125s$



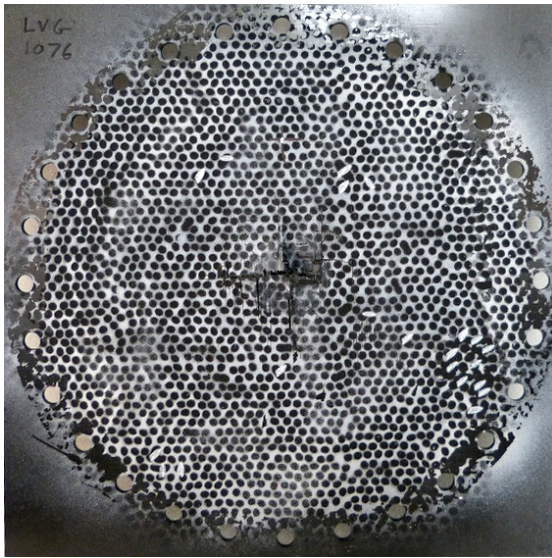
(f)  $t = 0.00150s$

Figure 6.8: LVG1076 ballistic impact simulation

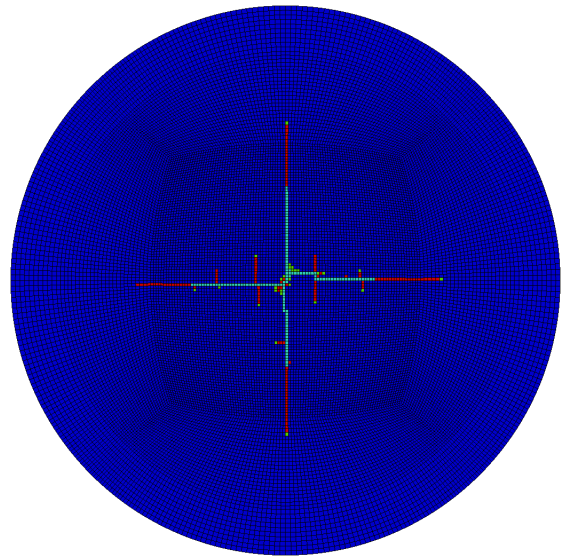
velocity with a vertical fiber direction in the top ply. Figure 6.9b shows the corresponding view at the last simulation time state. Visualization of deformation is turned off in the simulation image to show the exact failure pattern. While the test images represent the state of the plate after the projectile has long passed through the plate, simulating the rebound of the opening in the plate in the simulation would require very long time scales that cannot be simulated efficiently. The elements highlighted in turquoise are the eroded elements, while the elements highlighted in red show the maximum damage value (0.9) that the element reached. Apart from the “cross-like” failure pattern in both test and simulation, elements that were highly damaged along the fiber direction of the top ply can be seen extending up and down vertically from the horizontal crack. In the simulation these damaged elements correspond to similar vertical cracks best seen in Figure 6.9c, which shows a zoomed in view of Figure 6.9a. As a comparison to this zoomed view of the test specimen, Figure 6.9d depicts a close-up view of the same area in the simulation.

Similar images of the back side of the composite plate are shown in Figure 6.10. The fiber direction of the ply facing the camera is again aligned vertically. A “cross-like” fracture pattern can be seen in both the test and the simulation. In the test, damage in the top ply extended close to the clamping region of the plate with parts of this ply being completely separated from the plate. In the simulation, the damaged region also extended further outward in the fiber direction, and transverse to the fibers, showed a similar pattern as in the test. The small vertical fractures parallel to the fibers, similar to the ply facing the impact side, are again visible in both the test and the simulation.

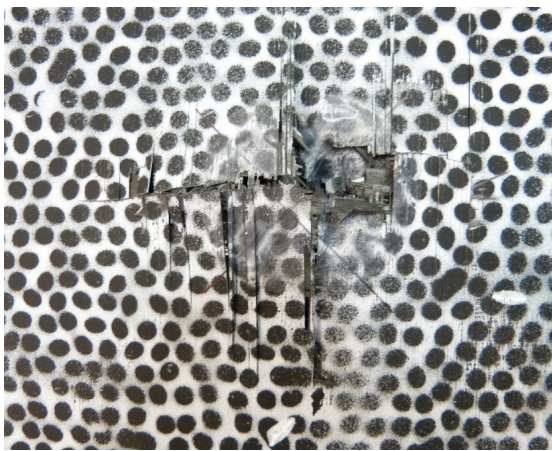
The mesh sensitivity of the erosion criterion was analyzed by repeating one of the simulations (LVG1075) with a rotated mesh. The whole plate was rotated around the z-axis by  $45^\circ$  without changing the fiber direction that was defined in the global coordinate system. Figure 6.11 shows the failure patterns in the simulation with the rotated mesh. The cross like failure pattern is rotated by  $45^\circ$ , which shows the sensitivity of failure to the alignment of the mesh. This is a general problem of the finite element method, as crack propagation can only occur along the mesh lines due to the erosion of elements. Reducing



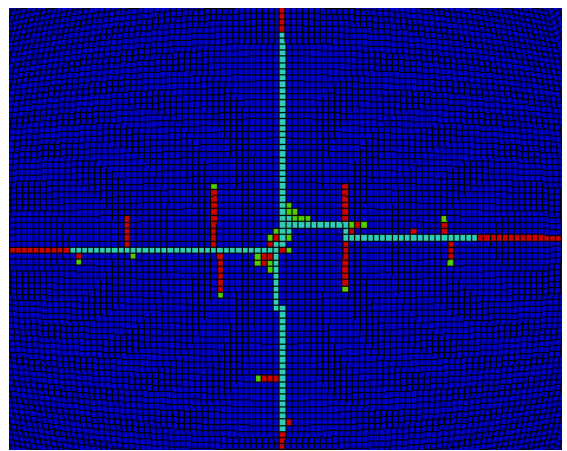
(a) Test impacted side



(b) Simulation impacted side

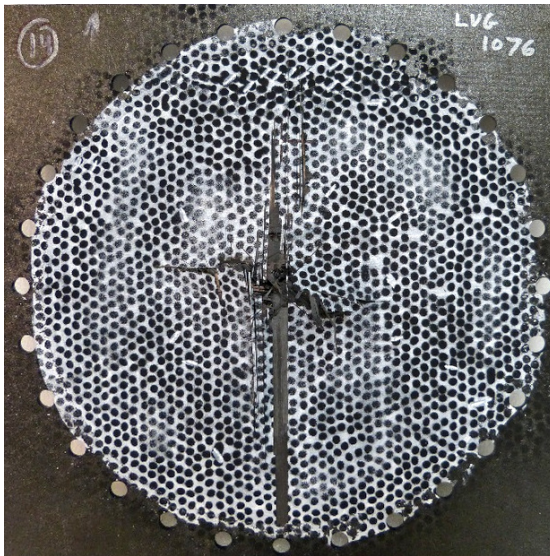


(c) Test impacted side (zoom)

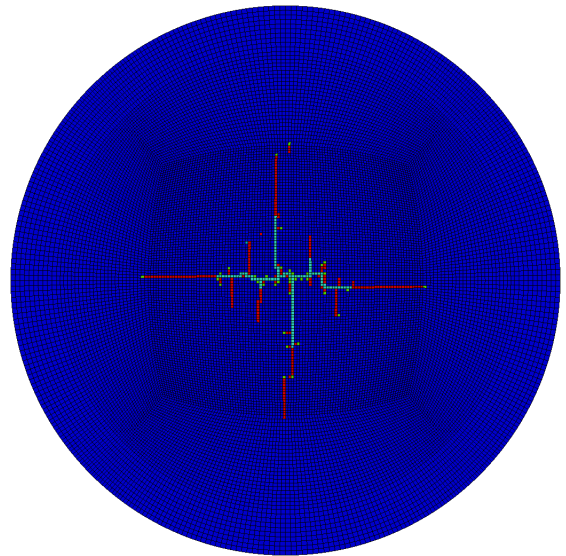


(d) Simulation impacted side (zoom)

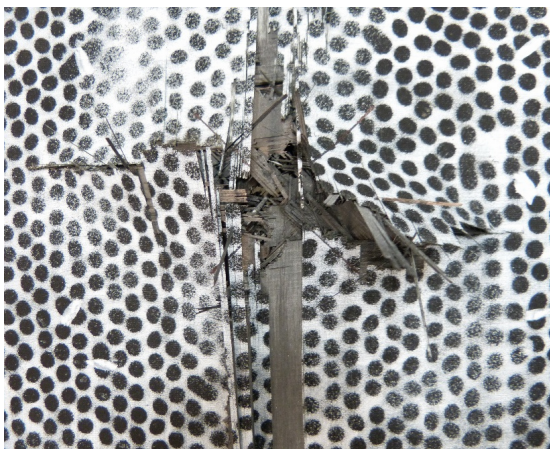
Figure 6.9: LVG1076 ballistic impact, failure patterns on impact side, test versus simulation



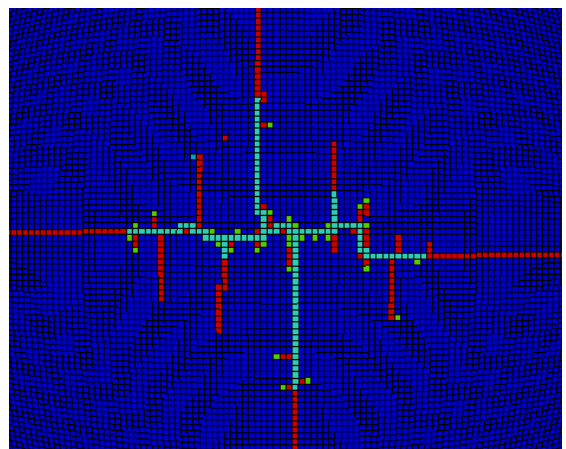
(a) Test back side



(b) Simulation back side



(c) Test back side (zoom)



(d) Simulation back side (zoom)

Figure 6.10: LVG1076 ballistic impact, failure patterns on back side, test versus simulation

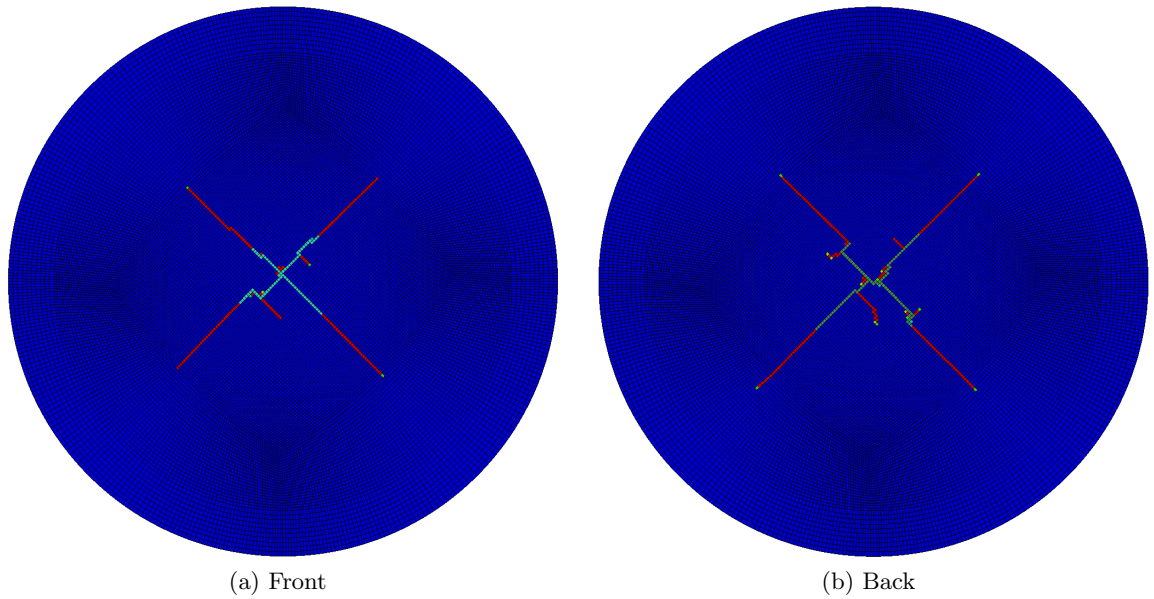


Figure 6.11: Failure patterns in LVG1075 simulation with rotated mesh

the size of the elements significantly can, in some cases, alleviate the sensitivity but might be computationally prohibitive.

Figure 6.12a shows a CT scan of the delaminated area in the LVG1074 impact test. To compare the delaminated area in the simulation, the eroded cohesive elements are highlighted in blue while making the cohesive part 90% transparent. This makes delaminated areas in all plies visible, similar to the CT scan. In the test and simulation delamination covered a similar area, while the shape seemed to be rotated about 45°. This might be an attribute of mesh dependency and alignment; further research to identify the causes would have to be conducted. Delamination can also be modeled using a tiebreak contact in LS-DYNA. Very similar results for the projectile velocities and the delaminated area were achieved using a tiebreak contact with the equivalent contact parameters, as shown in Table 6.1 for the cohesive material. The main advantage of using the tiebreak contact in the shown cases was a significant reduction in CPU time by factors of two to three.

For all three impact velocities, a good agreement between the projectile velocity and failure patterns in test and simulation was achieved. The only parameter that had to be

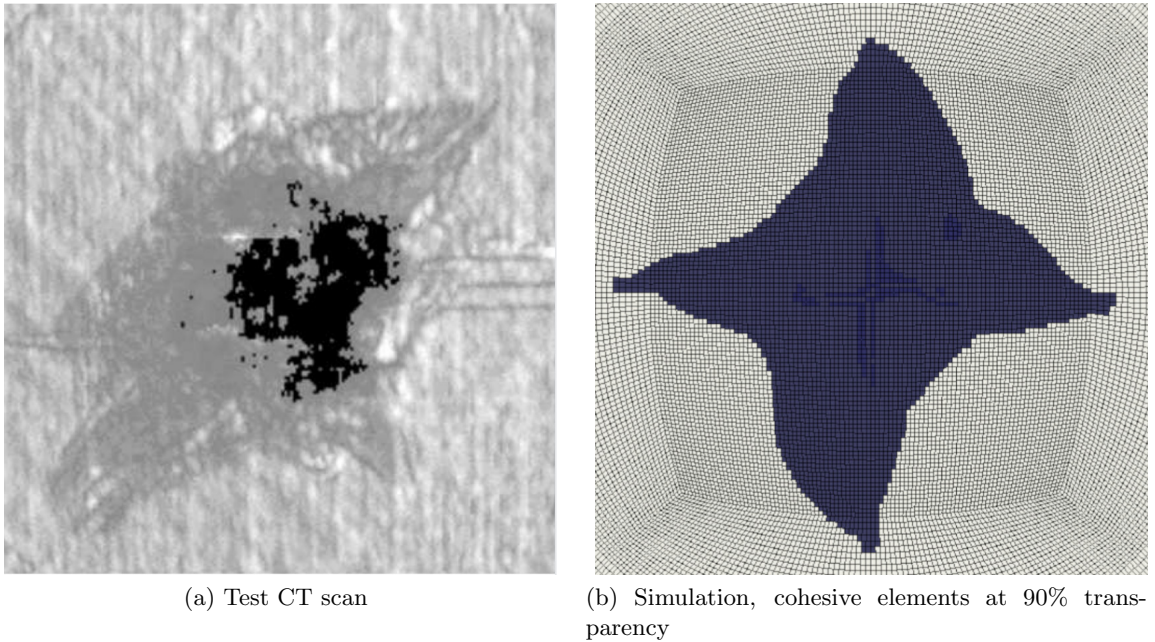


Figure 6.12: LVG1074 ballistic impact, delamination, test versus simulation

adjusted to match test and simulations was the equivalent erosion strain due to lack of experimental data. With more available data on uncoupled and coupled damage terms, the sensitivity of the erosion strain might diminish and make the material model more predictive. Overall, the capabilities to accurately and robustly model ballistic impacts with the shell element material model were shown.

## 6.2 Validation in Crush Loadcase

To reduce weight and increase specific energy absorption of components subjected to crush loading, composite materials have properties that make them valuable in such scenarios. In the best case, a composite component that crushes due to progressive splaying, fragmentation, and localized delamination, can absorb large amounts of energy. If, however, the crushing is not ideally initialized, buckling and global breakage of the part can occur, which reduces the energy absorbing capabilities of the component [65].

In a recent study, Dong et al. calibrated a material model in crush simulations using an adaptive meta-model based on a global optimization strategy to match force-displacement characteristics of several crush experiments [65]. The samples in the study were manufactured using Vacuum assisted Resin Transfer molding (VaRTM) to infuse dry carbon fibers with a low viscosity epoxy resin [65]. The LS-DYNA material model that was calibrated in the study was the continuum damage mechanics model MAT58 and a match between tests and simulations was achieved after several rounds of optimization.

To highlight the capabilities of the new material model, its results were compared to the force-time history obtained by Dong et al. in simulations using MAT58. The material test data that was available at the time of this study did not provide all required information to fully define all necessary inputs for the new material model. For example, test data for compression in fiber and transverse direction was not available. Some of the inputs were therefore defined based on experience from other material combinations of fiber matrix pairings or directly derived from the validated material input used by Dong et al. [65]. Tension in fiber and transverse direction was modeled similarly to what was shown in Chapter 6.1 with the stress and stiffness being degraded to 10% once the maximum stress was reached.

Test data was available for the in-plane shear direction and, therefore, the actual test data was used with the stress and stiffness being degraded to 10% after reaching the maximum stress. Compression in fiber and transverse direction was approximated by linear elastic-ideal plastic stress versus strain curves and no stress degradation. Overall, the material input was defined in a very similar way as shown before for the ballistic impact simulations with a different unidirectional composite. For the crush simulations, the equivalent erosion strain in the general tabulated failure criterion was set to 0.6.

The tested component was a C-channel with a laminate layup of  $[45, -45, 0, 90]_S$  that was crushed with an angle of the loading plate of  $0^\circ$ . The total thickness of the 8 ply layup was 1.889mm. Figure 6.13 shows the simulation setup with the composite plate in red, the fixture plate on the bottom in yellow, and the transparent loading plate that was modeled

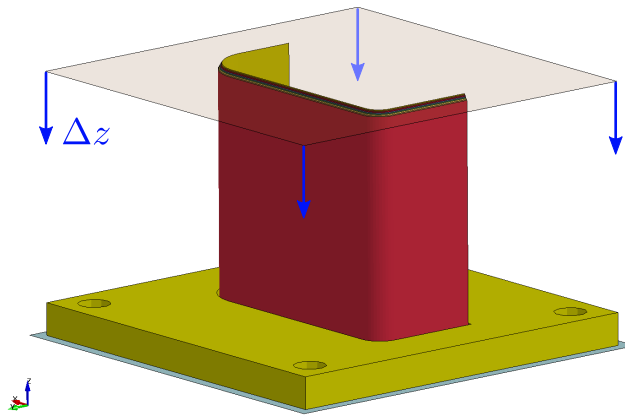


Figure 6.13: Crush simulation setup

using a rigid body. The plate was displaced in  $z$ -direction, as shown by the blue arrows, to crush the composite C-channel.

When modeling composites with shell elements, there are two approaches that are commonly used. First, the different plies with their material orientation can be accounted for by defining a single element through the thickness and having different properties on an integration point level. Figure 6.14a shows the edge of the composite C-channel modeled with a single element through the thickness. For a better distribution of the initial load, the plate was tapered at the top edge. This was modeled in the single element approach by defining a single ply for the top row of elements and two plies for the second row of elements until the full thickness of the plate was reached at the 8th element where all 8 plies were modeled with 8 integration points. With this modeling approach, delamination cannot be accounted for.

The second approach is to model the plies individually with one element per ply. Figure 6.14b shows the edge of the composite C-channel modeled following this approach. The first yellow layer of elements on the left represents the first  $45^\circ$  ply with the following other plies being slightly shorter to account for the tapering of the physical part. Delamination is accounted for by using a tiebreak contact between the individual plies.

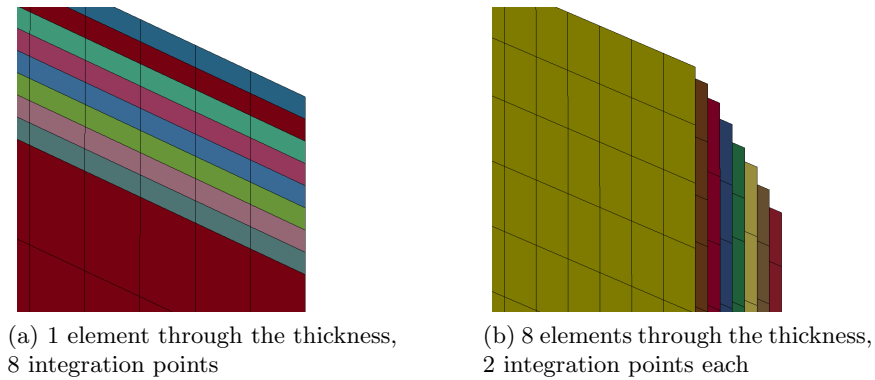


Figure 6.14: C-Channel modeling techniques, edge view

Figure 6.16 shows the deformed geometries at the end of the crush simulations. Unfortunately, no images of the deformed geometry after the physical tests were available. On the left, in Figures 6.15a, 6.15c and 6.15e, the deformed geometry of the part simulated with MAT58 is shown. The fringe colors represent the average amount of damage that has accumulated in the fiber direction in all through-thickness integration points on a scale from zero (blue) to one (red). The C-channel was highly damaged with significant stiffness degradation that extended far beyond the buckled areas. This highlights a potential shortcoming of the continuum damage model utilized in MAT58. Damage in MAT58 is fully coupled, meaning that loading in any material direction will influence the load bearing capabilities in all other directions. When observing a physical composite material, however, it is highly unlikely that this is the case. Consider, for example, loading in tension 2-direction. This type of loading will likely not affect tension in the fiber direction, as the fibers would stay intact even at fracture.

Using the same material input, the crush was also simulated using the modeling approach shown in Figure 6.14b. As the MAT58 material card was optimized for the modeling technique with only one element through the thickness, the material parameters represented an average of the material behavior including delamination and averaging the effects of damage throughout the material. This led to forces that were significantly lower to what

was measured in the test and, therefore, this modeling approach was abandoned for MAT58.

In the images on the right, Figure 6.15b, 6.15d and 6.15f, the deformed geometry obtained using the new material model (MAT213) is shown. The overall buckling modes in the simulations using the validated material model MAT58 and the new material model MAT213 are fairly similar. The maximum damage parameter (tension and shear) is fringe plotted on a scale from zero (blue) to 0.9 (red). Even though only the top and bottom plies are visible in this plot, damage obtained with the new material model is much more localized throughout all plies in the material. This seems to be a better representation of the physical composite material. Some localized delamination at the top of the C-channel can be seen and the part buckles in a more brittle manner when compared to MAT58, where the component folded more smoothly.

In Figure 6.16a the force versus displacement of the physical test specimen are shown as dotted black lines, while the baseline simulation using MAT58 is shown in green. The sudden increase of the force level in the MAT58 simulation can be attributed to the modeling technique with only one element through the thickness. The results using the new material model are shown in red with the maximum force matching the test results very well. Similar to the test, the force increased more slowly as the tapered top of the C-channel was loaded. The force in the tests then dropped to a level below what MAT213 predicted. This part of the force versus displacement curve MAT58 matches fairly well, however, the later increase of force in the region between a displacement of 20mm and 45mm is not represented by the baseline simulation with MAT58. In the available physical test results, in this region of the curve, a large variation between test one and the tests two and three is apparent. This deviation between the different tests can most likely be attributed to different buckling modes and highlights the need for stochastic modeling capabilities in composites. With the new material model, a second peak of the force is visible between a displacement of 30 and 40mm.

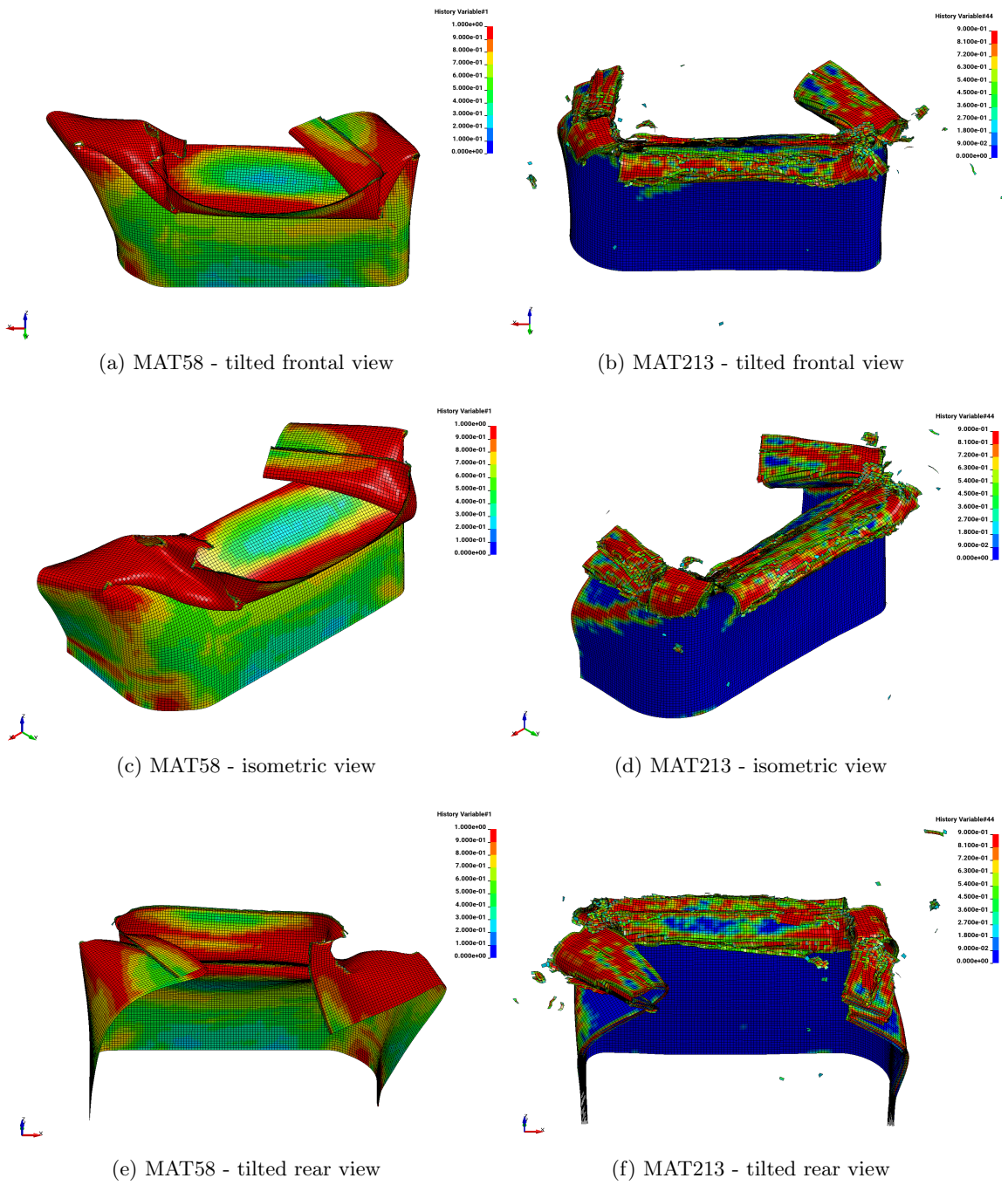


Figure 6.15: Comparison of C-channel crush simulations using MAT58 and MAT213

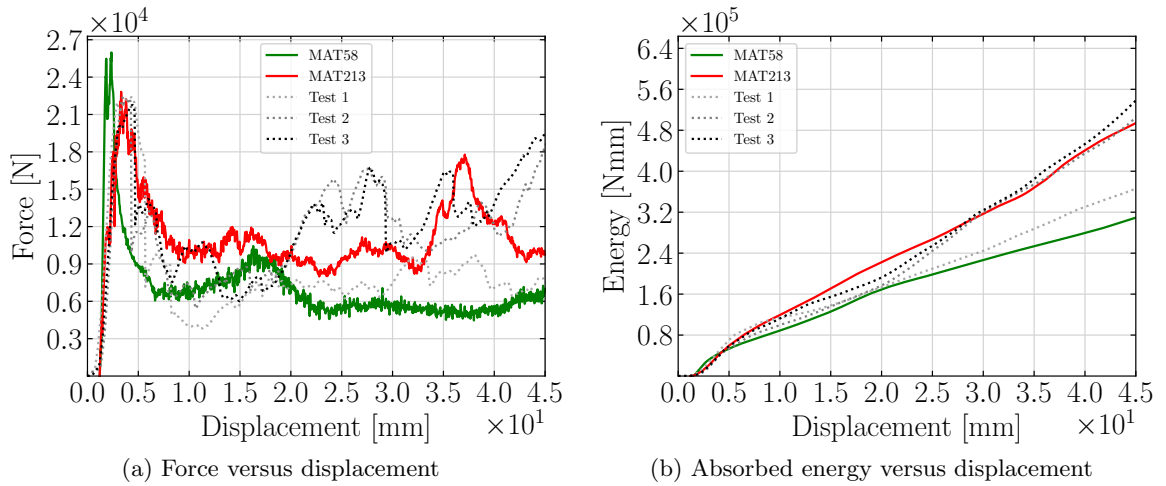


Figure 6.16: Comparison of crush simulations and test results

In automotive crush load cases, the energy absorbed by the component is of great importance. As much impact energy as possible should be absorbed by the crumple zone of the car. Figure 6.16b shows how much energy was absorbed by the composite C-Channel at any given displacement throughout the compressive loading. In tests two and three the absorbed energy was very similar, while the total absorbed energy in the first test was significantly lower. The difference in the test results can most likely be attributed to a different buckling mode that was excited in this test. This highlights the difficulty when dealing with composite materials, which often show a high variability in their material parameters and, consequently, in buckling and failure modes. The new material model matches the total absorbed energy in tests two and three quite accurately, while MAT58 under-predicts the total energy when compared to all three tests.

Even with the limited material test data available, a correlation was achieved between the test results and the simulation using the new material model. The overall buckling modes of the simulation with the new material model resembled the deformed geometry of the fully validated material (MAT58). With more available material test data available, the full potential of the newly developed material model can be utilized and more predictive simulations will be possible.

## Chapter 7: Summary and Conclusion

A new composite material model for plane stress shell elements was developed and implemented that allows the user to simulate a wide variety of composite materials and load cases.

The material model includes capabilities to define tabulated stress versus strain data for the individual material directions with strain-rate and temperature dependency. Strain-rate effects are accounted for in the elastic and plastic region by combining the theories of viscoelasticity and viscoplasticity. Yield stresses in the material are tracked in the individual directions using a generalized Tsai-Wu surface allowing for tension-compression asymmetry. Plasticity in the material is modeled using a non-associated flow rule to allow for precise definition in which material directions plastic flow is possible and to what extent.

Non-linearity of the material response due to damage is decoupled from plasticity based on the assumption of strain equivalency. A diagonal damage tensor is used, which is computed based on uncoupled and coupled damage terms, allowing to track damage accumulation in the material precisely. This ensures that, based on user defined damage versus strain curves, loading in a particular material direction can affect the stress and stiffness in any other direction.

A general tabulated failure model was developed and implemented that makes precise definition of erosion strains for any particular state of stress possible.

The stability of the model was improved by including abilities to smooth strain-rates in simulations with rate-dependent moduli. Robustness improvements have been made to the non-associated plasticity model by switching to an associated formulation on demand in the rare cases where no valid solution with the non-associated flow rule are possible. These robustness improvements are automatic and require no intervention of the user to invoke.

Single element verification simulations were utilized to extensively test the individual capabilities of the material model. Load controlled, minimally constrained single element simulations were conducted to verify the orthotropy, stability, and accuracy of the material model. The model matched the provided input stress versus strain curves precisely without causing instabilities or rigid body rotations or displacements. The yield surface evolution was visualized in these test cases showing the tension-compression asymmetry and directional dependency of the yield stresses in different material directions.

In rate-dependent simulations with the rate-dependent stress versus strain input defined, the model reproduced the corresponding input correctly in all material directions. Additionally, the correct implementation of the rate smoothing was verified, showing how oscillatory off-axis strain-rates can be dampened. Viscoelastic and viscoplastic creep and relaxation were demonstrated in single element simulations under constant stress or strain load, respectively.

When the material deforms plastically, part of the plastic work is converted to heat which leads to a change of the materials response. In temperature-dependent single element simulations, the thermal component of the material model was verified, showing the material model can accurately simulate the rise in temperature and the change of the materials yield stress.

With realistic material data, the material model was utilized in full scale ballistic impact simulations of plates with layups of a unidirectional composite. Only minimal correlation was required to match the measured exit velocities of projectiles in the test at three different impact velocities. In addition, failure patterns and delamination in the ballistic impact simulations were compared to test images and a close correlation was found.

To demonstrate the usability of the material model in crush load cases, a C-channel simulation was compared to test results and to the results of a fully validated industry standard material model. With the limited physical material test data available, a reasonably good correlation between test and simulation was accomplished and an improvement over the previously used material model was achieved.

High quality material data presupposed, the material model furthers the ability of scientists and engineers to accurately model the material behavior of composites in a variety of loading conditions. The model is based on physically meaningful material data and does not rely on time intensive computational calibration. In its current state, while not fully predictive, the new material model marks a step in the direction of achieving the first predictive composite material model. Further research into obtaining erosion criteria from mechanical property tests, rather than from correlation to impact or crush tests, will be required to enhance the predictive capabilities of the model.

One of the current limitations is that constant flow rule coefficients are assumed. In the physical unidirectional composite material, for example, while linear elastic in compression 1-direction at room temperature, plastic behavior at higher temperatures is highly likely. For an improvement of the model, the flow rule coefficients should therefore be made dependent on strain-rate and temperature to allow for a more precise definition of plastic flow behavior of the material. Furthermore, the implemented tabulated failure model could be further generalized to allow for definition of rate and temperature-dependent failure strains.

Future research and implementation efforts to improve the material model should focus on these limitations. This will ensure that all available test data can be taken into account in the future and improve the predictive capabilities of the material model.

## Appendix A: Matlab/Octave script

The simple Matlab [64] / Octave [63] script shown as Code A.1, allows to compute the required damage input for the material model for a given effective stress and true stress versus strain curve. Two CSV (Comma-separated value) files with the total strain in the first column and the true stress (*true\_stress\_vs\_strain\_input.csv*) and effective stress (*effective\_stress\_vs\_strain\_input.csv*) in the second column should be provided in the same folder as the script when executed. The total strain versus damage output will then be saved in the file *damage\_vs\_strain\_output.csv*. The true stress versus strain curve will then act as the input curve to the MAT213 material model while the damage versus strain curve is the input to the damage model for the corresponding direction.

Code A.1: Matlab/Octave script to compute damage curve for given effective and true stress versus strain curves

```
1 % Read filename of true stress vs. total strain input
2 filename_true = 'true_stress_vs_strain_input.csv';
3 % Read filename of effective stress vs. total strain input
4 filename_effective = 'effective_stress_vs_strain_input.csv';
5 % Read filename of damage vs. total strain output
6 filename_damage = 'damage_vs_strain_output.csv';
7 % Read data from true stress vs. strain input
8 true = csvread(filename_true);
9 strain_true = true(:,1);
10 stress_true = true(:,2);
11 % Read data from effective stress vs. strain input
12 effective = csvread(filename_effective);
13 strain_effective = effective(:,1);
14 stress_effective = effective(:,2);
15 % Use interpolation to make strain axis equivalent
16 stress_effective = interp1(strain_effective, stress_effective, strain_true);
17 strain_effective = strain_true;
18 % Compute damage vs. strain
19 d = 1 - stress_true ./ stress_effective;
20 % Plot damage vs. strain
21 subplot(1,2,1)
22 plot(strain_effective, d)
23 grid on
24 xlabel('Strain [-]');
```

```

25 ylabel('Damage parameter [-]');
26 legend('Damage parameter (output)')
27 % Plot true stress vs. strain
28 subplot(1,2,2)
29 plot(strain_true,stress_true)
30 % Plot effective stress vs. strain
31 hold on
32 plot(strain_effective,stress_effective)
33 grid on
34 xlabel('Strain [-]');
35 ylabel('Stress [psi]');
36 legend('True stress (input)', 'Effective stress (input)')
37 % Write damage vs. strain output to file
38 csvwrite(filename_damage,[strain_true(:),d(:)])

```

## Appendix B: Mathematica script

Figure B.1 shows the results obtained using Mathematica [66] to simplify Equations 4.26 and 4.27. Note that  $\frac{E_{22}\nu_{12}}{E_{11}} = \nu_{21}$ .

```

In[233]= q12 = (v21 + v31 * v23) / (E22 * E33);
          q13 = (v31 + v21 * v32) / (E22 * E33);
          q23 = (v32 + v12 * v31) / (E11 * E33);
          q11 = (1 - v23 * v32) / (E22 * E33);
          q22 = (1 - v13 * v31) / (E11 * E33);
          q33 = (1 - v21 * v12) / (E11 * E22);

          Simplify[(q12 - (q13 * q23) / (q33)) / (q22 - (q23^2) / (q33))]
          Simplify[(q12 - (q13 * q23) / (q33)) / (q11 - (q13^2) / (q33))]

Out[239]= v12

Out[240]=  $\frac{E_{22} \nu_{12}}{E_{11}}$ 

```

Figure B.1: Simplification of Equations 4.26 and 4.27

## Bibliography

## Bibliography

- [1] S. Hartmann, T. Klöppel, and C. Liebold, “Introduction to Composite Material Modeling with LS-DYNA,” Stuttgart, Germany, Mar. 2017.
- [2] B. Wade and P. Feraboli, “Crushing Behavior of Laminated Composite Structural Elements: Experiment and LS-DYNA Simulation,” Dec. 2016.
- [3] C. Hoffarth, “A Generalized Orthotropic Elasto-Plastic Material Model for Impact Analysis,” Ph.D., Arizona State University, Phoenix, Arizona, 2016. [Online]. Available: <http://search.proquest.com/docview/1841248778/abstract/9987E5EAC7364A3BPQ/1>
- [4] J. O. Hallquist, *LS-DYNA - Keyword User's Manual - Volume II - Material Models*. Livermore, California: Livermore Software Technology Corporation (LSTC), Sep. 2015.
- [5] B. Harris, *Engineering composite materials*. London: The Institute of Materials, 1999.
- [6] A. Gilat, R. K. Goldberg, and G. D. Roberts, “Experimental study of strain-rate-dependent behavior of carbon/epoxy composite,” *Composites Science and Technology*, vol. 62, no. 10-11, pp. 1469–1476, Aug. 2002. [Online]. Available: <https://linkinghub.elsevier.com/retrieve/pii/S0266353802001008>
- [7] C.-H. Shen and G. S. Springer, “Effects of moisture and temperature on the tensile strength of composite materials,” *Journal of Composite Materials*, vol. 11, no. 1, pp. 2–16, 1977.
- [8] F.-K. Chang and K.-Y. Chang, “A progressive damage model for laminated composites containing stress concentrations,” *Journal of composite materials*, vol. 21, no. 9, pp. 834–855, 1987. [Online]. Available: <http://journals.sagepub.com/doi/abs/10.1177/002199838702100904>
- [9] S. W. Tsai and E. M. Wu, “A general theory of strength for anisotropic materials,” *Journal of composite materials*, vol. 5, no. 1, pp. 58–80, 1971. [Online]. Available: <http://journals.sagepub.com/doi/abs/10.1177/002199837100500106>
- [10] A. Matzenmiller, J. Lubliner, and R. L. Taylor, “A constitutive model for anisotropic damage in fiber-composites,” *Mechanics of materials*, vol. 20, no. 2, pp. 125–152, 1995.
- [11] Z. Hashin, “Failure Criteria for Unidirectional Fiber Composites,” *Journal of Applied Mechanics*, vol. 47, pp. 329 – 334, Jun. 1980.

- [12] S. Pinho, L. Iannucci, and P. Robinson, “Physically-based failure models and criteria for laminated fibre-reinforced composites with emphasis on fibre kinking: Part I: Development,” *Composites Part A: Applied Science and Manufacturing*, vol. 37, no. 1, pp. 63–73, Jan. 2006. [Online]. Available: <https://linkinghub.elsevier.com/retrieve/pii/S1359835X05002198>
- [13] —, “Physically based failure models and criteria for laminated fibre-reinforced composites with emphasis on fibre kinking. Part II: FE implementation,” *Composites Part A: Applied Science and Manufacturing*, vol. 37, no. 5, pp. 766–777, May 2006. [Online]. Available: <https://linkinghub.elsevier.com/retrieve/pii/S1359835X05002708>
- [14] P. Maimí, P. Camanho, J. Mayugo, and C. Dávila, “A continuum damage model for composite laminates: Part I – Constitutive model,” *Mechanics of Materials*, vol. 39, no. 10, pp. 897–908, Oct. 2007. [Online]. Available: <https://linkinghub.elsevier.com/retrieve/pii/S0167663607000543>
- [15] —, “A continuum damage model for composite laminates: Part II – Computational implementation and validation,” *Mechanics of Materials*, vol. 39, no. 10, pp. 909–919, Oct. 2007. [Online]. Available: <https://linkinghub.elsevier.com/retrieve/pii/S0167663607000555>
- [16] R. Talreja, “A Continuum Mechanics Characterization of Damage in Composite Materials,” *Proceedings of the Royal Society A: Mathematical, Physical and Engineering Sciences*, vol. 399, no. 1817, pp. 195–216, Jun. 1985. [Online]. Available: <http://rspa.royalsocietypublishing.org/cgi/doi/10.1098/rspa.1985.0055>
- [17] E. J. Barbero, *Finite element analysis of composite materials using Abaqus*, ser. Composite materials, design and analysis. Boca Raton, FL: CRC Press, Taylor & Francis Group, 2013.
- [18] C. T. Sun and J. L. Chen, “A simple flow rule for characterizing nonlinear behavior of fiber composites,” *Journal of Composite Materials*, vol. 23, no. 10, pp. 1009–1020, 1989. [Online]. Available: <http://jcm.sagepub.com/content/23/10/1009.short>
- [19] Department of Defense, *Composite Materials Handbook - Volume 3, Polymer Matrix Composites Materials, Usage, Design, and Analysis*. United States of America, Pentagon: Departments of Defense, Jun. 2002.
- [20] B. W. Rosen, “Tensile failure of fibrous composites,” *AIAA journal*, vol. 2, no. 11, pp. 1985–1991, 1964.
- [21] D. Gücer and J. Gurland, “Comparison of the statistics of two fracture modes,” *Journal of the Mechanics and Physics of Solids*, vol. 10, no. 4, pp. 365–373, 1962.
- [22] B. W. Rosen and C. H. Zweben, “Tensile failure criteria for fiber composite materials,” 1972.
- [23] D. Harlow and S. Phoenix, “The Chain-of-Bundles Probability Model for the Strength of Fibrous Materials II: A Numerical Study of Convergence,” *Journal of Composite Materials*, vol. 12, no. 3, pp. 314–334, Oct. 1978. [Online]. Available: <http://journals.sagepub.com/doi/10.1177/002199837801200308>

- [24] B. Budiansky and N. Fleck, “Compressive failure of fibre composites,” *Journal of the Mechanics and Physics of Solids*, vol. 41, no. 1, pp. 183–211, Jan. 1993. [Online]. Available: <https://linkinghub.elsevier.com/retrieve/pii/002250969390068Q>
- [25] H. M. Deuschle and A. Puck, “Application of the Puck failure theory for fibre-reinforced composites under three-dimensional stress: Comparison with experimental results,” *Journal of Composite Materials*, vol. 47, no. 6-7, pp. 827–846, Mar. 2013. [Online]. Available: <http://journals.sagepub.com/doi/10.1177/0021998312462158>
- [26] H. M. Deuschle, *3D failure analysis of UD fibre reinforced composites: Puck’s theory within FEA*. Stuttgart: Inst. für Statik und Dynamik der Luft- und Raumfahrtkonstruktionen, 2010, oCLC: 706906152.
- [27] O. Mohr, “Welche umstände bedingen die elastizitätsgrenze und den bruch eines materials,” *Zeitschrift des Vereins Deutscher Ingenieure*, vol. 46, no. 1524-1530, pp. 1572–1577, 1900.
- [28] A. Puck and H. Schürmann, “Failure analysis of frp laminates by means of physically based phenomenological models,” in *Failure Criteria in Fibre-Reinforced-Polymer Composites*. Elsevier, 2004, pp. 832–876.
- [29] H. Matthias Deuschle and B.-H. Kröplin, “Finite element implementation of Puck’s failure theory for fibre-reinforced composites under three-dimensional stress,” *Journal of Composite Materials*, vol. 46, no. 19-20, pp. 2485–2513, Sep. 2012. [Online]. Available: <http://journals.sagepub.com/doi/10.1177/0021998312451480>
- [30] “Standard Test Method for Mode I Interlaminar Fracture Toughness of Unidirectional Fiber-Reinforced Polymer Matrix Composites,” ASTM International, Tech. Rep., 2013.
- [31] “Standard Test Method for Determination of the Mode II Interlaminar Fracture Toughness of Unidirectional Fiber-Reinforced Polymer Matrix Composites,” ASTM International, Tech. Rep., 2014.
- [32] V. Tvergaard and J. W. Hutchinson, “The relation between crack growth resistance and fracture process parameters in elastic-plastic solids,” *Journal of the Mechanics and Physics of Solids*, vol. 40, no. 6, pp. 1377–1397, 1992.
- [33] S. Marzi, O. Hesebeck, M. Brede, F. Kleiner, and H. Ag, “A Rate-Dependent, Elastoplastic Cohesive Zone Mixed-Mode Model for Crash Analysis of Adhesively Bonded Joints,” p. 11, 2009.
- [34] B. M. Khaled, L. Shyamsunder, N. Holt, C. G. Hoover, S. D. Rajan, and G. Blankenhorn, “Enhancing the predictive capabilities of a composite plasticity model using cohesive zone modeling,” *Composites Part A: Applied Science and Manufacturing*, vol. 121, pp. 1–17, Jun. 2019. [Online]. Available: <https://linkinghub.elsevier.com/retrieve/pii/S1359835X19300740>
- [35] G. Nilakantan, *Modeling the Impact of Flexible Textile Composites through Multiscale and Probabilistic Methods*. Newark: University of Delaware, 2010.

- [36] M. Goldsmith, “Probabilistic micromechanics of woven ceramic matrix composites,” Ph.D. dissertation, 2013, copyright - Database copyright ProQuest LLC; ProQuest does not claim copyright in the individual underlying works; Last updated - 2016-06-04. [Online]. Available: <https://search.proquest.com/docview/1547360227?accountid=14541>
- [37] M. B. Goldsmith, B. V. Sankar, R. T. Haftka, and R. K. Goldberg, “Effects of microstructural variability on thermo-mechanical properties of a woven ceramic matrix composite,” *Journal of Composite Materials*, vol. 49, no. 3, pp. 335–350, Feb. 2015. [Online]. Available: <http://journals.sagepub.com/doi/10.1177/0021998313519151>
- [38] T. M. Ricks, T. E. Lacy, B. A. Bednarczyk, S. M. Arnold, and J. W. Hutchins, “A Multiscale Progressive Failure Modeling Methodology for Composites That Includes Fiber Strength Stochastics,” p. 30, 2014.
- [39] T. Ricks, T. Lacy, B. Bednarczyk, and S. Arnold, “A Multiscale Modeling Methodology for Metal Matrix Composites Including Fiber Strength Stochastics.” Honolulu, Hawaii: American Institute of Aeronautics and Astronautics, Apr. 2012. [Online]. Available: <http://arc.aiaa.org/doi/abs/10.2514/6.2012-1965>
- [40] K. Liu, “Micromechanics Based Multiscale Modeling of the Inelastic Response and Failure of Complex Architecture Composites,” Ph.D. dissertation, Arizona State University, Dec. 2011.
- [41] E. A. d. S. Neto, D. Perić, and D. R. J. Owen, *Computational methods for plasticity: theory and applications*. Chichester, West Sussex, UK: Wiley, 2008, oCLC: ocn209799487.
- [42] B. M. Lempriere, “Poisson’s ratio in orthotropic materials.” *AIAA Journal*, vol. 6, no. 11, pp. 2226–2227, 1968.
- [43] Univ.-Prof. Dr.-Ing. habil. Alexander Lion, “Einführung in die Lineare Viskoeplastizität,” *Beiträge zur Materialtheorie*, no. 4/07, May 2007. [Online]. Available: [https://www.unibw.de/lrt4/veroeffentlichungen/bzm\\_heft\\_4.07.pdf](https://www.unibw.de/lrt4/veroeffentlichungen/bzm_heft_4.07.pdf)
- [44] W. Feng, K. Reifsnider, G. Sendecyk, T. Chiao, G. Rodericks, W. Stinchcomb, L. de Vore, W. Feng, and W. Yang, “General and Specific Quadratic Yield Functions,” *Journal of Composites Technology and Research*, vol. 6, no. 1, p. 19, 1984. [Online]. Available: <http://www.astm.org/doiLink.cgi?CTR10878J>
- [45] R. K. Goldberg, K. S. Carney, P. Du Bois, C. Hoffarth, J. Harrington, S. Rajan, and G. Blankenhorn, “Development of an Orthotropic Elastoplastic Generalized Composite Material Model Suitable for Impact Problems,” *Journal of Aerospace Engineering*, p. 04015083, 2015. [Online]. Available: [http://ascelibrary.org/doi/abs/10.1061/\(ASCE\)AS.1943-5525.0000580](http://ascelibrary.org/doi/abs/10.1061/(ASCE)AS.1943-5525.0000580)
- [46] R. V. Mises, “Mechanik der plastischen Formänderung von Kristallen,” *ZAMM - Journal of Applied Mathematics and Mechanics / Zeitschrift für Angewandte Mathematik und Mechanik*, vol. 8, no. 3, pp. 161–185, 1928. [Online]. Available: <https://onlinelibrary.wiley.com/doi/abs/10.1002/zamm.19280080302>

- [47] A. S. Khan and S. Huang, *Continuum theory of plasticity*. John Wiley & Sons, 1995.
- [48] A. Trojanowski, C. Ruiz, and J. Harding, “Thermomechanical Properties of Polymers at High Rates of Strain,” *Le Journal de Physique IV*, vol. 07, no. C3, pp. C3–447–C3–452, Aug. 1997. [Online]. Available: <http://www.edpsciences.org/10.1051/jp4:1997377>
- [49] W. S. Farren and G. I. Taylor, “The heat developed during plastic extension of metals,” *Proceedings of the Royal Society of London. Series A, Containing Papers of a Mathematical and Physical Character*, vol. 107, no. 743, pp. 422–451, 1925.
- [50] G. I. Taylor and H. Quinney, “The Latent Energy Remaining in a Metal after Cold Working,” *Proceedings of the Royal Society A: Mathematical, Physical and Engineering Sciences*, vol. 143, no. 849, pp. 307–326, Jan. 1934. [Online]. Available: <http://rspa.royalsocietypublishing.org/cgi/doi/10.1098/rspa.1934.0004>
- [51] D. Rittel, “On the conversion of plastic work to heat during high strain rate deformation of glassy polymers,” *Mechanics of Materials*, vol. 31, no. 2, pp. 131–139, Feb. 1999. [Online]. Available: <https://linkinghub.elsevier.com/retrieve/pii/S0167663698000635>
- [52] J. Lemaitre and R. Desmorat, *Engineering damage mechanics: ductile, creep, fatigue and brittle failures*. Springer Science & Business Media, 2005.
- [53] R. K. Goldberg, K. S. Carney, P. Du Bois, C. Hoffarth, S. Rajan, and G. Blackenhorn, “Incorporation of Plasticity and Damage Into an Orthotropic Three-Dimensional Model with Tabulated Input Suitable for Use in Composite Impact Problems,” 2015. [Online]. Available: <http://ntrs.nasa.gov/search.jsp?R=20150019390>
- [54] T. Ogasawara, T. Ishikawa, T. Yokozeki, T. Shiraishi, and N. Watanabe, “Effect of on-axis tensile loading on shear properties of an orthogonal 3d woven SiC/SiC composite,” *Composites Science and Technology*, vol. 65, no. 15-16, pp. 2541–2549, Dec. 2005. [Online]. Available: <https://linkinghub.elsevier.com/retrieve/pii/S026635380500206X>
- [55] M. Salavatian and L. Smith, “The effect of transverse damage on the shear response of fiber reinforced laminates,” *Composites Science and Technology*, vol. 95, pp. 44–49, May 2014. [Online]. Available: <https://linkinghub.elsevier.com/retrieve/pii/S026635381400058X>
- [56] R. K. Goldberg, K. S. Carney, P. Du Bois, C. Hoffarth, S. Rajan, and G. Blankenhorn, “Analysis and Characterization of Damage Utilizing an Orthotropic Generalized Composite Material Model Suitable for Use in Impact Problems,” 2016.
- [57] R. K. Goldberg, K. S. Carney, P. Du Bois, C. Hoffarth, B. Khaled, L. Shyamsunder, S. Rajan, and G. Blankenhorn, “Incorporation of Failure Into an Orthotropic Three-Dimensional Model with Tabulated Input Suitable for Use in Composite Impact Problems,” 2017.
- [58] C. Hoffarth, S. D. Rajan, R. K. Goldberg, K. S. Carney, P. Du Bois, and G. Blankenhorn, “Implementation and Validation of a Three-Dimensional Material Model for Orthotropic Composites,” Tech. Rep., 2015.

- [59] J. O. Hallquist, *LS-DYNA - Keyword User's Manual - Volume I*. Livermore, California: Livermore Software Technology Corporation (LSTC), Sep. 2015.
- [60] B. Khaled, L. Shyamsunder, C. Hoffarth, S. D. Rajan, R. K. Goldberg, K. S. Carney, P. Du Bois, and G. Blankenhorn, "Experimental characterization of composites to support an orthotropic plasticity material model," *Journal of Composite Materials*, vol. 52, no. 14, pp. 1847–1872, Jun. 2018. [Online]. Available: <http://journals.sagepub.com/doi/10.1177/0021998317733319>
- [61] D. L. Smith and M. B. Dow, "Properties of Three Resin Composites," *NASA Technical Paper 3102*, p. 50, Sep. 1991. [Online]. Available: <https://ntrs.nasa.gov/archive/nasa/casi.ntrs.nasa.gov/19920000849.pdf>
- [62] J.-L. Battaglia, M. Saboul, J. Pailhes, A. Saci, A. Kusiak, and O. Fudym, "Carbon epoxy composites thermal conductivity at 77 k and 300 k," *Journal of Applied Physics*, vol. 115, no. 22, p. 223516, 2014.
- [63] J. W. Eaton, D. Bateman, S. Hauberg, and R. Wehbring, *GNU Octave version 4.2.1 manual: a high-level interactive language for numerical computations*, 2017. [Online]. Available: <https://www.gnu.org/software/octave/doc/v4.2.1/>
- [64] *MATLAB version 9.5.0.944444 (R2018b)*, The Mathworks, Inc., Natick, Massachusetts, 2018. [Online]. Available: <https://www.mathworks.com/matlab>
- [65] S. Dong, A. Sheldon, and K. Carney, "Modeling of Carbon-Fiber-Reinforced Polymer (CFRP) Composites in LS-DYNA® with Optimization of Material and Failure Parameters in LS-OPT®." 15th International LS-DYNA Users Conference, 2018.
- [66] Wolfram Research, Inc., "Mathematica, Version 12.0," champaign, IL, 2019. [Online]. Available: <https://www.wolfram.com/mathematica>

## Curriculum Vitae

Tobias Achstetter graduated from Matthias Grünwald Gymnasium, Tauberbischofsheim, Germany (High School) in 2010. In 2014, he received his Bachelor of Science in Mechanical Engineering from the University of Stuttgart, Germany. In 2015, he received his Masters of Science from George Mason University in Computational Science.